Methodological developments in electron spin resonance (ESR) low-temperature thermochronometry

Fang Fang

Thesis submitted for the degree of Doctor of Philosophy

of The Australian National University

March 2020

Declaration

Hereby I declare and confirm that this thesis represents my own work, except where otherwise acknowledged.

Fang Fang

Abstract

Low-temperature thermochronometry provides a means of understanding the interaction between surface processes and underlying tectonics by quantifying the cooling histories of rocks. Electron spin resonance (ESR) thermochronometry works by determining the timing and rate at which electrons are trapped and thermally released in quartz in response to *in situ* ionizing radiation and rock cooling. This technique has great potential in reconstructing thermal histories of the upper ~ 2 km of the Earth's crust during the Quaternary. Its application, however, faces many challenges for methodological improvement since little work has been done on ESR thermochronometry after being first introduced in the late 1990s.

Quantitative investigations of thermal histories by ESR thermochronometry rely on the determination of trap parameters of paramagnetic centres in quartz. This study has evaluated the activation energy and frequency factor of Al and Ti centres by analysing borehole samples with well-defined thermal histories and storage temperatures. Fergusons Hill-1 core is located at Otway Basin (Australia) where it is in a thermally steady state, while Eldzhurtinskiy Granite core is located in the Caucasus where it has experienced rapid cooling at a rate of ~ 520 °C/Ma. The best-fit parameters were determined by a first-order kinetic model which quantifies the irradiation-induced trapping and thermally-related detrapping processes.

In heterogeneous rocks, numerical simulation is an ideal solution for accurate estimation of beta dose rate. Identification of mineral distribution is the basis for creating a model, and 2D mapping facilities are more effective than 3D X-ray computed tomography in this aspect. Thus, a 2D model “DosiVox-2D” was established for heterogeneous but isotropic samples, and verified by the comparison with the 3D model and infinite matrix dose method. The practical procedures were then investigated for applying 2D simulation on uniform and layered igneous rocks, including sample selection, mineral mapping, and estimation of radioelement concentrations.

Thereafter, ESR thermochronometry was applied to Namche Barwa massif, the eastern Himalayan syntaxis. Samples were collected from a vertical transect to the south of the massif. ESR results, on one hand, have improved our understanding of the localised structural settings. On the other hand, the comparison of cooling history with the region adjacent to the north of the massif, has shed light on the domal development of Namche Barwa massif during Mid-late Pleistocene.

Table of Contents

Declaration ii

Abstract iii

Table of Contents v

List of Tables ix

List of Figures x

List of Acronyms xvi

List of Publications xix

Acknowledgements xx

1 Scope of the project 1

2 Introduction to electron spin resonance dating 3

2.1 Physical basis 3

2.2 Paramagnetic centres 5

2.2.1 Structure and spectroscopic features 5

2.2.2 Thermal properties 8

2.3 Estimation of equivalent dose (D_e) 12

2.4 Estimation of dose rate ($\dot{D}$) 14

2.4.1 Beta dose rate 15

2.4.2 Gamma dose rate 16

2.5 Applications in thermochronometry 17

2.5.1 Geological process and thermochronometry 17

2.5.2 Current status and challenges of ESR thermochronometry 20

3 ESR thermochronometry of Al and Ti centres in quartz: A case study of the Fergusons Hill-1 borehole from the Otway Basin, Australia 23

3.1 Introduction 24

3.2 Sample descriptions 26

3.3 Methodology 27

3.3.1 Sample preparation 27

3.3.2 ESR measurements 28

3.3.3 Test for sensitivity change 29
3.3.4 Estimation of equivalent dose (D_e) 30
3.3.5 Dose rate ($\dot{D}$) calculation 31
3.4 First order kinetic model 31
3.4.1 Mathematical equations 31
3.4.2 Fitting procedure 33
3.5 Results 34
3.5.1 Ambient temperature of selected FH1 samples 34
3.5.2 The estimation of trap parameters 35
3.6 Discussion 37
3.6.1 Comparison with trap parameters determined from the Eldzhutinskiy Granite 37
3.6.2 Comparison of results from lab annealing experiments and natural settings 39
3.6.3 Comparison of closure temperatures between ESR and other thermochronometry 41
3.7 Summary and conclusions 42
4 2D modelling: a Monte Carlo approach for assessing heterogeneous beta dose rate in luminescence and ESR dating 43
4.1 The comparison of scanning techniques in mineral identification 45
4.1.1 Introduction 45
4.1.2 Sample description and preparation 46
4.1.3 Methodology 47
4.1.4 Results and discussion 48
4.1.5 Summary 53
4.2 Paper I, Theory and verification 55
4.3 Paper II, Application to igneous rocks 69
5 ESR thermochronometric evidence for accelerated Mid-Pleistocene exhumation of the Namche Barwa massif, eastern Himalayan syntaxis 81
5.1 Introduction 82

5.2 Background 83
5.2.1 Geological and geomorphological settings 83
5.2.2 Previous thermochronometric constraints 85
5.3 Methodology 86
5.3.1 Sample collection and preparation 86
5.3.2 ESR measurements 87
5.3.3 Estimation of equivalent dose (D_e) and dose rate ($\dot{D}$) 89
5.3.4 The calculation of cooling rate 89
5.4 Results 91
5.4.1 I_1/I_2 ratio 91
5.4.2 ESR ages of Al and Ti centres 92
5.4.3 The cooling and exhumation rates 95
5.5 Discussion 96
5.5.1 The localised geological structure and thermochronometric results 96
5.5.2 The development of Namche Barwa massif during Mid to Late Pleistocene 97
5.6 Summary and conclusions 98
6 Conclusions and future directions 99
7 References 103
8 Appendix 117
8.1 Supplementary material: ESR thermochronometry of Al and Ti centres in quartz: A case study of the Fergusons Hill-1 borehole from the Otway Basin, Australia 118
8.1.1 The calibration of in-air X-ray dose rate 118
8.1.2 The calibration of X-ray dose rate on quartz 119
8.2 Supplementary material: ESR thermochronometric evidence for accelerated Mid-Pleistocene exhumation of the Namche Barwa massif, eastern Himalayan syntaxis 121
8.2.1 Sample collection and preparation 121
8.2.2 Microwave power 122

8.2.3 Isothermal annealing time 123
8.3 A comprehensive chronology of the Neanderthal site Moula-Guercy, Ardèche, France 125
8.4 The Acheulian and Early Middle Paleolithic in Latium (Italy): Stability and Innovation 126
8.5 U-series and combined US-ESR dating of fossil teeth from the late Middle Pleistocene vertebrate locality Khok Sung, Nakhon Ratchasima Province, Northeastern Thailand 127

List of Tables

3.1: The results of chemical analyses, total dose rates and ESR ages. 36

3.2: Experimentally determined trap parameters for Al and Ti centres. 40

3.3: The estimated T_c for ESR thermochronometry of Al and Ti centres in quartz and the reported T_c for Na-feldspar OSL, AHe and AFT thermochronometry under the surface temperature of 0 ºC. 41

4.1: Composition of the modelled environments. 58

4.2: The mineral composition and relative abundance (area%) of BB86, HIM31 and HIM59. 72

4.3: Average K, U and Th concentrations. 73

4.4: The K concentrations (%) of four major minerals (K-feldspar, biotite, hornblende and plagioclase) in three rocks measured by LA-ICP-MS. 74

4.5: The beta dose rates of quartz and K-feldspar in three slices. 75

4.6: The beta dose rates of quartz and K-feldspar in three slices of HIM31. 77

4.7: The beta dose rate of quartz and K-feldspar with different U and Th contents in host mineral. 78

5.1: The results of chemical analyses, total dose rate calculations, ESR ages of Al and Ti centres, and their corresponding cooling rates. 94

List of Figures

2.1: (a) Trapping scheme of electrons in quartz (after Grün, 1989). E_a is the activation energy, the minimum energy that is required for trapping electrons. E_a is related to trap depth and varied by paramagnetic centres. (b) The trapped electrons can be thermally activated and transfer following two pathways, either retrapping or recombining with hole centres (after Grün, 1994). 4

2.2: The formation of Al and Ti centres in α-quartz. 5

2.3: ESR spectrum of the Al centre measured at a temperature of 77 ºK (after Grün et al., 1999). 6

2.4: ESR spectrum of the Ti centre measured at a temperature of 77 ºK (after Duval and Guilarte, 2015; Toyoda, 2015). Option A is measured as the difference between the top of the peak at g = 1.979 and the position at g = 1.913. Option B is a peak-to-peak amplitude measurement around g = 1.931. Option C is taken from the baseline to the bottom of the peak (labeled 1 in the figure) at g = 1.915. Option D is measured as the difference between the baseline and the position at g = 1.913. Option E is a peak-to-baseline amplitude at g = 1.979. 7

2.5: (a) A part of the atomic configuration of normal α-quartz. (b) Schematic representation of an O vacancy in SiO_2 due to asymmetric relaxation. The unpaired electron is shown as e^- (after Rudra and Fowler, 1987). (c) ESR spectrum of the E' centre obtained at room temperature. 8

2.6: The determination of reaction order by the differential method. 10

2.7: The determination of activation energy and escape frequency in an Arrhenius plot. The obtained rate constants at a series of temperatures (blue points), and the linear relationship must be extrapolated to natural settings (red point). 11

2.8: (a) The determination of D_e by the additive dose method. (b) The dose response curve and estimated D_e by the regeneration dose method. 13

2.9: Schematic illustration of external radioactive interaction surrounding a quartz grain and the influential factors in the dose rate calculation. 14

2.10: The concept of closure temperature (Dodson, 1973). (a) Temperature decreasing

monotonically with time. (b) The accumulation of daughter nuclide with time. D/P refers to the ratio of daughter nuclides versus parent nuclides. 18

2.11: The closure temperatures of various thermochronometers for a cooling rate of 100 ºC/Ma (Harrison, 1981; Harrison et al., 1985; Grün et al., 1999; Reiners and Farley, 1999; Ehlers et al., 2005; Bernet, 2009; Harrison et al., 2009; Herman et al., 2010; Guralnik et al., 2015a; Fang and Grün, in review). 19

3.1: (a) The location of Fergusons Hill-1 borehole (after Dickinson et al., 2002), and the varied grey levels indicate different units. (b) The sample depth, stratigraphic formation (Ypma and Hochman, 1991), temperature record (BT), and estimated temperatures of five samples (T-1, T-2, discussed in section 3.5.1). The samples belong to the early Cretaceous units of the Otway Group. 27

3.2: The ESR spectrum of FH1-8 after adding a 612 Gy X-ray dose on top of the natural signal and subtracting the peroxy signal obtained from annealed ESR spectrum. The intensity of the Al centre is calculated from A1 to A2, and the intensity of the Ti-Li centre is quantified from T1 to T2. 29

3.3: (a, b) Regenerative dose response curves of Al and Ti centres, and fitted by SSE function. (c, d) The regenerative-additive plots of Al and Ti centres. 30

3.4: (a) Apparent age as a function of isothermal holding time at a series of temperatures. (b) Apparent age as a function of temperature for a variety of cooling rates. 33

3.5: (a) The blue points are *in situ* measured temperatures of FH1 borehole and the red points are assumed surface temperature (15 ºC) and corrected bottom hole temperature (133 ºC). The blue and red lines are fitting curves of applied approaches for obtaining storage temperatures of samples in this study. The horizontal grey bar indicates the depths of samples. (b) The obtained ambient temperatures (T-1 and T-2) of samples by using first approach and second approach in calculation. 35

3.6: Overview of thermochronometric results from the FH1 borehole. The predicted He age envelopes (after House et al., 2002) with grain radii of 35–100 μm using

the thermal history of Duddy (1994) are compared with the present day estimated temperature profiles of T-1 (black contour) and T-2 (red contour). 36

3.7: The measured ages of the Al centre compared to the modelled ages by optimal trap parameters for an isothermal holding time of 10 Ma. (b) The measured ages of the Ti centre. 37

3.8: The calculated apparent ages of Al and Ti centres (Grün et al., 1999) compared with the modelled ages calculated by best-fit trap parameters for the lower core from the Eldzhurtinskiy Granite. 38

4.1: Samples and corresponding slices for analysis. (a) A 20 mm cube was cut from HIM82 for 3D CT scanning, and a slice from the middle section of the cube for QEM-EDS mapping. (b) A slice of HIM59 was selected from the leucosome section of the specimen. (c) A slice was cut from HIM31 vertical to lineation and foliation. 46

4.2: (a) The 3D CT image of the sample cube. (b) The QEM-EDS image of a slice cut from the middle part of the cube, which showed four main mineral phases. (c) The segmented CT image of the slice obtained from image registration. Biotite and K-feldspar phases were identified but quartz and plagioclase were unable to be separated. 49

4.3: The quartz phase in QEM-EDS image and segmented low-energy CT image. ...50

4.4: (a) Mineral mapping of HIM31 by QEM-EDS. (b) XRF image of Si with colour scale indicating X-ray count. (c) XRF map of quartz abundance close to that in QEM-EDS image. (d) XRF map with low quartz abundance. 51

4.5: (a) QEM-EDS image of HIM59. (b) XRF image of HIM59. The distribution and abundance of major minerals are consistent in QEM-EDS and XRF images. The slight differences between grain boundaries result from the filtering of noisy XRF maps and de-resolution of QEM-EDS image. (c) Minor minerals identified by QEM-EDS. (d) Minor minerals classified by XRF. The epidote and different type of Fe-rich minerals cannot be classified and the abundance of zircon is much higher than that in the QEM-EDS image. 53

4.6: Illustration of volume, surface and linear fractions in an isotropic heterogeneous sample. 57
4.7: Visualization of a slice of each virtual environment. 59
4.8: Beta dose rates calculated by simulations and standard methods in four heterogeneous environments. 60
4.9: Comparison of the beta dose rate in the different mineral phases calculated by simulations and standard methods. The dose rates are presented in relative percent to the dose rates of sphere packing modellings. The red cross indicates the absence of calculation of Dr_{mm} because there is no fraction under a millimeter except the matrix. 60
4.10: 2D simulations from mapping images with different resolution. 62
4.11: Comparison of the shape of the beta dose rate distribution from 3D and 2D modellings. a – Dr distribution in the clay matrix of environment B. b – Dr distribution in the clay matrix of environment D. c – Dr distribution in the quartz_plagioclase phase of the granite sample of part 7. 63
4.12: Schemas of the DosiVox modelling for beta dose rate attenuation in a grain next to a heterogeneous environment. 64
4.13: Beta dose rate attenuation in a grain next to an interface between two mineral phases. Wiggles of the lines result of stochastic uncertainty of the Monte Carlo simulation. a – environment I: radioactive dry clay next to an inert carbonate. b – environment J: radioactive moist clay next to an inert carbonate. c – environment I: inert clay next to a radioactive K-feldspar. 64
4.14: 3D view of the CT-scan and 2D view of one of the slice. 65
4.15: Comparison of the ^{40}K beta dose rates from 3D modelling, 2D modelling and standard self-dose and attenuation factors for 100 µm, 200 µm and 300 µm grains in a granite sample. 65
4.16: Samples and corresponding slices for analysis. (a) Three slices cut from BB86 were vertical to each other and share a vertex. (b) HIM59-1 was selected from the leucosome section of the specimen. (c) HIM31-1 contained the whole mineral

information vertical to foliation. The other three slices were made from a 20 mm cube from the middle section of the specimen. 70
4.17: The QEM-EDS images of three slices from BB86. 71
4.18: (a) Mineral mapping of HIM31-1. The three distinctive layers are indicated by the dashed lines. (b) Image of minor and accessory minerals of HIM31-1. (c) Mineral maps of three slices cut from a 20 mm cube. 72
4.19: (a) Mineral map of HIM59-1. (b) The accessory minerals are presented as interstitial or inclusions to biotite. 73
4.20: Cathodoluminescence image of zircons from HIM59. The red circles indicate the spot locations of the SHRIMP analyses and the local U concentrations. 74
4.21: Beta dose rate histograms of quartz (a, b) and K-feldspar (c). The quartz dose rates have a log-normal distribution, while K-feldspar dose rates approach a normal distribution. (d, e) beta dose rate distribution map of quartz and K-feldspar. The areas with 0 Gy/ka dose rate are background. 75
4.22: (a) Beta dose rate histograms of quartz are presented in separate layers. (b) The histogram K-feldspar dose rates is negatively skewed. (c, d) Beta dose rate distribution map of quartz and K-feldspar. The three distinctive layers are indicated by the dashed lines, and the areas with 0 Gy/ka dose rate are background. 76
4.23: Beta dose rate maps of quartz and K-feldspar in three faces of HIM31. 77
4.24: (a) The uncertainties of beta dose rate in calculations with sample size decreasing from 30 × 30 to 10 × 10 mm. The positive and negative errors indicate the maximum and minimum beta dose rates in their corresponding sample sizes. (b) The beta dose rates of quartz and K-feldspar with decreasing spatial resolution from 15 to 90 μm. 78
5.1: (a) The geological map of the eastern Himalayan syntaxis and its surrounding area, showing major lithological units and faults, towns, and the transect location (after Geng et al., 2006; Booth et al., 2009; Bracciali et al., 2016). Regional geographic location of the eastern Himalayan syntaxis shown in inset. 84

5.2: Maps of cooling ages determined using various thermochronometric techniques. (a) $^{40}Ar/^{39}Ar$ biotite ages. (b) (U-Th)/He zircon ages. (c) (U-Th)/He apatite ages. (d) OSL feldspar ages. 86

5.3: (a) Topographic map of sample locations. Thrust NML1 belongs to the south part of the Nam-La thrust zone, separating zone A on its north side. Thrust DF2 and a normal fault separate zone B (footwall) and zone C (hanging wall). (b) The elevation as a function of horizontal distance from sample PC-9 to PC-1. 87

5.4: (a) ESR spectrum of the E' centre obtained at room temperature. (b) ESR spectrum of the Al and Ti centres measured at a temperature of 77 ºK. 88

5.5: Apparent ages of the Al centre for an exhumation from 100 ºC to 10ºC for a range of constant cooling rates. 90

5.6: (a) ESR intensity of natural E' centre (I_1) and heated at 250 °C for 100 min (I_2). (b) The I_1/I_2 ratio is related to palaeotemperature, and sample PC-5 shows a higher ratio than the rest of the samples. 92

5.7: The apparent ages of Ti (triangle) and Al centres (square) are sorted for the three zones. In each zone, the elevation of samples decreases from left to right. 93

5.8 The estimated cooling rates from the Ti and Al centres. In each structural zone, the elevations of samples decrease from left to right. 95

8.1: (a) Rad Cal Real-Time dosimeter and probe for in-air dose rate calibration. (b) In the sample holder, weighted aliquots are enclosed in quartz tubes for irradiation. 118

8.2: (a) Increased ESR intensities of X-ray irradiation versus that of Gamma irradiation. The data points start with the dose step of 40 Gy and end with the dose step of 800 Gy. 120

8.3: The geological map of eastern Himalayan syntaxis. 121

8.4: The relationship between microwave power and attenuation factor. 122

8.5: ESR intensity of E' centre as a function of increasing attenuation factor. 123

8.6: (a) The furnace used for isothermal annealing experiment at 250 °C. (b) ESR intensity of E'centre as a function of increasing annealing time at 250 °C. 124

List of Acronyms

3D	Three Dimensions
AFT	Apatite Fission Track
AHe	Apatite (U-Th)/He
ANU	Australian National University
β	Reaction order
BAr	Biotite $^{40}Ar/^{39}Ar$
BSE	Back-Scattered Electron
BT	Borehole Temperature
C	Proportional to the ESR intensity of a paramagnetic centre
CAM	Central Age Model; Centre for Advanced Microscopy
CT	Computed Tomography
$\dot{D}$	Dose Rate
D_e	Equivalent dose
D_0	Characteristic Saturation Dose
DRC	Dose Response Curve
E_a	Activation Energy
EDX	Energy Dispersive X-Ray Spectroscopy
EHS	Eastern Himalayan Syntaxis
EmMass	Energy emitted by unit of Mass
EMP	Electron Microprobe
EPL	Exponential + Linear
ESR	Electron Spin Resonance
FH1	Fergusons Hill-1
FMM	Finite Mixture Age Model
FSQP	Feasible Sequential Quadratic Programming

FT	Fission Track
ICP-OES	Inductively Coupled Plasma Optical Emission Spectrometry
ICP-MS	Inductively Coupled Plasma Mass Spectrometry
k	Rate constant
k_B	Boltzmann's constant
LA-ICP-MS	Laser Ablation Inductively Coupled Plasma Mass Spectrometry
N	Total number of traps
n	Number of occupied traps
MAM	Minimum Age Model
MET	Multi-Elevated-Temperature
MCT	Main Central Thrust
MRE	Mineral Reference Editor
OSL	Optically Stimulated Luminescence
PRZ	Partial Retention Zone
QEMSCAN, QEM-EDS	Quantitative Evaluation of Minerals using Energy Dispersive Spectroscopy
RAM	Random Access Memory
REE	Rare Earth Elements
RSES	Research School of Earth Sciences
SAR	Regenerative dose method
SARA	Regenerative-Additive method
SEM	Scanning Electron Microscope
SHRIMP	Sensitive High Resolution Ion Microprobe
SIMS	Secondary Ion Mass Spectroscopy
SSE	Single Saturating Exponential
STD	South Tibetan Detachment system

T_a	Apparent Age
T_c	Closure Temperature
TL	Thermoluminescence
μCT	Micro-Computed Tomography
ν_0	Frequency Factor
VR	Vitrinite Reflectance
XRF	X-ray Fluorescence
YTSZ	Yarlung Tsangpo Suture Zone
ZHe	Zircon (U-Th)/He
τ	Theoretical lifetime of the trapped charges
τ'	Effective lifetime
ŋ	Cooling rate

List of Publications

Publications on ESR thermochronometry:

Fang, F., Grün, R. (in review). ESR thermochronometry of Al and Ti centres in quartz: A case study of the Fergusons Hill-1 borehole from the Otway Basin, Australia. Radiation Measurements.

Martin, L., **Fang, F.**, Mercier, N., Incerti, S., Grün, R., Lefrais, Y., 2018. 2D modelling: A Monte Carlo approach for assessing heterogeneous beta dose rate in luminescence and ESR dating: Paper I, Theory and verification. Quaternary Geochronology, 48, 25-37.

Fang, F., Martin, L., Williams, I., Brink, F., Mercier, N., Grün, R., 2018. 2D modelling: A Monte Carlo approach for assessing heterogeneous beta dose rate in luminescence and ESR dating: Paper II, Application to igneous rocks. Quaternary Geochronology, 48, 195-206.

Fang, F., Grün, R. (in preparation). ESR thermochronometric evidence for accelerated Mid-Pleistocene exhumation of the Namche Barwa massif, eastern Himalayan syntaxis.

Publications on ESR dating in archaeology:

Duval, M., **Fang, F.**, Grün, R., Suraprasit, K., Jaeger, J-J., Benammi, M., Chaimanee, Y., 2019. U-series and combined US-ESR dating of fossil teeth from the late Middle Pleistocene vertebrate locality Khok Sung, Nakhon Ratchasima Province, Northeastern Thailand. Palaeontologia Electronica 22.3.69, 1-25.

Willmes, M., Grün, R., Douka, K., Michel, V., Armstrong, R., Benson, A., Crégut-Bonnoure, E., Desclaux, E., **Fang, F.**, Kinsley, L., Saos, T., Defleur, A.R., 2016. A comprehensive chronology of the Neanderthal site Moula-Guercy, Ardèche, France. Journal of Archaeological Science: Reports, 9, 309-319.

Villa, P., Soriano, S., Grün, R., Marra, F., Nomade, S., Pereira, A., Boschian, G., Pollarolo, L., **Fang, F.**, Bahain, J-J., 2016. The Acheulian and Early Middle Paleolithic in Latium (Italy): Stability and Innovation. PLoS ONE 11(8): e0160516.

Acknowledgements

This project has been more challenging than I have imagined in the very beginning. I would like to thank everyone who has helped me in this difficult but meaningful adventure.

To begin with, I really appreciate Rainer Grün for guiding me through this new research direction, providing me with many collaboration opportunities, allowing me to try new techniques and going over my manuscripts. Without his limitless support, this thesis should still be a work in progress. I would like to thank Ian Williams for kindly agreeing to supervise me one year after Rainer moved to Griffith University. I have had a very tough and frustrating time, and Ian was a good mentor in helping me back to track. Also, he has signed various forms for me and provided valuable comments on my manuscripts. Thanks also to Mark Kendrick for his support and helpful suggestions, Marnie Forster and Gordon Lister for introducing me to structural geology and Argon dating and kindly providing rock samples from northwestern Indian Himalaya.

Next, the completion of this project cannot come true without the help from my collaborators. For the study on estimating thermal stabilities of paramagnetic centres, Barry Kohn (University of Melbourne) has kindly provided the Otway Basin samples and helpful discussions in diffusion parameter calculation and borehole temperature correction. I am grateful to P. Morthekai (Birbal Sahni Institute of Palaeosciences) for discussion on the kinetic model and Shijie Shu (University of Illinois at Urbana-Champaign) for translating the mathematical solutions into Fortran code. For beta dose rate simulation of heterogeneous rocks, I have spent a long time trying different analytical techniques, failed over and restarted, until found an acceptable solution. I would like to thank Loïc Martin (Université Bordeaux Montaigne--BMU) who has developed the 2D model, offered me plenty of constructive suggestions, and helped me in running simulations. Thanks to Norbert Mercier (BMU) for kindly inviting me to Bordeaux for a short-time lab visiting. I appreciate Frank Brink from the Centre for

Advanced Microscopy (ANU) for running QEM-EDS and Yannick Lefrais (BMU) for SEM and XRF mineral mapping. The CT lab at Research School of Physics and Engineering (ANU) is acknowledged for offering me free analysis with dual-energy equipment. Thanks to Tim Senden, Adrian Sheppard and Michael Turner for helpful discussion on CT scanning, Jill Middleton, Holger Averdunk and Chenghao Qian for their help in image segmentation. For the application study in the eastern Himalayan syntaxis, the fieldwork would not have been possible without the enthusiastic support of Shenghua Li and Shuangli Tang from the University of Hong Kong and Gang Hu from Chinese Academy of Science. I would like to thank Ping Wang, Jingtang Qin and Wenjun Kang from the Institute of Geology, China Earthquake Administration, for helpful discussions on the geological interpretation of ESR data.

The technical and analytical aspects of this research project were supported by a large number of people in the Research School of Earth Sciences (RSES), ANU. Linda McMorrow helped me to set up the fluorosilicic acid etching experiment, which made the quartz signal visible from the interference. Les Kinsley showed me how to use the LA-ICP-MS and provided me with helpful suggestions on data reduction. Shane Paxton introduced me to the mineral crushing and separation lab, and spent a long time polishing the rock slices. Benda Armstrong organised radiation monitors and Josephine Margo arranged experiment and travel-related bookings for me. The radiocarbon dating group is thanked for kindly sharing their liquid nitrogen. I would also like to thank Julian Byrne for his help in setting simulations through terrawulf, and thank Herb McQueen, Paul Davidson and Duncan Bolt for their support with anything IT related. I appreciate the people of the Engineering and Electronic workshop at RSES for their support in fixing parts of our ESR spectrometer, specifically to Daniel Cummins and Hideo Sadaki. I would also like extend my thanks to Debbie Howard at John Curtin School of Medical Research for setting and calibrating the X-ray irradiator, and Jeffrey Harmer at the University of Queensland for providing access to the UQ ESR facility.

My colleagues at the RSES have provided insightful discussion and advice, as well as

enjoyable coffee and food. In particular, I am thankful to archaeogeochemistry group members Mathieu Duval, Malte Willmes, Kelsie Long, and Hannah James for their friendship and advice. I am grateful to structure and tectonic team members Oleg Koudashev, Sareh Rajabi, Devood Vasegh and Jonathan Pownall for sharing their knowledge on structural geology and Argon dating. Thanks to Mimi Chen, Siyuan Tian, Jiade Wu, Li Liu, Yuhao Dai, Pujiao Chen and Lu Wang for their company and comfort.

My family and friends formed my spiritual prop. I would like to thank my parents for their constant support, encourage and care. I really appreciate Weiping Tu for always on my side, and sharing my happiness and sadness. Pengxiang Hu and Chuan Lu offered me a warm home in Canberra, and I would never forget those days we were together. Wei Cheng, Nan Li, Chenyin Dong and Shijie Shu are thanked for a long friendship since undergraduate and sharing their PhD experiences with me. Wen Xu is appreciated for visiting me several times and hosting me when I was doing experiments in Hong Kong.

Finally, I would like to acknowledge ANU-CSC Scholarship for supporting my study and living in Australia, RSES student travel fund for providing me several chances to attend conferences and undertake field trip, and Research Grants Council of Hong Kong (17303014) for supporting the field trip in the eastern Himalayan syntaxis.

1 Scope of the project

The research reported in this thesis had three main objectives for methodological developments in ESR thermochronometry (listed below). The results are presented as a series of chapters (3-5), each in a format suitable for journal publication. The specific contributions of the author are outlined at the beginning of each chapter. These chapters are preceded by an introduction to ESR dating (Chapter 2) that discusses its physical basis, the properties of paramagnetic centres in quartz, methods for estimating equivalent dose and dose rate, the current status of ESR dating and the main challenges faced in applying ESR to thermochronometry. The thesis ends with a summary of the main conclusions resulting from this study and proposed directions for future research (Chapter 6). The appendix (Chapter 8) contains the supplementary material of the publications and the first page of publications outside of the main content of the thesis.

(1) Determining trap parameters of Al and Ti centres in quartz in natural geological settings

Trap kinetics characterise the thermal stabilities of paramagnetic centres in quartz, and affect the temperature and time range that ESR thermochronometry can cover. Traditionally, trap parameters are obtained through a series of isothermal annealing experiments, but the extrapolation of laboratory results to the natural settings can lead to large uncertainties. Borehole samples, with a well-defined thermal history and ambient temperature record, can be used to estimate realistic trap parameters (Chapter 3). Fergusons Hill-1 borehole from the eastern Otway Basin, has remained in an approximately stable thermal condition for the last few million years. Eldzhurtinskiy Granite core is located in the Caucasus and has experienced rapid cooling. A first-order kinetic model, combined with feasible sequential quadratic programming optimisation algorithms, has been applied to determine the optimal trap parameters for both the Al and Ti centres. Results have been compared with published laboratory data as a test of the reliability of the isothermal annealing approach. The limits of ESR thermochronometry (e.g., closure temperature and minimum cooling rate) have also been investigated.

(2) Developing a 2D model and analytical procedure for calculating beta dose rate in heterogeneous rocks

The commonly applied infinite matrix dose rate calculations might not be applicable to heterogeneous samples. A 3D model (e.g., DosiVox), into which realistic sample geometries can be uploaded, is an ideal solution. Mineral identification in 3D by X-ray computed tomography is challenging, however, due to the similar X-ray attenuation coefficients for some of the common rock-forming minerals (e.g., quartz and plagioclase). This can be solved by 2D X-ray mapping techniques. A 2D model has therefore been developed for evaluating beta dose rates in samples with a uniform/regular mineral distribution pattern. The theory behind, and verification of, this model are presented in Chapter 4.2. The potential application of DosiVox-2D has been confirmed for ESR and luminescence dating of sediments and rocks by comparing the beta dose rates obtained from 2D modelling, 3D modelling and standard calculations. To adopt DosiVox-2D as a routine analytical process for heterogeneous rocks, investigations have been carried out on sample selection, mineral mapping, analysis of radioelement concentrations in minerals, and the calculation of uncertainty for simulations (Chapter 4.3).

(3) Applying ESR thermochronometry to evaluate late-stage exhumation history of the Namche Barwa massif, eastern Himalayan syntaxis

The Namche Barwa massif is located at the eastern end of the Himalayan orogen where structural trends have rotated in a clockwise direction. This massif has undergone localised rapid exhumation since the Late Miocene. The topography is dominated by river incision, glaciation and differential uplift on currently active faults. Various thermochronometric techniques have been applied in this region, but the late-stage exhumation history remains unclear. ESR dating of rocks from a vertical profile of 1000 m has provided new insights into the time-temperature history over the last ~ 0.7 Ma from the south massif boundary (Chapter 5). Combined with the reported cooling history of the north adjacent region to the massif, constraints have been placed on the timing and rates of exhumation from the Mid-Pleistocene to the present day.

2 Introduction to electron spin resonance dating

The use of electron spin resonance (ESR) as a method for dating geological materials was first suggested in the late 1960s by Zeller and co-workers (Zeller et al., 1967; Zeller, 1968). The first actual dating work using the method was carried out by Ikeya on a stalactite from the Akiyoshi cave (Ikeya, 1975). Since then many materials have been examined for ESR dating, including quartz, flint, travertine and calcrete, and biominerals such as hydroxyapatite, aragonite and calcite (e.g., Grün, 1989; Rink, 1997; Fattibene and Callens, 2010; Toyoda, 2015; Blackwell et al., 2016). Tooth enamel and quartz are the minerals most widely used for studies in archaeology and landscape evolution. By the turn of the century, the theory and analytical methods for ESR dating had largely been developed. The fundamental basis and current status of ESR dating of quartz of igneous origin are briefly summarised below.

2.1 Physical basis

ESR dating is based on the measurement of paramagnetic centres that build up at crystal defects in a mineral as a result of natural irradiation. The number of paramagnetic centres present at any given time is a balance between the rate of production and the rate of decay. The former depends on the number of available empty traps and the radiation flux. The latter is a function of temperature and thermal kinetics.

The formation of paramagnetic centres in quartz is illustrated in Figure 2.1a. Quartz is an electrical insulator in which there are two energy levels that electrons can occupy; the valence band (lower energy) and the conduction band (higher energy). At the time a mineral is formed, all electrons are in the valence band. With natural irradiation (α and β particles, γ and cosmic rays), electrons can be excited and transferred to the conduction band, leaving positively charged hole centres near the valance band. After a short period of diffusion, most of these excited electrons recombine with those holes. Some electrons, however, are trapped in positively charged lattice defects, forming electron centres. This accumulation of trapped electrons can be reset by annihilation processes (Figure 2.1b).

For example, when quartz is sufficiently heated, the trapped electrons are transferred from the trap into the conduction band. The free electrons can then either recombine with holes and/or fall back into the trap from which they were released (retrapping). This process is controlled by trap kinetics.

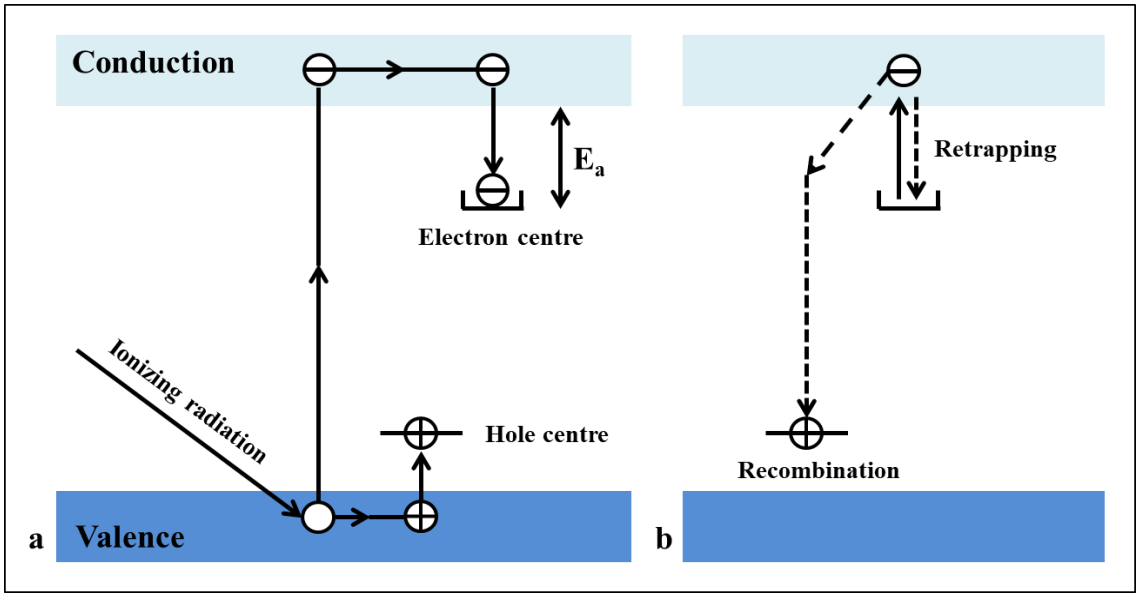

Figure 2.1: (a) Trapping scheme of electrons in quartz (after Grün, 1989). E_a is the activation energy, the minimum energy that is required for trapping electrons. E_a is related to trap depth and varied between paramagnetic centres. (b) The trapped electrons can be thermally activated and transfer following two pathways, either retrapping or recombining with hole centres (after Grün, 1994).

ESR dating records the time interval since mineral grains commenced trapping electrons in response to environmental radiation (mainly from *in situ* decay of nearby radioactive elements: U, Th, K) after cooling of the mineral through its effective closure temperature range. Assuming the dose rate ($\dot{D}$) is constant, the ESR age of a paramagnetic centre can be defined as:

$$\text{Age} = \frac{\text{equivalent dose } (D_e)}{\text{dose rate } (\dot{D})} \qquad (2.1)$$

The estimation of the value of D_e is described in Section 2.3 and of $\dot{D}$ in Section 2.4 below.

2.2 Paramagnetic centres

Many different paramagnetic defects in quartz have been used for ESR dating (Weil, 1984). The present study is focused on using Al, Ti and E' centres, and the properties of which are discussed in the following section.

2.2.1 Structure and spectroscopic features

The Al and Ti centres are formed by atom substitution in α-quartz (Figure 2.2). The Al centre is a hole centre, formed by an Al atom substituting for a Si atom. For charge compensation, the replacement Al atom is accompanied by an alkali ion (M^+). When irradiation creates a hole available to $[AlO_4/M^+]^0$, the compensating ion is no longer necessary and diffuses away, forming an $[AlO_4]^0$ centre. The Ti centre is an electron centre. The substitution of Ti^{4+} for Si^{4+} in the crystal lattice forms the diamagnetic centre $[TiO_4]^0$. A $[TiO_4/e]^-$ is formed by capturing an electron excited by irradiation. Due to the resultant negative charge, an alkali ion (M^+) is required to compensate the charge excess. The incorporated ion (H^+, Li^+ or Na^+) forms sub-centres as Ti-Li, Ti-H and Ti-Na, respectively. The Ti-Na centre is rarely observed in natural quartz.

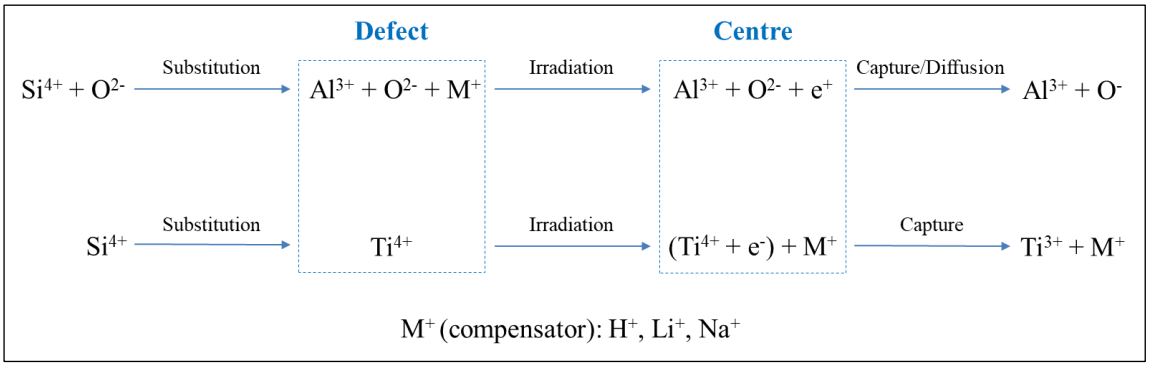

Figure 2.2: The formation of Al and Ti centres in α-quartz.

The ESR spectrum of the Al centre was first recorded by Griffiths et al. (1954) in α-quartz. It can only be obtained at low temperature (e.g., 77 °K) because of relaxation broadening effects (Schnadt and Räuber, 1971). The spectrum of the Al centre (Figure 2.3) has three main components with g factors of 2.060, 2.009 and 2.002, which are characterised by hyperfine splitting and the nuclear Zeeman effect (Nuttall and Weil, 1981). The ESR intensity of Al centre is measured as the difference between the top of

the peak at g = 2.018 and the bottom of the peak at g = 1.993. This avoids the variation of an incompletely averaged powder spectrum and the influence of the overlapping peroxy centre (Toyoda and Falguères, 2003).

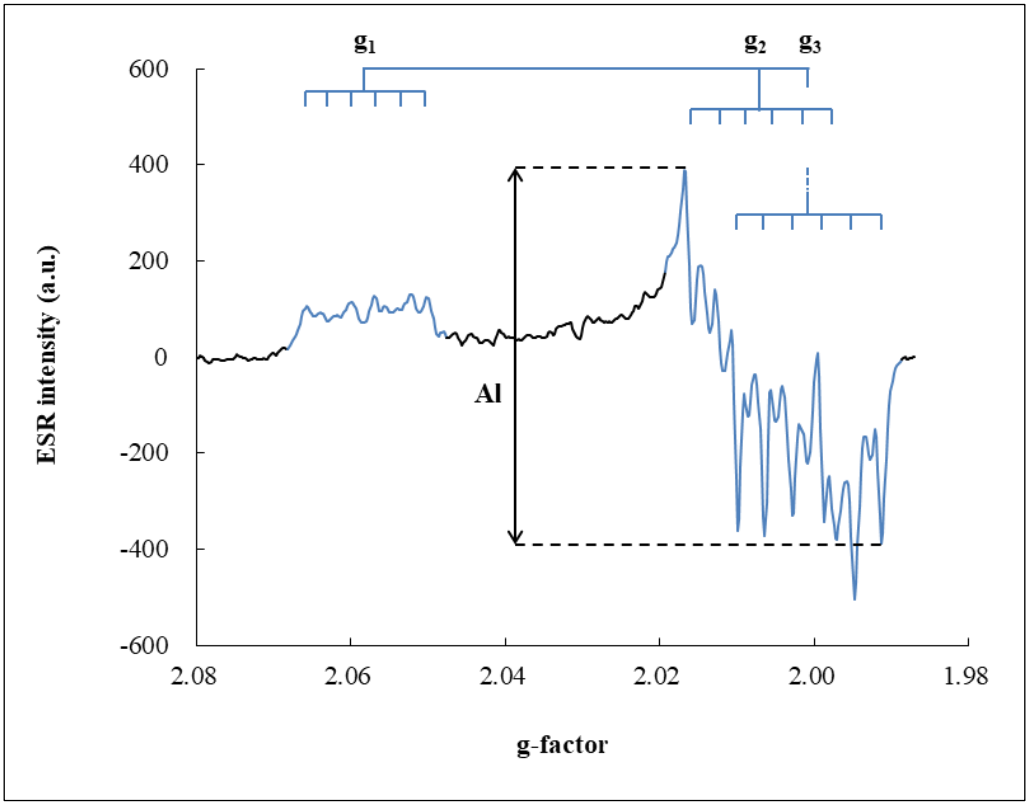

Figure 2.3: ESR spectrum of the Al centre measured at a temperature of 77 °K (after Grün et al., 1999).

In the ESR spectrum of the Ti centre (Figure 2.4) there are three main absorption lines from the Ti-Li centre, with g factors of 1.979, 1.931 and 1.912 (Isoya et al., 1983). The Ti-H centre has anisotropic g factors of 1.986, 1.931, and 1.915 (Rinneberg and Weil, 1972). The absorption signals of the two sub-centres overlap at g = 1.931, and the signal of the Ti-Li centre at g = 1.915 is partly influenced by that of the Ti-H centre at g = 1.912. Five options have been evaluated for quantifying the intensity of these centres (Duval and Guilarte, 2015; Toyoda, 2015). Option E is the only way to obtain a pure Ti-Li signal, and options A and D can also be used to measure the Ti-Li centre. Option C provides the intensity of the Ti-H centre, and option B is a mixture of the two Ti-related centres.

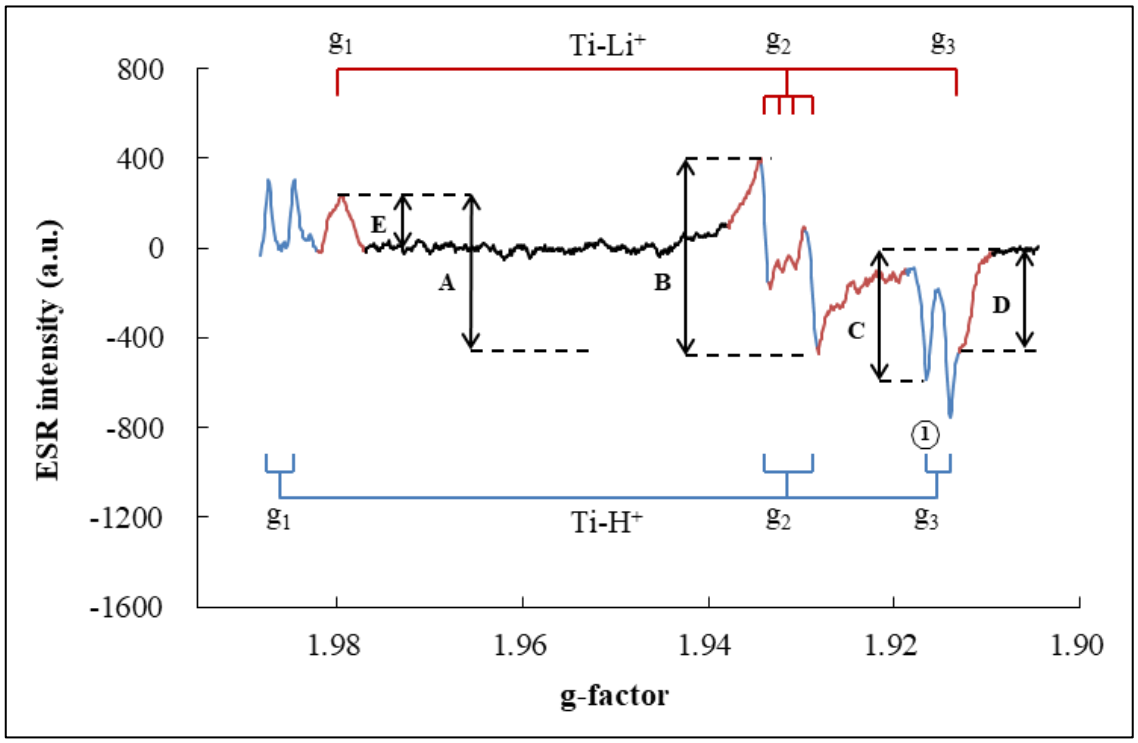

Figure 2.4: ESR spectrum of the Ti centre measured at a temperature of 77 °K (after Duval and Guilarte, 2015; Toyoda, 2015). Option A is measured as the difference between the top of the peak at g = 1.979 and the position at g = 1.913. Option B is a peak-to-peak amplitude measurement around g = 1.931. Option C is taken from the baseline to the bottom of the peak (labeled 1 in the figure) at g = 1.915. Option D is measured as the difference between the baseline and the position at g = 1.913. Option E is a peak-to-baseline amplitude at g = 1.979.

The E' centre, first observed by Weeks (1956), is an unpaired electron trapped in an oxygen vacancy site (Weeks, 1994). The widely accepted model for this centre proposed by Feigl et al. (1974) was subsequently modified by Rudra and Fowler (1987). In α-quartz, each oxygen (O) atom is linked to two silicon (Si) atoms by inequivalent bonds, and each Si contributes an electron in an sp^3 orbital to the Si-O bond (Figure 2.5a). With the formation of an O vacancy and the asymmetric relaxation of adjacent Si atoms, the unpaired electron in the sp^3 orbital (mostly localised on the Si atom on the short bond side) is oriented into the vacancy, while the other Si atom (long bond side) moves close to the plane of its three neighbouring O atoms (Figure 2.5b). The ESR spectrum is obtained at

room temperature, and the intensity of E' centre is calculated as the peak-to-peak height at g = 2.0005 (Figure 2.5c).

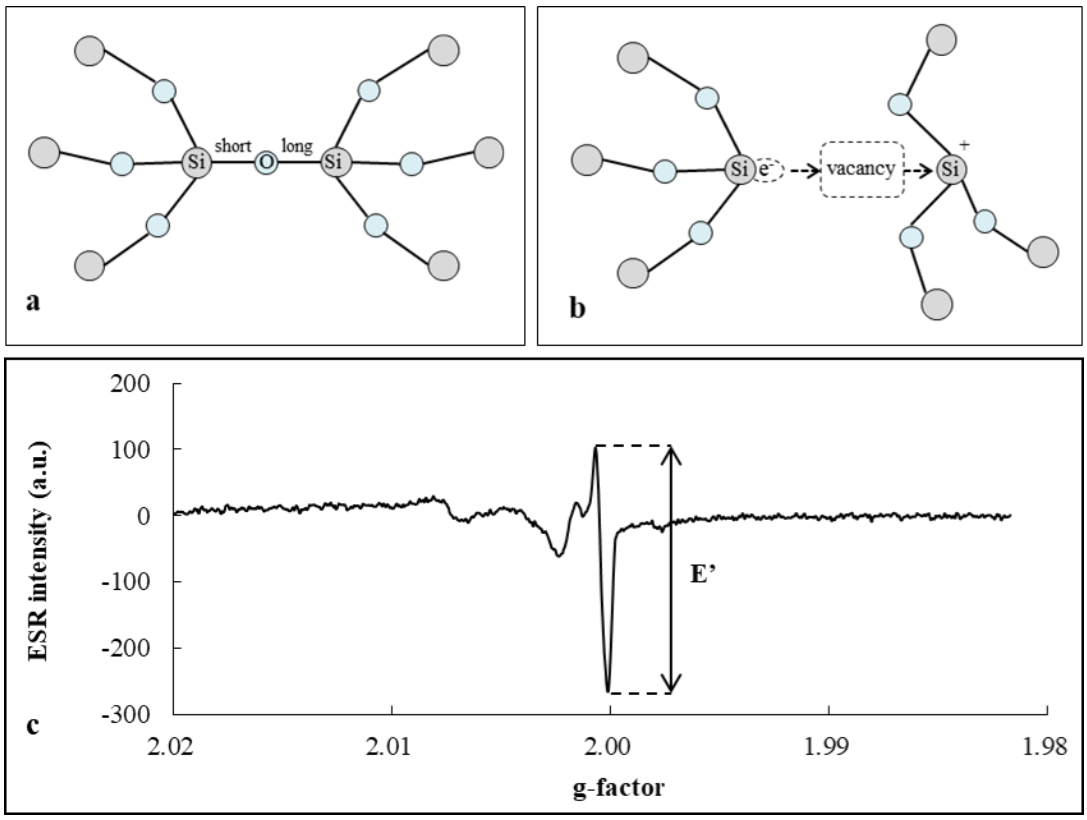

Figure 2.5: (a) A part of the atomic configuration of normal α-quartz. (b) Schematic representation of an O vacancy in SiO_2 due to asymmetric relaxation. The unpaired electron is shown as e^- (after Rudra and Fowler, 1987). (c) ESR spectrum of the E' centre obtained at room temperature.

2.2.2 Thermal properties

The thermal property of a paramagnetic centre refers to the rate of ESR intensity decay with heating and the kinetics of the centre (i.e., kinetic order, activation energy and escape frequency factor). The former can be investigated through isochronal annealing experiments, and the latter is commonly assessed by isothermal annealing experiments.

In isochronal annealing experiments, the ESR intensities of the Al and Ti centres start to decrease at ~ 200 ºC and are completely annealed in the temperature range 250–450 ºC, depending on the specific nature of the samples (Imai et al., 1985; Shimokawa and Imai, 1987; Shimokawa et al., 1988; Toyoda and Ikeya, 1991a, 1994; Tsukamoto et al., 2015).

Further investigations of the Ti-Li centre (Toyoda and Ikeya, 1991b) have shown that this centre contains both thermally stable and unstable components, and thus preheating procedures were suggested as part of routine analysis. However, preheating is not always effective (Toyoda and Ikeya, 1994; Toyoda et al., 2006). For the E' centre, an increase of ESR intensity with heating in the low-temperature range has been observed (McMorris, 1970). Detailed isochronal annealing studies showed that the intensity of the E' centre reaches to a maximum by heating between 250 to 300 ºC and then decreases to complete annealing (Toyoda and Ikeya, 1991a; Falguères et al., 1994; Chen et al., 1997; Toyoda and Schwarcz, 1997). The mechanism for intensity increase is unclear. Toyoda and Ikeya (1991b) suggested that the increase in E' intensity was correlated with a decrease in the concentration of Ti and Al centres, but this was not observed by Toyoda and Ikeya (1991a) or Grün et al. (1999). Jani et al. (1983) proposed that the increase might be due to the combination of invisible trapped holes at sites with the E' centre, or the re-distribution of compensators such as H^+, Li^+ and Na^+. Whatever the mechanism, the annealing characteristics of the E' centre can be used for palaeothermometry studies. The ratio of the E' intensity in the unheated sample (I_1) to the maximum intensity (I_2) at 250 ºC has been shown to be closely associated with storage temperature (Chen et al., 1997), and was applied in estimating temperatures in the upper core of the Eldzhurtinskiy Granite (Grün et al., 1999). The use of the E' centre for age determinations is limited, partly due to the intensity saturation in natural samples (Falguères et al., 1994).

Trap kinetics reflect the manner of energy transfer and the lifetime of a paramagnetic centre. The thermal stability of a paramagnetic centre is described as:

$$r = kC^{\beta} = \nu_0 e^{-E_a/k_B T} C^{\beta} \qquad (2.2)$$

Where r is the rate of reaction, k is the rate constant, C is proportional to the ESR intensity of a paramagnetic centre, β is the reaction order, ν_0 is the attempt to escape frequency factor (s^{-1}), E_a is the activation factor (eV), k_B is Boltzmann's constant (8.617×10^{-5} eV/K), and T is temperature (K).

For ESR dating the detrapping process is usually assumed to be of first order (β=1),

indicating that all electrons evicted from the trap recombine with holes and no retrapping occurs. Toyoda and Ikeya (1991a) have shown that their data followed a second order (β=2) relationship, indicating that half of the evicted elections were retrapped and the other half recombined with holes. Accurate estimations of the detrapping order have yet to be carried out in ESR dating, which theoretically can be determined by the differential method (Figure 2.6).

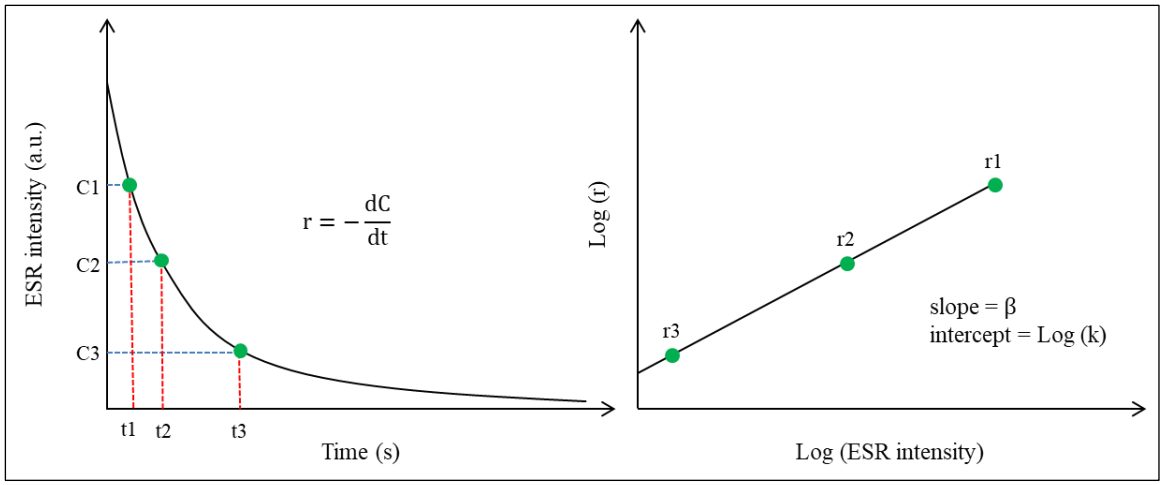

Figure 2.6: The determination of reaction order by the differential method.

The activation energy (E_a) and escape frequency factor (ν_0) can be obtained from an Arrhenius diagram by plotting the estimated mean lives or reaction rates versus the reciprocals of corresponding temperatures (Figure 2.7). Few studies have been carried out in an attempt to determine ESR trap parameters. The estimated values of E_a and ν_0 range from 1.3 to 2.4 eV and 10^9 to 10^{13} s^{-1}, respectively, for the Al centre, and from 1.0 to 1.7 eV and 10^7 to 10^{11} s^{-1}, respectively, for the Ti centre (Imai et al., 1985; Ikeya and Toyoda, 1991; Toyoda and Ikeya, 1991a; Fukuchi, 1992). The wide range of the results has been attributed to the variations in sampling location and the origin of the quartz (Marfunin, 2012).

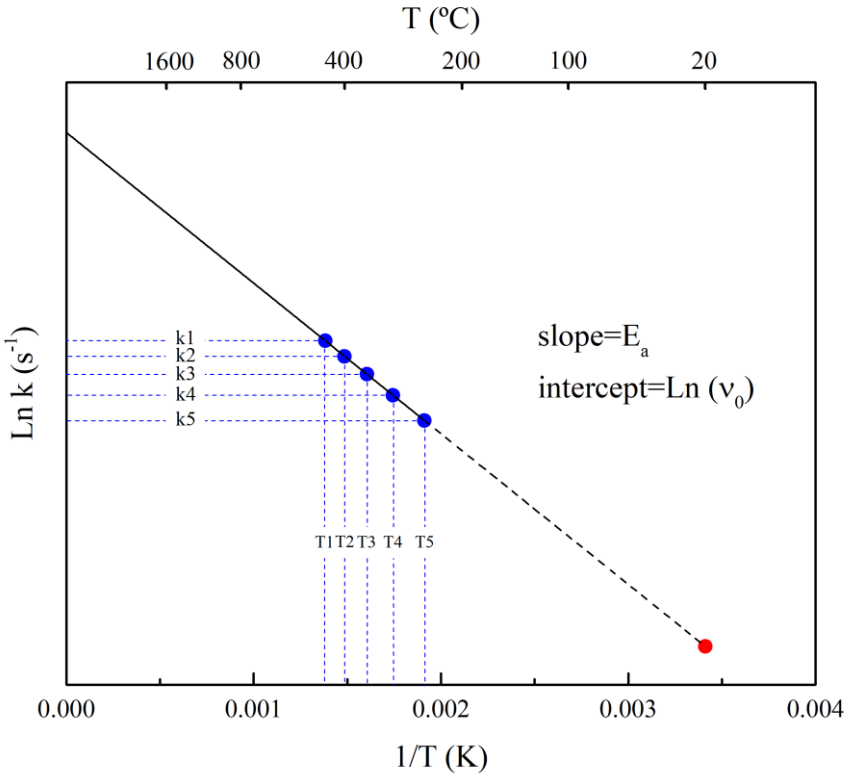

Figure 2.7: The determination of activation energy and escape frequency in an Arrhenius plot. The obtained rate constants at a series of temperatures (blue points), and the linear relationship must be extrapolated to natural settings (red point).

The laboratory studies were carried out under well-controlled and simplified conditions, but the time range for the experiments is 7 to 8 orders of magnitude shorter than that of natural conditions. The extrapolation of the laboratory results to natural settings is therefore subject to large uncertainties. A straightforward way to cross check laboratory-based trap parameters is through investigations of borehole samples with well-characterised thermal histories and measured downhole temperatures (Tagami et al., 1996; House et al., 1999; Guralnik et al., 2015a; Brown et al., 2017). Such samples taken from ESR partial retention zones characterise the ingrowth-annealing behaviour of paramagnetic centres under natural conditions. The corresponding age-temperature profile can shed light on the realistic estimation of trap parameters. It should be noticed that if the thermal stability of a paramagnetic centre is sample dependent, the obtained trap parameters from one sampling site cannot be simply applied to other sites.

2.3 Estimation of equivalent dose (D_e)

The accumulation of paramagnetic centres is quantified using ESR spectroscopy by measuring the resonance absorption of microwave power by unpaired electron spins in an external magnetic field. The ESR intensity is proportional to the number of paramagnetic centres. Accurate evaluation of D_e requires the generation of a dose response curve (DRC) and fitting the curve with an appropriate function.

DRCs can be produced using multi-aliquots, a single aliquot, or a single grain. The multi-aliquot technique is most commonly applied in ESR dating. It simplifies the irradiation process, but variations in properties between different aliquots can compromise the accuracy of the D_e evaluation. The precision of D_e values can be enhanced by using the single aliquot method, but its application has been limited by the need to have access to a gamma irradiation source. The introduction of X-ray irradiation may change this to a routine method for future studies (Tsukamoto et al., 2015). ESR dating of single quartz grains was first applied to fluvial sediment by Beerten et al. (2003). This method provides the possibility of detecting insufficient bleaching, but its application requires access to a Q-band ESR spectrometer, long measurement times, and involves large errors that need to be minimised (Beerten and Stesmans, 2007).

The DRC can be determined by two approaches. In the additive dose method (Figure 2.8a), the sample is usually irradiated with 10-12 dose steps and the D_e value is obtained by extrapolating the DRC back to the x-axis. In the regenerative dose method (Figure 2.8b), the sample is first reset by heating, and then irradiated with 5-7 dose steps. The DRC is established from the zeroed sample, and the D_e value is obtained by projecting the natural ESR intensity onto the curve. The regenerative method has the advantage of being less dependent on the applied fitting function and it requires less sample material when using the multi-aliquot technique. On the other hand, it has the disadvantage that the sensitivity of the sample might be changed by the heating procedure (Prescott et al., 1993). Even though this effect has been found to be minimal (Toyoda, 2015), a test for sensitivity change needs to be applied routinely when the regenerative method is used.

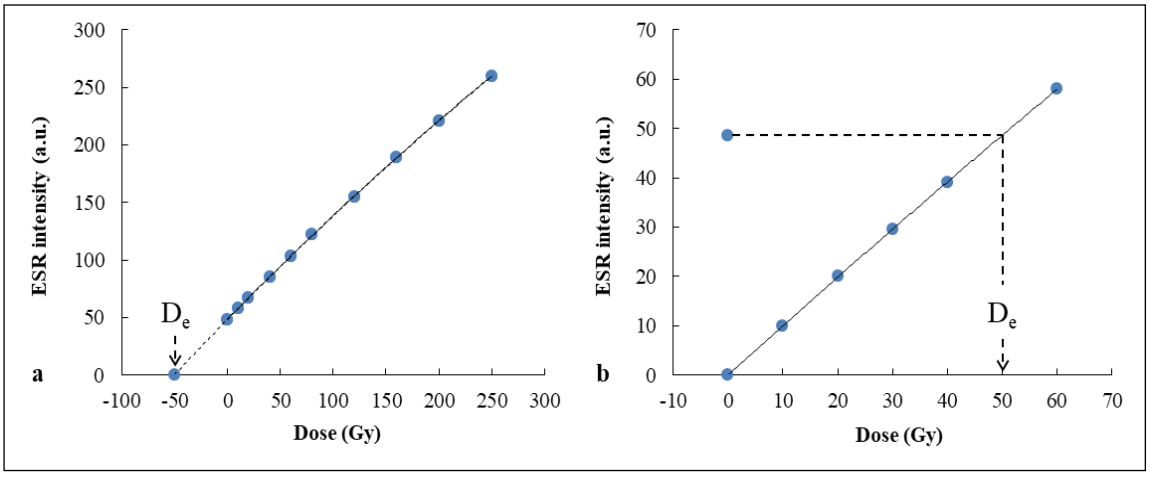

Figure 2.8: (a) The determination of D_e by the additive dose method. (b) The dose response curve and estimated D_e by the regeneration dose method.

Using an appropriate mathematical function plays a crucial role in the estimation of D_e, especially when the additive dose method is applied. A single saturating exponential (SSE) function is generally used to fit the data. This assumes that the ESR signal is dominated by a single paramagnetic centre. This assumption is not necessarily applicable to all conditions, however. Duval (2012) showed that the ESR intensity of the Al centre can show a rapid increase with a dose of a few kGy, and then grow more slowly at higher doses without reaching saturation, even up to 40 kGy. He suggested using an exponential + linear (EPL) function for curve fitting, assuming that two components generate the ESR signal, one having such a high saturation level that it can be approximated by a straight line. Woda and Wagner (2007) showed that the Ti centre has a non-monotonic behaviour as a function of absorbed dose. The signal decrease at higher doses was explained by double electron capture neutralising charge near the Ti centre, causing the centre to lose its paramagnetic properties. Consequently, an SSE function might not suitable to evaluate D_e for the Ti centre, and an empirical function was proposed to describe the decreasing behaviour (Woda and Wagner, 2007). A systematic comparison of several fitting functions was carried out by Duval and Guilarte (2015) to evaluate the ESR signals associated with the Ti-centres. The results indicated that the function suggested by Woda and Wagner (2007) could be used for the DRC of the Ti-Li centre when the maximum irradiation doses exceeded 6-10 kGy, while the SSE was able to provide reliable D_e estimations for

maximum irradiation doses below 6.0-6.5 kGy.

2.4 Estimation of dose rate (Ḋ)

The total dose rate is the combined contribution from alpha and beta particles, gamma and cosmic rays. The radioelement contents of quartz are negligible, so only the external dose rate is considered in the calculation (Figure 2.9).

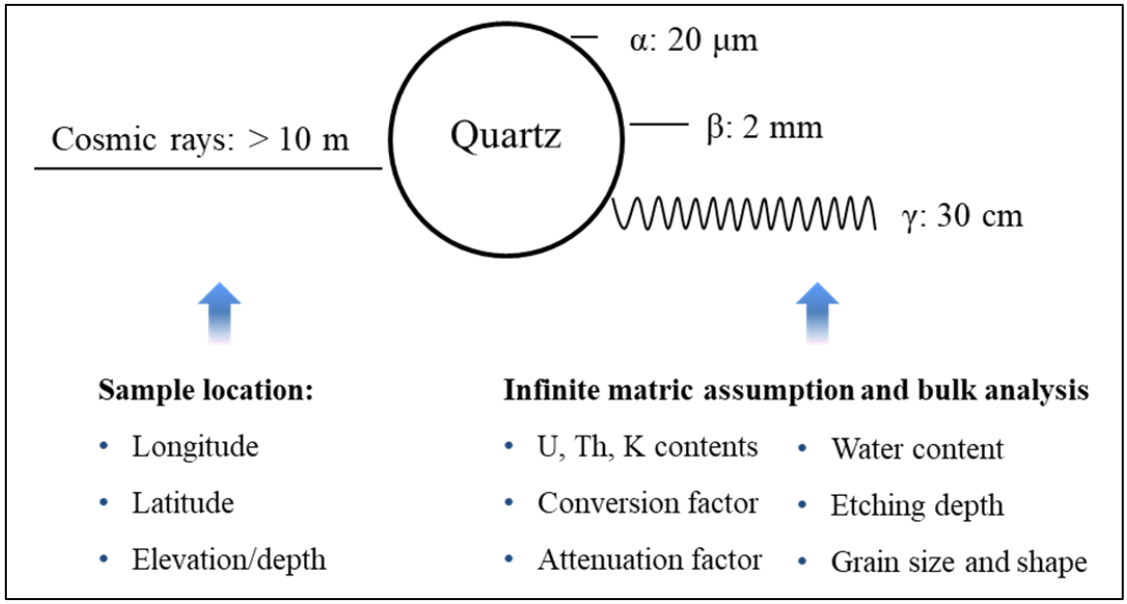

Figure 2.9: Schematic illustration of external radioactive interaction surrounding a quartz grain and the influential factors in the dose rate calculation.

Alpha particles (Helium nuclei) are produced by α-decay. They have high energy but, because of their large size, only a short range of ~ 20 μm in rock or soil. Their influence can be eliminated by using HF etching to remove the outer layers of the quartz grains once separated from a bulk sample. Beta particles are high-energy, high-velocity electrons/positrons emitted by radioactive nuclei during β-decay. They have a range of about 2 mm, and thus a heterogeneous environment can have a large effect on the beta dose rate received by quartz. Gamma rays are highly energetic photons with a range of 30 cm. Their relatively strong penetration of matter may simplify the gamma dose rate calculation as being an infinite matrix dose rate when the densities of most components are closely similar. The dose rate generated by the above contributors is a function of the

concentrations of radioactive elements (U, Th and K) surrounding the quartz grains, the various attenuation and conversion factors, water content, etching depth, and the size and shape of the quartz grains. The additional effect of cosmic rays (high-energy interstellar protons and atomic nuclei) can be determined from the sample's location (i.e., longitude, latitude, elevation, depth etc.; Prescott and Hutton, 1988). Beta and gamma dose rates are the major components in quartz dosimetry. Methods by which they are determined are described below.

2.4.1 Beta dose rate

The commonly applied method for calculating beta dose rate involves measuring the radionuclide concentrations or beta activity in bulk samples (Aitken, 1985). This is based on the assumption of an infinite matrix (Mejdahl, 1979). In reality, however, many samples exhibit complex microdosimetries, hindering the utilisation of this method (Guérin et al., 2012). In heterogeneous samples, the mean dose rate of a particular mineral (e.g., quartz, K-feldspar) is not the mean dose rate of the bulk sample. Most of the sample radioactivity comes from coarse grains or grain aggregates, so a significant part of the beta dose rate is self-absorbed by those radioactive grains. As a consequence, the dose rate in grains with low radioactivity, like quartz, can be significantly lower than the mean beta dose rate of the bulk. The mean dose rate of a mineral and the bulk would be closely similar only if all the grains are small and randomly distributed within the sample.

Although the accurate estimation of beta dose rate in a heterogeneous environment is difficult, several attempts have been made to address the issue. Direct surface measurements have been carried out on intact samples to estimate the spatial distribution of the beta dose rate. Such studies have used α-Al_2O_3:C grains (Kalchgruber et al., 2003), neutron-induced fission tracks (Wagner et al., 2005), autoradiography (Rufer and Preusser, 2009) and Timepix detectors (Romanyukha et al., 2017). The quantitative determination of beta dose rate distribution in natural samples remains a challenge, however.

Numerical modelling has been used to investigate the influence of mineral shape, grain

size and radioelement distribution on the beta dose rate. Taking quartz as an example, the differences in beta dose rate between grains of varied shapes are significant on an mm to cm scale, but grain shape has little influence for grains smaller than ~ 200 μm (Fain et al., 1999). The effects of grain size and radioelement content on dose rate distributions have been evaluated for K-feldspar. The skewness and dispersion of quartz dose rate distributions within a sample increase with increasing average grain size (Nathan et al., 2003; Guérin et al., 2015) and decreasing K-feldspar content (Mayya et al., 2006; Chauhan and Singhvi, 2011; Cunningham et al., 2012).

The development of DosiVox software (Martin et al., 2015) allows dose rate modelling of uploaded, realistic 3D geometries. DosiVox is a Geant4-based model which simulates particle-matter interactions using a Monte-Carlo approach and calculates the paths and interactions of each particle and secondary particles according to interaction probabilities. The beta dose rate is recorded in each voxel, and the results are displayed as the averaged beta dose rate of each mineral, a dose rate distribution map and a dose-frequency histogram. This method has enabled beta dose rate calculations at a single grain level and has shed new light on accurate estimations of dose rates in heterogeneous environments.

2.4.2 Gamma dose rate

The external gamma dose rate can be determined by *in situ* measurements and laboratory analyses. The former approach, using thermoluminescence dosimeters or a portable gamma spectrometer, has the advantage of taking water content and radioactive disequilibria into consideration. The latter approach is based on the measurement of radioelement concentrations in the surrounding environment, the conversion factors between radioelement activity and dose rate, and water content. For this method, the infinite matrix gamma dose rate can be applied as the dose rate for a specific mineral if the densities of most components in the sample are closely similar. Otherwise, it is necessary to consider the gamma attenuation factors of various mineral types in the calculations.

2.5 Applications in thermochronometry

2.5.1 Geological process and thermochronometry

Changes in the elevation of the Earth's surface are a function of many factors, chief amongst them tectonics (e.g., orogeny, isostasy) and erosion (e.g., by precipitation, rivers and glaciers) (Bonnet and Crave, 2003). Theoretically, a geomorphic system should tend to equilibrate with tectonic uplift because of negative feedbacks, for example an increase in uplift rate can lead to higher relief and thus to a higher denudation rate (Ahnert, 1970). Cases that reach steady state are rare, however (Adams, 1980). Instead, a multitude of examples demonstrate processes out of balance: uplifting landscapes driven by tectonic processes with little erosion, or deeply incised landforms overwhelmed by the rapidity of erosional processes (Molnar and England, 1990; Zhang et al., 2001).

Thermochronometry provides a method for determining the timing and rate of geological processes, helping to understand landscape evolution and the broader implications of landscape dynamics. Radioisotopic techniques (e.g., $^{40}Ar/^{39}Ar$, fission track, (U-Th)/He, and $^{4}He/^{3}He$ dating) are commonly-applied thermochronometers that utilise the relationship between radioactive decay of a parent nuclide and the accumulation of a corresponding daughter product. With the increasing interest in the timing of processes taking place at lower temperatures (< 100 ºC), trapped charge dating methods (electron spin resonance and luminescence) have become more widely applied. These methods utilise the production of radiation-induced charge trapping, thermally controlled detrapping and athermal loss. Thermochronometric techniques applied to different minerals provide records of unique temperature and time ranges. Specific combinations of these methods can be used to evaluate the time-temperature history of a region in detail. If the local geothermal gradient and surface temperature are known, the exhumation rate can be calculated. Then, thermo-kinematic modelling, combining a rock’s exhumation history with its potential influencing parameters (e.g., precipitation or glacial erosion, fault movement), makes it possible to reconstruct the nature of the tectonic forces and surface erosion processes (Braun et al., 2012; Zeitler et al., 2014).

The concept of closure (or blocking) temperature (T_c) was introduced by Dodson (1973). It was defined as the temperature of a system at the time corresponding to its apparent age (t_a), thereby providing a clear theoretical basis for understanding many mineral ages as cooling ages, a function of the interplay between the kinetics of diffusion (or annealing) and accumulation rates in cooling radioisotopic systems (Figure 2.10). The closure temperatures of commonly applied thermochronometers are shown in Figure 2.11 (Harrison, 1981; Harrison et al., 1985; Grün et al., 1999; Reiners and Farley, 1999; Ehlers et al., 2005; Bernet, 2009; Harrison et al., 2009; Herman et al., 2010; Guralnik et al., 2015a; Fang and Grün, in review).

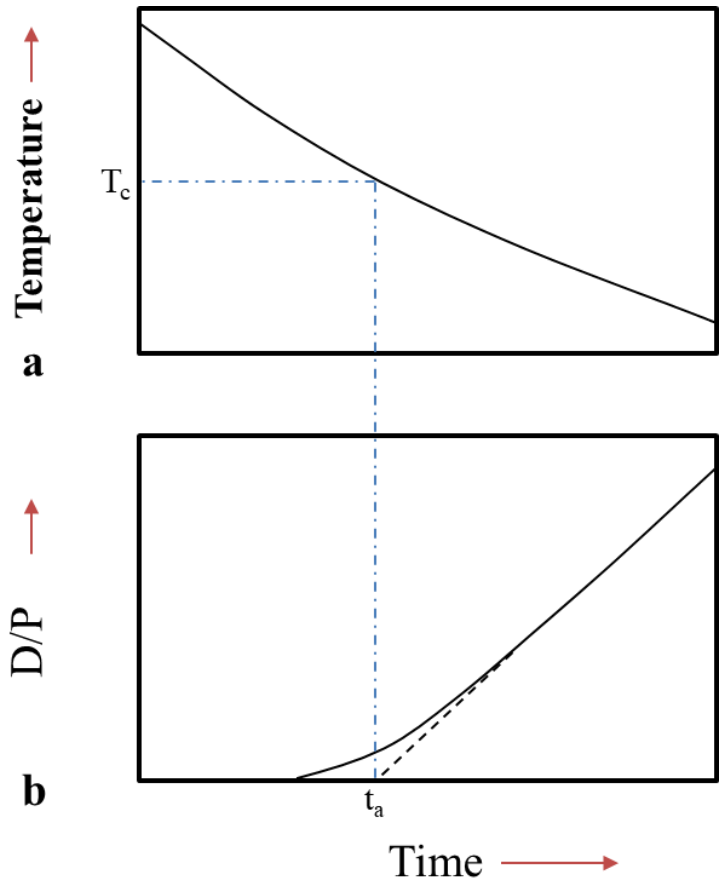

Figure 2.10: The concept of closure temperature (Dodson, 1973). (a) Temperature decreasing monotonically with time. (b) The accumulation of daughter nuclide with time. D/P refers to the ratio of daughter nuclides versus parent nuclides.

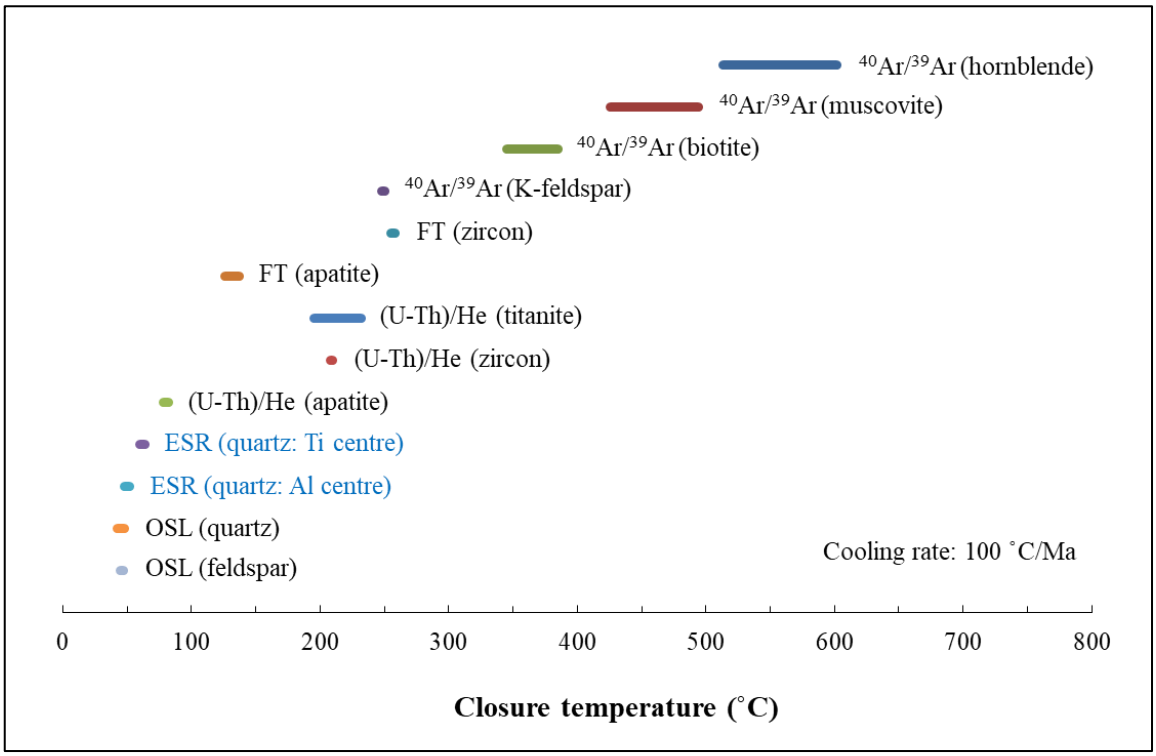

Figure 2.11: The closure temperatures of various thermochronometers for a cooling rate of 100 ºC/Ma (Harrison, 1981; Harrison et al., 1985; Grün et al., 1999; Reiners and Farley, 1999; Ehlers et al., 2005; Bernet, 2009; Harrison et al., 2009; Herman et al., 2010; Guralnik et al., 2015a; Fang and Grün, in review).

As radioisotopic dating techniques were developed further, researchers realised that the concept of a specific blocking temperature was not able to fully describe the influences of temperature and time on diffusion (or annealing). The notion of a partial annealing zone was first raised in fission track dating (Wagner et al., 1989). This has subsequently been adapted to a diffusive context as the partial retention zone (PRZ) for determining a temperature range above which the daughter product immediately diffuses out of the system when produced by radioactive decay and below which the daughter product is entirely retained (Baldwin and Lister, 1998; Wolf et al., 1998). It should be noted that both closure temperature and PRZ are negatively correlated with the cooling rate; the faster the cooling, the higher the temperature.

The other consideration in using a particular thermochronometer is its applicable age range. The lower limits of radiometric dating methods, depending on the detection limits

for the target isotopes or visible fission tracks, are approximately 0.1-0.2 Ma (Zeitler et al., 2014; Bracciali et al., 2016). The upper limits of these methods depend upon the half-lives of the relevant isotopes, which are ~ 4 Ga for $^{40}Ar/^{39}Ar$ dating, ~ 2 Ga for fission track (FT) dating (another main limitation being track density), and ~ 100 Ma for (U-Th)/He dating. Considering trapped charge techniques, luminescence dating (e.g., OSL—optically stimulated luminescence) can estimate ages down to between about 1 and 200 ka (Guralnik et al., 2015a; King et al., 2016b), whereas ESR dating covers the time range from 10 ka to 2 Ma (Rink et al., 2007).

2.5.2 Current status and challenges of ESR thermochronometry

During the last two decades, developments in both theoretical and analytical techniques have significantly improved trapped charge dating methods. Luminescence thermochronometry has been developed rapidly since its introduction (Herman et al., 2010). Numerical simulations have been used to describe the ingrowth-annealing behaviour of paramagnetic centres, and models from the basic first order to general order kinetics have been developed (Whitehead et al., 2009; Li and Li, 2012; Guralnik et al., 2015b). The study of Guralnik et al. (2015a) has proved that laboratory-obtained trap parameters can be extrapolated to conditions relevant in nature. Then, the development of luminescence as a multi-thermochronometer which is based on the establishment of multi-elevated-temperature (MET) measurement protocol (Li and Li, 2011), provides a series of time-temperature constraints from one sample (King et al., 2016a; Biswas et al., 2018). In the last five years, luminescence thermochronometry has been successfully applied in a range of geological settings for exploring their cooling histories over the past 0.2 Ma (Guralnik et al., 2015a; Tang, 2015; King et al., 2016a; Brown, 2017). For ESR thermochronometry, Scherer et al. (1993; 1994) carried out ESR measurements on borehole samples from KTB and Eldzhurtinskiy Granite, and pointed out the paramegnetic centres decreased with depth, which paved the way for a further study conducted by Grün et al. (1999). Based on the explorations of thermal stabilities of paramagnetic centres in quartz, Grün et al. (1999) assessed the cooling rate of Eldzhurtinskiy Granite from the Caucasus, and calculated the effective closure

temperatures for the Al centre (49 and 64 ºC) and Ti centre (55 and 82 ºC) for the cooling rates of 40 and 1000 ºC/Ma. This study indicated the potential of using ESR dating in evaluating geological processes, but ESR thermochronometry was not further pursued thereafter.

Compared to radioisotopic thermochronometers, ESR dating has a lower range of PRZ for the same cooling rate, which makes it possible to investigate the neotectonic movement and landscape process. Compared to luminescence thermochronometry, ESR dating has the advantage of recording a longer thermal history on the timescale of ~ 2 Ma, which provides better time constraints between the upper age limit of luminescence dating and the lower limit of (U-Th)/He dating. ESR dating has only occasionally been used in thermochronometry, however, and faces some challenges for methodological improvement and in its practical application.

Firstly, the extrapolation of laboratory-based measurements of trap parameters to natural settings needs to be verified. This can be approached by the analysis of borehole samples with a well-defined thermal history and known ambient temperatures. The accumulation of paramagnetic centres is a balance between the processes of production and decay in natural samples. The rate of production depends on the number of available empty traps and the strength of the radioactive field, and the rate of decay is controlled by temperature and thermal kinetics. Numerical simulations can be used to quantify the trap parameters under natural geologic conditions, and models from the basic first order to general order kinetics have been developed (Whitehead et al., 2009; Li and Li, 2012; Guralnik et al., 2015b).

Secondly, a rigorous method for estimating dose rates in heterogeneous rocks is required. Most rocks have complex fabrics, mineral structures and compositions, and quartz grains can have any shape, size, and external dose rate environment according to the rock's texture. For example, quartz surrounded by K-feldspars or micas will receive higher beta doses than those located close to plagioclase. After crushing of the rocks, it is impossible to gain any information about the heterogeneity of the original average beta dose rate. The ideal solution is to apply 3D calculations. However, 3D images of rock are difficult

to obtain by X-ray CT (computed tomography) scanning because this equipment is not easily accessible for routine analysis and complete mineral identification is almost impossible (e.g., some minerals, such as quartz and plagioclase, have similar X-ray attenuation coefficients). These problems can be solved by 2D X-ray mapping and beta ray modelling techniques. A critical issue of representativeness arises for the reconstruction of 3D geometries from 2D simulations. The study of Plachy and Sutton (1982) used a dose point kernel method to estimate beta dose rate received by quartz in a granite rock cube. The 3D geometry was reconstructed by combining 2D maps of different mineral phases created by Cathodoluminescence photography while abrading the sample slice after slice. This pioneering work showed that a 2D model can represent a 3D simulation when the mineral distributions in 2D slices are isotropic. There is a pressing need for the development of a suitable 2D model for obtaining realistic dose rates from heterogeneous rocks.

Thirdly, due to ESR's low closure temperature and applicable dating range (10 ka to 2 Ma), field saturation of the ESR signal restricts the application of this dating method to areas that have experienced recent rapid cooling. In this regard, the Namche Barwa massif, located at the eastern end of the Himalayan orogen, is an ideal sampling location. This region is well known as a site of the most pronounced and recent tectonic movements, as well as rapid exhumation processes. Additionally, combining multiple thermochronometers enables the derivation of continuous thermal histories, but this approach has not previously been applied using ESR thermochronometry.

For applying ESR thermochronometry in estimating cooling and exhumation histories, it is essential to obtain realistic trap parameters of Al and Ti centres, as well as establish a method for accurate estimation of beta dose rate on heterogeneous rocks. In this project, trap parameters of paramagnetic centres in quartz were first measured with borehole samples under natural geological settings. Then, a new method was developed for more accurately estimating beta dose rate by 2D modelling. Finally, ESR thermochronometry has been applied to Namche Barwa massif for understanding its late-stage domal development process.

3 ESR thermochronometry of Al and Ti centres in quartz: A case study of the Fergusons Hill-1 borehole from the Otway Basin, Australia

This chapter is under review in the Radiation Measurements: Fang, F., Grün, R. ESR thermochronometry of Al and Ti centres in quartz: A case study of the Fergusons Hill-1 borehole from the Otway Basin, Australia. Radiation Measurements.

The authors' contributions to the publication are: Fang F. has conducted the ESR analyses, evaluated the data and wrote the article. Grün R. provided suggestions on the experiment and data analysis, and corrected the manuscript.

Abstract

Electron spin resonance (ESR) thermochronometry can, in principle, be used for reconstructing thermal histories of the upper ~ 2 km of the Earth's crust. We have analysed the ESR ages of Al and Ti centres in quartz from Fergusons Hill-1 borehole in the Otway Basin, Australia, to assess their trap parameters under natural conditions. The apparent ESR ages of both centres decrease with increasing temperature (42.9–56.2 ºC). Feasible sequential quadratic programming optimisation algorithm was applied to determine the optimal trap parameters based on the first order kinetic assumption and thermally static condition. The estimated activation energy and frequency factor of the Al centre in quartz were 1.5 eV and 1.1×10^{11} s^{-1}, respectively. This was in excellent agreement with a re-analysis of samples from the Eldzhurtinskiy granite, representing a highly dynamic geologic system, for which we obtained 1.5 eV and 1.0×10^{11} s^{-1}. The trap parameters of the Ti centre could not be obtained from first order kinetics for the Fergusons Hill samples, but the samples from the Eldzhurtinskiy yielded 1.6 eV and 2.4×10^{11} s^{-1}. Further studies on trap kinetics under better controlled laboratory conditions are required for ESR thermochronometry.

Keywords: low-temperature thermochronometry; quartz; trap kinetics

3.1 Introduction

Low temperature thermochronometry has been used to evaluate the timing and rate of Earth-surface processes and to understand the broader implications of the Earth's dynamics (Reiners et al., 2005; Peyton and Carrapa, 2013). Trapped charge dating techniques, including electron spin resonance (ESR), optically stimulated luminescence (OSL) and thermoluminescence (TL), record the production of radiation-induced charge trapping, thermally-controlled detrapping and athermal loss. These techniques have been introduced as low temperature thermochronometers for assessing the most recent thermal history because of their high sensitivity in the temperature range < 100 ºC (Grün et al., 1999; Herman et al., 2010; Li and Li, 2012). In recent years, luminescence thermochronometers have been developed and applied in a range of geological settings (Guralnik et al., 2015a; Tang, 2015; King et al., 2016a; Brown, 2017), while virtually no progress was made in ESR thermochronometry. The age limits of ESR and luminescence dating are defined by the signal saturation doses and thermal stabilities (Tsukamoto et al., 2018). ESR dating has a great potential to record longer thermal history on the timescale of ~ 2 Ma (Rink et al., 2007), which is beyond the upper age limit (~ 200 ka) of luminescence dating (Guralnik et al., 2015a; King et al., 2016b). Thus, there is much to be gained from further developing this method.

Quantitative investigations of thermal histories by ESR thermochronometry rely on the determination of trap kinetics, which are commonly estimated by a series of laboratory isothermal annealing experiments. First order kinetics are usually assumed in calculations, but Toyoda and Ikeya (1991) have shown that their results followed second order kinetics. The published values for the activation energy (E_a) and escape frequency factor (ν_0) of quartz vary greatly (Imai et al., 1985; Melnikov et al., 1989; Fukuchi, 1992; Toyoda and Ikeya, 1991, 1994). This may be attributed to the different origins of the quartz sampled (Marfunin, 2012). In addition to the discrepancies in laboratory calibrations of trap parameters, laboratory results require validation from natural settings. The time range of laboratory studies is 7–8 orders of magnitude shorter than that of natural conditions, so large uncertainties inherent in the extrapolation of the laboratory results to natural settings

may compromise the geological application of ESR thermochronometry. A straightforward way to obtain realistic trap parameters is through investigations of samples from bore holes with well-characterised thermal histories and measured downhole temperatures (Tagami et al., 1996; House et al., 1999; Guralnik et al., 2015a; Brown et al., 2017). Samples from the ESR partial retention zone (a temperature range that above which the trapped electrons can be immediately reset when produced by ionizing radiation and below which the trapped electrons can be entirely retained) characterise annealing under natural conditions, and the corresponding age-temperature profile sheds light on the realistic estimation of trap parameters. Scherer et al. (1993; 1994) carried out ESR measurements on borehole samples from KTB and Eldzhurtinskiy Granite, and pointed out the ESR intensities of paramagnetic centres decreased with increasing depth, which paved the way for a further study conducted by Grün et al. (1999). Based on the explorations of thermal stabilities of paramagnetic centres in quartz, Grün et al. (1999) assessed the cooling rate of Eldzhurtinskiy Granite from the Caucasus, and calculated the effective closure temperatures for the Al centre (49 and 64 ºC) and Ti centre (55 and 82 ºC) for the cooling rates of 40 and 1000 ºC/Ma.

Numerical simulations have previously been used to describe the ingrowth-annealing behaviour of paramagnetic centres, and models from the basic first order to general order kinetics have been developed (Whitehead et al., 2009; Li and Li, 2012; Guralnik et al., 2015b). The number of paramagnetic centres in a sample results from the balance between the processes of production and decay. The rate of production depends on the number of available empty traps and the strength of the radioactive field, the rate of decay is controlled by temperature and thermal kinetics. For ESR, OSL and TL, first order kinetics assumes that all electrons evicted from the traps recombine with holes and no retrapping occurs (Randall and Wilkins, 1945), and second order assumes that the probability of recombination and retrapping is 50% (Garlick and Gibson, 1948).

In this study, we attempt to estimate the trap parameters of Al and Ti centres in quartz in natural settings using first order kinetics. Samples of detrital quartz were taken from the Fergusons Hill-1 (FH1) borehole from the eastern Otway Basin, which has remained in an

approximately stable thermal condition for the last few million years (House et al., 1999). To assess the possible influence of the origin of the quartz, the trap parameters of quartz from the Eldzhurtinskiy granite (lower core) were recalculated from the data published by Grün et al. (1999). We also discuss the applicability of data extrapolation in ESR thermochronometry by comparing the borehole data with published trap parameters from laboratory experiments. Moreover, the closure temperature and dating range of ESR thermochronometry were compared to other low temperature thermochronometric techniques.

3.2 Sample descriptions

The FH1 borehole penetrates 3546 m of the eastern Otway Basin, which formed in conjunction with Mesozoic continental rifting along the southern margin of Australia (Duddy, 1983). The FH1 borehole is composed of relatively uniform non-marine sediments. Five samples, from early Cretaceous units of the Otway Group, were selected from depths of 941, 1138, 1248, 1548 and 1693 m (Figure 3.1). The borehole temperatures (BT) were recorded at seven depths from 940 to 3541 m when drilling and the present day geothermal gradient is reported to be 33 ºC/km (Struckmeyer, 1988). Previous thermochronometry by apatite fission track (AFT) and apatite (U-Th)/He (AHe) techniques yielded ages that decreased consistently with increasing depth and temperature (French, 1984; House et al., 2002). In addition, TL analysis of quartz had been used to establish a relationship between temperature and glow curve characteristics (Ypma and Hochman, 1991).

The thermal history of the FH1 borehole has been estimated from vitrinite reflectance (VR), AFT, AHe and quartz TL data (French, 1984; Ypma and Hochman, 1991; Duddy, 1994; Cooper and Hill, 1997; House et al., 1999; House et al., 2002; Green et al., 2004). Deposition of the Otway Group at the location of FH1 was approximately contemporaneous with volcanism at ~ 120 Ma, and followed by cooling to present temperatures during the late Eocene-Pliocene (Duddy, 1994; Cooper and Hill, 1997). The

cooling is solely due to the regional uplift at a rate of < 3°C/Ma (House et al., 1999), but the timing is poorly constrained. The thermal histories of other drill cores (Anglesea-1, Nerita-1) from the eastern Otway Basin have shown that the cooling started at between 12 and 5 Ma (Green et al., 2004; Holford et al., 2011). Recently, reverse slip along the underlying faults between 2 and 1 Ma has been suggested as the cause of the present-day topographic relief of ~ 245 m (Sandiford, 2003; Clark et al., 2011). Strictly speaking, the samples from FH1 borehole have not been stored at constant temperatures, while they are unlikely to have been heated or cooled significantly over the last few million years.

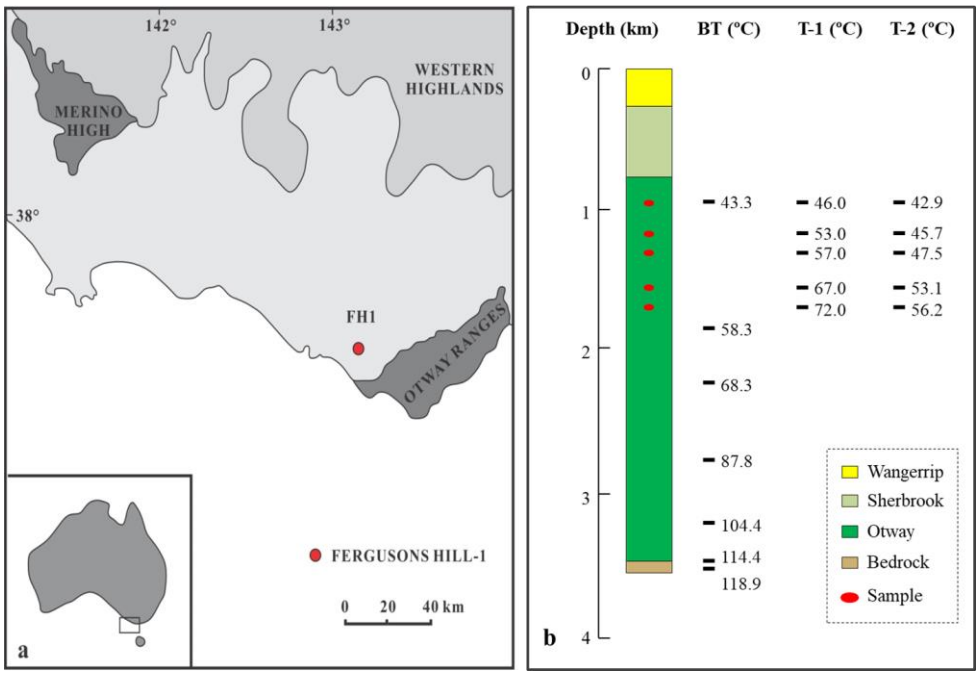

Figure 3.1: (a) The location of Fergusons Hill-1 borehole (after Dickinson et al., 2002), and the varied grey levels indicate different units. (b) The sample depth, stratigraphic formation (Ypma and Hochman, 1991), temperature record (BT), and estimated temperatures of five samples (T-1, T-2, discussed in section 3.5.1). The samples belong to the early Cretaceous units of the Otway Group.

3.3 Methodology

3.3.1 Sample preparation

The borehole samples were stored and prepared under the condition of avoiding sunlight

exposure. The quartz-rich fractions were separated at the Australian National University (ANU), and HF etching was conducted at the University of Hong Kong. The crushed samples were sieved to extract the 150–250 μm grain size, and non-magnetic fractions were obtained by Frantz separator using a magnet current of 1.5 Amp and side-slope of 5º. Density separation in tetrabromoethane was used to obtain quartz in the density range 2.62–2.68 g/cm^3. The quartz-rich fractions were etched in 40% HF for 40 min to remove both possibly alpha damaged surfaces and remaining feldspars, and subsequently rinsed with 10% HCl to dissolve fluorides. Samples were dried at room temperature and re-sieved at 100 μm.

3.3.2 ESR measurements

ESR measurements were carried out on an X-band Bruker spectrometer with a 1.5T magnet and a rectangular 4102 ST cavity. The measurements of Al and Ti centres were conducted at 77 °K by inserting a quartz-glass tube into a finger dewar filled with liquid nitrogen. The parameters for Al and Ti centres were accumulation of 20 scans with 100 kHz modulation frequency, 0.1 mT modulation amplitude, 10.24 ms conversion factor, 20.48 ms time constant, 1024 bit spectrum resolution, 5.065 mW microwave power (Grün et al., 1999), centre field of 3410 G and sweep width of 360 G. Considering the angular dependence of the ESR signal, each aliquot was measured six times after a 60° rotation of the dewar in the cavity. The peak to peak height between A1 (g=2.018) and A2 (g=1.993) was used as the intensity of the Al centre (Figure 3.2). The ESR intensity of Ti-Li centre was defined as the amplitude between the top of peak T1 at g=1.979 and the bottom of peak T2 around g =1.913 (Figure 3.2).

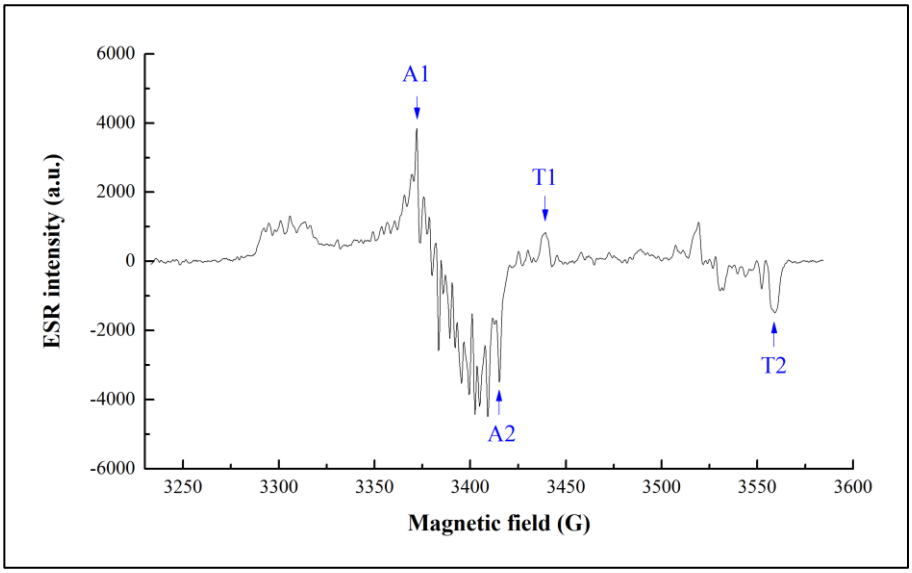

Figure 3.2: The ESR spectrum of FH1-8 after adding a 612 Gy X-ray dose on top of the natural signal and subtracting the peroxy signal obtained from annealed ESR spectrum. The intensity of the Al centre is calculated from A1 to A2, and the intensity of the Ti-Li centre is quantified from T1 to T2.

3.3.3 Test for sensitivity change

Sample FH1-8 was used to detect sensitivity change caused by the annealing through a regenerative-additive plot (Toyoda et al., 2009; Asagoe et al., 2011). This plot is based on the same idea as the "single aliquot regeneration/added dose" procedure used in luminescence dating (Mejdahl and Bøtter-Jensen, 1994). Two sample sets were irradiated by a RS2000 X-ray irradiator (160 kV, 25 mA) at ANU. The calibration of X-ray dose rate on quartz grains is explained in Appendix. Firstly, a regeneration dose response was established with dose steps of 0, 306, 612, 918, 1224, 2295 and 3825 Gy (Figure 3.3a, b). Then the natural samples were exposed to additive doses of 0, 153, 306, 612 and 1224 Gy. To evaluate sensitivity changes, the intensities of the additive dosed samples were projected onto the regeneration dose response yielding apparent dose values on the X-axis (see dotted lines in Figure 3.3a, b). These apparent dose values were then plotted against the added dose values (Figure 3.3c, d). Slopes deviating from 1 indicate sensitivity changes. It can be seen that the changes are < 6%. Compared the equivalent dose (D_e) values calculated by regenerative dose method (SAR) and regenerative-additive method

(SARA), the differences of D_e values of Al and Ti centres are within ~ 10% between SAR and SARS methods. This indicates that there is no significant sensitivity change occurring by the annealing step, and thus D_e values can be obtained by the regenerative dose method.

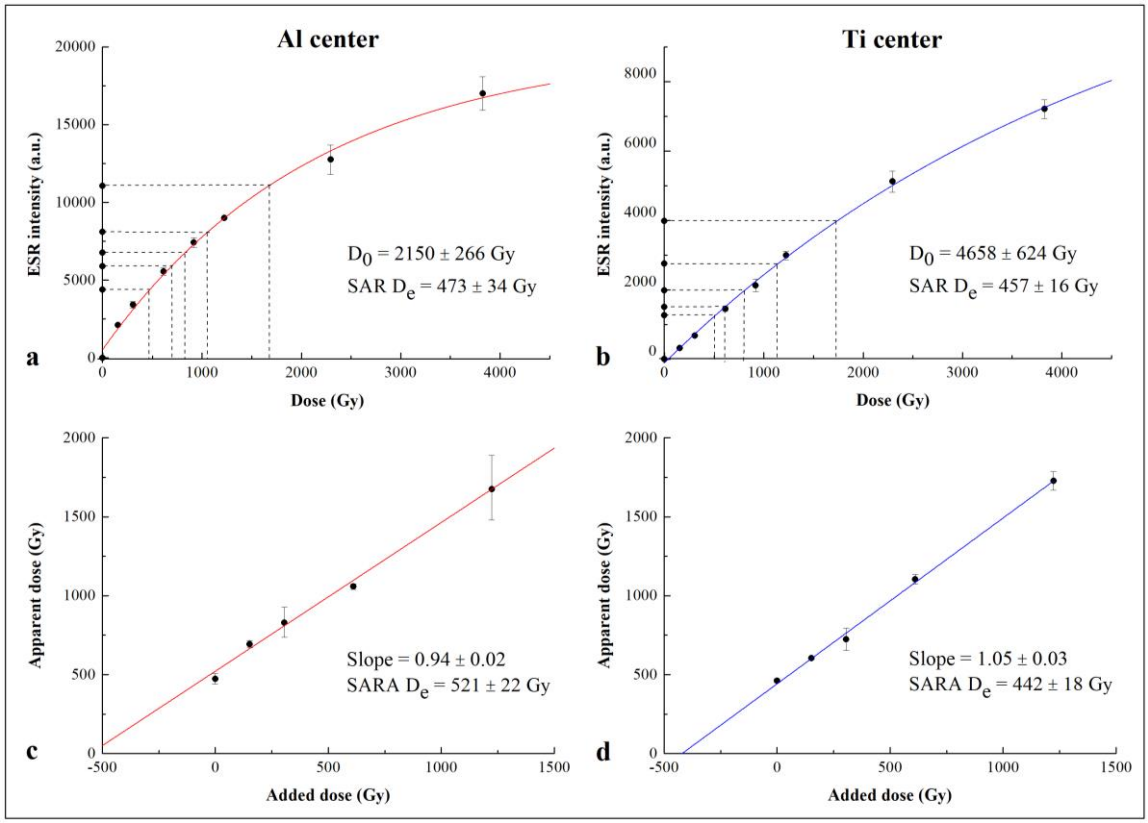

Figure 3.3: (a, b) Regenerative dose response curves of Al and Ti centres, and fitted by SSE function. (c, d) The regenerative-additive plots of Al and Ti centres.

3.3.4 Estimation of equivalent dose (D_e)

The single aliquot regenerative method was applied for determining D_e, and each aliquot contained 60 mg quartz grains. The intensities of the Al and Ti centres were firstly measured on natural samples. After samples were heated at 350 °C for 120 min, the ESR measurements were carried out on annealed samples to check the signal intensities were completely zeroed. To generate dose response curve (DRC), annealed samples were irradiated with total dose steps of 0, 306, 612, and 918 Gy delivered by an X-ray source. ESR measurements were then conducted following each irradiation step. The single saturation exponential (SSE) function was applied for fitting the dose response curve of

the Al centre, and weighted by the inverse of the squared ESR intensity. Linear fitting was applied to the data points of the dose response of the Ti centre. The D_e values were obtained by projecting the natural ESR intensities of Al and Ti centres onto their corresponding DRCs, respectively. The peroxy centre overlaps the Al centre in all samples, and its intensity after annealing at 350 °C for 120 min was subtracted from that of the Al centre in natural and irradiated samples (Tsukamoto et al., 2015).

3.3.5 Dose rate (Ḋ) calculation

The bulk sample radionuclide concentrations were analysed by inductively coupled plasma optical emission spectrometry (ICP-OES) for K and inductively coupled plasma mass spectrometry (ICP-MS) for U and Th at Genalysis, Perth, Australia. The radioelement concentrations of quartz were assumed to be negligible. The original grain size of quartz cannot be obtained after crushing, and is also difficult to be estimated from the thin sections of sedimentary core samples. Thus, the crushed grain size of 150-250 μm with etching depth of 10-20 μm was utilized in the calculations. A water content of 4±2% was assumed for all samples. The dose rate from cosmic rays was negligible due to the deep burial. The dose rate calculation was conducted in DRAC 1.2 (Durcan et al., 2015), using the conversion factors of Guérin et al. (2011), the beta attenuation factors of Guérin et al. (2012), and the beta etch depth attenuation factor of Bell (1979).

3.4 First order kinetic model

3.4.1 Mathematical equations

Dating minerals by ESR relies on two processes that control the accumulation and annihilation of paramagnetic centres. In the natural geological system, we assumed that these processes followed first order kinetics. The equations for the calculation of apparent age under steady state and cooling scenarios are described below, and are based on the theoretical study of Li and Li (2012). The relation between trapping and detrapping is quantified by:

$$\frac{dn}{dt} = \frac{\dot{D}}{D_0}(N - n) - \frac{n}{\tau} \quad (3.1)$$

where D_0 (Gy) is the characteristic saturation dose, $\dot{D}$ (Gy/ka) is the total dose rate of irradiation, N is the total number of traps, n is the number of occupied traps at time t, and τ is the theoretical lifetime of the trapped charges. Due to the influence of D_0 and $\dot{D}$, the effective lifetime (τ') of the trapped charges is described by equation (3.2). The values of τ and τ' are the same at high temperatures, and τ' gradually gets smaller with decreasing temperature.

$$\tau' = \left(\frac{\dot{D}}{D_0} + \frac{1}{\tau}\right)^{-1} = \left(\frac{\dot{D}}{D_0} + \nu_0 e^{-E_a/k_B T}\right)^{-1} \quad (3.2)$$

where T (K) is the temperature, E_a (eV) is the activation energy, ν_0 (s^{-1}) is the escape frequency factor, and k_B is Boltzmann's constant (8.617×10^{-5} eV/K).

At a fixed temperature, the apparent age (t_a) increases with the change of isothermal holding time (t), and the maximum age that can be measured is within $2D_0/\dot{D}$.

$$t_a = -\frac{D_0}{\dot{D}} \ln\left(1 - \frac{\dot{D}}{D_0}\tau'\left(1 - e^{-\frac{t}{\tau'}}\right)\right) \quad (3.3)$$

To explore the ESR signal accumulation at a variety of temperatures, the trap parameter of the Al centre in a virtual quartz sample was applied by assuming D_0 = 3000 Gy, E_a = 1.6 eV and $\nu_0 = 10^{12}$ s^{-1}. The changes of apparent ESR age with time are shown in Figure 3.4a, using $\dot{D}$ = 3 Gy/ka and t = 10 Ma. At 30 ºC, the apparent age will reach equilibrium at 2 Ma because of the maximum age limitation. The equilibrium age is reached much quicker at higher temperatures, and samples being held at 50 ºC and 80 ºC require ~ 1300 ka and 10 ka respectively to equilibrate.

Under the condition of an averaged cooling rate (η), temperature (T) is a function of cooling time (t) and initial temperature (T_0):

$$T(t) = T_0 - \eta t \quad (3.4)$$

$$\frac{dt_a}{dt} = 1 - \frac{D_0}{\dot{D}\tau}\left(e^{\frac{t_a}{\dot{D}D_0}} - 1\right) \quad (3.5)$$

Equation (3.5) yields the apparent age as a function of cooling time. Figure 3.4b shows

the scenarios for different cooling rates, and same trap parameter was used as in steady state.

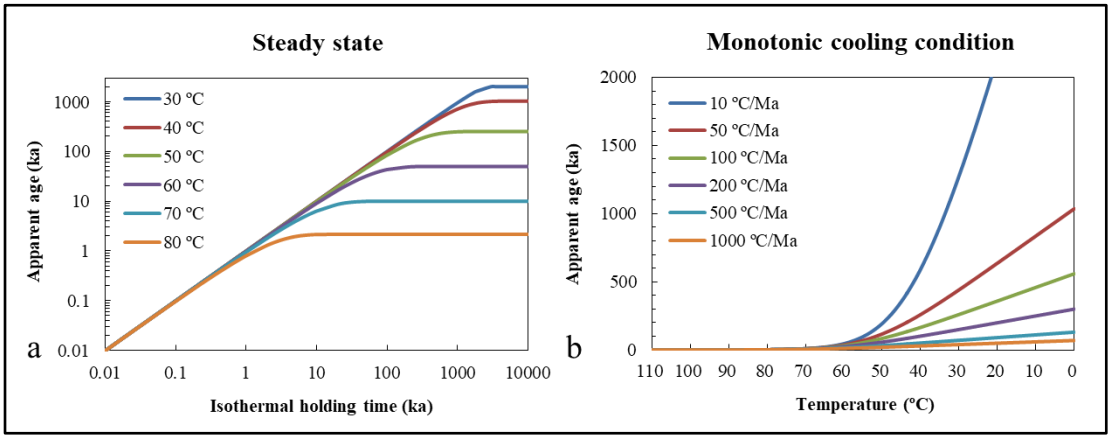

Figure 3.4: (a) Apparent age as a function of isothermal holding time at a series of temperatures. (b) Apparent age as a function of temperature for a variety of cooling rates.

3.4.2 Fitting procedure

For borehole samples, the apparent ages of a paramagnetic centre can be calculated if trap parameters, storage temperature and thermal history are known. Vice versa, trap parameters can be obtained by fitting the relationship between ages and temperatures for a given thermal history. Thus, the equations in section 3.4.1 were transferred into FORTRAN90 code with E_a and ν_0 set as flexible parameters. The feasible sequential quadratic programming (FSQP) optimisation package (Zhou et al., 1997) was utilised to obtain the optimised solution for trap parameters. The FSQP algorithm is a method for solving nonlinearly constrained optimisation problems. The input data included the D_0 of the corresponding paramagnetic centre, the $\dot{D}$ and apparent ages of the measured paramagnetic centre, ambient and initial temperatures (T_p, T_0) of the samples, isothermal holding time t for steady state conditions and cooling rate η for cooling conditions. The root mean square error between simulated and measured ESR ages was set as the objective function for the optimisation program.

3.5 Results

3.5.1 Ambient temperature of selected FH1 samples

The *in situ* BTs were measured at seven depths from 940 to 3541 m in the FH1 borehole. The calculation of ambient temperatures for selected samples is essential to estimate trap parameters, so two calculation approaches were compared in this study. The first approach (T-1) was based on the constant present-day geothermal gradient. The measured bottom hole temperature (118.9 ºC at the depth of 3541 m) was firstly corrected for drilling disturbances by increasing its value to 133 ºC (Struckmeyer, 1988), which is consistent with the results obtained by following the correction method of Andrews-Speed et al. (1984). Assuming a surface temperature of 15 ºC, linear fitting of corrected data provided the estimation of ambient temperatures for five samples. However, for the *in situ* BTs (Figure 3.5a), the data points deviate from linear and approach higher temperatures at shallower depths.

The second approach (T-2) used the initial BTs (provided by the Victorian state government) fitted by a second order polynomial function. The grey bar in Figure 3.5a shows the depth of selected samples, and the differences between estimated temperatures by the two methods increase from 3.1 ºC at 941 m to 15.8 ºC at 1693 m (Figure 3.5b). Low temperature thermochronometers (<100 ºC) are very sensitive to the change in temperature. The measured AHe ages were compared with the modelled age profiles (after House et al., 2002) based on the thermal history reported by Duddy (1994) and the temperatures obtained by the two approaches. The observed ages are better fitted with age profiles determined by T-2 (Figure 3.6, red contour). Thus, the ambient temperatures obtained from second approach (T-2) were used for calculating trap parameters, which may better quantify the realistic conditions within such a depth range.

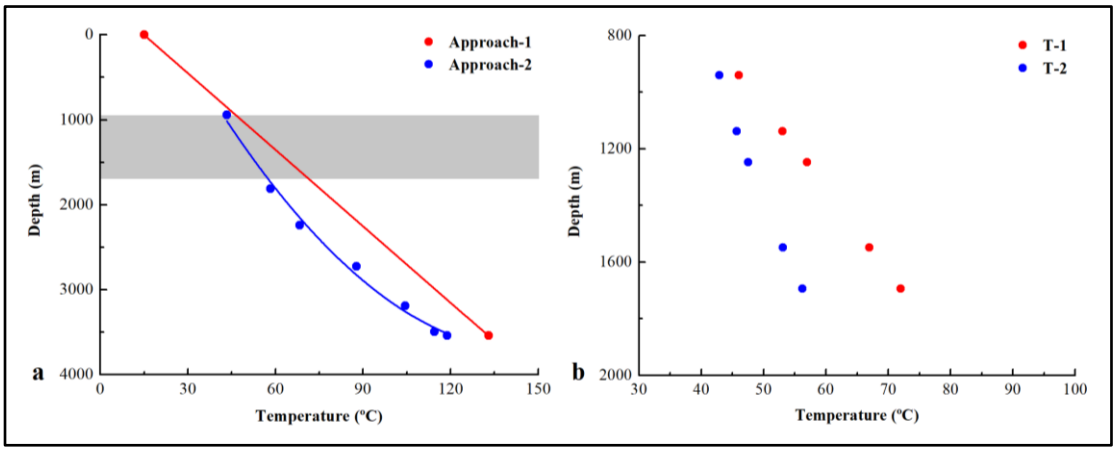

Figure 3.5: (a) The blue points are *in situ* measured temperatures of FH1 borehole and the red points are assumed surface temperature (15 ºC) and corrected bottom hole temperature (133 ºC). The blue and red lines are fitting curves of applied approaches for obtaining storage temperatures of samples in this study. The horizontal grey bar indicates the depths of samples. (b) The obtained ambient temperatures (T-1 and T-2) of samples by using first approach and second approach in calculation.

3.5.2 The estimation of trap parameters

The total dose rates and ESR ages of the Al and Ti centres are listed in Table 3.1. The Ḋ values are closely similar, indicating uniform sediment sources for the samples. The ESR ages of the Al centre decrease with depth and downhole temperature from 208 ± 16 to 32 ± 2 ka, and the ages of the Ti centre decrease from 201 ± 10 to 76 ± 4 ka. Compared to the ages determined by AHe and AFT dating, the ESR ages of the Al and Ti centres are consistently younger by 2–4 orders of magnitude (Figure 3.6). This indicates that ESR thermochronometry could have the advantage of providing more precise low temperature histories for the Quaternary.

Table 3.1: The results of chemical analyses, total dose rates and ESR ages.

Sample	Depth	Bulk sample				Al centre		Ti centre	
		U	Th	K	Ḋ	D_e	Age	D_e	Age
	m	ppm	ppm	%	Gy/ka	Gy	ka	Gy	Ka
FH1-8	941	1.65±0.09	5.50±0.24	1.65±0.06	2.27±0.07	473±34	208±16	457±16	201±10
FH1-11	1138	1.48±0.09	6.36±0.27	1.70±0.07	2.33±0.07	311±7	134±5	389±24	167±1
FH1-12	1248	2.31±0.11	9.12±0.38	1.83±0.07	2.82±0.08	275±6	98±4	410±18	146±8
FH1-14	1548	2.41±0.11	7.61±0.32	1.52±0.06	2.45±0.07	138±7	57±3	278±13	114±6
FH1-15	1693	2.06±0.10	7.69±0.33	1.51±0.06	2.36±0.07	75±5	32±2	179±9	76±4

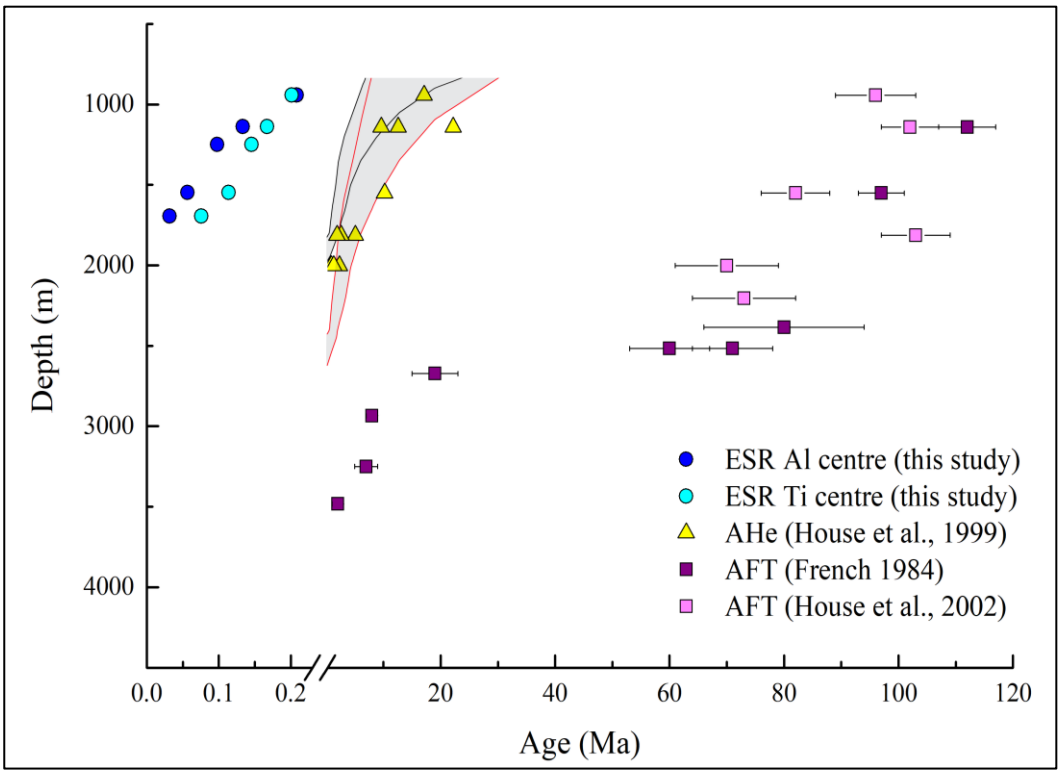

Figure 3.6: Overview of thermochronometric results from the FH1 borehole. The predicted He age envelopes (after House et al., 2002) with grain radii of 35–100 μm using the thermal history of Duddy (1994) are compared with the present day estimated temperature profiles of T-1 (black contour) and T-2 (red contour).

The samples from the FH1 borehole can be considered to be in a steady state (the number of thermally released electrons from the traps is equal to the number of newly trapped elections due to environmental radiation) since the cooling rate during the last few million years is < 3 ºC/Ma (House et al., 1999). The optimal trap parameters were simulated by fitting the measured ESR ages of Al and Ti centres based on equation 3.3. The input parameters are: D_0 values of Al (2150 ± 270 Gy) and Ti (4660 ± 620 Gy) centres calculated from FH1-8, the dose rates, ESR ages and ambient temperatures of T-2, isothermal holding time of 10 Ma. The best fit E_a and ν_0 for the Al centre are 1.5 eV and 1.1×10^{11} s^{-1}. However, data from the Ti centre cannot be fitted well by a first order kinetic model as the increase of the Ti ages is not exponential (Figure 3.7b).

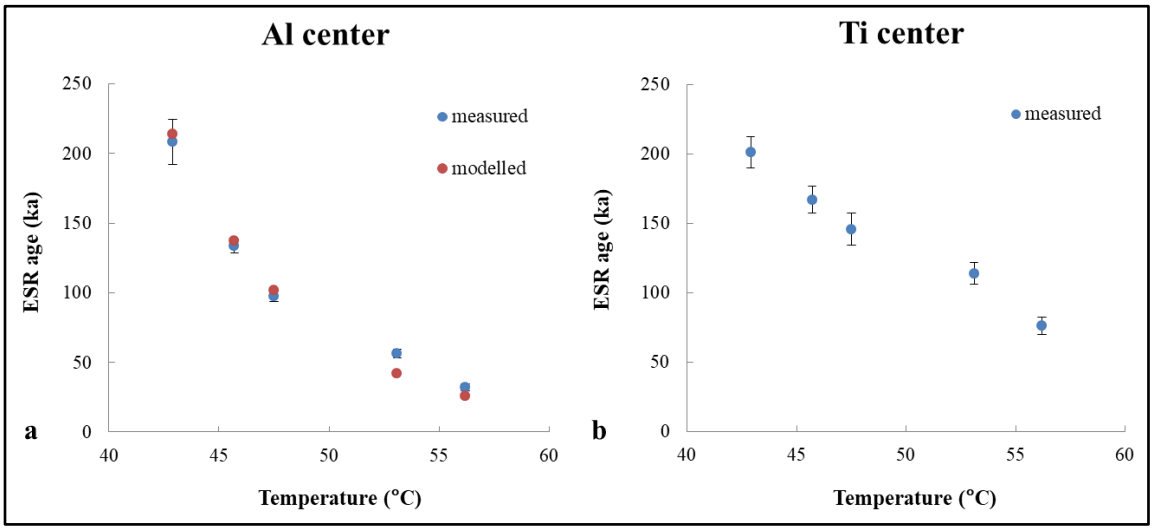

Figure 3.7: The measured ages of the Al centre compared to the modelled ages by optimal trap parameters for an isothermal holding time of 10 Ma. (b) The measured ages of the Ti centre.

3.6 Discussion

3.6.1 Comparison with trap parameters determined from the Eldzhurtinskiy Granite

The pioneering study of the Eldzhurtinskiy Granite boreholes has introduced ESR dating of quartz as a means of estimating thermal history (Grün et al., 1999). The trap

parameters of Al and Ti centres were calculated empirically based on first order kinetic assumptions and the estimated cooling rate. The results of E_a were 1.9 (Al) and 1.1 eV (Ti), and the corresponding ν_0 were 6×10^{16} (Al) and 5300 s^{-1} (Ti), respectively. But these trap parameters were unlikely to be correct. Here, we have recalculated the trap parameters (Figure 3.8) for the lower core from the Eldzhurtinskiy Granite by adopting the ingrowth-annealing equations (equation 3.4 and 3.5) which record the number of paramagnetic centres by radiation-induced charge trapping and thermally-controlled detrapping. The ESR ages and dose rates were obtained from Grün et al (1999), the initial temperature was set as 111 ºC since the ESR ages of Al and Ti centres were 0 ka under this temperature (Grün et al., 1999) and the values of D_0 from the FH1 borehole were used in the calculation as these data were not available in the original paper and the results were not sensitive to D_0 in the rapid cooling scenario. A cooling rate of 520 ºC/Ma was determined from the results of a heat transfer model and the ESR age and temperature differences with geothermal gradient. The optimised E_a and ν_0 values of the Al centre were 1.5 eV and 1.0×10^{11} s^{-1}, the Ti could be tentatively fitted with E_a of 1.6 eV and ν_0 of 2.4×10^{11} s^{-1}.

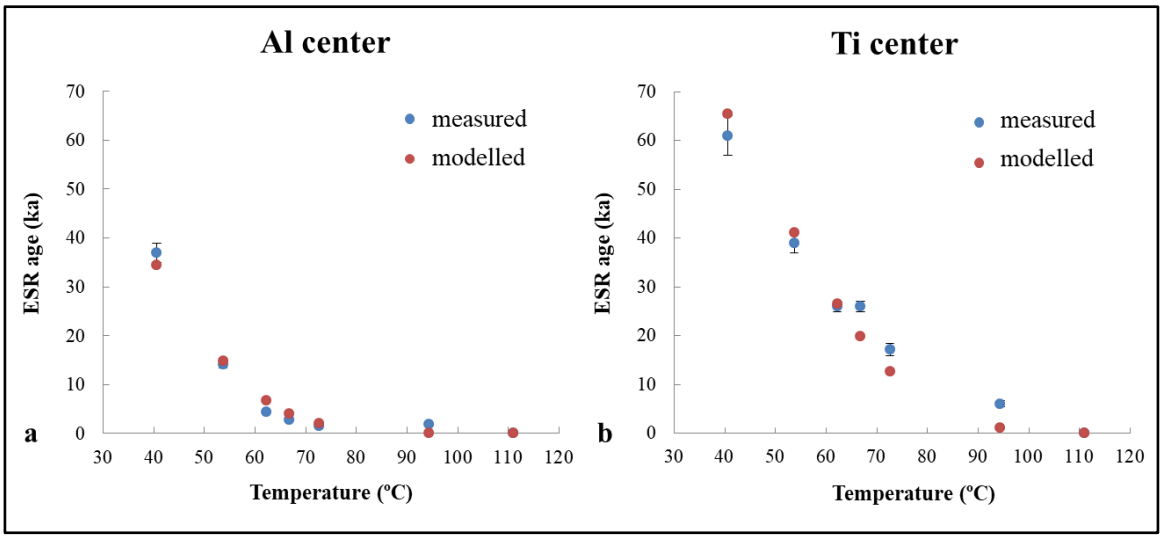

Figure 3.8: The calculated apparent ages of Al and Ti centres (Grün et al., 1999) compared with the modelled ages calculated by best-fit trap parameters for the lower core from the Eldzhurtinskiy Granite.

The trap parameters for the Al centre are consistent between quartz from non-marine

sediments (FH1 borehole) and granite (Eldzhurtinskiy). Of course, the results of two sample sets do not allow the conclusion that quartz samples from all different origins have identical trap parameters. Further studies are required on samples from a wider range of locations and origins. The ESR ages of the Ti centre from both cores cannot be well fitted, especially for the FH1 borehole. The Ti centre (peak-peak) used in the calculation is a mixture of Ti-Li and Ti-H^+, and their percentages control the shape of the signal accumulation with depth/temperature. This may be the reason why the application of first order kinetics was not able to provide reasonable results for all cases. Studies on a multi-exponential kinetics model will be carried out in the future.

3.6.2 Comparison of results from lab annealing experiments and natural settings

The applicability of trap parameters determined from laboratory annealing experiments to natural geologic settings is a critical issue for low temperature thermochronometry (House et al., 1999; Guralnik et al., 2015a; Brown et al., 2017). The extrapolation requires 7–8 orders of magnitude, which results in large uncertainties. The published trap parameters of Al and Ti centres by isothermal annealing experiments are listed in Table 3.2. The values of activation energy and frequency factor range from 1.3 to 2.4 eV and 10^7 to 10^{18} s^{-1}, respectively, for the Al centre and from 1.0 to 1.9 eV and 10^7 to 10^{17} s^{-1}, respectively, for the Ti centre. The trap parameters obtained from borehole analyses fall in the range of published data provided by laboratory annealing experiments. This supports that extrapolation of laboratory results to conditions relevant in nature, but the firm conclusion could only be made once isothermal annealing experiments have been carried out for borehole samples.

Kinetic studies of trap parameters by annealing experiments are particularly time consuming. The wide range of values obtained has generally been explained by the different origins of the quartz as well as the intrinsic nature and position of compensators (Marfunin, 2012). However, the assumed order of kinetics, the small number of data points used in calculations as well as signal interferences from mixing of more than one paramagnetic centre may also have influenced final results. For example, the kinetic order for annealing processes is generally assumed rather than experimentally obtained in ESR

dating, and neither first nor second order may actually represent the actual decay process. For example, Ti data could not be well fitted with first order kinetics in this study, neither could Toyoda and Ikeya (1994) do so using second order kinetics. Therefore, systematic isothermal annealing studies are required to understand the kinetic behaviour of the Ti centre. Whether the scatter in the results is due to the above mentioned extrapolation uncertainties, or to different physical properties of the quartz samples analysed cannot be determined conclusively. Recently, a multi-first order kinetic model has been developed (Lambert et al., in review) and applied to analyse ESR data where electrons can be trapped in a variety of different defects (Tsukamoto et al., 2018; King et al., in review). Moreover, it is necessary to establish the kinetic order of the dose accumulation process for the reconstruction of thermal histories. This work has not yet been carried out for ESR dating as was for in luminescence thermochronometry (Guralnik et al., 2015b).

Table 3.2: Experimentally determined trap parameters for Al and Ti centres.

Centre	E (eV)	ν_0 (s^{-1})	Kinetic order	Reference
Al	2.4	3.0×10^{12}	First	Imai et al. (1985)
Al	1.3	1.0×10^{9}	First	Melnikov et al. (1989)
Al	1.5	9.0×10^{12}	First	Ikeya and Toyoda (1991)
Al	1.7	1.1×10^{7}	Second	Toyoda and Ikeya (1991)
Al	1.4	3.2×10^{11}	Second	Toyoda and Ikeya (1994)
Al	1.4	3.6×10^{11}	Second	Toyoda and Ikeya (1994)
Al	1.8	5.0×10^{14}	Multiple first	Tsukamoto et al. (2018)
Al	1.3-1.9	6.6×10^{10}-1.9×10^{18}	Multiple first	King et al. (2019)
Ti	1.0	2.9×10^{7}	First	Fukuchi (1992)
Ti	1.7	4.1×10^{11}	Second	Toyoda and Ikeya (1991)
Ti	1.4	5.3×10^{11}	Second	Toyoda and Ikeya (1994)
Ti	1.5	4.2×10^{11}	Second	Toyoda and Ikeya (1994)
Ti	1.5	1.3×10^{12}	Multiple first	Tsukamoto et al. (2018)
Ti	1.4-1.9	5.2×10^{12}-7.6×10^{17}	Multiple first	King et al. (2019)

3.6.3 Comparison of closure temperature between ESR and other thermochronometry

The concept of closure temperature (T_c) was introduced by Dodson (1973). It was defined as the temperature of a system at the time corresponding to its apparent age, thereby providing a clear theoretical basis for understanding many mineral ages as cooling ages, a function of the interplay between the kinetics of diffusion (or annealing) and accumulation rates in cooling systems. For comparison, the closure temperatures of ESR, AHe, AFT and Na-feldspar OSL thermochronometers under a series of cooling rates (100, 200, 400, and 1000 ºC/Ma) are listed in Table 3.3. The T_c values of ESR Al and Ti centres in quartz were calculated based on: the estimated trap parameters in this study (i.e., activation energy and frequency factor of the Al centre were 1.5 eV and 1.1×10^{11} s^{-1} and these of Ti centre were 1.6 eV and 2.4×10^{11} s^{-1}, respectively), the initial temperature of 111 ºC and the surface temperature of 0 ºC. The T_c values of AHe, AFT and Na-feldspar OSL (i.e., infrared stimulated luminescence measured at 50 ºC – $IRSL_{50}$) were obtained from the study of Guralnik et al. (2015a).

Table 3.3: The estimated T_c for ESR thermochronometry of Al and Ti centres in quartz and the reported T_c for Na-feldspar OSL, AHe and AFT thermochronometry under the surface temperature of 0 ºC.

Method	Mineral	Cooling rate (ºC/Ma)			
		100	200	400	1000
ESR	quartz Al centre	48	52	56	62
ESR	quartz Ti centre	64	69	73	79
$IRSL_{50}$	Na-feldspar	/	54	62	75
(U-Th)/He	Apatite	78	84	89	96
FT	Apatite	133	139	145	155

Compared to AHe and AFT thermochronometry, the trapped charge thermochronometric techniques have lower closure temperatures corresponding to cooling rates which enable the exploration of the recent landscape evolution of the upper crust. Specifically, ESR

thermochronometry using the Al centre show the lowest closure temperature and the T_c values of Ti centre are higher than those of Na-feldspar $IRSL_{50}$ system. Due to the signal field saturation, OSL dating can only record the time range of about 1 and 200 ka (Guralnik et al., 2015a; King et al., 2016b). Thus, Na-feldspar $IRSL_{50}$ system is unable to estimate a cooling history < 190 ºC/Ma when the surface temperature is 0 ºC (Guralnik et al., 2015a). ESR thermochronometry has the dating range from 10 ka to 2 Ma (Rink et al., 2007), which can be applied to record the thermal history under a lower cooling condition (> 30 ºC/Ma) during the Quaternary.

3.7 Summary and conclusions

In this study, the first order kinetic model was applied to obtain the trap parameters of Al and Ti centres for quartz ESR thermochronometry. The best-fit parameters for the Al centre from Otway Basin and Eldzhurtinskiy Granite boreholes are consistent and fall within the range of published data obtained from laboratory annealing experiments. The trap parameters of Ti centre were tentatively obtained from Eldzhurtinskiy Granite borehole, and showed higher thermal stabilities than the Al centre which were in agreement with the apparent ESR ages of Al and Ti centres in this study. However, the data for the Ti centre in the two boreholes are not well fitted, especially for Otway basin samples, suggesting that a first order kinetic model is not universally applicable. This study presents an initial step towards a more elaborate physical formulation incorporating additional dosimetric variables and the effects from other kinetic orders. Further studies are required to investigate the realistic kinetic orders of trapping and annealing processes, and to make a systematic comparison between trap kinetics determined from samples with various origins and locations for ESR thermochronometry. Compared with other low temperature thermochronometric techniques, ESR thermochronometry of Al and Ti centres in quartz has lower closure temperature and the dating range of 20 ka to 2 Ma is suitable for constraining cooling history of the upper crust over the Quaternary.

4 2D modelling: A Monte Carlo approach for assessing heterogeneous beta dose rate in luminescence and ESR dating

This chapter is composed of three parts:

Section 4.1: The identification of mineral types and their distribution patterns is essential for creating a dose rate model. This section has compared 3D X-ray computed tomography, 2D XRF (X-ray fluorescence) scanning and 2D QEM-EDS (quantitative evaluation of minerals using energy dispersive spectroscopy) scanning in mineral identification for granitic rocks.

Section 4.2: Martin, L., Fang, F., Mercier, N., Incerti, S., Grün, R., Lefrais, Y., 2018. 2D modelling: A Monte Carlo approach for assessing heterogeneous beta dose rate in luminescence and ESR dating: Paper I, Theory and verification. Quaternary Geochronology, 48, 25-37.

The contribution of Fang F. to the publication is: FF has conducted the image segmentation on 3D X-ray CT data of the granite rock, measured the radioelement concentrations of target minerals in the rock sample by LA-ICP-MS, and corrected this paper and DosiVox-2D user manual.

Section 4.3: Fang, F., Martin, L., Williams, I., Brink, F., Mercier, N., Grün, R., 2018. 2D modelling: A Monte Carlo approach for assessing heterogeneous beta dose rate in luminescence and ESR dating: Paper II, Application to igneous rocks. Quaternary Geochronology, 48, 195-206.

The authors' contributions to the publication are: Fang F. has prepared all samples, conducted image analyses on QEM-EDS maps, analysed radioelement concentrations of target minerals in rock samples by LA-ICP-MS, run 60% simulations in this study and

written the manuscript. All co-authors have corrected and provided constructive comments on the manuscript. Except this, Martin, L. has run the other 40% simulations; Williams, I. has provided rock BB86 and related sample information; Brink, F. has run the QEM-EDS scanning for all samples and written the analytical method of QEM-EDS scan; Mercier, N. has provided lab access in Université Bordeaux Montaigne for comparing various 2D mapping facilities in mineral identification; Grün, R. has raised the initial ideal about beta dose rate modelling on heterogeneous rock and provided scientific and financial support through this study.

4.1 The comparison of scanning techniques in mineral identification

4.1.1 Introduction

In ESR thermochronometry, accurate estimation of beta dose rate is challenging for heterogeneous rocks. Numerical simulation provides a possible solution for solving this issue, and the recently developed software DosiVox allowing a matrix creation from directly uploaded 3D images which can enhance the representativeness of geometric construction (Martin et al., 2015). Thus, the identification of mineral types and their distribution patterns has become essential for creating a dose rate model.

The X-ray micro-computed tomography (μCT) has been used to visualise and analyse geological samples in three dimensions (3D). μCT imaging uses the differences in X-ray attenuation arising from different minerals within the specimen. The X-ray linear attenuation coefficient depends on the atomic composition and density of a mineral phase, and the X-ray energy applied in scanning. But some mineral phases (e.g., quartz and albite) are challenging to be identified due to their similar attenuation coefficients (Boone et al., 2011). The dual-energy scan may be an effective solution, which includes scanning the same location within the rock twice using a different X-ray energy each time. The higher energy image (> 100 kV) is proportional to bulk density, while the lower energy image (< 100 kV) is proportional to the atomic number (Siddiqui and Khame 2004). To acquire mineral distributions on rock surfaces, 2D image processing techniques (e.g., XRF - X-ray fluorescence, SEM – scanning electron microscope and QEM-EDS – quantitative evaluation of minerals using energy dispersive spectroscopy) are widely used and specific equipment is selected depending on the sample size and the chosen magnification. From the perspective of the beta dose rate calculation, the optimal mapping resolution depends on the minimum grain size of the target mineral, usually in the range of 10-100 μm. The map size is based on the beta particle range and the representativeness of a chosen area. The minimum size of an ideal representative sample is 10×10 mm (Martin et al., 2018). Considering the requirements of beta dose rate simulation, 3D dual-energy CT scanning was first applied in building realistic rock geometry, and meanwhile XRF and QEM-EDS are compared in mineral identification of

rock surface.

4.1.2 Sample description and preparation

Three samples were collected from the Kullu valley, Northwestern Indian Himalaya (Figure 4.1). HIM82 is migmatite with visible leucosome (light-coloured band of melted minerals) and melanosome (dark-coloured band of a partially melted framework consisting of residual minerals). A rock cube (23×23×20 mm) was cut from melanosome part for 3D CT scanning, and a slice (23×23 mm) was prepared from the middle of the cube for 2D QEM-EDS. HIM59 and HIM31 were selected to represent rocks with complex and simple minor mineral combinations, respectively. HIM-59 is coarse-grain migmatite, and a slice (24×25 mm) was selected and cut from its leucosome. HIM-31 is fine-layered migmatite, and a slice (20×20 mm) was prepared vertical to lineation and foliation.

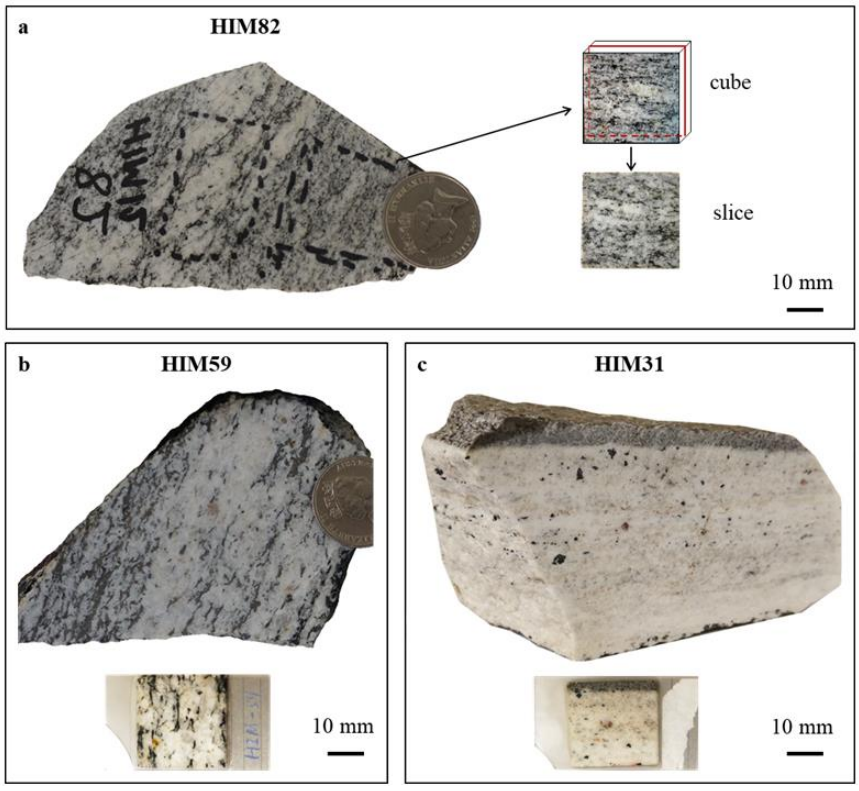

Figure 4.1: Samples and corresponding slices for analysis. (a) A 20 mm cube was cut from HIM82 for 3D CT scanning, and a slice from the middle section of the cube for QEM-EDS mapping. (b) A slice of HIM59 was selected from the leucosome section of the specimen. (c) A slice was cut from HIM31 vertical to lineation and foliation.

4.1.3 Methodology

4.1.3.1 3D CT scanning

In HIM82, plagioclase is composed of $NaAlSi_3O_8$ and $CaAl_2Si_2O_8$, and their molar ratios are 70:30 to 74:26 between grains. As roughly calculated, the linear attenuation factors of quartz and plagioclase were 0.513 and 0.526 cm^{-1} at the voltage of 80 kV. The detecting limit of the equipment can reach to 0.001 cm^{-1}, and thus these minerals are theoretically separable. The dual-energy CT scanning was performed at Research School of Physics and Engineering, ANU. The experiment parameters were: voltages of 120 kV and 80 kV, target current of 105 μA, and resolution of 22 μm. The image segmentation was carried out in software Qmango. The bilateral iteration and anisotropic diffusion filters were applied to reduce the noise, and level intensity filter was used in X and Y directions for balancing the intensity from inside to the edge of the sample. Mineral phases were segmented by different gradient thresholds, and the results were compared with a registered 2D mineral map of a rock slice cut from the middle part of the specimen and scanned by QEM-EDS.

4.1.3.2 2D XRF mapping

XRF mapping characterises element distributions by measuring the intensities of fluorescent radiation emitted from excited electrons in particular elements. The analyses were carried out on samples HIM31 and HIM59 using a SEIKO SEA 6000VX XRF system at Bordeaux Montaigne University. The element data were collected with voltages of 15 kV and 50 kV, a beam current of 1 mA, and a resolution of 40 μm. The mapping of a 20×20 mm area takes 432 min, while it takes less than 60 min for QEM-EDS analysis. The XRF images were acquired for Si, Ca, Fe, Mn, K, Rb, Ti, Zr, Nb, Y and Ce. The detection limit of element content ranges from 100 to 1000 ppm. The mineral phases were manually distinguished in ImageJ software based on the combination of characteristic cations (e.g., biotite can be distinguished by using Fe and K maps) and the level of X-ray counts (e.g., apatite is distinguished using a Ca map). Each pixel is assumed to contain only one type of mineral. The pores and undefined minerals account

for 1.9% in HIM59. In HIM31, plagioclase cannot be identified from any elemental map, and thus we attributed the residual area after identification of all other minerals to plagioclase.

4.1.3.3 2D QEM-EDS mapping

The 2D QEM-EDS analyses were performed using the FEI Quanta QEMSCAN® system at the Centre for Advanced Microscopy (CAM) at the ANU. Data were collected in field image scan mode, 15 kV accelerating voltage, 10 nA probe current step sizes of 15 μm. Since scan deflection is limited to a field size of 1.5 mm or less during mapping, each finished QEM-EDS map typically consists of multiple acquisitions and stage translation. FEI iMeasure and iDiscover were used for the acquisition of X-ray spectral map data and subsequent field stitching. FEI Nanomin software was used for final mineral identification and the derivation of modal fractions. Nanomin examines the spectrum acquired at each pixel and compares it to a library of known mineral reference spectra held within the Mineral Reference Editor (MRE). Mineral classification is assigned to a pixel only if a spectral match better than a pre-set value (i.e., 85%) has been achieved. Minerals belonging to a wide compositional range species can be successfully classified by solid solution series for the best fit using a suitable combination of end-member mineral reference spectra. For example, plagioclase can be defined by a combination of albite and anorthite. Failure in classification of some areas or pixels can either be due to a mineral being absent from the MRE or due to pixels being located on the boundary between two different mineral grains where a mixed spectrum is obtained. In this study, one mineral per pixel is defined for classification, and the undefined minerals were controlled to be less than 1% of the total abundance.

4.1.4 Results and discussion

4.1.4.1 Mineral identification of 3D CT images

For beta dose rate modelling, the first attempt is to solve the 3D problem in a 3D way, i.e., build the rock geometry based on direct X-ray CT scan (Figure 4.2a). Sample HIM82 is mainly composed of four minerals: quartz, plagioclase, K-feldspar and biotite, as shown

in the mineral map produced by QEM-EDS scanning (Figure 4.2b). In the higher energy CT map, the slice which has the same mineral distribution pattern as the QEM-EDS map was obtained by image registration. For mineral identification (Figure 4.2c), K-feldspar and biotite were easily separated from other mineral phases, while quartz and plagioclase were unable to be separated as expected due to their similarity in linear attenuation coefficients.

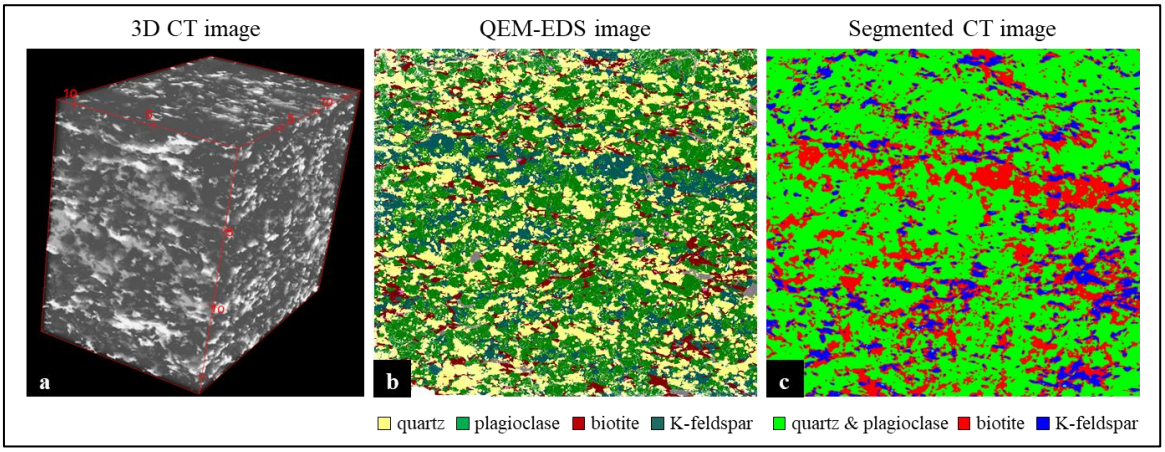

Figure 4.2: (a) The 3D CT image of the sample cube. (b) The QEM-EDS image of a slice cut from the middle part of the cube, which showed four main mineral phases. (c) The segmented CT image of the slice obtained from image registration. Biotite and K-feldspar phases were identified but quartz and plagioclase were unable to be separated.

In the lower energy CT image, the contrast of quartz and plagioclase was slightly increased. To avoid the beam hardening effect, the image size was reduced by cropping the outer part. The segmentation result indicated that quartz and plagioclase were still not fully separated (Figure 4.3). A possible reason might be the insufficient penetrating power of lower energy, which could lead to the weak signals and noisy data. Higher quality data can be provided by reducing the sample size, and the ideal size is a core with a diameter less than 10 mm. However, the range of beta particle is 2 mm and then comparing to the whole rock, the representativeness of such a sample would be doubtful.

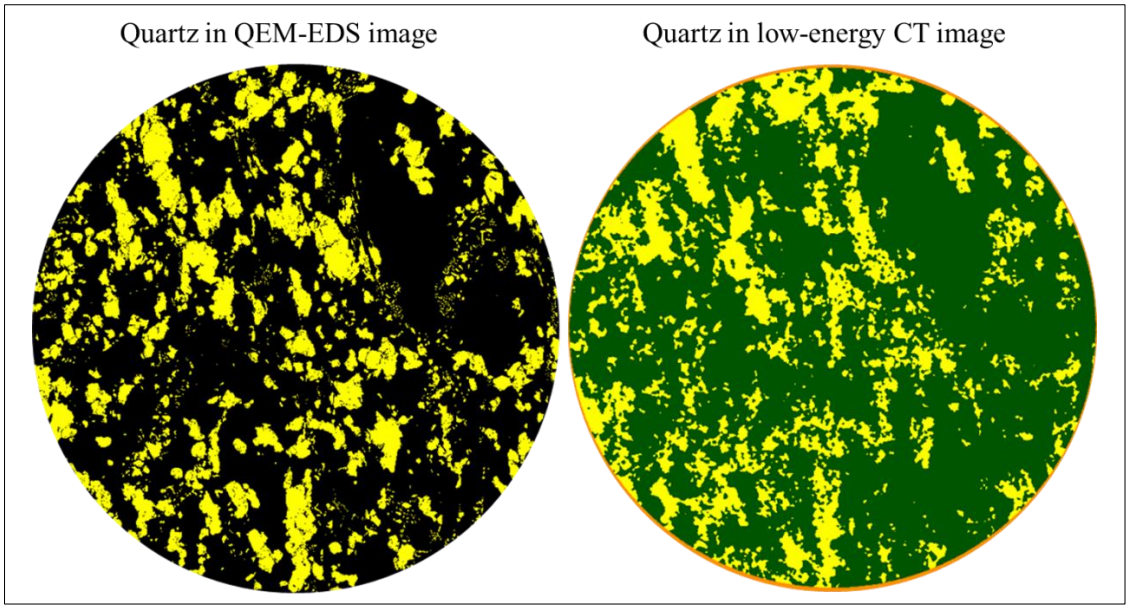

Figure 4.3: The quartz phase in QEM-EDS image and segmented low-energy CT image.

In the current stage, it is still challenging in completely separating quartz and plagioclase from dual-energy CT images, which has hindered the application of this technique in accurate beta dose rate modelling. But if a rock has no/negligible plagioclase, 3D simulation is still the best way for dose rates evaluation.

4.1.4.2 The comparison of XRF and QEM-EDS mapping

2D mapping facilities have advantages in providing reliable mineral maps. In this part, XRF and QEM-EDS mapping results were compared.

For XRF scanning, mineral identification requires setting thresholds of X-ray counts on target minerals but it could be highly subjective. The minor minerals in HIM31 were relatively simple and could be easily segmented with a combination of characteristic cations. However, accurate identification of quartz and plagioclase was difficult. The plagioclase in this sample is mainly oligoclase (as identified by QEM-EDS, Figure 4.4a), but this phase could not be separated from the XRF element maps. The separation of quartz from Si map became important. The assignment to quartz depended on the setting of a threshold of Si counts. When the Si map was noisy (Figure 4.4b), different threshold settings resulted in vastly different distributions (Figure 4.4c, d). The QEM-EDS image showed that the quartz abundance of 33.4% while the setting in Figure 4.4c (31.6%) was

close to this value but largely underestimated in Figure 4.4d (25.6%). Even though semi-automatic analysis software was developed for XRF mineral identification, the analysis is time-consuming and limited to simple cases with a small number of minerals. The results may depend on the choices for initialising the analysis (i.e., threshold parameters and the algorithms applied for segmentation)(Prêt et al., 2010).

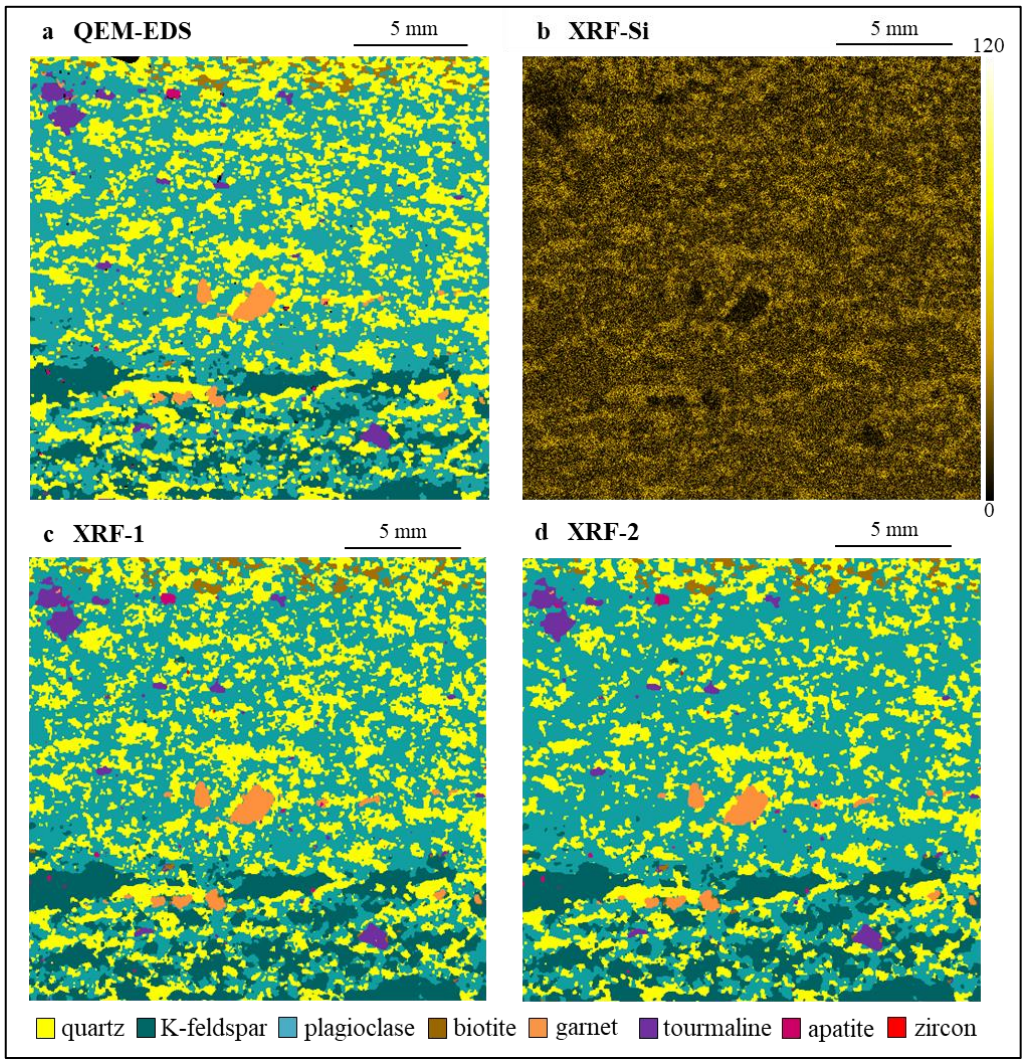

Figure 4.4: (a) Mineral mapping of HIM31 by QEM-EDS. (b) XRF image of Si with colour scale indicating X-ray count. (c) XRF map of quartz abundance close to that in QEM-EDS image. (d) XRF map with low quartz abundance.

In identifying minor minerals, QEM-EDS was found more efficient. On one hand, XRF mapping requires all minerals present in the sample to be known prior to analysis. Otherwise, they may not be recognised from XRF elemental images due to a lack of

characteristic elements or the chemical composition of various minerals. However, the QEM-EDS data analysis software can provide the best-fit minerals by direct comparison to reference mineral X-ray spectra, which is helpful in the identification of unknown minerals. Even though the initial best-fit results may not always be correct, an inspection of the full spectrum can provide clues to a possible mineral type. This can be crucial when the researcher only has limited prior knowledge of the sample. For example, the Fe-rich minerals in HIM59 were identified as hematite, pyrrhotite and fayalite by QEM-EDS mapping (Figure 4.5c), whilst they were all (incorrectly) classified as hematite by XRF because prior knowledge of this sample included hematite, but not the other iron-rich minerals. Additionally, a range of characteristic elements (e.g. S required for the identification of pyrrhotite) were not measured (Figure 4.5d). On the other hand, QEM-EDS reflects a realistic mineral abundance of the mapping surface. The probing depths of QEM-EDS and XRF are 2-3 μm and 100-150 μm, respectively. In XRF the mineral distributions obtained may depend on probing depth and erroneous due to averaging the element signal received from different mineral grains. For instance, the abundance of zircon only accounted for 0.004% in the QEM-EDS map, while it reached to 0.156% in the XRF image.

In separating minerals of a solid solution series (e.g. plagioclase, garnet, chlorite), QEM-EDS has advantage on searching for the best fit using a suitable combination of end-member mineral reference spectra. This function is helpful in defining the reference element concentration for estimating the radioelement concentrations by LA-ICP-MS analysis. For example, plagioclase can have various compositions between the end-members albite and anorthite, resulting in the Si content varying from 20.75% to 31.50%. If the separation of the various plagioclase minerals is not possible, this may result in significant uncertainties in the estimation of radioelement concentrations and consequently influence the beta dose simulation results.

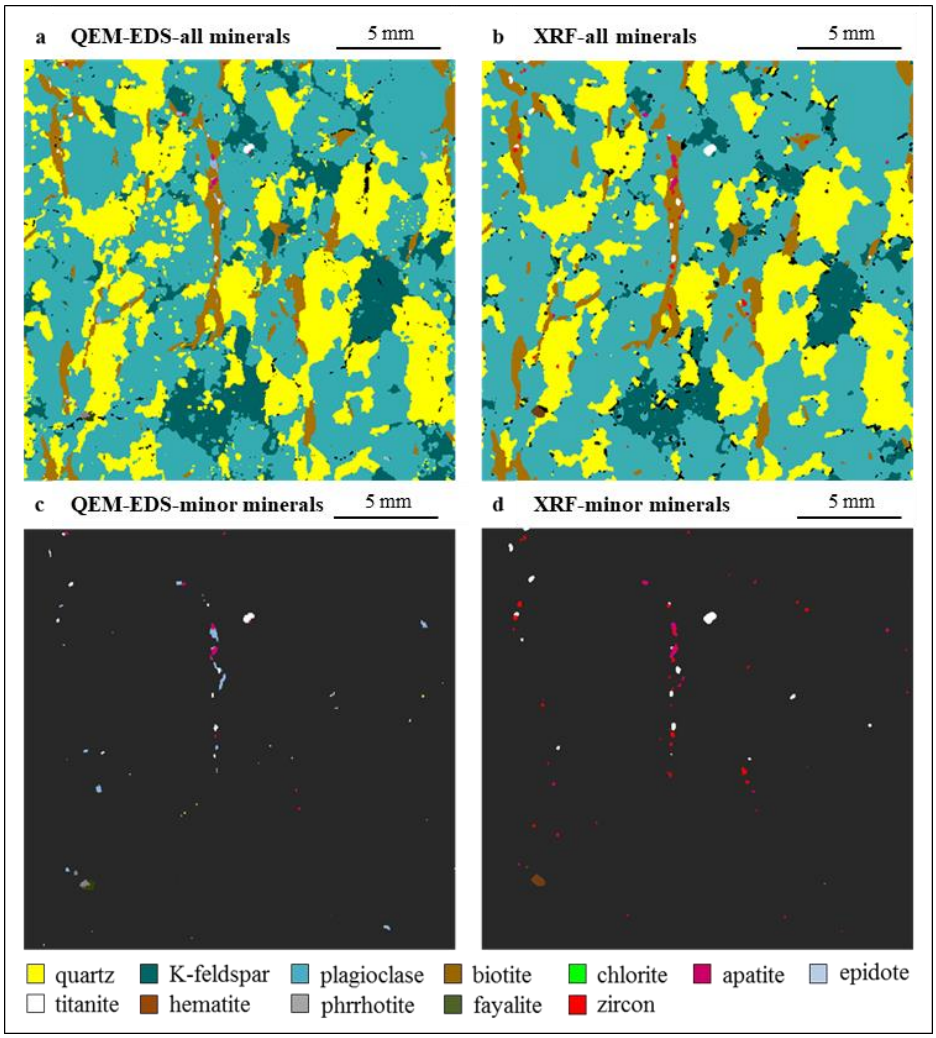

Figure 4.5: (a) QEM-EDS image of HIM59. (b) XRF image of HIM59. The distribution and abundance of major minerals are consistent in QEM-EDS and XRF images. The slight differences between grain boundaries result from the filtering of noisy XRF maps and de-resolution of QEM-EDS image. (c) Minor minerals identified by QEM-EDS. (d) Minor minerals classified by XRF. The epidote and different type of Fe-rich minerals cannot be classified and the abundance of zircon is much higher than that in the QEM-EDS image.

4.1.5 Summary

In ESR thermochronometry, accurate beta dose rate simulation relies on the uploaded geometry containing rock structures and mineral compositions. 2D mapping facilities are more efficient in mineral identification, since quartz and plagioclase cannot be fully separated by 3D dual-energy CT scanning. Thus, a 2D model is necessary to be

developed for an easier and faster assessment of the beta dose rate of heterogeneous rocks if they have even texture or mineral distributions have preferred orientation. In 2D mapping, QEM-EDS is recommended for more rapid map production and more efficient mineral identification. If this facility is not available, XRF can be an alternative option for samples with relatively simple mineral compositions. But one should carefully choose the elements for mapping and the thresholds for separation, to ensure the correct identification of target minerals.

Quaternary Geochronology 48 (2018) 25–37

Contents lists available at ScienceDirect

Quaternary Geochronology

journal homepage: www.elsevier.com/locate/quageo

Research paper

2D modelling: A Monte Carlo approach for assessing heterogeneous beta dose rate in luminescence and ESR dating: Paper I, theory and verification

Loïc Martin[a,*], Fang Fang[b], Norbert Mercier[a], Sébastien Incerti[c,d], Rainer Grün[b,e], Yannick Lefrais[a]

[a] Institut de Recherche sur les Archéomatériaux, UMR 5060 CNRS – Université Bordeaux Montaigne, Centre de Recherche en Physique Appliquée à l'Archéologie (CRP2A), Maison de l'archéologie, 33607, PESSAC Cedex, France
[b] Research School of Earth Sciences, The Australian National University, Canberra, ACT 2601, Australia
[c] CNRS, IN2P3, CENBG, UMR 5797, 33170, Gradignan, France
[d] Université Bordeaux, CENBG, UMR 5797, 33170, Gradignan, France
[e] Australian Research Centre for Human Evolution, Griffith University, Nathan, QLD 4111, Australia

ARTICLE INFO

Keywords:
Beta dose rate
Modelling
Dating
Luminescence
ESR

ABSTRACT

Many samples used for luminescence and ESR dating show complex mineralogical structures, resulting in heterogeneous beta dose rates. Ideally, the beta dose rate distribution could be reconstructed using softwares like DosiVox, which can both upload 3D-scans recorded with X-ray tomography and distributions of radioactive elements. However, some minerals often exhibit only small X-ray contrasts making them difficult to distinguish in 3D-scans. For example, quartz and plagioclase have closely similar X-ray characteristics, which limit the applicability of this approach. Here, we introduced a Monte Carlo simulation of beta particles in two dimensions, in order to calculate the dose rate from 2D images. The simulation results are compared between 2D modelling, 3D modelling and standard calculation. The implications for beta dose rate heterogeneity in grains are discussed. Using the "DosiVox-2D" software, we show that 2D scans may characterize complex heterogeneous 3D beta dose rate distributions. This approach could lead to a better understanding of micro-dosimetric phenomena and the improvements in the accuracy of dose rate calculation for heterogeneous samples.

1. Introduction

In ESR and luminescence dating, it is essential to determine the dose rate for age calculation. Even if samples are often heterogeneous at different scales, in respect of mineralogical structure and/or distribution of radioactive elements in the sample and its surroundings (Nathan et al., 2003; Guérin et al., 2012a; Urbanova et al., 2015), it is usual to determine the U, Th, K contents (by beta counting, gamma spectrometry or ICPMS measurements), apply the infinite matrix assumption and consider attenuation factors based on the individual grain size and the bulk moisture content (Fleming, 1973; Zimmerman, 1971; Mejdahl, 1979) as well as, eventually, disequilibrium in the natural radioactive decay series (Krbetschek et al., 1994). However, the beta dose rate received by the mineral phase containing the dated grains (e.g., quartz or feldspar phases in rocks, clay in sediment or pottery, and etc.) can be significantly different from that of the bulk beta dose rate, depending on the sizes and proportions of the different mineral phases, and the contrasts in the radioactive element contents (Nathan et al., 2003). Determining the specific beta dose rate in the phase used for the equivalent dose determination is then of paramount importance in heterogeneous samples, but remains delicate due to the complexity and variety of the structures observable in these samples.

One option to tackle this problem is directly map the dose distribution (Rufer and Preusser, 2009; Guérin et al., 2012b) but since beta particles have a range of a few millimeters, this approach is rather difficult. An alternative is to develop numerical simulations (Nathan et al., 2003; Mayya et al., 2006; Guérin, 2011; Cunningham et al., 2012; Martin, 2015; Martin et al., 2015a) and this approach has already shown promising results for investigating beta microdosimetry. Some of them show that, in heterogeneous samples, in particular when the presence of high radioactivity contrasts between different minerals and/or coarse materials (millimeter or centimeter size) is attested, the standard method may lead to biased estimations that can sometimes be more than twice the simulated beta dose rate (Nathan et al., 2003). However, it has to be noted that only few of these studies have received an experimental validation that would be necessary for confirming the

* Corresponding author.
E-mail address: loic.martin@u-bordeaux-montaigne.fr (L. Martin).

https://doi.org/10.1016/j.quageo.2018.07.004
Received 26 September 2017; Received in revised form 3 June 2018; Accepted 18 July 2018
Available online 21 July 2018
1871-1014/

order of magnitude of the observed differences. In addition, a numerical approach usually requires the creation of 3D models, what remains a complex task, as well as the necessary characterisation of the structure and composition of the sample, used for the creation of the numerical model itself.

The recent development of the DosiVox software, which includes the Geant4 database for particles-to-matter interactions and allows users to compute dose rate simulations without programming skills, makes this approach more accessible. Although this tool has simplified the modelling process, the major issues are still remaining on acquiring data of sample's structure, mineral's chemical composition and its radioactivity. Even when it is possible to extrapolate the three dimensional structure from a slice analysis (for instance obtained using LA-ICP-MS or X-ray fluorescence mapping) (Martin et al., 2015b), a 3D approach is still time consuming as it requires several days or weeks of calculation on standard computers (without considering the time for the analysis and processing). Another possibility is to model a sediment or a rock sample by packing randomly spherical grains distributed in a compact structure (Nathan et al., 2003; Guérin et al., 2012a). This approach is limited by the efficiency of the algorithm (Donev et al., 2005) and the representativeness of the geometric construction. The shape of the grain may also have an impact on the calculated beta dose rate, depending on their size compared to beta particle range since a significant effect can be observed for grains close or larger than the beta average range in sediment (i.e. few millimeters) (Fain et al., 1999; Nathan, 2010). If dating are usually performed on smaller grains – few hundred of micrometers for the quartz inclusion technique (Fleming, 1973) or less than 20 μm for the fine grain method (Zimmerman, 1971) – the shape of larger fractions that can be present in the sample (for instance, calcite or granite grains or small stones) is likely to have a significant effect on the beta dose rate, especially if the contrast between the coarse material and the mineral phases containing the dated grains is strong (Nathan et al., 2003). In addition, random grain distributions cannot represent agglomerated grains or layered samples with different granulometric distributions.

X-ray computed tomography (CT) may be an alternative since it allows the visualization and quantification of the internal structure of objects (Aso et al., 2007; Mena et al., 2015). However, CT equipments are not easy accessible and sample scanning is expensive. More importantly, it cannot be used for samples rich in quartz and plagioclases since these two minerals are almost impossible to be distinguished in CT images (Boone et al., 2011).

Plachy and Sutton (1982) used a dose point kernel method to integrate the beta dose rate contributions to quartz from the main mineral phases present in a granite. They used cathodoluminescence photography to create 2D maps of the different phases while abrasing the sample slice after slice. They showed in particular that one can obtain the equivalent beta dose rate in applying their calculation method in two dimensions (to the individual images) or three dimensions (to the 3D images reconstituted by assembling the 2D images). This observation can probably be related to the isotropy of the mineral distribution in the sample, as stereology can predict the conservation of size ratios (volume fractions, surface fractions and intercepted length fractions of the different phases) and the mean intercept length between two and three dimensions for an isotropic texture (Underwood, 1970; Degallaix and Ilschner, 2007). As beta dose rate distribution is related to the size ratio and distance (it is in fact the basic of the dose point kernel method) between different mineral phases, the conservation of the beta dose rate between two and three dimension can be seen as a consequence of the isotropy of the sample, according to stereology.

Calculating or modelling the beta dose rate in 2D, as Plachy and Sutton (1982) did, has a strong potential for dating heterogeneous samples, as it is easier to obtain data about composition, radioactivity and spatial distribution of the different mineral phases from two dimensional analysis than three dimensional analysis, or mineral separation. In order to take advantage of this method and provide a user-friendly tool for the dosimetric dating community, the DosiVox-2D software has been developed (Martin, 2015, chapter 11). Contrary to DosiVox, DosiVox-2D allows 2D-modelling but is only applicable to heterogeneous sediments and rock samples whose minerals are randomly distributed in space (isotropic), i.e. the probability of encountering a particular mineral phase is equal in all the three directions. However, this property has only to apply at the beta particle range (around 2 mm) and at the sampling size required for the dating (usually from a millimeter to a centimeter). Sample slices are used to obtain mineral compositions, distributions and radioactive element concentrations for subsequent simulations.

In this paper, we first explain the concept of 2D modelling, introduce the DosiVox-2D software, and then examine this new modelling approach with virtual and natural examples. The results are compared to those obtained with voxelised 3D models run with DosiVox (Martin et al., 2015a), grains packing models (Nathan et al., 2003; Guérin et al., 2012a), and the standard approach based on the infinite matrix dose rate concept (Fleming, 1973; Zimmerman, 1971; Aitken, 1985). The shape of the beta dose rate distributions obtained with the 3D and 2D modellings are also compared. The application of tabulated attenuation factors for calculating the beta dose rate to the modelled mineral phases is also discussed. At this stage of demonstration of the concept and its potential, we made the approximation that all samples considered here are isotropic. The effect of anisotropy on the modelling results will only be slightly discussed in this paper, and more developed in Fang et al. (2018).

2. Principles and theory of 2D modelling

Like previously explain, the principle of 2D-modelling relies on the conservation of several properties between 2D and 3D in isotropic samples. In particular, the surface fractions of the different phases on a representative 2D image are equal to the volume fractions (in the 3D), which ensure that the mineral proportions are respected. The mean intercept length, which can be defined as the average chord length of a particular phase measured in random directions, is also conserved in 2D if the sample is isotropic (Underwood, 1970; Degallaix and Ilschner, 2007). One can assume that this properties lead to the accurate calculation in 2D of beta dose rate, done by Plachy and Sutton (1982), as the dose point kernel method is like an integration of dose deposit along chords in all directions of the image plan: this can be seen as an integration of the dose deposit function during the calculation of the mean intercept length, which is the same in 2D than in 3D. The calculation of dose rate in 2D by DosiVox-2D is a little bit different, as the beta dose is not integrated along chords but all the individual beta particles trajectories and interactions are simulated in a 2D representation of the sample, with the Monte Carlo method. However, the equivalence between 2D and 3D calculations relies on the same principle, as the trajectories of beta particles can be seen as successions of chords in random directions, with the same probability of crossing and interaction with the different mineral phases in 2D as that in 3D (Fig. 1).

These modellings rely on the hypothesis that two dimensional images are representative of the three dimensional sample. This can be assumed if the sample is isotropic (which can be confirmed by image analysis of the sample in different perpendicular directions, or sometimes assumed from the nature of the sample, like well mixed sediment) and if the surface used for the calculation is large enough to be representative of the sample heterogeneity (including the mineral and radioactivity distributions) and the beta particle emissions. In practice, it may be complicated to determine the size for correctly representing a sample heterogeneity, but tools as variogram and covariogram can be useful for this purpose (Degallaix and Ilschner, 2007). However, we can reasonably assume that the minimum surface necessary for 2D modelling is at least one square centimeter, as the average range of beta particles in sediments is a few millimeters. Obviously, the larger the

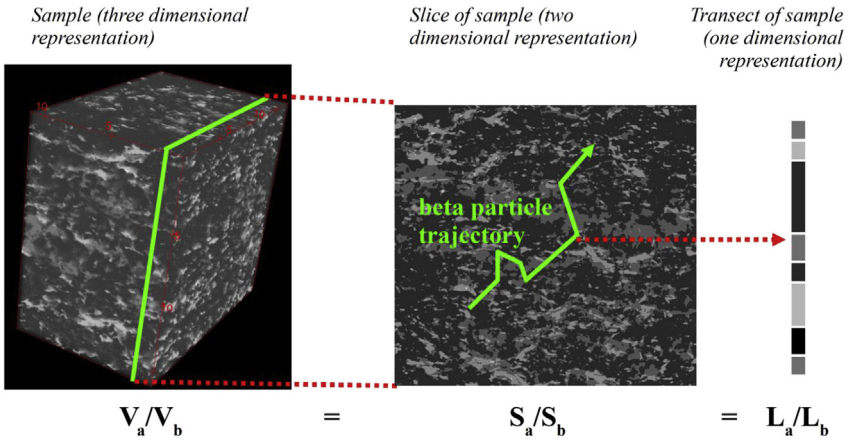

Fig. 1. Illustration of volume, surface and linear fractions in an isotropic heterogeneous sample.

surface used, the more representative the modelling will be, but the size can be limited by the analytical technique (for instance, U and Th usually require ICPMS or SIMS measurements). The representativeness of the analysed surface is indeed the predominant source of uncertainty of the method (Plachy and Sutton, 1982).

The main advantage of 2D modelling is the simplification and the efficiency of the analysis. Instead of processing the successive images required for 3D modelling, only one slice is needed in 2D modelling. Moreover, 2D mapping equipment is usually easy to access (e.g., SEM-EDX, micro-XRF, QEMSCAN) and users can choose a facility that best suits their needs. For example, if correctly calibrated, a SEM allows assessing a quantitative distribution for potassium, which is often the major contributor to the beta dose rate and whose distribution is consequently important for modelling. In addition, the different mineral phases are easier to separate in 2D mapping methods because the analysis does not only rely on the variations of X-ray absorption (like computed tomography), but also on the variations of the chemical composition inside the sample (the EDX, QEMSCAN and XRF methods being relative to the elemental composition). Plachy and Sutton (1982) used cathodoluminescence photography in order to map the major mineral phases of their granite sample, after checking with a microprobe analysis proven that different minerals were correctly identified. However, it seems difficult to apply it for mapping small inclusions or grains even if they may contain the most part of uranium and thorium and therefore have a significant weight on the beta dose rate.

3. Software description

DosiVox-2D is a Geant4 based software for creating fast dosimetric models. It simulates particles-to-matter interactions by a Monte-Carlo approach (Agostinelli et al., 2003; Allison et al., 2006, 2016), calculating the paths and interactions of each primary particle and secondary particles, step by step, according to interaction probabilities in the material. This process displays the particle's behavior in the matter, and has already shown its usefulness for dose rate calculation in dosimetric dating (Morthekai et al., 2007; Guérin et al., 2012a; Martin et al., 2015c).

As a user-friendly software, DosiVox-2D requires no programming skills and can run on a standard computer. The construction of the model is achieved through an annotated text file or a graphical interface running under Java. The user defines a 2D-grid and sets for each voxel the materials (corresponding to the different mineral phases identified in the sample), their chemical composition, density, water content, and radioactivity. Specifically, a 2D-grid can be created manually into the interface, or directly by uploading a 2D image with segmented mineral phases coded in 8-bits grey scale. The image analysis and processing can be achieved by ImageJ (Abràmoff et al., 2004; Rasband., 1997–2012; Schneider et al., 2012). In DosiVox-2D, the beta particles can be emitted with the energy spectrum of the ^{40}K, the U- and Th-series (available and editable in the data folder of the software), or according to a user-defined spectrum. Each radioactive element or series is simulated independently from the other, in order to distinguish the different contributions to the total beta dose rate. The quantity of particle emissions in each voxel is derived from the contents of radioactive elements set in the different materials, according to those measured by analytical techniques (e.g. ICP-MS). After the information is provided and linked, a pilot file is created in a text format for launching the simulation. Detailed information about creating a pilot file and data processing can be found in the DosiVox-2D user manual (http://www.iramat-crp2a.cnrs.fr/spip/spip.php?article144).

As a 2D environment differs from a 3D one, different processes characterising particles emission in 2D as well as their behavior were investigated in order to assure consistency with the requirements of 2D calculation of beta dose rate. First of all, a particle reflection process at the edges of the modelled environment was set, in the modelling plane direction (X and Y) and in the perpendicular direction Z. This ensures that no particle leaves the 2D environment in the Z direction, which would be contradictory with the principle of a 2D calculation; the reflection in X and Y allows to obtain a macroscopic infinite medium (the particles leaving the modelled environment equal the particles entering it), which is necessary to ensure the continuity of beta flux and low energy photon flux near the edges of the 2D environment. A similar process were used by Guérin and Mercier (2012) for gamma particle simulations. For beta particles emission and path, three methods were considered:

(1) The emission of beta particles is random in the three directions: this is the simplest method of emission. However, with the particle reflection in the Z direction, the model behaves as a 3D modelling but with an infinite height in the Z direction, which is not compatible with the 2D calculation principles. The beta dose rates calculated using this emission process were significantly different from those obtained with standard 3D modellings.
(2) The random emission of beta particles in the two directions of the modelling plan, with no possibility for primary or secondary particles to move in the Z direction, even after an interaction: this is a complete 2D behavior, for which the Z dimension no longer exists. The conservation of particles impulsion is assured by a redistribution of the intensity of the impulsion component in the Z direction (noted p_z) to the impulsion components in the X and Y axis (respectively p_x and p_y). However, with this redistribution, the beta particles travel significantly further in the sample geometry than they will do in 3D. As a consequence, the distribution of dose deposit in the sample is not respected, leading to significant

Table 1
Composition of the modelled environments.

Environment	Material[a]	Grain size (mm)	Percentage (%)	Radioactive element content
A	Clay matrix	–	70.00	5 ppm of U
	Quartz	0.5	30.00	0 ppm of U
B	Clay matrix	–	65.00	5 ppm of Th
	Carbonate	3.0	26.25	0 ppm of Th
	Quartz	0.5	8.75	1 ppm of Th
C	Clay matrix	–	70.00	1% of K_2O
	Quartz	0.5	27.00	0% of K_2O
	K-feldspar	0.5	3.00	14% of K_2O
D	Clay matrix	–	65.00	0.75% of K_2O
	Carbonate	1.5	25.00	0% of K_2O
	Quartz	1.0	8.00	0.14% of K_2O
	K-feldspar	0.2	2.00	14% of K_2O

[a] Mineral description: Clay matrix: SiO_2 54%, Al_2O_3 46%, density 1.8 g.cm^{-3}, moisture 10% in mass. Quartz: SiO_2 100%, density 2.65 g.cm^{-3}, moisture 0% in mass. K-feldspar (potassium feldspar): $KAlSi_3O_8$ 100%, density 2.6 g.cm^{-3}, moisture 0% in mass. Carbonate: $CaCO_3$ 70%, $MgCO_3$ 30%, density 2.7 g.cm^{-3}, moisture 0% in mass.

differences of the beta dose rates compared to 3D modellings.

(3) The random emission of beta particles in the two directions of the modelling plane, but with possible movements in the Z direction: this process of emission and particles path calculation is respectful of the distribution of dose deposit in the sample, which is thereby conserved between 2D and 3D modellings as there is no modification of the particle impulsion calculation. It is also compatible with the principle of a 2D calculation as only beta particles emitted in the XY plan are considered, and only the p_x and p_y components of impulsion allow particles (beta or low energy photon) to move from a voxel to another in the geometry (the p_z component is neutral, like in a projection of the particle trajectory on the XY plane). This process was therefore selected for DosiVox-2D. We confirm in this paper the match between 2D calculation of the beta dose rate using this process with the standard 3D modellings.

The dose deposited during particle interactions is recorded in each voxel, as well as the quantity of energy carried by the particles emitted by mass. This last quantity (noted EmMass in the software for Energy emitted by unit of Mass) is equivalent to a local infinite matrix dose, that can be defined for any material quantity in the modelling, such as one voxel of material, one material phase or the whole modelling volume. To these local infinite matrix doses correspond a reference dose rate, calculated from the K, U and/or Th contents multiplied by their respective dose rate conversion factor (Guérin et al., 2011), allowing the calibration of the results by a proportionality law (see Martin, 2015, chapter 1). Edge effects may appear at the physical edges of the modelling, due to the rupture of the sample structure and isotropy. In order to avoid these effects to create a bias of the results, the dosimetric data of the voxels within 3–5 mm (depending on the average density and water content) to the edges of the model are not recorded.

The dose is integrated over the voxels of each material for calculating the effective beta dose rate (in Grey per kiloyear – Gy. ka^{-1} – using the conversion factors from Guérin et al., 2011) of each mineral phase. These effective beta dose rates are provided independently for the K, and U- and Th-series, and combined for calculating the total effective beta dose rate. Details about the dose and EmMass are also provided for each material and radioactive emitter. Basic histograms of the effective beta dose rates are constructed in order to investigate the beta dose distribution in the sample. Maps of the beta dose rates from the different radioactive elements and series are constructed by assigning each voxel of the modelling to a pixel of the image. These maps provide a visual representation of the beta dose rate distribution, allowing more detailed investigations.

2D-modellings are usually faster and lighter, in terms of computer resources, than 3D modelling. For simulation of a 2 × 2 cm sediment or rock sample with a resolution of 100 µm, the requested RAM is around 40 MB and the stochastic uncertainty (related mostly to the number of particles simulated and to the number of interactions by voxel) fall under 0.1% after few hours of calculation on modern standard computers, while a 2 × 2 × 2 cm 3D modelling on DosiVox, with the same resolution, requires10 times more memory and at least 24 h for equivalent stochastic accuracy. Of course, this comes at the cost of the statistic representativeness of the slice modelled in the 2D-modelling, compared to a larger 3D modelling. Moreover, it can be necessary to simulate larger area in order to increase representativeness of the sample, or use a higher resolution for explicitly representing small grain fractions that can have a significant effect on the beta dose rate (such as highly radioactive minerals like zircon). In those cases, it may be necessary to simulate more beta particles emissions to reduce the stochastic uncertainty, knowing that the simulation time is approximately proportional to the number of particles generated. Higher resolutions tend to slow down the calculation speed, but the exact relation with the duration of the simulation still has to be defined. DosiVox-2D supports multithreading calculations, and therefore several computer cores can be used for a simulation in order to reduce the duration. Another solution for increasing the calculation speed is to launch several parallel simulations, on computer clusters for example, and average the results.

4. 2D-modelling in virtual sample

To investigate the applicability of DosiVox-2D, four mineralogical environments (Table 1 and Fig. 2) were generated in DosiSed (Martin, 2015, chapter 13), a software that generates distributions of randomly packed spherical grains of different minerals and radioactivities, and simulates their dose rates (Nathan et al., 2003; Guérin et al., 2012a). In this test, the results of 2D and 3D model are compared with that of standard approach (infinite matrix dose and attenuation factors).

For each environment, three simulations were carried out to calculate the beta dose rate received by each mineral component. The first simulation was conducted by DosiSed, recording the dose rates in 3D geometries made of randomly packed spheres. The second simulation used DosiVox with 3D voxelised geometries. In that case, each environment was divided into cubic voxels and each voxel was filled with material in its centre. The third simulation was carried out with DosiVox-2D with 2D voxelised geometries. Five slices of raster images were obtained from the preceding 3D image. To match the standard setups for mapping minerals in 3D and 2D, the voxelised volumes were 16 × 16 × 16 mm with voxelisation resolutions of both 50 and 100 µm. As the smallest grain size Environment D is 200 µm, only the 50 µm resolution was used to correctly keep the shape and dimension of the grains. The beta spectra of ^{40}K, U-series and Th-series from Guérin (2011) were used for the beta particle emissions in the different simulations.

For comparison, beta dose rates in the grains and in the clay matrix were calculated for the different environments using the standard approach. This method, which is the most widely used in luminescence and ESR dating, relies on the calculation of the infinite matrix dose rate (from the radioactive contents and conversion factors (Guérin et al., 2011), corrected by the fraction absorbed by water (using the attenuation factors for moisture content from Zimmerman, 1971; Nathan and Mauz, 2008). Additionally, grain size attenuation factors are applied (Mejdahl, 1979; Guérin et al., 2012a). The external attenuation factor and internal self-dose fraction (Guérin et al., 2012a) add up to 1. If the grain is radioactive, its internal dose rate is derived from the dose rate of its U, Th and K contents, multiplied by the self-dose fraction. The corresponding equation for the standard calculation of the beta dose rate in a grain is then:

$$Dr_{grain} = Dr_{xt.} \times (1\text{-}F_{self\ dose})/(1 + F_{moisture}.M) + Dr_{int} \times F_{self\ dose} \quad (1)$$

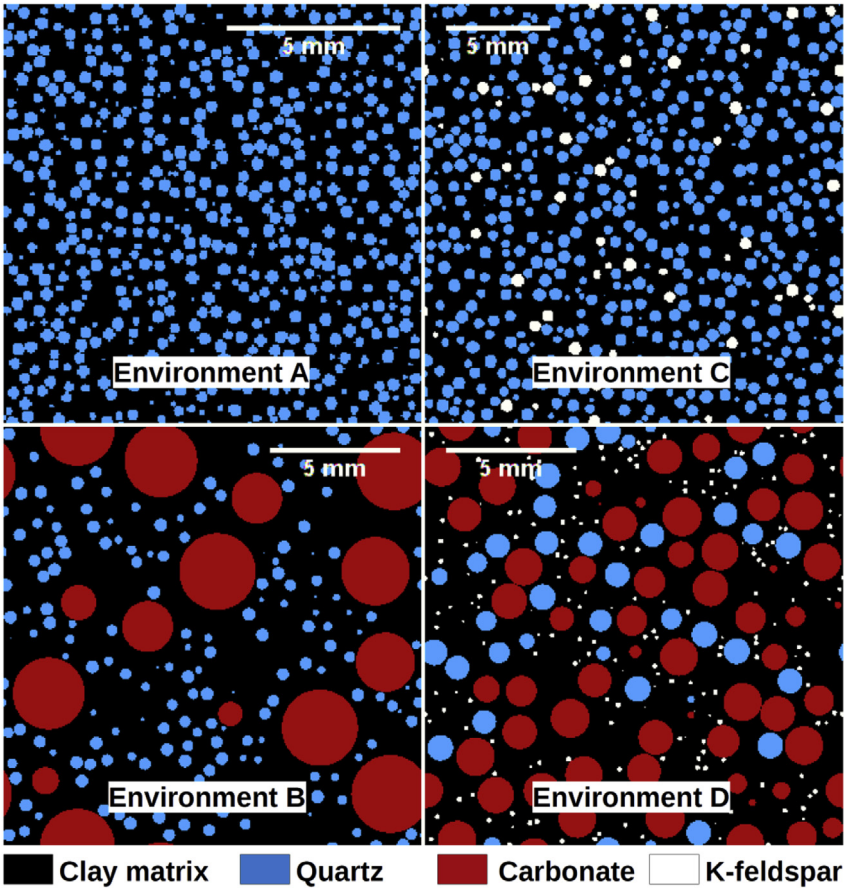

Fig. 2. Visualization of a slice of each virtual environment.

Where Dr_{grain} is the beta dose rate in the grain, Dr_{xt} is the beta dose rate in the external environment of the grain (usually equal to the infinite matrix dose rate of the sample), Dr_{int} is the infinite matrix dose rate of the grain material. $F_{self\ dose}$ is the self-dose fraction absorbed by the grain. M is the moisture content of the sediment and $F_{moisture}$ is the water attenuation factor. For the beta dose rate of fine grains ($< 10\,\mu m$) in the matrix, the equation is the same with $F_{self\ dose}$ being zero or negligible. The attenuation factors may vary depending on the radioactive elements or series considered, and the different contributions from the K, U- and Th-series are usually calculated separately (Mejdahl, 1979).

Dr_{xt} results from the measurements of the radioactive elements in the sample. In most cases, samples are completely homogenized. However, Nathan et al. (2003) showed that removing the fraction larger than 10 mm leads to a more realistic calculation of the external beta dose rate. This is due to the fact that a significant part of the coarse fraction does not contribute to the beta dose rate received by the grains used for dating (due to the range of the beta particles, unable to totally cross the objects of this size). However, if it is crushed with the rest of the sample, this fraction contributes to the average content of radioactive elements. The standard method was used to investigate three cases for beta dose rate (Dr) calculation:

1) Dr_{bulk} is derived from the infinite matrix dose rate (Dr_{xt}) calculated from the average K, U or Th contents of different size fractions and using the conversion factors from Guérin et al. (2011) corrected for moisture and internal dose rate.
2) Dr_{mm} is calculated from the average content of radioactive elements from the fraction < 1 mm (which excludes the carbonate grains in the environments B and D, and the quartz grains in environment D).
3) Dr_{mtx} is calculated from the radioactive element contents of the clay matrix.
4) The self-dose fraction factors calculated by Guérin et al. (2012a) were applied to grains between 1 and 1000 µm, and those for carbonate grains of 1.5 mm and 3 mm were calculated by DosiVox (Martin et al., 2015c).

Fig. 3 shows the comparisons between the three standard calculations and modelling (spheres packing, 3D and 2D) for the four considered environments. For direct comparison, the part of the beta dose absorbed by moisture in the clay matrices were removed according to Zimmerman (1971), and Nathan and Mauz (2008). The 2D modelling error is 2-σ standard deviation of the results from different slices. It represents the uncertainty in the beta dose rate due to the representativeness of these slices compared to the whole sample volume. The sphere packing and 3D errors are not given since the random errors between two simulations are less than 1%. Nevertheless, these small errors do not indicate the accuracy of the model runs, they just show that a sufficient number of particles in simulation can obtain statistically reproducible results.

The beta dose rates received by the different mineral fractions and calculated with the three models agree within errors (Fig. 3), except for the K-feldspars dose rate that is slightly overestimated by 2D and 3D modellings (Fig. 4). A part of the differences between grain packing and the voxelised models (3D and 2D) can be attributed to approximations in the voxelisation process. The results of individual 2D simulations have large statistical variations due to the lower representativeness of slices over the whole sample volume, nevertheless the mean dose rate values of the five slices are comparable with those obtained by the other methods. This shows that 2D-modelling gives similar results as the 3D approaches. It should be noted that the statistical accuracy of the 2D modelling can be enhanced by increasing the slice size.

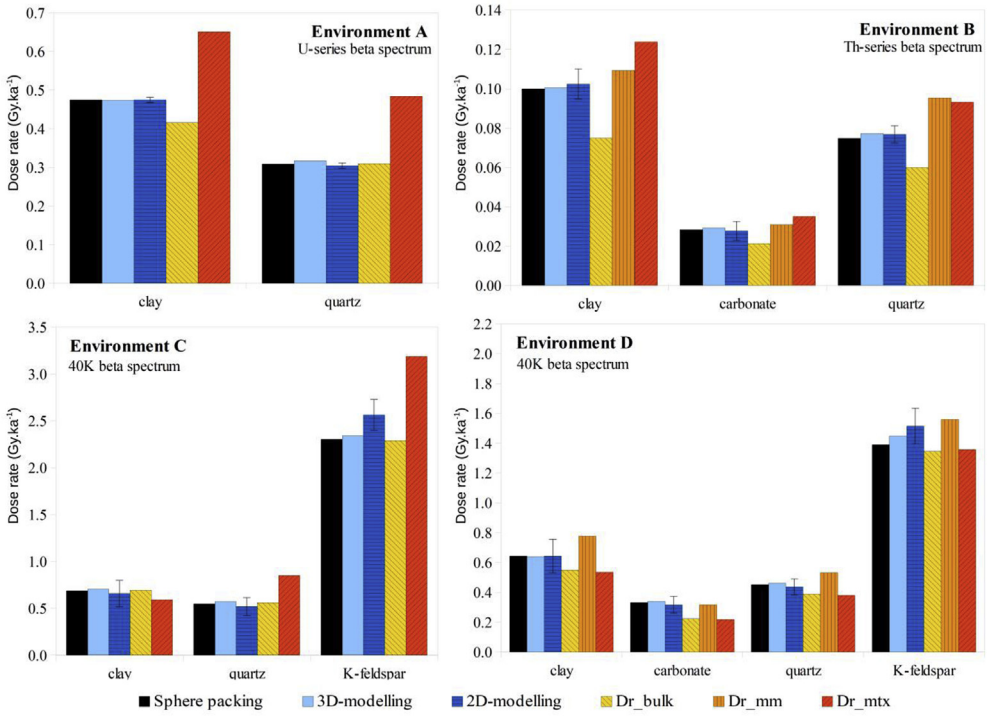

Fig. 3. Beta dose rates calculated by simulations and standard methods in four heterogeneous environments.

The dose rates deposited in the different materials are also compared (Fig. 4). The dose rates were normalised by those of the sphere packing modelling, which has been proved efficient in heterogeneous dose rate calculations (Nathan et al., 2003; Guérin et al., 2012a; Martin et al., 2015b). Moreover, the sphere packing geometries are the original models which the 3D and 2D modellings were made from, and the standard calculation also considers spherical grains (even if the grain packing situation is not considered). Consequently the sphere packing modellings should deliver the closest dose rates to the investigated virtual samples.

Fig. 4 highlights that 2D modelling gives results within the 5% range of deviation from the reference beta dose rate, except for the K-feldspars case. These results seems comparable, in terms of exactness, to the 3D modelling ones but are yet subject to an additional uncertainty due to the statistical representativeness of the area used for creating the 2D modellings (Fig. 3). In contrast, the beta dose rates received by the different sediment fractions and calculated using the standard method exhibit large deviations compared to the reference dose rate (more than 50%), or sometimes gives dose rates closer to the reference than the voxelised modellings (specially the bulk dose rate). As no general trend can be observed for the different materials or for the different fractions used in the calculation (except in the case of the K-feldspar grains, which is developed next), it seems difficult to predict the possible underestimation or overestimation of the beta dose rates, nor the extent of variation when applying these calculation methods to heterogeneous samples. This additional and potentially significant uncertainty is usually not estimated, nor taken in account in the standard method of beta dose rate calculation. On the other hand, it seems that the use of simulations in these cases allows limiting the possible bias on the beta dose rate, even if additional uncertainties from the sample analysis and

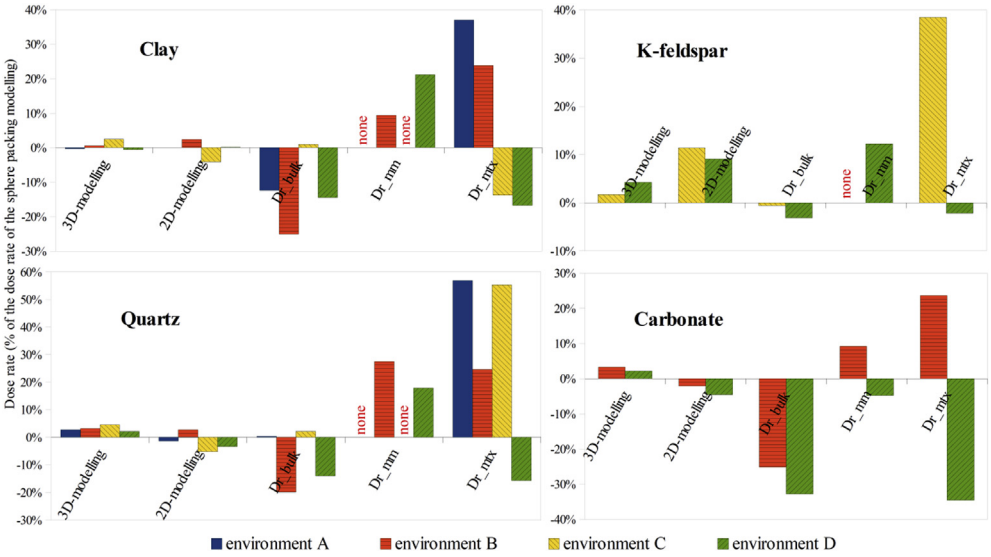

Fig. 4. Comparison of the beta dose rate in the different mineral phases calculated by simulations and standard methods. The dose rates are presented in relative percent to the dose rates of sphere packing modellings. The red cross indicates the absence of calculation of Dr_{mm} because there is no fraction under the millimeter except the matrix. (For interpretation of the references to colour in this figure legend, the reader is referred to the Web version of this article.)

geometry creation have to be added.

The K-feldspars exhibit a significant difference between the 2D and sphere packing dose rates (Fig. 4). A difference of more than 10% is observed for Environment C, which is more than the uncertainty caused by the representativeness of the slices (Fig. 3). The 3D modelling results vary by less than 5%, but the results which closest to the reference dose rate are provided by the Dr_{bulk} calculation. The error in the 2D modelling results can be interpreted as an underestimation of the slice representativeness uncertainty, which is possible because of the small volume fraction represented by the K-feldspar grains: the standard deviation calculation over this small fraction from only five slices may not suffice in obtaining a statistically correct evaluation of the uncertainty on the K-feldspar beta dose rate. Another explanation is that 2D-modelling gives less accurate results in the case of internal hotspots, possibly because the simulation of the internal dose rate of small (in regard of the beta particle range) spherical grains does not fit with the principle of isotropy necessary for 2D-modellings. The accuracy of the Dr_{bulk} calculation for K-feldspar grains can be attributed to their larger beta self-dose, which reduces the effect of external dose rate heterogeneity. This seems to confirm the common assumption that K-feldspars are more suitable for heterogeneous sediment dating. More investigations have to be done to confirm these patterns and to determine the actual reason why 2D-modelling is less accurate in this particular case. This could eventually lead to an enhancement of 2D-modelling, or confirm that Dr_{bulk} will always be more accurate for calculating the dose rate in a localized hotspot.

It is noticeable that for Environment C, the Dr_{bulk} calculation is closer to the sphere packing dose rate than any other simulation or calculation, even if the simulated dose rates differ by less than 5% in most cases. The explanation can be that for this environment, the effects of the different heterogeneities (the quartz and K-feldspar grains) compensate each other, due to the fact that all the grains have the same size and closely similar densities, resulting in the similar self-dose fractions for quartz and K-feldspar grains. More investigations are also required to determine whether this is a particular case or the results can be extended to a wider range of environments, allowing fast calculations of the beta dose rate without requiring simulations.

The beta dose rates obtained with the models running with a 50 μm and 100 μm resolution, show small to negligible differences (Fig. 5). Note that only the 50 μm resolution was used for Environment D, to keep the shape of the smallest grains. Then, it seems that a resolution of 100 μm is sufficient to accurately model the beta dose rate of the coarse fraction (> 500 μm). However, this does not mean that all objects larger than the applied resolution will be represented in the mapping, since the depth of analysis and the efficiency of the deconvolution have to be taken into account. For instance, SEM and QEMSCAN radiations penetrate only a few micrometers in a sample, while the X-rays from XRF can reach a depth of 1 mm. As a consequence, the resolution for XRF needs to be carefully chosen. Only objects and mineral phases whose thickness is in the millimeter range will be correctly represented. To minimize analysis time and consumption of computer resources, we recommend using lower resolution images. One should keep in mind however that the shape and size of the smallest objects may change. The user has to balance the resolution with the necessity of conserving sufficient information about the modelled objects.

5. Comparison of the beta dose rate distribution shape between 3D and 2D models

The use of the single grain dating technique (Duller et al., 1999) often leads to the observation of large equivalent doses overdispersions in sediment samples. Various factors may be involved like incomplete bleaching or sensibility changes and beta dose rate variations at the grain scale (Nathan et al., 2003; Guérin et al., 2012a). These variations may be visualized and investigated for different grain sizes and mineral phases of a sample with DosiVox and DosiVox-2D (Martin, 2015, chapter 11, 12, 13). In order to test if 2D-modelling can be an efficient tool for this purpose, we compared the shapes of beta dose rate distributions in 2D and 3D simulations (Fig. 6).

There is a general agreement in the shape between 2D and 3D dose rate distributions. Differences can either be attributed to the lower statistical representativeness of the 2D-mapping or the fact that 2D-modelling process itself may have caused some divergences. More tests need to be carried out to address this matter. It is likely that a larger number of 2D runs are required to match the 3D results. Nevertheless, 2D runs are a reasonable approximation of the beta dose distributions, thus allowing the investigation of the role of beta dose rates in the dose over-dispersion of single grain data sets (Mayya et al., 2006).

With 2D beta dose mapping and distribution, it is possible to consider new strategies to investigate these effects on beta dosimetry and age calculation. Applied to rock beta dosimetry, this method could help investigating the effect of radioactive hotspots: in the presence of small but highly radioactive inclusions, like it can be the case in granites, the local beta dose rate can be significantly underestimated, and even dose saturation areas can be created. Beta dose mapping and distribution could help to identify and take in account these effects. Combined with the recent development of spatially resolved OSL (Clark-Balzan and Schwenninger, 2012), it could also be possible to cross compare the mappings of natural luminescence signal, luminescence sensitivity (after artificial irradiation of zeroed sample slices) and beta dose rate. This comparison would allow investigating the cross-effects of beta micro-dosimetry and sensitivity variations in a sample, and their potential implications for the dating process and age calculation.

6. Beta dose rate in non-apparent grains

Luminescence and ESR measurements are usually not performed on bulk material or on the millimeter or larger fraction, but rather on grain size fractions ranging from few micrometers (fine grains) to few hundreds of micrometers (coarse grains). These grains may not explicitly appear on the mapping analysis for various reasons: they can be smaller than the resolution of the analysis, or impossible to deconvolve because of the probing range, or indistinguishable from the surrounding material (like small quartz grains in a larger quartz phase). These grains may represent a heterogeneity that is not taken into account in the different simulation methods. As a consequence, the beta dose rate in these grains may be different from that of its mineral phase represented in the modelling. The 2D and 3D runs only provide the effective beta dose rate for a given mineral phase, and it is therefore necessary to calculate the beta dose rates in grain size fractions of this phase. We distinguish three cases:

(1) For fine grains (< 10 μm), the beta dose rate attenuation is negligible. Thus, their beta dose rate is the same as the effective beta dose rate of the mineral phase containing them calculated by 3D and 2D runs. For example, the beta dose rate of fine grains in the clay matrices modelled in part 4 is equal to the effective dose rate of the respective matrices. It may be necessary to correct for water contents (Zimmerman, 1971).
(2) In granites or similar heterogeneous rocks, the grains (fine or coarse fractions) may be packed together in aggregates or veins of millimeter to centimeter scale, resulting in a very different dosimetric system for the beta particles than what it is usually considered for heterogeneous sediments (grains scattered in a fine matrix). An aggregate can be considered as a local homogeneous medium because there is no different material between the grains. The variation of the beta self-dose fraction with the grain size is compensated by the variation of the beta dose rate contribution from the surrounding material, like in an infinite homogeneous matrix. Consequently, the size of a single grain does not influence its beta dose rate, *i.e.* in an aggregate all the grain size fractions receive the same averaged beta dose rate, independently of their individual

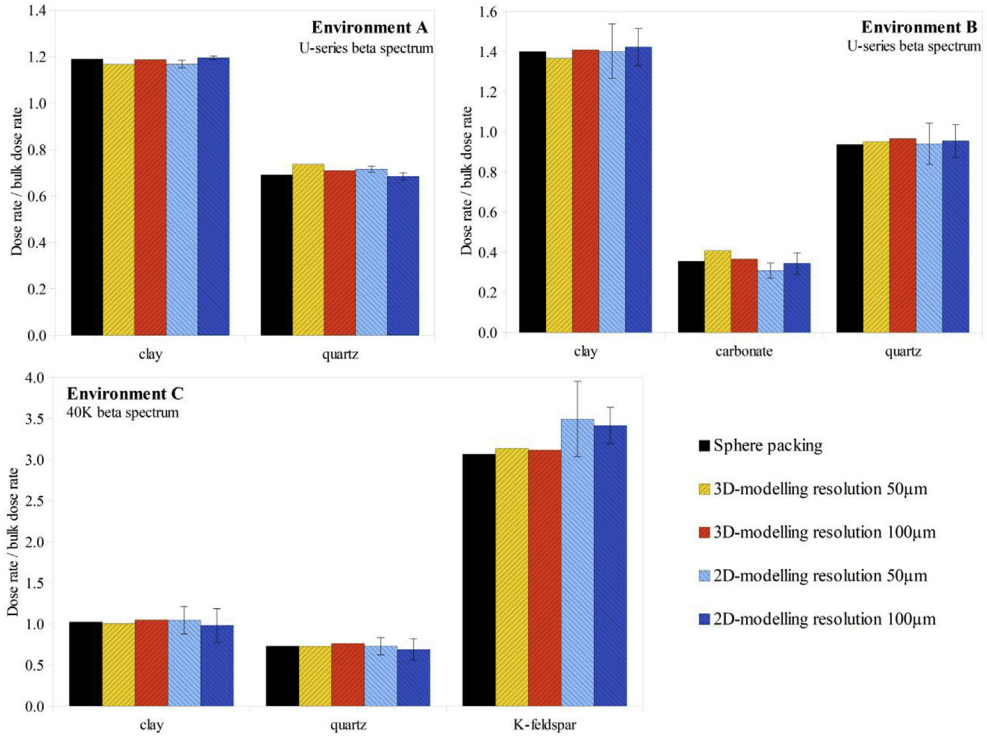

Fig. 5. 2D simulations from mapping images with different resolution.

size. However, the aggregate is not infinite in regard to the beta dose rate and so, instead of receiving the infinite matrix dose rate, it receives an effective beta dose rate from its own radioactivity and from the radioactivity of the surrounding aggregates and veins of other minerals. This postulate has been assumed by Plachy and Sutton (1982) for calculating the beta dose rate in their granite sample. The effective beta dose rate depends on the size, shape, composition and radioactivity of the aggregate, as well as the surrounding aggregates and veins and their distribution around the considered aggregate (Plachy and Sutton, 1982). Simkins et al. (2016) highlighted the importance of the crystal size in beta dose rate of rock samples, and Kaipa et al. (1988) calculated the effective beta dose attenuation for spherical agglomerates of quartz in bricks, exposing an increase of the beta dose rate attenuation from 12% to 47% of the infinite matrix dose rate for similar individual grain size distributions, but different agglomerate sizes. However, the calculation from Kaipa et al. (1988) is difficultly transposable to heterogeneous rocks such as granites, as the grain aggregates are often not spherical and the shapes of objects in millimeter to centimetre have a significant effect on the beta dose rate attenuation (Fain et al., 1999; Nathan, 2010).

The negligible effect of the individual grain size can also be deduced from Fig. 5: if each mineral phase (matrix of grain) is considered as a set of aggregates of voxels, and each voxel is assigned to a grain (cubical instead of spherical), the result is an environment composed of grain aggregates. Therefore, changing the resolution of the model runs corresponds to changing the size of the grains forming the aggregate. However, no significant variation of the beta dose rate can be observed between the runs with different resolutions. This supports the hypothesis that the size of the grains forming the aggregates has no significant effect on the beta dose rate of these grains.

(3) The last case considered here corresponds to coarse grains (diameter higher than 10 µm) embedded in a matrix of a different material. The mineral phase considered in the model runs represents the mixed matrix and grain materials. The grains represent an heterogeneity inside the phase, whose effect on the beta dose rate will depend on their differences of radioactivity, composition and density compared to the surrounding material, but also on their size (they are scattered in the matrix and not packed together like in a granite) and their volume fraction (Nathan et al., 2003; Guérin et al., 2012a; Martin et al., 2015b). If the volume fraction of these grains is small, the dosimetric system is on the local scale of the mineral phase similar to the pottery case described by Fleming (1973) and Aitken (1985). Therefore, it seems reasonable to think that it should be possible to calculate the beta dose rate in the grains by applying their standard calculation method not to the infinite matrix dose rate, but to the effective beta dose rate provided by the model runs. In order to test if the standard attenuation factors are still relevant when applied to an effective dose rate inside a mineral phase next to an interface with a different mineral phase, a DosiVox model was created by positioning a single 200 µm quartz grain at different distances from this interface. The beta dose rates recorded by the grain were compared to the effective beta dose rate (recorded in the absence of the grain) attenuated by the standard factors for that grain size (Guérin et al., 2012b) and moisture (Zimmerman, 1971), noted “Attenuated effective beta dose rate”. Three cases were simulated (Fig. 7): a block of dry and radioactive clay matrix next to a block of non-radioactive carbonate (environment I), a block of moist and radioactive clay (30% of water in mass) next to a block of non-radioactive carbonate (environment J), and a block of dry and non-radioactive clay matrix next to a block of radioactive K-feldspar (environment K). The beta spectrum of the U-series was used for the simulation of environment I and J, and the beta spectrum of K was used for environment K. The results, already presented in Martin (2015, chapter 12), are shown in Fig. 8.

The beta dose rate recorded by the quartz grains follows the trend of the effective beta dose rate, but with a slight decrease in environment I when the grain is close to the interface. This variation can reasonably

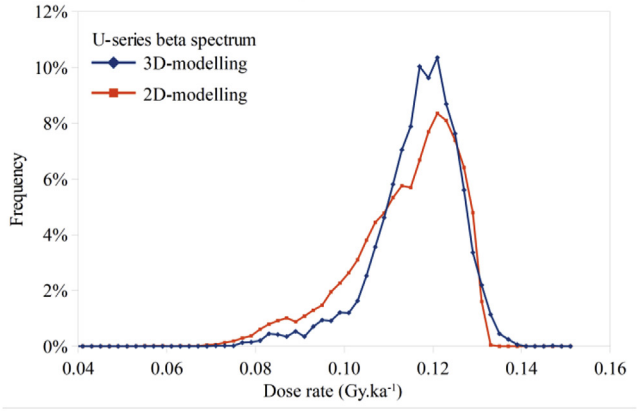

a – Dr distribution in the clay matrix of environment B

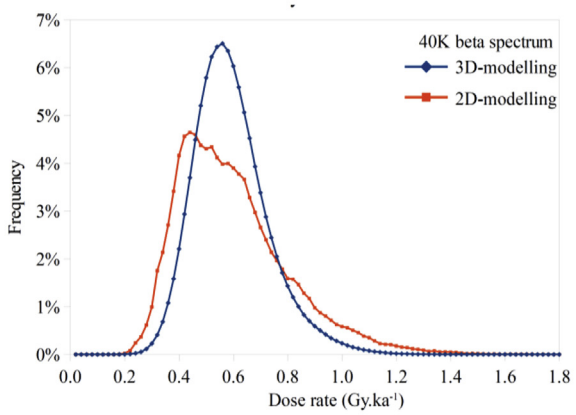

b – Dr distribution in the clay matrix of environment D

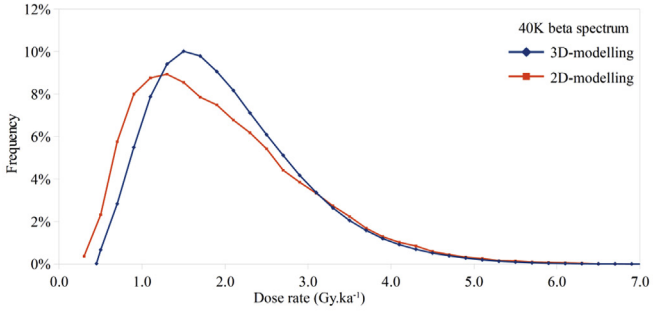

c – Dr distribution in the quartz_plagioclase phase of the granite sample of part 7

Fig. 6. Comparison of the shape of the beta dose rate distribution from 3D and 2D modellings. a – Dr distribution in the clay matrix of environment B. b – Dr distribution in the clay matrix of environment D. c – Dr distribution in the quartz_plagioclase phase of the granite sample of part 7.

be attributed to the variation of range of the beta particles in the calcite, resulting in less particles being back-scattered in the direction of the grain. However, this effect is small and probably negligible when the beta dose rate is averaged among the whole mineral phase. In addition, it is reduced in a moist environment, where we can observe no significant difference between the beta dose rate recorded by the grain and the effective beta dose rate. This is due to the smaller range of the beta particles in moist environment. The same observation can be made for the environment K considering the ^{40}K beta spectrum: because of the smaller average range of the beta particles from this spectrum (Brennan et al., 2000; Martin et al., 2015c), compared to the beta from the U-series spectrum, the effect of the proximity of a different material on the dose rate is reduced, if not negligible. This should equally apply to rock samples, like granites, where the ranges of the beta particles in the more represented minerals are usually similar, due to their close densities.

The last simulations consider a single grain in a clay matrix. Other studies (Guérin et al., 2012a; Martin, 2015, chapter 4) have shown that the increase of the volume fraction of grains in the sediment has an increasing effect on the effective beta dose rate compared to the pottery case (Zimmerman, 1971; Aitken, 1985). This can be seen as an intermediate situation between this last situation (low fraction of single grains scattered in a homogeneous matrix), and a mineral phase composed of an agglomerate of grains like the granite. Thus, the standard calculations are not reliable in this situation. Martin (2015, chapter 12) showed that for grains between 50 µm and 200 µm and with a volume fraction of grains $>$ 10%, the effective beta dose rate in the grains is close to the effective beta dose rate of the mineral phase. It can thus be assumed that 2D modelling provides a first good approximation for the beta dose rate in sedimentary grains. It is always necessary to remove the part absorbed by the water from the effective dose rate. Guérin and Mercier (2012) showed that the volume fraction of grains in sediment has a non-negligible effect on the moisture attenuation factor for the gamma dose rate. This needs to be investigated for the beta dose rate in order to calculate an accurate attenuation of the effective beta dose rate in the case of a non-negligible volume fraction of grains. If required, accurate attenuation of the effective beta dose rate could still be calculated by reproducing the sediment in DosiVox.

The various simulations presented in this part of the study assume random distributions of the grain size fractions in the considered phase. However, if there is evidence of a non-random distribution of the fraction used for the dating (for example, if coarse grains are more frequent in the centre of the phase than fine grains, or if the grains only come from a specific part of the sample), then the effective beta dose rate cannot be calculated by averaging the dose rate in the voxels. Here, one has to use image processing for dose rate mapping, the average beta dose rate results from the voxels containing the grains of interest.

7. Comparison between 3D and 2D modelling in a granite sample

The following simulations are used to compare the results and accuracy of 3D and 2D modelling of a natural granite sample (migmatite type) from Kullu valley, Northwestern Indian Himalaya. However, we assumed for this demonstration that the effect of this slight anisotropy does not affect significantly the beta dose rate. The sample is mainly composed of quartz (30% in mass), plagioclase (39% in mass), K-feldspar (18% in mass) and mica (13% in mass). It has been determined by ICPMS and ICPOES that the bulk sample contains 4.27 ppm of U, 19.17 ppm of Th and 3.72% of K. The K is distributed in the four main mineral phases and negligible in the minor phases, while the U and Th are concentrated in the small inclusions (representing less than 1% of the sample mass) and negligible in the main mineral phases. The beta emission from ^{40}K desintegration represents 72% of the total beta dose rate. The aim of the study is to illustrate the method of 2D modelling on a rock sample, and thus we will only represent the main mineral phases and we will focus on the beta dose rate from ^{40}K in the simulation. Plachy and Sutton (1982) used the same simplification for their granite sample, and assumed that uranium and thorium beta dose rates in quartz mostly came from mica phases, with an attenuation factor calculated from the K beta dose rate attenuation factor for mica to quartz. For our sample, another method should be used for taking into account

the U- and Th-series beta dose rates, as these elements are negligible in mica but distributed in small inclusions such as zircons. It could be assumed for example that these inclusions are randomly dispersed into the sample, and we could simply calculate their contribution to the beta dose rate by using the attenuation factor for individual grain sizes to take into account the beta self-dose and the attenuation in quartz grains. However, this would necessitate to know the complete size distribution of the different inclusions and of the quartz grains, as well as their respective contents in U and Th. These data are not available, and we simply continue with the modelling of only the ^{40}K beta dose rate in the sample.

The 3D distribution of the minerals in the sample was obtained from X-ray CT scan performed at Research School of Physics and Engineering (RSPE), the Australian National University. The X-ray source was operated at a tube voltage of 120 kV and a target current of 105 µA. The images were acquired with a voxel size of 22 µm. The data segmentation was carried out in Qmango program at RSPE. The bilateral iteration and anisotropic diffusion filters were applied to reduce the noise, and level intensity filter was used in X and Y directions for balancing the intensity from inside to the edge of the sample. The quartz and plagioclase phases cannot be separated because they have similar X-ray attenuation coefficients (Cnudde and Boone, 2013). As a consequence, the image shows a major phase of about 70% of the surface and volume composed of quartz and plagioclase, as a single phase. The segmentation of the major mineral phases of the sample was confirmed by QEMSCAN analysis.

The 3D-modelling was created by transferring the whole CT-scan to DosiVox via its interface and by associating the different grey levels with the indicated minerals and their radioactivity (Fig. 9). As the 3D CT image results from the combination of successive 2D images, it was possible to randomly select five of these images for 2D-model runs. For the 3D and 2D simulations, we assumed that the K contents of the quartz_plagioclase phase, of the K-feldspar phase and of the mica phase were respectively equal to 0.14%, 10.8% and 7.68% in mass, and that K was homogeneously distributed in the respective phase. More recent and accurate measurements show that the contents of K in K-feldspar and mica of the sample are respectively closer to 13.3% and 8.6%, but this does not affect the pertinence of the modelling or the implications of the dose rate results.

The average beta dose rates of the five 2D runs (with 2-σ errors) are shown in Fig. 10 and compared with the 3D runs. Standard beta dose rate calculations used equation (1) for spherical grains of 100, 200 and 300 µm. The self-dose fraction factors for quartz were used for the quartz_plagioclase phase, and the factors for K-feldspar were used for the K-feldspar phase (Guérin et al., 2011). The self-dose fraction of the mica grains of 100, 200 and 300 µm were calculated using DosiVox to 0.040, 0.083 and 0.128, respectively.

We observe on Fig. 10 that the dose rates obtained with the standard approach can be significantly different to the 2D and 3D simulations, in

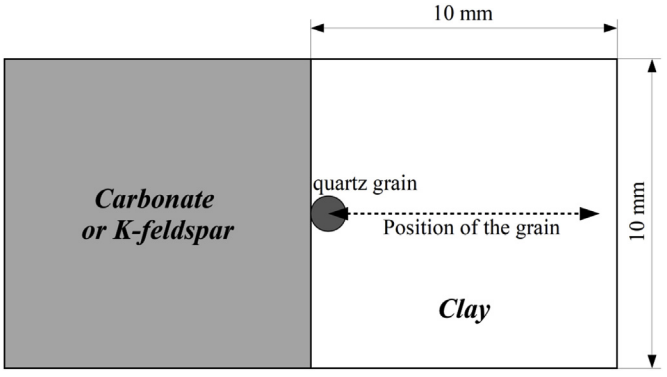

Fig. 7. Schemas of the DosiVox modelling for beta dose rate attenuation in a grain next to a heterogeneous environment.

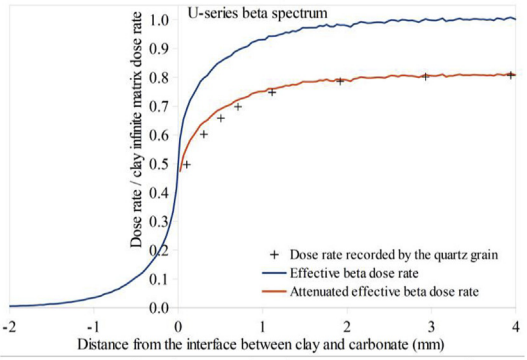

a – environment I: radioactive dry clay next to an inert carbonate

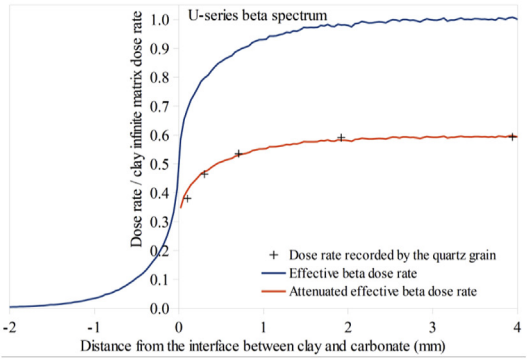

b – environment J: radioactive moist clay next to an inert carbonate

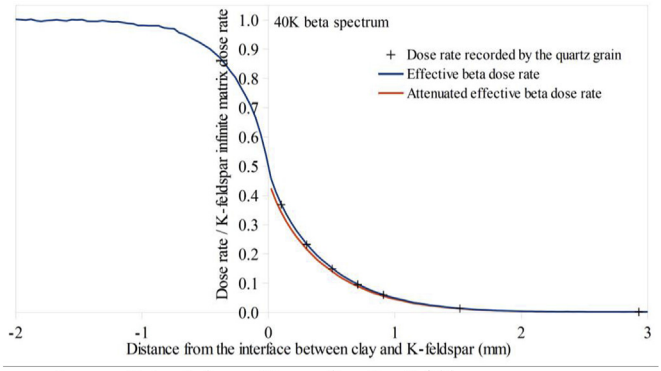

c – environment I: inert clay next to a radioactive K-feldspar

Fig. 8. Beta dose rate attenuation in a grain next to an interface between two mineral phases. Wiggles of the lines result of stochastic uncertainty of the Monte Carlo simulation. a – environment I: radioactive dry clay next to an inert carbonate. b – environment J: radioactive moist clay next to an inert carbonate. c – environment I: inert clay next to a radioactive K-feldspar.

particular for minerals with high K concentrations (K-feldspar and mica). These variations can be attributed to the basic assumptions of the standard approach, that considers single grain in a homogeneous and infinite matrix, and are obviously not verified in granite as the grains are not single but aggregated, and the surrounding environment of the aggregate is not homogeneous at the beta particle range scale. It is worth to notice that simulations of single grains in an homogeneous matrix with DosiVox are in good agreement with the tabulated attenuation factors for beta dose rates (Martin et al., 2015c), which indicates that the differences here are related to the sample characteristic, not to the simulation tool. The differences between the beta dose rate calculations for the quartz_plagioclase phase are significantly smaller than for the other minerals. It can be explained by the proximity

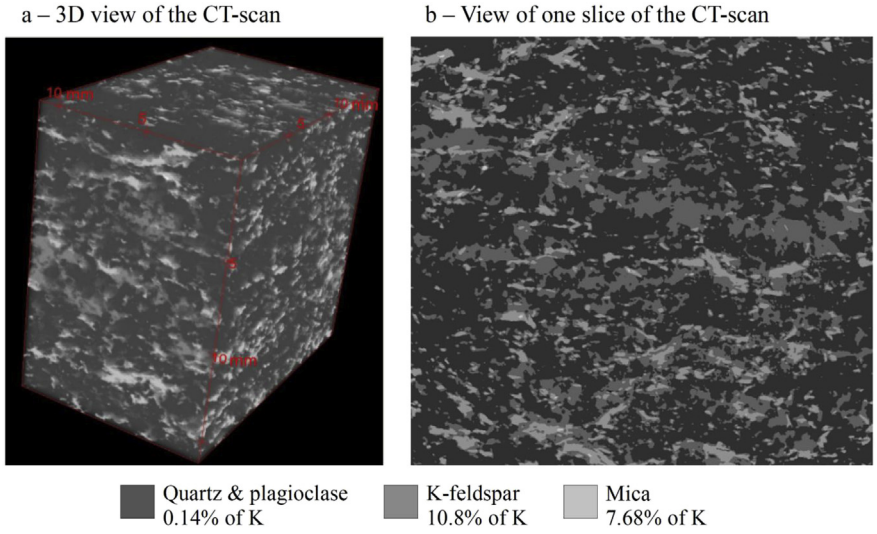

Fig. 9. 3D view of the CT-scan and 2D view of one of the slice.

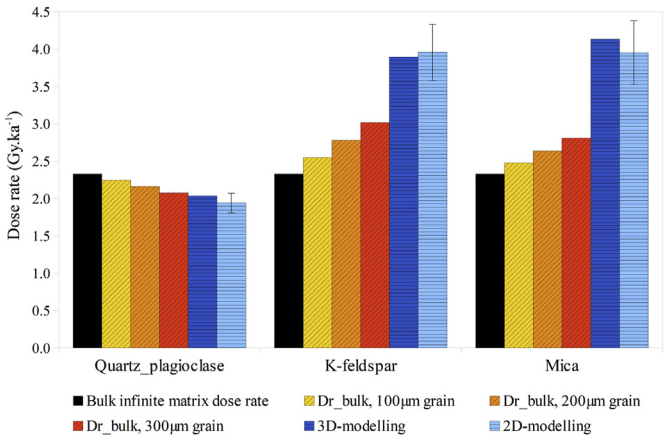

Fig. 10. Comparison of the ^{40}K beta dose rates from 3D modelling, 2D modelling and standard self-dose and attenuation factors for 100 µm, 200 µm and 300 µm grains in a granite sample.

between the bulk infinite matrix dose rate and the simulated dose rate: the beta dose attenuation calculated for 100 µm–300 µm grains is smaller than that of a simulation that considers larger clusters of quartz grains. As a consequence, the standard calculation gives intermediate values between the infinite matrix dose rate and the simulated dose rates. Considering that the difference between infinite and simulated dose rates is small for the quartz_plagioclase phase, it is logical that the difference with the standard calculated dose rates is also small. It is worth to notice that Kaipa et al. (1988) calculated an increasing of beta dose rate attenuation from 12% to 47% for millimeter size aggregates of quartz grains in bricks, whose individual diameters were 106 µm–250 µm. This increase inthe attenuation would lead to a decrease of the beta dose rate by 40%, while the difference observed between simulated beta dose rate and beta dose rate calculated with the standard approach is between 2% and 9% for the quartz_plagioclase phase. Of course, the result here is the average beta dose rage over the quartz and plagioclase phase; considering that these minerals have different K contents in this sample (respectively 0.005% and 0.245% of K), a decrease of the quartz beta dose rate and an increase of the plagioclase one have to be expected if these two phases were segmented in the modellings, as Fang et al. (2018) did with 2D-modellings from QEMSCAN analysis of granite slices.

The differences between beta dose rate calculations for K-feldspar and mica phases can also be explained by the clustering of the grains that increase the self-beta dose rate inside the clusters. The difference between the simulation and the standard approach seems stronger for these minerals because of the gap between the bulk infinite matrix dose rate and the infinite matrix dose rate calculated for K-feldspar or mica. The effect of grains clustering seems to increase with the difference between bulk and grains radioactivity. An increase of the beta self-dose from 12% to 47% can be extrapolated from calculation for quartz grains clustering Kaipa et al. (1988), indicating that this effect could potentially increases the contribution of grains radioactivity to the beta dose rate by 400% for a millimeter size cluster of grains, compared to the case of scattered grains. We are here in a more moderated situation, where the increase of beta dose rate from clustering effects is between 30% and 70% compared to the case of discrete grains of 300 µm, 200 µm or 100 µm). Even if these values would need experimental validation, it highlights an important effect of grains clustering to the beta dose rate, previously discussed in part 6, which could lead to significant inaccuracy for age calculation. However, this has to be relativised by the other contribution to the beta dose rate (U and Th represent 28% of the bulk beta dose rate) and to the total dose rate (usually, beta dose rate account for about a third of the total dose rate), that would bring back the increase to about 7%–17% of the total dose rate for those minerals (considering a random distribution of the U and Th rich inclusions and negligible beta self-dose).

As Plachy and Sutton (1982) observed from their calculations for a granite sample, there is good agreement between the 3D and 2D model runs for all mineral phases. The somewhat lower accuracy of the 2D analysis will be balanced by the better mineral discrimination. The applicability of the method is therefore not limited to the modelling of spherical objects but can be extended to more complex and random shapes that one may encounter in dating applications. The implications for ESR and luminescence thermochronology are discussed by Fang et al. (2018), where these results are completed with 2D-modelling constructed from QEMSCAN mappings, which enables to separate the quartz and plagioclase phases.

It can be noticed that the basic assumption about the isotropy of the sample does not seem to be a limiting factor: although the granite sample is slightly foliated, and thereby is not perfectly isotropic, the 2D-results provide similar beta dose rates to the 3D-runs for this sample, for the slices cut perpendicularly to the plane of foliation. Under this condition, the slices remain representative for the whole sample. Fang et al. (2018) discuss the various approaches to mineral mapping and compare the results of 2D modellings from orthogonal slices of isotropic and partially isotropic samples. Even without modelling, the mineral mappings of orthogonal slices can be used for investigating the isotropy

of samples, by considering the mineral proportion and distribution in different directions. This analysis would allow determining the best direction of slicing for 2D modellings (Fang et al., 2018), or even, in the case of a strong anisotropy, guiding to 3D modelling rather than 2D modelling. It has to be noticed that for sediment modelling, due to the deposit process, there is at least anisotropy in the direction of stratification. However, a single sediment layer can often be considered as locally isotropic if it is well mixed and thick enough (at the beta particle range scale), but it would be wise to check it.

8. Conclusions

We verified that 2D-modelling provides similar results as 3D modelling (and also as spheres packing modelling for the first cases) for both the virtual sediment cases and the granite sample. By integrating many more parameters about the distribution of minerals and radioactivity, this method allows calculating beta dose rates in heterogeneous samples for which the standard calculation method and attenuation factors are not fully reliable, or for which the uncertainty relative to their application on heterogeneous samples is not evaluated. Even if the standard calculation method applied to the bulk dose rate occasionally provides more accurate results (in particular for the beta dose rate in K-feldspar grains), the beta dose rate obtained by 2D-modelling is closer to the reference dose rate in most cases. The deviations of 2D modelling from the reference dose rate are usually acceptable while standard calculations may exhibit very large deviations. The shape of the beta dose rate distribution, as well as the dose rate in grains contained in the modelled mineral phases, can also be investigated by 2D-modelling, assuming some simple approximations. However, the results are usually less accurate than that of 3D-modelling because of the lower representativeness of the slices used to construct the 2D-modelling compared to the whole sample used in 3D-modelling. Nevertheless, this lower accuracy can be compensated by the superior 2D mineral discrimination compared to 3D analysis, or by analysing a larger sample area. It has to be noticed that the results obtained by modelling still lack of experimental validation, that could confirm the different effects observed.

2D-modelling simulations provide an efficient tool for fast beta dose rate characterisation for heterogeneous samples. This method could easily be integrated in the dating process, and could result in a better accuracy of the age calculation and a better understanding of the variation of the equivalent dose and over-dispersion, in particular for single grain analysis. 2D-modelling is accessible by the software DosiVox-2D which does not require programming skills and proposes a graphical interface for easier construction of the modelling and image loading. In addition, the simulation is relatively fast and can be run on a standard office computer (it takes only few hours to one day for performing a basic 2D simulation on recent computer but heavier modellings can still necessitate few days of calculation, and about a week for high resolution or large modellings, *i.e.* less than 30 µm of resolution or larger than 4 × 4 cm). Moreover, DosiVox-2D is compatible with multithreading computation, which allows speeding up the simulation by simultaneously using several cores of the computer. Ultimately, the aim of the software is to be freely distributed online, as it is the case of DosiVox, for the benefit the whole dosimetric dating community.

Both 2D and 3D modelling methods showed that mass fraction, shape, agglomeration and distribution of the minerals can have significant effects on the beta dose rate, and therefore on the exactness of the dating. Standard calculation models of beta dose rate are not adapted to take into account all these parameters, while Monte Carlo modelling offers a suitable solution for heterogeneous cases. Even when making assumptions (e.g., on the radioactive element distribution, on the water content, or on the isotropy of the sample), it is still possible to use it for determining dose rate variations between different scenarios, and to estimate the induced uncertainties. In addition, modelling could help to a better understanding of the beta dosimetry at the grain scale, and identifying influence factors. This could lead to the development of advanced dose rate calculation methods, which could be suitable for heterogeneous cases. Geomorphology and stereology offer several mathematical tools and variables (for example, the use of specific surface, mean chord length, variogram and covarioram described in Underwood, 1970, or Degallaix and Ilschner, 2007) for characterising in 2D mineral mappings the size and shape of mineral phases, as well as how they are related to each other. We can easily assume that putting in relation 2D-modelling with 2D image analysis with such tools might highlight the relationships between the mineral distribution and the complexity of the beta dose rates in heterogeneous samples.

DosiVox-2D, its interface and manual can be freely downloaded at: http://www.iramat-crp2a.cnrs.fr/spip/spip.php?article144.

Acknowledgments

This work was funded by the research programme LaScArBx (Labex Sciences Archéologiques de Bordeaux) supported by the ANR, and the Nouvelle-Aquitaine region. The authors are grateful to Alan Guitard for the adaptation of DosiVox interface and the development of DosiVox-2D interface. We are thankful to Prof. Gordon Lister and Dr. Marnie Forster for providing the rock sample. We also thank Prof. Tim Senden and Dr. Michael Turner for CT scanning, Mr. Holger Averdunk and Mrs. Jill Middleton for their help on CT segmentation.

References

Abràmoff, M.D., Magalhães, P.J., Ram, S.J., 2004. Image processing with Image. J. Biophot. Int. 11 (7), 36–42.

Agostinelli, S., Allison, J., Amako, K., Apostolakis, J., Araujo, H., Arce, P., Asai, M., Axen, D., Banerjee, S., Barrand, G., Behner, F., Bellagamba, L., Boudreau, J., Broglia, L., Brunengo, A., Burkhardt, H., Chauvie, S., Chuma, J., Chytracek, R., Cooperman, G., Cosmo, G., Degtyarenko, P., Dell'Acqua, A., Depaola, G., Dietrich, D., Enami, R., Feliciello, A., Ferguson, C., Fesefeldt, H., Folger, G., Foppiano, F., Forti, A., Garelli, S., Giani, S., Giannitrapani, R., Gibin, D., Cadenas, J.J. Gomez, Gonzlez, I., Abril, G. Gracia, Greeniaus, G., Greiner, W., Grichine, V., Grossheim, A., Guatelli, S., Gumplinger, P., Hamatsu, R., Hashimoto, K., Hasui, H., Heikkinen, A., Howard, A., Ivanchenko, V., Johnson, A., Jones, F.W., Kallenbach, J., Kanaya, N., Kawabata, M., Kawabata, Y., Kawaguti, M., Kelner, S., Kent, P., Kimura, A., Kodama, T., Kokoulin, R., Kossov, M., Kurashige, H., Lamanna, E., Lampen, T., Lara, V., Lefebure, V., Lei, F., Liendl, M., Lockman, W., Longo, F., Magni, S., Maire, M., Medernach, E., Minamimoto, K., de Freitas, Mora, P., Morita, Y., Murakami, K., Nagamatu, M., Nartallo, R., Nieminen, P., Nishimura, T., Ohtsubo, K., Okamura, M., O'Neale, S., Oohata, Y., Paech, K., Perl, J., Pfeiffer, A., Pia, M.G., Ranjard, F., Rybin, A., Sadilov, S., Salvo, E. Di, Santin, G., Sasaki, T., Savvas, N., Sawada, Y., Scherer, S., Sei, S., Sirotenko, V., Smith, D., Starkov, N., Stoecker, H., Sulkimo, J., Takahata, M., Tanaka, S., Tcherniaev, E., Tehrani, E. Safai, Tropeano, M., Truscott, P., Uno, H., Urban, L., Urban, P., Verderi, M., Walkden, A., Wander, W., Weber, H., Wellisch, J.P., Wenaus, T., Williams, D.C., Wright, D., Yamada, T., Yoshida, H., Zschiesche, D., 2003. Geant4–a simulation toolkit. Nuclear instruments and methods in Physics research section a: accelerators, spectrometers. Detectors and Associated Equipment 506 (3), 250–303.

Aitken, M.J., 1985. Thermoluminescence Dating. Academic Press, London 378 p.

Allison, J., Amako, K., Apostolakis, J., Araujo, H., Dubois, P.A., Asai, M., Barrand, G., Capra, R., Chauvie, S., Chytracek, R., Cirrone, G.A.P., Cooperman, G., Cosmo, G., Cuttone, G., Daquino, G.G., Donszelmann, M., Dressel, M., Folger, G., Foppiano, F., Generowicz, J., Grichine, V., Guatelli, S., Gumplinger, P., Heikkinen, A., Hrivnacova, I., Howard, A., Incerti, S., Ivanchenko, V., Johnson, T., Jones, F., Koi, T., Kokoulin, R., Kossov, M., Kurashige, H., Lara, V., Larsson, S., Lei, F., Link, O., Longo, F., Maire, M., Mantero, A., Mascialino, B., McLaren, I., Lorenzo, P.M., Minamimoto, K., Murakami, K., Nieminen, P., Pandola, L., Parlati, S., Peralta, L., Perl, J., Pfeiffer, A., Pia, M.G., Ribon, A., Rodrigues, P., Russo, G., Sadilov, S., Santin, G., Sasaki, T., Smith, D., Starkov, N., Tanaka, S., Tcherniaev, E., Tome, B., Trindade, A., Truscott, P., Urban, L., Verderi, M., Walkden, A., Wellisch, J.P., Williams, D.C., Wright, D., Yoshida, H., 2006. Geant4 developments and applications. Nuclear Science, IEEE Transactions on 53 (1), 270–278.

Allison, J., Amako, K., Apostolakis, J., Arce, P., Asai, M., Aso, T., Bagli, E., Bagulya, A., Banerjee, S., Barrand, G., Beck, B.R., Bogdanov, A.G., Brandt, D., Brown, J.M.C., Burkhardt, H., Canal, Ph, Cano-Ott, D., Chauvie, S., Cho, K., Cirrone, G.A.P., Cooperman, G., Cortés-Giraldo, M.A., Cosmo, G., Cuttone, G., Depaola, G., Desorgher, L., Dong, X., Dotti, A., Elvira, V.D., Folger, G., Francis, Z., Galoyan, A., Garnier, L., Gayer, M., Genser, K.L., Grichine, V.M., Guatelli, S., Guèye, P., Gumplinger, P., Howard, A.S., Hřivnáčová, I., Hwang, S., Incerti, S., Ivanchenko, A., Ivanchenko, V.N., Jones, F.W., Jun, S.Y., Kaitaniemi, P., Karakatsanis, N., Karamitros, M., Kelsey, M., Kimura, A., Koi, T., Kurashige, H., Lechner, A., Lee, S.B., Longo, F., Maire, M., Mancusi, D., Mantero, A., Mendoza, E., Morgan, B., Murakami, K., Nikitina, T., Pandola, L., Paprocki, P., Perl, J., Petrović, I., Pia, M.G., Pokorski, W., Quesada, J.M.,

Raine, M., Reis, M.A., Ribon, A., Ristić Fira, A., Romano, F., Russo, G., Santin, G., Sasaki, T., Sawkey, D., Shin, J.I., Strakovsky, I.I., Taborda, A., Tanaka, S., Tomé, B., Toshito, T., Tran, H.N., Truscott, P.R., Urban, L., Uzhinsky, V., Verbeke, J.M., Verderi, M., Wendt, B.L., Wenzel, H., Wright, D.H., Wright, D.M., Yamashita, T., Yarba, J., Yoshida, H., 2016. Recent developments in GEANT4. Nucl. Instrum. Meth. Phys. Res. 835, 186–225.

Aso, T., Kimura, A., Yamashita, T., Sasaki, T., 2007. Optimization of patient geometry based on CT data in GEANT4 for medical application. Nuclear Science Symposium Conference Record, NSS'07. IEEE ASME J. Microelectromech. Syst. 4.

Boone, M., Dewanckele, J., Boone, M., Cnudde, V., Silversmit, G., Van Ranst, E., Jacobs, P., Vincze, L., Van Hoorebeke, L., 2011. Three-dimensional phase separation and identification in granite. Geosphere 7, 79–86.

Brennan, B.J., Prestwich, W.V., Rink, W.J., Marsh, R.E., Schwarcz, H.P., 2000. Alpha and Beta dose gradients in tooth enamel. Radiat. Meas. 32, 759–765.

Clark-Balzan, L., Schwenninger, J.L., 2012. First steps toward spatially resolved OSL dating with electron multiplying charge-coupled devices (EMCCDs): system design and image analysis. Radiat. Meas. 47, 797–802.

Cnudde, V., Boone, M.N., 2013. High-resolution X-ray computed tomography in geosciences: a review of the current technology and applications. Earth Sci. Rev. 123, 1–17.

Cunningham, A.C., DeVries, D.J., Schaart, D.R., 2012. Experiment and computational simulation of beta-dose heterogeneity in sediment. Radiat. Meas. 47, 1060–1067.

Degallaix, S., Ilschner, B., 2007. Caractérisation expérimentale des matériaux I (TM volume 2), chapter 3. Presses Polytechniques et Universitaires Romandes 9782880745677.

Donev, A., Stillinger, F.H., Torquato, S., 2005. Neighbor list collision-driven molecular dynamics simulation for nonspherical particles. I. Algorithmic details II. Applications to ellipses and ellipsoids. J. Comput. Phys. 202 (2) 737–764 (part I) and 765-793 (part II).

Duller, G.A.T., Bøtter-Jensen, L., Murray, A.S., Truscott, A.J., 1999. Single grain laser luminescence (SGLL) measurements using a novel automated reader. Nucl. Instrum. Meth. B 155, 506–514.

Fain, J., Soumana, S., Montret, M., Miallier, D., Pilleyre, T., Sanzelle, S., 1999. Luminescence and ESR dating Beta-dose attenuation for various grain shapes calculated by Monte-Carlo method. Quat. Geochronol. 18, 231–234.

Fang, F., Martin, L., Williams, I., Brink, F., Mercier, N., Grün, R., 2018. 2D Modelling: a Monte Carlo Approach for Assessing Heterogeneous Beta Dose Rate in Luminescence and ESR Dating, II: Application to Igneous Rocks. (In preparation).

Fleming, S.J., 1973. Thermoluminescence dating: refinement of the quartz inclusion method. Archaeometry 12, 133–147.

Guérin, G., 2011. Modélisation et simulations numériques des effets dosimétriques dans les sédiments quaternaires: application aux méthodes de datation par luminescence. Thèse de doctorat en Physique des archéomatériaux, Bordeaux, université Michel de Montaigne Bordeaux. vol. 3 242p.

Guérin, G., Mercier, N., 2012. Preliminary insight into dose deposition processes in sedimentary media on a scale of single grains: Monte Carlo modelling of the effect of water on the gamma dose rate. Radiat. Meas. 47 (7), 541–547.

Guérin, G., Mercier, N., Adamiec, G., 2011. Dose-rate conversion factors: update. Ancient TL 29, 5–8.

Guérin, G., Mercier, N., Nathan, R., Adamiec, G., Lefrais, Y., 2012a. On the use of the infinite matrix assumption and associated concepts: a critical review. Radiat. Meas. 47, 778–785.

Guérin, G., Discamps, E., Lahaye, C., Mercier, N., Guibert, P., Turq, A., Dibble, H.L., McPherron, S.P., Sandgathe, D., Goldberg, P., Jain, M., Thomsen, K., Patou-Mathis, M., Castel, J.-C., Soulier, M.-C., 2012b. Multi-method (TL and OSL), multi-material (quartz and flint) dating of the Mousterian site of Roc de Marsal (Dordogne, France): correlating Neanderthal occupations with the climatic variability of MIS 5–3. J. Archaeol. Sci. 39, 3071–3084.

Kaipa, P.L., Haskell, E.H., Kenner, G.H., 1988. Beta dose attenuation and calculations of effective grain size in brick samples. Int. J. Radiat. Appl. Instrum. Nucl. Tracks Radiat. Meas. 14 (1–2), 215–217.

Krbetschek, M.R., Rieser, U., Zöller, L., Heinicke, J., 1994. Radioactive disequilibria in palaeodosimetric dating of sediments. Radiat. Meas. 23, 485–489.

Martin, L., 2015. Caractérisation et modélisation d'objets archéologiques en vue de leur datation par des méthodes paléo-dosimétriques : simulation des paramètres dosimétriques sous Geant4. Doctoral thesis in Physique des archéomatériaux, Bordeaux. université Bordeaux-Montaigne 304p.

Martin, L., Incerti, S., Mercier, N., 2015a. DosiVox: a Geant 4-based software for dosimetry simulations relevant to luminescence and ESR dating techniques. Ancient TL 33–1, 1–10.

Martin, L., Mercier, N., Incerti, S., Lefrais, Y., Pecheyran, C., Guerin, G., Jarry, M., Bruxelles, L., Bon, F., Pallier, C., 2015b. Dosimetric study of sediments at the Beta dose rate scale : characterization and modelization with the DosiVox software. Radiat. Meas. 81, 134–141.

Martin, L., Incerti, S., Mercier, N., 2015c. Comparison of DosiVox simulation results with tabulated data and standard calculations. Ancient TL 33–2, 1–9.

Mayya, Y.S., Morthekai, P., Murari, M.K., Singhvi, A.K., 2006. Towards quantifying beta microdosimetric effects in single-grain quartz dose distribution. Radiat. Meas. 41, 1032–1039.

Mejdahl, V., 1979. Thermoluminescence dating: beta-dose attenuation in quartz grains. Archaeometry 21, 61–72.

Mena, A., Francés, G., Pérez-Arlucea, M., Aguiar, P., Barreiro-Vázquez, J.D., Iglesiasd, A., Andrés Barreiro-Lois, A., 2015. A novel sedimentological method based on CT-scanning: use for tomographic characterization of the Galicia Interior Basin. Sediment. Geol. 321, 123–138.

Morthekai, P., Jain, M., Dartnell, L., Murray, A.S., Bøtter-Jensen, L., Desorgher, L., 2007. Modelling of the dose-rate variations with depth in the martian regolith using GEANT4. Nuclear instruments and methods in Physics research section a: accelerators, spectrometers. Detectors and Associated Equipment 580 (1), 667–670.

Nathan, R.P., 2010. Numerical Modelling of the Environmental Dose Rate for Trapped Charge Dating. Doctoral thesis in Archaeology. University of Oxford, unpublished, St Hugh's College 207p.

Nathan, R.P., Mauz, B., 2008. On the dose-rate estimate of carbonate-rich sediments for trapped charge dating. Radiat. Meas. 43 (1) (January).

Nathan, R.P., Thomas, P.J., Jain, M., Murray, A.S., Rhodes, E.J., 2003. Environmental dose rate heterogeneity of beta radiation and its implications for luminescence dating: Monte Carlo modelling and experimental validation. Radiat. Meas. 37, 305–313.

Plachy, A.L., Sutton, S.R., 1982. Determination of the dose-rate to quartz in granite. PACT 6, 188–194.

Rasband, W.S., 1997 – 2012. ImageJ, U.S. National Institutes of Health, Bethesda, Maryland, USA. imagej.nih.gov/ij/.

Rufer, D., Preusser, F., 2009. Potential of autoradiography to detect spatially resolved radiation patterns in the context of trapped charge dating. Geochronometria 34, 1–13.

Schneider, C.A., Rasband, W.S., Eliceiri, K.W., 2012. NIH Image to ImageJ: 25 years of image analysis. Nat. Methods 671. https://doi.org/10.1038/nmeth.2089.

Simkins, L.M., DeWitt, R., Simms, A.,R., Briggs, S., Shapiro, R.S., 2016. Investigation of optically stimulated luminescence behavior of quartz from crystalline rock surfaces: a look forward. Quat. Geochronol. 36, 161–173.

Underwood, E.E., 1970. Quantitative Stereology. Addison-Wesley 274p. ISBN-13: 978–0201076509.

Urbanova, P., Hourcade, D., Ney, C., Guibert, P., 2015. Sources of uncertainties in OSL dating of archaeological mortars: the case study of the Roman amphitheatre "Palais-Gallien" in Bordeaux. Radiat. Meas. 72, 100–110.

Zimmerman, D.W., 1971. Thermoluminescent dating using fine grains from pottery. Archaeometry 10, 26–28.

Quaternary Geochronology 48 (2018) 195–206

Contents lists available at ScienceDirect

Quaternary Geochronology

journal homepage: www.elsevier.com/locate/quageo

Research paper

2D modelling: A Monte Carlo approach for assessing heterogeneous beta dose rates in luminescence and ESR dating: Paper II, application to igneous rocks

Fang Fang[a,*], Loïc Martin[b], Ian S. Williams[a], Frank Brink[c], Norbert Mercier[b], Rainer Grün[a,d]

[a] Research School of Earth Sciences, The Australian National University, Canberra ACT 2601, Australia
[b] Institut de Recherche sur les Archéomatériaux, UMR 5060 CNRS, Université Bordeaux Montaigne, Centre de Recherche en Physique Appliquée à l'Archéologie (CRP2A), Maison de l'archéologie, PESSAC Cedex, 33607, France
[c] Centre for Advanced Microscopy, The Australian National University, Canberra ACT 2601, Australia
[d] Australian Research Centre for Human Evolution, Griffith University, Nathan QLD 4111, Australia

ARTICLE INFO

Keywords:
Dose rate
Modelling
Thermochronology
Igneous rock
Mineral mapping

ABSTRACT

Accurate evaluations of beta dose rates are crucial in luminescence and electron spin resonance (ESR) thermochronology. Most igneous rocks are heterogeneous and have complex mineralogical structures that render them unsuitable for the conventional methods of beta dose rate calculations based on infinite matrix assumptions. The recently developed software DosiVox-2D provides a Monte-Carlo approach for calculating beta dose rates in realistic heterogeneous geometries. In this paper, we present 2D simulations of uniform and layered igneous rocks. For the modelling, mineral distribution maps were obtained by QEM-EDS (quantitative evaluation of minerals using energy dispersive spectroscopy) and radionuclide concentrations in minerals were determined by laser ablation (LA) ICP-MS. The results show that the skewness of beta dose rate distributions in quartz reduces as the K concentration in a rock increases, and the estimation of the beta dose rate can be critically influenced by the U and Th concentrations and distributions.

1. Introduction

Age estimates in luminescence and ESR dating are derived from dividing the accumulated dose (D_e) by the dose rate ($\dot{D}$). The methods used to evaluate D_e have significantly increased in reliability and accuracy in recent years (e.g., Murray and Wintle, 2000; Schellmann and Radtke, 2001; Duval, 2012; Tissoux et al., 2012; Voinchet et al., 2015), but the approach to calculating $\dot{D}$ has barely changed.

The total dose rate is the combined contribution from alpha and beta particles, gamma and cosmic rays. The beta dose rate in rocks is its major component (60–70%), but an accurate estimation is difficult because *in situ* measurements are challenging. The commonly applied method for calculating beta dose rates is based on infinite matrix assumptions (Mejdahl, 1979) and measurements of the radionuclide concentrations or beta activity in bulk samples (Aitken, 1985). In reality, however, many samples exhibit complex microdosimetries. Several attempts have been made to address this issue in the dating of sediments by applying numerical modelling. The influences of mineral shape (Fain et al., 1999), grain size (Guérin et al., 2015; Nathan et al., 2003) and radioelement distribution (Chauhan and Singhvi, 2011; Cunningham et al., 2012; Mayya et al., 2006) on the beta dose rate have been investigated. The modelling and corresponding experimental results have shown that the validity of the infinite matrix assumption is limited to specific cases. Nevertheless, using the arithmetic means of D_e and $\dot{D}$ estimations has still been suggested as the optimal method for calculating single-grain ages in the absence of direct measurements of the dose rate distributions (Guérin et al., 2015). The development of DosiVox software (Martin et al., 2015) allows dose rate modelling by uploading realistic 3D geometries, which has shed new light on accurate beta dose rate calculations for heterogeneous environments.

With the recent development of luminescence and ESR thermochronology, rocks are analysed for investigating the timing and rate of earth-surface processes (Grün et al., 1999; Herman et al., 2010; King et al., 2016). Most rocks are heterogeneous and have complex mineralogical structures, which has raised an urgent issue of making realistic beta dose estimations. The ideal solution is to apply 3D simulations. However, 3D images of rock are difficult to obtain by X-ray CT (computed tomography) scanning because quartz and plagioclase are almost inseparable due to their closely similar X-ray attenuation coefficients

* Corresponding author.
E-mail address: fang.fang@anu.edu.au (F. Fang).

https://doi.org/10.1016/j.quageo.2018.07.005
Received 26 September 2017; Received in revised form 9 July 2018; Accepted 18 July 2018
Available online 21 July 2018
1871-1014/

(Boone et al., 2011; Ketcham, 2005). Quartz and plagioclase can easily be distinguished, however, by 2D X-ray mapping techniques (e.g., SEM - scanning electron microscope, QEM-EDS - quantitative evaluation of minerals using energy dispersive spectroscopy, or EMP - electron microprobe), showing the potential of estimating dose rates by 2D simulations.

A critical issue for the reconstruction of 3D geometries from 2D simulations is representativeness. The pioneering work of Plachy and Sutton (1982) on estimating dose rates in granites showed that a 2D model can represent a 3D simulation when the mineral distributions in 2D slices are isotropic. Based on this hypothesis, DosiVox-2D was developed for beta dose rate evaluations of samples with regular mineral distribution patterns (Martin et al., 2018). DosiVox-2D is a Geant4-based model which simulates particle-matter interactions using a Monte-Carlo approach and calculates the paths and interactions of each particle and secondary particles according to interaction probabilities. The 2D geometry can be defined manually or directly using an image with separated mineral phases. Each voxel is associated with a material and its property (i.e., chemical composition, density, water content, and radioactivity). The dose deposited during the particle interactions is recorded in each voxel, and the simulation results are displayed as the averaged beta dose rate of each mineral, a dose rate distribution map and a dose-frequency histogram.

This study explores the feasibility of applying DosiVox-2D to beta dose rate calculations of heterogeneous rocks and provides several examples as the basis for further investigations. The paper will discuss: (1) the feasibility and limitation of QEM-EDS for mineral mapping; (2) the applicability of using a single set of averaged radionuclide concentrations for a given mineral type; (3) the influence of radionuclide concentrations on averaged beta dose rates and dose rate distributions and (4) the calculation of uncertainty in the simulations.

2. Samples and methodology

2.1. Sample preparation

Three samples were selected for this study (Fig. 1). BB86 is a sample of the medium-grained, texturally isotropic, Tara Granodiorite from the Berridale Batholith, southeastern Australia. The minerals, including the grains of zircon, are evenly distributed in the sample (Williams et al., 1975). Slices were cut from three different faces of a cube of the rock (BB86-1: 51.5 × 58.5 mm, BB86-2: 23 × 22 mm, BB86-3: 25 × 23 mm), each sharing a vertex (Fig. 1a). HIM59 is coarse-grained migmatite from the Kullu valley, northwestern Indian Himalaya (Fig. 1b). HIM59-1 (24 × 25 mm) was cut from its leucosome (light-colored band of crystallised partial melt). HIM31 is finely-layered migmatite also from the Kullu valley. Four slices were prepared (Fig. 1c): HIM31-1 (57 × 46 mm) and HIM31-2 (20 × 20 mm) were vertical to lineation and foliation, HIM31-3 (20 × 20 mm) was vertical to foliation but parallel to lineation, and HIM31-4 (19 × 20 mm) was parallel to foliation. The last three slices shared a vertex.

The BB86-1 and HIM31-1 slices were each 4 mm thick. The other slices were mounted onto glass slides and reduced to a thickness of 1 mm. All surfaces were polished with 3 µm and 1 µm diamond paste, and carbon coated for QEM-EDS analysis.

2.2. 2D mineral mapping

The mineral maps in this study were collected using the FEI Quanta QEMSCAN® system at the Centre for Advanced Microscopy at the Australian National University (ANU). Data were collected in field image scan mode with 15 kV accelerating voltage, 10 nA probe current, a resolution of 30 µm for the three HIM31 slices (HIM31-3, HIM31-4,

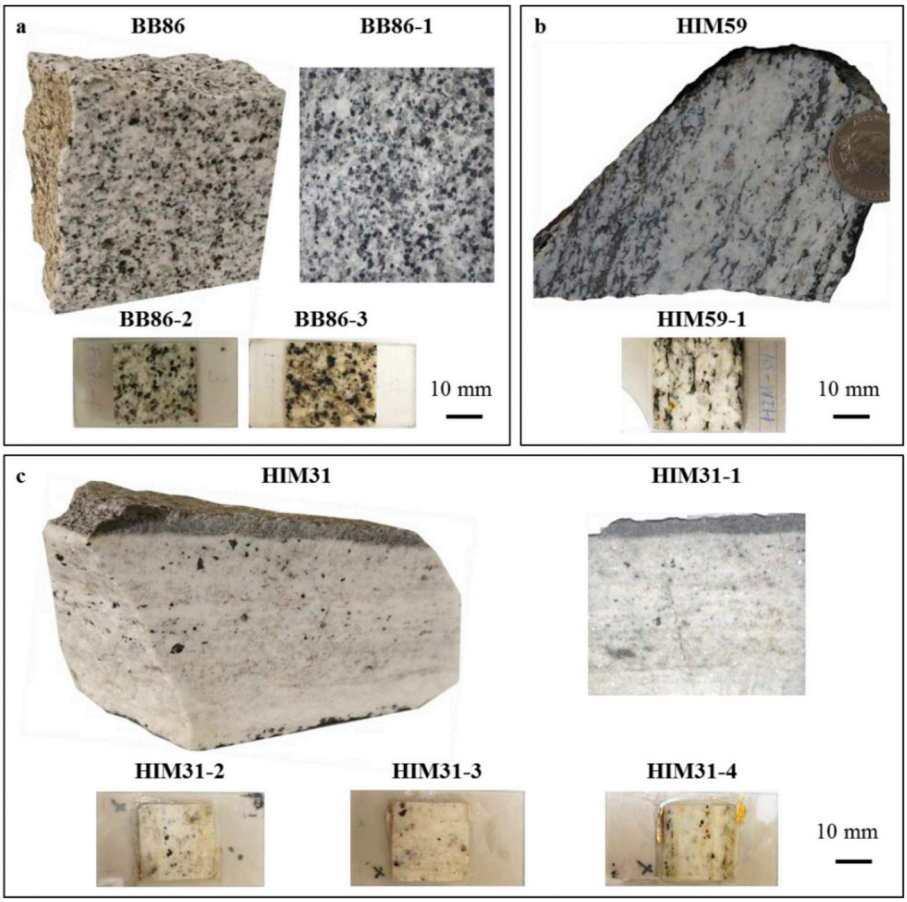

Fig. 1. Samples and corresponding slices for analysis. (a) Three slices cut from BB86 were vertical to each other and share a vertex. (b) HIM59-1 was selected from the leucosome section of the specimen. (c) HIM31-1 contained the whole mineral information vertical to foliation. The other three slices were made from a 20 mm cube from the middle section of the specimen.

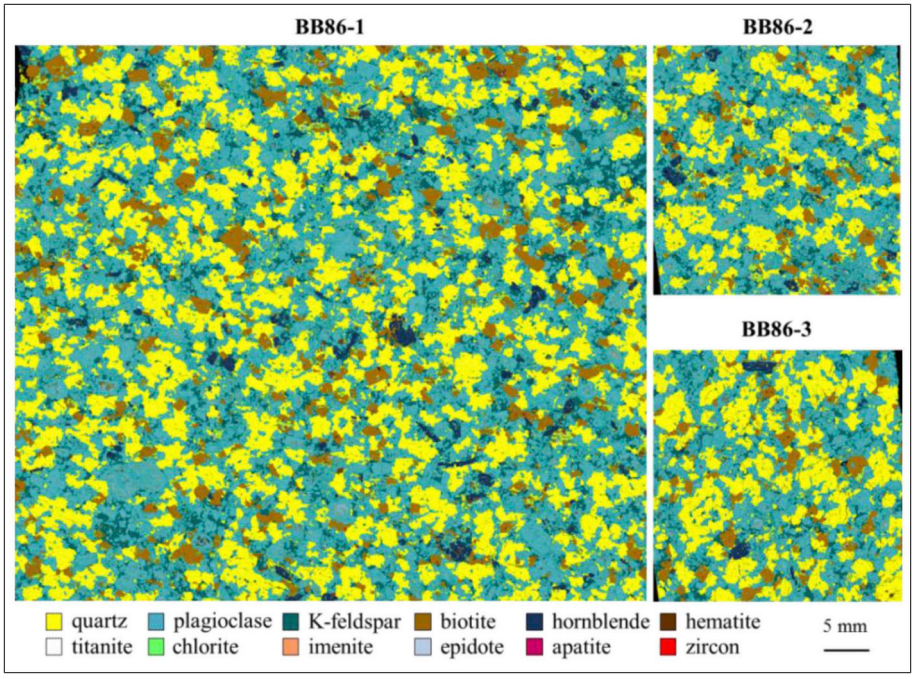

Fig. 2. The QEM-EDS images of three slices from BB86.

HIM31-5) and a resolution of 15 μm for the other samples. The FEI QEMSCAN® is a SEM fitted with multiple light-element energy dispersive (EDS) X-ray spectrometers facilitating a high count rate (400 kcps). A full X-ray spectrum, typically containing 2000–3000 counts, was collected and stored at each point visited during the scan. The back-scattered electron (BSE) signal was used to restrict collection of spectra to specific minerals rather than embedding resin, holes or organic content (Pirrie et al., 2004). The probe depth was 2–3 μm, and the detection limits were 1–2% for most major elements and 3–4% for the rare earth elements (REE).

As the scan deflection during mapping was limited to a field of 1.5 mm or less, each finished QEM-EDS map typically consisted of multiple acquisitions and stage translation. FEI iMeasure® and iDiscover® were used for the acquisition of X-ray spectral map data and subsequent field stitching. The FEI Nanomin® software was used for final mineral identification and the derivation of modal fractions. Nanomin examines the acquired spectrum at each pixel and compares it to a library of known mineral reference spectra held within the Mineral Reference Editor (MRE). Minerals, which form part of a solid solution series (i.e., plagioclase, garnet and chlorite), were successfully classified over a wide compositional range by searching for a best fit using a suitable combination of appropriate end member mineral reference spectra. A mineral classification was assigned to a pixel only if a spectral match of better than a pre-set value (85% in this study) was obtained. Undefined minerals were usually at grain boundaries and less than 1% of the total.

2.3. Radioactive element concentrations

The radioactive element concentrations of various minerals were determined *in situ* on polished slices by LA-ICP-MS. The measurements were carried out at the Research School of Earth Sciences (RSES), ANU. Based on the QEM-EDS images, target minerals were chosen and analysed with a laser spot size of 30 μm, and a pulse frequency of 5 Hz. The elemental concentrations were determined relative to the glass standard NIST 610, and normalised to the concentration of one major element (i.e., Ca for apatite, Fe for hematite, Ti for ilmenite and Si for the rest). Due to its small grain size, the U and Th concentrations of the zircon in HIM31 were measured by sensitive high resolution ion microprobe (SHRIMP) at RSES. The U and Th concentrations in zircon grains from HIM59 were measured by two methods: spot analysis by SHRIMP at RSES and single grain solution analysis by a second-generation Varian quadrupole ICP-MS at the School of Earth Sciences, University of Melbourne. The radioelement concentrations in allanite from BB86 were obtained from Gregory et al. (2007), and those of epidote were derived from theoretical calculations as no grain could be analysed (the epidote grains were small and intergrown with plagioclase). The U and Th concentrations of epidote were estimated by extracting the corresponding element concentrations of other minerals from bulk rock compositions measured by X-ray fluorescence spectrometer (Chappell et al., 1991) and weighted by their densities.

2.4. Modelling

This paper accompanies that of Martin et al. (2018), which covers all computational aspects of DosiVox-2D. Hence the theory behind the computations is not repeated here.

The geometries in the present study were constructed by uploading the 2D grey-scale mineral images provided by QEM-EDS. Each mineral phase corresponds to a user-defined grey value, and thus each voxel is linked to a mineral phase and its radioactivity. Simulation of beta particles was carried out for spectra of ^{40}K, U- and Th-series, assuming the radioactive decay chain to be in secular equilibrium. The radioactive decay data were derived from Guérin (2011). For a sample with size 20 × 20 mm, the paths of 10^8 beta particles were calculated, and the emitted particle number increased with sample size to control the stochastic uncertainty. A voxelised detector was used for recording the presence of particles and subsequently the emitted energy and deposited dose. To avoid edge effects, the dosimetric data within 3 mm of the edge were not recorded. Detailed data processing and procedures for creating pilot files followed the steps outlined in the DosiVox-2D user guide. The dose was integrated over the voxels of each material, returning as an effective beta dose rate given in Gy/ka using the conversion factors of Guérin et al. (2011). For simulation results, the average beta dose rate was calculated for each mineral phase. The dose rate distribution of each mineral was illustrated by a dose rate

Table 1
The mineral composition and relative abundance (area%) of BB86, HIM31 and HIM59.

Mineral	BB86-1	BB86-2	BB86-3	HIM31-1	HIM31-2	HIM31-3	HIM31-4	HIM59-1
Quartz	31.82	27.75	37.56	30.47	28.49	25.99	32.61	28.14
K-feldspar	8.91	9.29	7.37	29.87	40.37	37.47	0.06	12.68
Plagioclase	44.68	49.16	42.55	35.27	28.29	34.58	64.58	51.75
Biotite	8.57	7.63	8.55	1.37	0.24	0.19	0.27	5.86
Chlorite	1.72	1.98	1.21	0.62	0.08	0.07	0.08	0.13
Zircon	0.01	0.01	0.01	< 0.01	< 0.01	< 0.01	0.02	0.01
Apatite	0.17	0.19	0.16	0.41	0.34	0.13	0.33	0.07
Epidote	0.93	1.14	0.89					0.25
Hematite	0.34	0.31	0.21					0.01
Ilmentite	0.01	0.02	0.01					
Hornblende	1.67	1.69	0.99					
Titanite	0.18	0.21	0.11					0.14
Phrrhotite								0.02
Fayalite								0.01
Allanite	< 0.01							
Garnet				0.30	0.61	0.43	1.00	
Tourmaline				0.47	1.29	0.73	1.04	
Unclassified	0.99	0.62	0.38	0.99	0.29	0.41	0.01	0.93

histogram and a dose rate map.

3. Results

3.1. Mineral maps

The maps of BB86 were obtained from three faces of the rock (Fig. 2). The mineral distributions are almost isotropic, except for hornblende. Plagioclase is the dominant mineral, occurring as crystals mostly 1–2 mm in length. Some grains are intergrown with epidote. Quartz occurs as anhedral crystals between and including other minerals. K-feldspar is present as small crystals interstitial to plagioclase and quartz. Most biotite is unaltered, but some grains are partly replaced by chlorite and epidote. The euhedral prisms of hornblende are up to about 5 mm in length. The rock also contains accessory apatite, zircon, magnetite, titanite, ilmenite and allanite. The detailed mineral compositions and relative abundances are listed in Table 1. The slight discrepancies between the different slices indicate that the mineralogical distributions are not entirely isotropic in this sample.

The mapping of HIM31-1 shows three layers with very different mineral combinations (Fig. 3a). The top layer is composed of biotite, plagioclase, quartz, chlorite, and accessory apatite and zircon. The leucosome (light mineral band) has two parts. The middle layer is enriched in plagioclase and quartz, while the bottom layer is mainly composed of K-feldspar, plagioclase and quartz. Garnet appears as euhedral crystals mostly in 1–2 mm in length, and only in the mid-bottom layer. Tourmaline is present in the top layer to the mid-bottom layer, occurring as prisms up to 5 mm long. Accessory apatite has a wide range of grain sizes from a few microns to 0.5 mm. Zircon ranges in size up to 250 μm. The distributions of major minerals in each layer have regular patterns, while the distributions of minor and accessory minerals are uneven (Fig. 3b). HIM31-2 and HIM31-3 were cut vertical to

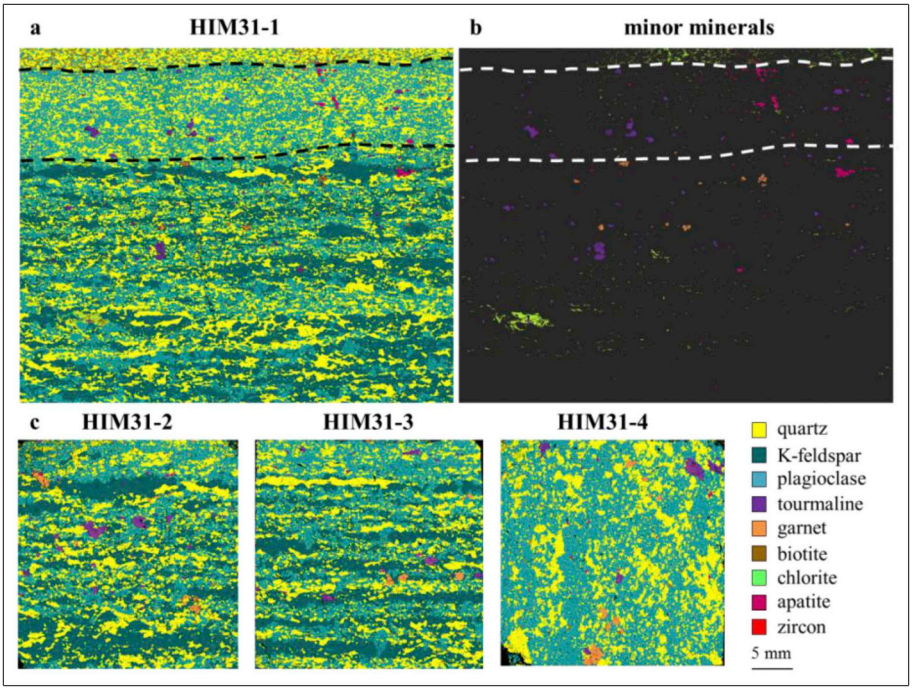

Fig. 3. (a) Mineral mapping of HIM31-1. The three distinctive layers are indicated by the dashed lines. (b) Image of minor and accessory minerals of HIM31-1. (c) Mineral maps of three slices cut from a 20 mm cube.

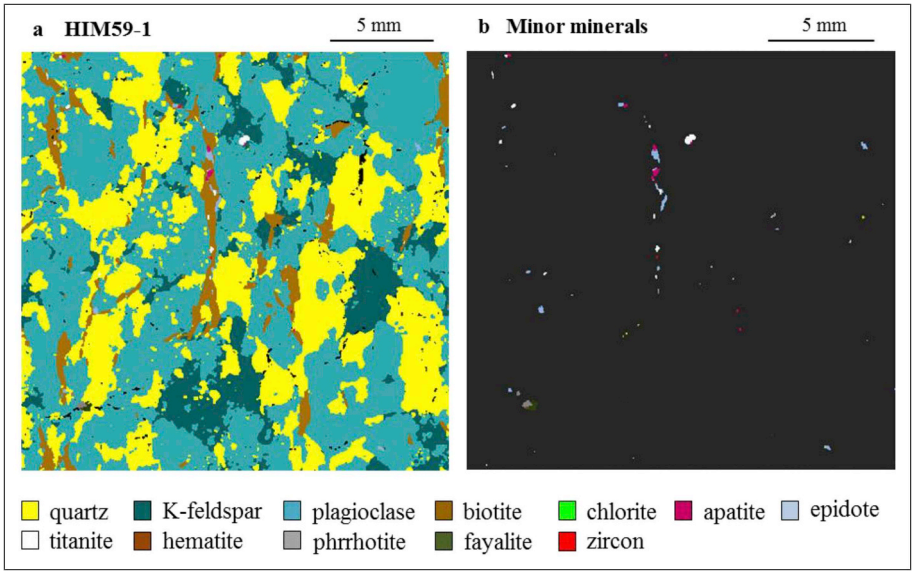

Fig. 4. (a) Mineral map of HIM59-1. (b) The accessory minerals are presented as interstitial or inclusions to biotite.

foliation from the bottom layer, and their mineral compositions are similar to each other. HIM31-4 is parallel to the quartz-plagioclase layer, and its mineral components differ significantly from the other two slices (see Fig. 3c).

HIM59-1 is mainly composed of plagioclase and quartz (Fig. 4). K-feldspar is interstitial and ranges in size from small crystals to large clusters. The distribution of K-feldspar is uneven, while other major minerals are more randomly distributed in this slice. Biotite is altered and partly replaced by chlorite. Most accessory minerals (zircon, apatite, titanite and epidote) occur as inclusions in the mica.

QEM-EDS is an effective method for mineral identification, and has been successfully applied in many geoscience studies (Ayling et al., 2012; Knappett et al., 2011; Meyer et al., 2013; Rollinson et al., 2011). It is not a cure-all remedy, however, and the mineral identification can be wrong. The user needs to have a basic understanding of the mineralogy of the sample. For example, the garnets in HIM31 are wrongly identified as tourmaline, while tourmaline is identified as kaolinite. Even though the data analysis software can provide the best-fit minerals by direct comparison to reference mineral X-ray spectra, which is helpful in identification of unknown minerals, the initial best-fit results may not always be correct. Inspection of the full spectrum can provide clues for a possible mineral type. Another issue in mineral identification is that a small proportion of minerals in the mapped area cannot be classified. This can be due either to a mineral being absent from the MRE or the pixels being located on the boundary between two different mineral grains so that a mixed spectrum is obtained. Even though the unclassified area in mineral map is less than 1% in this study, it may still result in large uncertainties in the assessment of accessory mineral abundances since their abundances are low (< 1%), see Table 1.

3.2. Determination of radionuclide concentrations in minerals

In the 2D dose simulation, a single set of averaged radioelement concentrations is applied based on the assumption that radionuclide concentrations are uniformly distributed within a grain as well as between different grains for a same type of mineral. The average

Table 2
Average K, U and Th concentrations.

Mineral	BB86			HIM31			HIM59		
	U ppm	Th ppm	K %	U ppm	Th ppm	K %	U ppm	Th ppm	K %
Quartz	0.018	0.011	0.005	0.030	0.012	0.005	0.022	0.018	0.013
K-feldspar	0.005	0.012	13.23	0.025	0.024	13.60	0.009	0.008	12.74
Plagioclase	0.045	0.045	0.186	0.060	0.019	0.208	0.008	0.010	0.244
Biotite	0.039	0.035	8.107	0.101	0.029	8.482	0.005	0.006	8.194
Chlorite	0.194	0.361	0.036	0.003	0.004	0.050	0.003	0.004	0.050
Zircon	193.3	84.28	0.002	25000	25.00	0.000	1675	831.6	0.000
Apatite	6.307	12.66	0.053	45.44	8.612	0.005	16.30	10.82	0.003
Epidote	170.0	890.0	0.000				0.777	0.098	0.005
							682.9	370.7	0.005
Hematite	0.010	0.005	0.003				0.363	0.002	0.015
Ilmenite	0.614	0.042	0.007						
Hornblende	0.443	0.546	0.398						
Titanite	15.71	1.523	0.004				50.04	2.473	0.017
Pyrrhotite							0.363	0.002	0.015
Fayalite							0.363	0.002	0.015
Allanite	57.95	8890	0.000						
Garnet				0.237	0.030	0.005			
Tourmaline				0.016	0.018	0.037			

Table 3
The K concentrations (%) of four major minerals (K-feldspar, biotite, hornblende and plagioclase) in three rocks measured by LA-ICP-MS.

Mineral	K-feldspar			Biotite			Plagioclase			Hornblende
Sample	BB86	HIM31	HIM59	BB86	HIM31	HIM59	BB86	HIM31	HIM59	BB86
Grain No.	6	10	7	8	6	8	7	7	10	4
Mean	13.232	13.597	12.735	8.107	8.537	8.194	0.186	0.208	0.244	0.398
SD	0.291	0.530	0.344	0.413	0.120	0.082	0.040	0.053	0.072	0.093

concentrations of K, U and Th are listed in Table 2.

The radionuclide distributions have been investigated in various minerals. For K, it is appropriate to use the averaged concentrations of all minerals based on LA-ICP-MS analyses (Table 3). K-feldspars host significant proportions of the whole rock K contents. K is homogenously distributed within individual grains (Zhao and Li, 2005). The spatially distributed K-feldspar in the three samples yielded a mean value of 13.19 ± 0.43%, which is consistent with other K concentration measurements in the range 10–14% (Prescott and Fox, 1993; Spooner, 1992; Zhao and Li, 2005). Biotite is another major K contributor, and the spatial K distributions of biotite are approximately uniform in three rocks with the mean K concentration of 8.28 ± 0.28%. The mean K concentrations of plagioclase and hornblende are 0.21 ± 0.03% and 0.40 ± 0.09%, respectively. Although the variations between different grains are in the range of 20–30%, their influences on the external beta dose rate are relatively small. The averaged K concentrations in all other minerals are below 0.2% (Table 2).

The concentration and distribution of U and Th are more complex in minerals. It is acceptable to use the averaged values for major minerals and accessory minerals with low U and Th concentrations (< 1 ppm). The concentrations of U and Th in quartz are below 70 and 50 ppb respectively, and those in K-feldspar grains are < 150 ppb. Therefore, their impact on the internal dose rates of quartz and K-feldspar is negligible. For plagioclase and biotite, the results of most spot analyses yielded U and Th concentrations < 80 ppb, but few spots showed higher U and Th concentrations, although still < 1 ppm.

For accessory minerals enriched in U and Th, the complicated distributions of radionuclides can lead to significant uncertainties in using averaged concentrations based on a few spot analyses. HIM59 is taken as an example to show the U and Th distributions in zircon, epidote, apatite and titanite. U-concentrations in zircon can range between ~1 and > 20,000 ppm and Th between ~0.5 and > 5000 ppm (Heaman and Parrish, 1991). Zonation in zircon grains defines the boundaries of distinct closed geochemical systems. The element and isotopic compositions of each system can vary significantly due to the timing and conditions of growth events (Hanchar and Miller, 1993). Cathodoluminescence images of zircon grains from HIM59 showed a range of zonation patterns (Fig. 5). A negative correlation between cathodoluminescence brightness and U concentrations is commonly observed (e.g., Hanchar and Miller, 1993; Poller et al., 2001; Williams et al., 1996), indicating the highly heterogeneous distribution of U in zircon grains. The U concentrations in the different zones range from 2200 to 35,600 ppm in the first grain and 680 to 14,700 ppm in the second. Such variations indicate that a mean value of U concentration is impossible to derive from a few spot analyses. Thus, solution ICP-MS analyses were applied for obtaining radionuclide concentrations from single grains, resulting in U concentrations ranging from 370 to 1980 ppm in 4 grains, and the corresponding Th concentrations from 75 to 1100 ppm.

The epidote group is also composed of minerals with a wide range of U and Th concentrations (i.e., trace to minor amounts; Gieré and Sorensen, 2004). Among them, allanite commonly contains Th between 17,500 and 26,400 ppm and U < 1000 ppm. Similarly, zonation complicates the exact estimation of elemental concentrations in allanite grain using spot analyses. Furthermore, allanite is commonly closely intermixed with epidote-clinozoisite (Gieré and Sorensen, 2004), which can result in widely different U and Th concentrations between different grains. In HIM59, two distinctive sets of U and Th concentrations were identified by LA-ICP-MS analyses (Table 2).

For apatite and titanite, their U and Th concentrations are relatively low compared to zircon and epidotes, but their abundances are usually higher (~0.2%). The LA-ICP-MS spot measurements (n = 8) yielded U concentrations in apatite from 1.67 to 104 ppm and the Th from 0.024 to 50.3 ppm. The averaged U and Th concentrations of titanite are 50 ± 42 and 2.06 ± 0.89 ppm, respectively.

Based on above radioelement data, it is appropriate to use averaged K concentrations for dose rate modelling. However, the U and Th distributions exhibit huge differences within a grain and between different grains for their major contributors. This can be caused by zonation, or mineral mixing due to solid-solution. Thus, a single set of U and Th contents will not give a realistic representation for such minerals. To better quantify the dose rates from U and Th, an alternative solution is

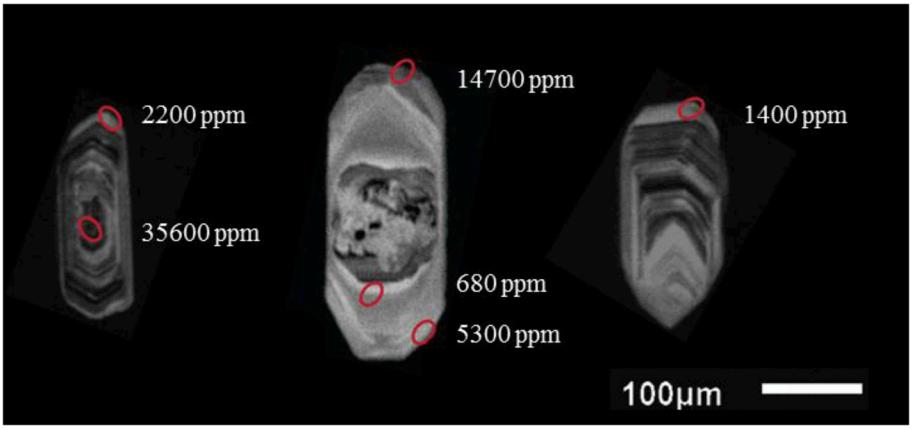

Fig. 5. Cathodoluminescence image of zircons from HIM59. The red circles indicate the spot locations of the SHRIMP analyses and the local U concentrations. (For interpretation of the references to color in this figure legend, the reader is referred to the Web version of this article.)

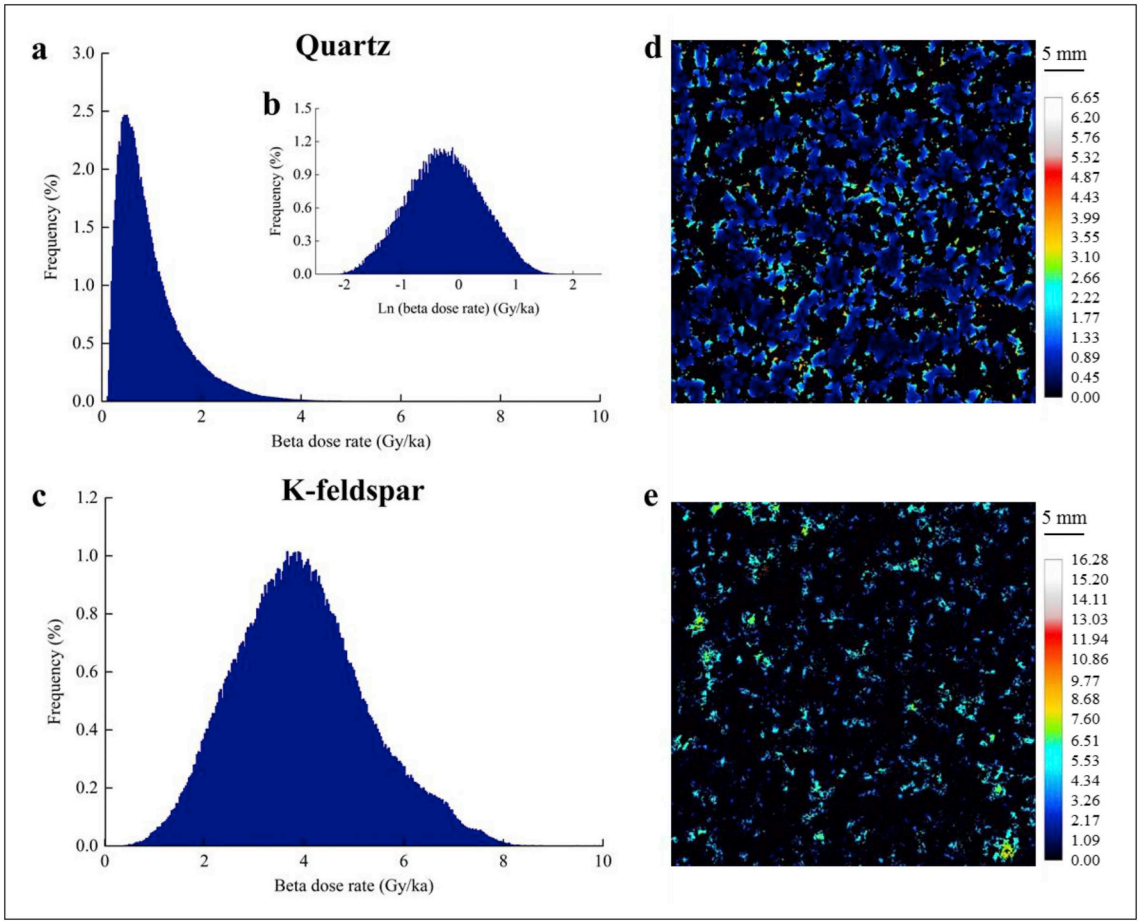

Fig. 6. Beta dose rate histograms of quartz (a, b) and K-feldspar (c). The quartz dose rates have a log-normal distribution, while K-feldspar dose rates approach a normal distribution. (d, e) Beta dose rate distribution map of quartz and K-feldspar. The areas with 0 Gy/ka dose rate are background.

direct uploading of U and Th intensity maps (e.g., fission track method, Selo et al., 2009) into the simulation, and this is planned for a future study.

3.3. Beta dose rate modelling

The most important issue for using 2D modelling is representativeness, which means a selected mapping surface represents the whole sample that was used for the estimation of D_e. In the following section, two situations are presented to illustrate the importance of sample selection. The first example (BB86) is a rock with even texture, which approximately fits the assumption of spatial homogeneity for 2D modelling. Most samples are more complicated, however. The second example (HIM31) is a rock with microstructures having preferred orientations of the minerals. Additionally, simulation of HIM59 is used to investigate the influence of U and Th concentrations on beta dose rates of quartz and K-feldspar.

3.3.1. Uniform granodiorite (BB86)

The beta dose rate distribution maps of quartz and K-feldspar for BB86-1 are shown in Fig. 6. Unlike sediments, in which mineral grains occur singly, the grains are packed together in aggregates. The beta dose rate of quartz aggregates decreases from its edge to centre with randomly distributed radioactive sources. The dose rate shows a positive skewed distribution, which falls sharply at lower doses and has long tails at higher doses. The dose rate distribution of K-feldspar depends on the size of the aggregate and the surrounding radionuclide sources (i.e., abundance and concentration). In BB86, the maximum width of K-feldspar aggregates is less than 2 mm and coupled with external beta emission, the beta dose rate has a normal distribution.

To check the beta dose rate uniformity in this sample, simulations were carried out on three slices from different faces of the rock. The beta dose rates are presented as arithmetic and geometric means (Table 4). The latter is more appropriate for log-normal distributions (see Fig. 6b). The 1-σ uncertainties were determined from the dose rate histogram, indicating the dose rate variations in different voxels. Detailed discussion of the simulation uncertainties follows in section 4.3. The averaged arithmetic and geometric mean dose rates of quartz are 0.96 ± 0.65 and $0.78^{+0.70}_{-0.37}$ Gy/ka. The mean beta dose rate of K-feldspar is four times that of quartz, with an averaged dose rate of 3.78 ± 1.26 Gy/ka. The high dose rate of K-feldspar is partly due to the internal dose contribution, and partly caused by grain aggregation. The dose rate discrepancies between different faces indicate this sample is not exactly isotropic in mineral distribution.

Table 4
The beta dose rates of quartz and K-feldspar in three slices.

Sample	Quartz		K-feldspar
	Mean (Gy/ka)	Geomean (Gy/ka)	Mean (Gy/ka)
BB86-1	0.98 ± 0.67	$0.79^{+0.72}_{-0.38}$	3.97 ± 1.34
BB86-2	1.01 ± 0.64	$0.85^{+0.68}_{-038}$	3.87 ± 1.31
BB86-3	0.89 ± 0.65	$0.70^{+0.70}_{-0.35}$	3.52 ± 1.14
Average	0.96 ± 0.65	$0.78^{+0.70}_{-0.37}$	3.78 ± 1.26

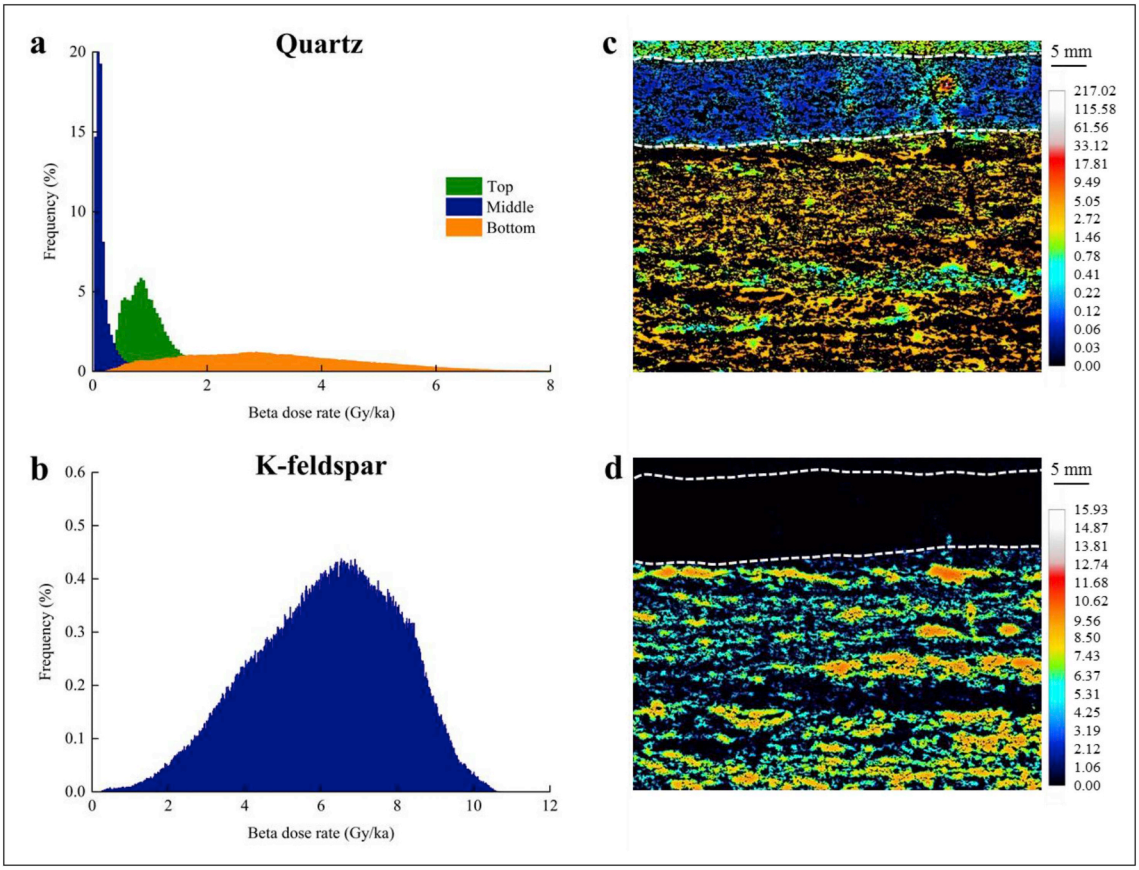

Fig. 7. (a) beta dose rate histograms of quartz are presented in separate layers. (b) The histogram K-feldspar dose rates is negatively skewed. (c, d) Beta dose rate distribution map of quartz and K-feldspar. The three distinctive layers are indicated by the dashed lines, and the areas with 0 Gy/ka dose rate are background.

3.3.2. Layered migmatite (HIM31)

Rocks with uniform mineral distributions are uncommon at most sampling sites, and many rocks are layered. The layering results from foliation and/or lineation. Foliation describes layering caused by shearing forces or differential pressure, while lineation indicates mineral alignment due to deformation and/or recrystallization. Theoretically, a representative plane can be obtained from the face vertical to both foliation and lineation.

The beta dose rate map of HIM31-1 shows three distinctive dose rate values, which correspond to the differences in the mineral composition and distribution pattern of each layer (Fig. 7). The dose rate of quartz approximates an isotropic distribution in a vertical direction, excluding a few dose rate hotspots produced by zircon and apatite. The mean quartz dose rates from top to bottom layer are 0.94 ± 0.35, 0.34 ± 2.22 and 3.19 ± 1.62 Gy/ka, respectively. K-feldspar mainly appears in the bottom layer, and was less influenced by U and Th hotspots. The dose rate distributions in quartz are positively skewed in the three layers with different patterns, and the K-feldspar dose rate distribution is negatively skewed. This indicates that the mineral aggregation pattern is not uniform along the direction of lineation for K-feldspar. To avoid D_e over-dispersion in luminescence dating, we suggest that target dating material is best taken from a single layer, especially for single grain procedures.

The cutting direction is very important for obtaining representative slices of a layered sample (Fig. 8). Three slices were prepared from a cube located in upper bottom part of HIM31. They shared a vertex and were vertical to each other. The beta dose rates of HIM31-2 and HIM31-3 are broadly consistent with each other (see Table 5). The averaged mean dose rates of quartz and K-feldspar are 3.41 ± 1.67 and 6.25 ± 1.96 Gy/ka. The slightly higher variation on K-feldspar dose rate is mainly due to the grain aggregation. HIM31-4 was cut parallel to the layering, and its beta dose rates of quartz and K-feldspar are significantly lower than those of other slices. There is large discrepancy between the arithmetic and geometric mean dose rates of quartz (1.48 ± 6.09 and $0.35^{+1.04}_{-0.26}$ Gy/ka). This is caused by the sparsely distributed zircon, apatite and K-feldspar. But such influence has largely reduced in beta dose rate of K-feldspar, and the arithmetic and geometric mean dose rate of K-feldspar are 1.20 ± 1.93 and $0.86^{+0.77}_{-0.41}$ Gy/ka, respectively.

3.3.3. The influences of mapping size and resolution

For obtaining a representative mineral map, one question is how big should the map be? In luminescence and ESR thermochronology, multi-aliquots are commonly used for D_e determinations. Thus, a sample with a weight of about 500 g (corresponding to a ~60 mm cube) is required for analysis. Ideally, mineral scans should be carried out on the original cube to obtain an accurate estimation of the beta dose rate. However, mineral mapping of such a large size is time consuming. To investigate the influence of reducing map size, uncertainties on beta dose rates of various map sizes (10 × 10 to 30 × 30 mm) were calculated based on the BB86-1 dose map (Fig. 9a).

20 sub-slices were separated for each size. The averaged beta dose rates of quartz and K-feldspar are consistent in all sizes, while the dose rate variations significantly decreased with increasing sample size. As expected, the results indicate that more accurate beta dose rate estimations can either be obtained by increasing the sample size or the number of slices. It should be noted that the minimum size required for 2D modelling is 10 × 10 mm, since the range of the beta particles is ~2 mm and the edge effect in simulations.

Another question in mapping is resolution. To show the impact of reducing resolution, simulations are carried out by decreasing map resolutions from 15 μm to 90 μm with a step size of 15 μm based on a

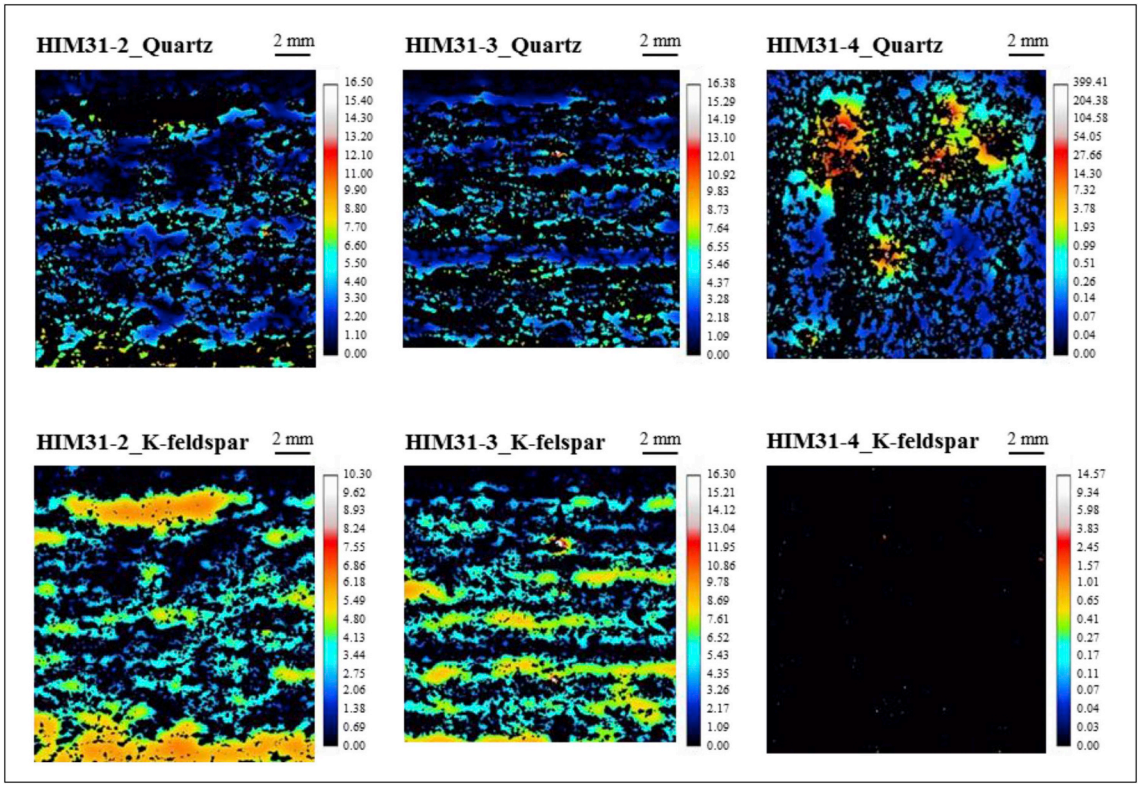

Fig. 8. Beta dose rate maps of quartz and K-feldspar in three faces of HIM31.

Table 5
The beta dose rates of quartz and K-feldspar in three slices of HIM31.

Sample	Quartz		K-feldspar	
	Mean (Gy/ka)	Geomean (Gy/ka)	Mean (Gy/ka)	Geomean (Gy/ka)
HIM31-2	3.39 ± 1.64	$2.93^{+2.41}_{-1.32}$	6.52 ± 2.03	$6.07^{+3.20}_{-2.09}$
HIM31-3	3.43 ± 1.70	$2.95^{+2.41}_{-1.33}$	5.98 ± 1.88	$5.64^{+2.67}_{-1.81}$
Average	3.41 ± 1.67	$2.94^{+2.41}_{-1.33}$	6.25 ± 1.96	$5.86^{+2.94}_{-1.95}$
HIM31-4	1.48 ± 6.09	$0.35^{+1.04}_{-0.26}$	1.20 ± 1.93	$0.86^{+0.77}_{-0.41}$

20 × 20 mm mineral map located in the middle of BB86-1. The image processing was conducted with the ImageJ software, using the bin method of median to keep the original grain shape. When the resolution was decreased from 15 to 30 μm (Fig. 9b), the beta dose rates of quartz and K-feldspar decreased significantly due to the loss of small sized minerals containing high U and Th concentrations (zircon, epidote and apatite). After that, any resolution changes caused only minor changes in the calculated dose rate. The dose rates contributed by ^{40}K changed slightly with reducing resolution, but overall the mapping resolution for this sample has to be 15 μm or better. In general, the resolution is selected based on the size and abundance of the target mineral. This is particularly important for fine-grained, radioactive trace minerals. Higher resolutions are recommended for mineral scans.

3.3.4. Influences of U and Th concentrations

As shown in section 3.2, the U and Th concentrations in zircon and the epidotes showed huge variations between the different grains in HIM59-1. Moreover, the abundance of zircon is only 0.01% and that of the epidotes is 0.25%, which provides an opportunity to investigate the influence of U and Th concentrations and mineral abundance on the beta dose rates.

Four scenarios were simulated with the measured minimum and maximum U and Th concentrations for two minerals. The modelling results are listed in Table 6. With U and Th contents increasing in zircon, the mean beta dose rate of quartz changes only slightly (0.02 Gy/ka) and that of K-feldspar is almost unchanged (0.006 Gy/ka). This results from the extremely low zircon abundance in this sample (0.01%). Nevertheless, a hotspot effect from zircon with high radioelement concentrations cannot be neglected, especially for single grain dating of quartz. For the impact of epidote, the difference of beta dose rate in quartz between two simulations is about 15.4%, mainly due to the increase of U concentrations. For K-feldspar, the dose rate variation remains small, only 1.9%. These results indicate that the influence of U and Th contents on quartz is not negligible when the host mineral is present in a relatively high abundance (here 0.25%).

4. Discussion

4.1. The dose rate distribution with the presence of potassium sources

In well-sorted sediments, the influence of potassium sources, especially K-feldspar, on the beta dose distribution of quartz has been quantitatively investigated (Mayya et al., 2006; Cunningham et al., 2012; Guérin et al., 2015). Unlike sediments, the mineral grains in rocks are commonly packed together in aggregates. Thus, the dose rate distribution can be influenced by aggregate size and potassium content.

With increasing quartz aggregate size and/or decreasing the number of K-rich grains, the skewness and dispersion of quartz dose rate distributions increase. This can be understood by considering that the average distance between a high beta emitting source and the dosimeter grains is increased. As the number of feldspar or mica grains is reduced, fewer quartz grains are close to K sources. On the other hand, with K-feldspar aggregate size increasing and/or the number of K-rich grains increasing, the skewness of dose rate distributions in K-feldspars may decrease and the dispersion may increase.

The heterogeneous distributions of radionuclides raise the important question about age calculation. In single grain dating, several

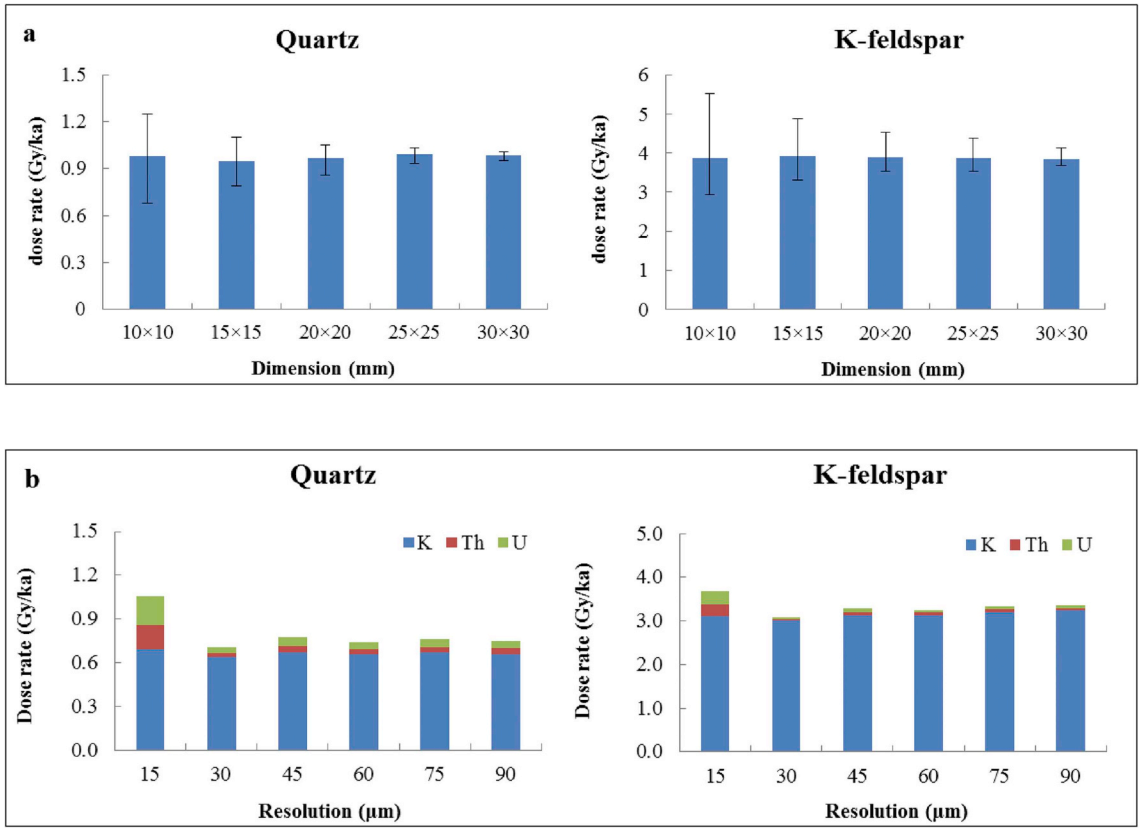

Fig. 9. (a) The uncertainties of beta dose rate in calculations with sample size decreasing from 30 × 30 to 10 × 10 mm. The positive and negative errors indicate the maximum and minimum beta dose rates in their corresponding sample sizes. (b) The beta dose rates of quartz and K-feldspar with decreasing spatial resolution from 15 to 90 μm.

age models (e.g., CAM, MAM, FMM) were developed for obtaining representative D_e values. Among them, the log-normal models offer a good representation of D_e distribution in natural samples, since the log-normal distributions describe both the natural dispersion arising from dose rates and the dispersion induced during measurements. Due to the limitations of direct measurements on single-grain dose rate distributions, Guérin et al. (2015) suggested that the age would be best calculated considering the arithmetic mean D_e and $\dot{D}$. In this study, we have presented the potential of DosiVox-2D in direct measurements, and thus the age would be determined by geometric mean dose rate with a log-normal age model in future studies. When using multi-grain analysis, the D_e value is determined by the unweighted arithmetic mean, and thus it is more appropriate to use the arithmetic mean dose rates for age calculations. Overall, equivalent dose derived from measured D_e distributions using any age model should be as close as possible to the average of the underlying dose rate distribution. Otherwise the age could either be over- or underestimated.

4.2. The influence of U and Th concentrations on beta dose rate

In sediments, the spatial distributions of U and Th are generally considered uniform and their influence on beta dose rate has not been systematically investigated. However, uniform concentration assumptions do not apply to rocks.

The distributions of U and Th are usually uneven, especially shown in U- and Th- enriched minerals. The heterogeneity is presented in three aspects: (1) concentration variations within a grain; (2) differences between grains; (3) uneven mineral spatial distribution. When the abundance of minerals is very low (e.g., zircon in HIM59), it may result in dose saturation on the nearby quartz and K-feldspar grains. But its influence is limited to the beta particle range and may be insignificant to mean beta dose rate, particularly for K-feldspar. On the other hand, at higher abundance, the hotspot effect will abate due to increasing overlap of the localized radiation fields. But the uncertainties on the beta dose rates received by quartz and K-feldspar may enlarge due to

Table 6
The beta dose rate of quartz and K-feldspar with different U and Th contents in host mineral.

Scenario	Zircon/Epidote		Quartz			K-feldspar		
	U (ppm)	Th (ppm)	$\dot{D}_\beta$ (Gy/ka)	$U/\dot{D}_\beta$ (%)[a]	$Th/\dot{D}_\beta$ (%)[b]	$\dot{D}_\beta$ (Gy/ka)	$U/\dot{D}_\beta$ (%)	$Th/\dot{D}_\beta$ (%)
Zircon-min	370.9	75.79	0.970	1.423	0.076	5.857	0.315	0.010
Zircon-max	1982	1106	0.990	3.258	0.281	5.863	0.408	0.020
Epidote-min	0.777	0.098	0.986	2.915	0.227	5.862	0.390	0.018
Epidote-max	682.9	370.7	1.165	15.98	1.452	5.972	2.285	0.193

[a] The U contribution to the total beta dose rate.
[b] The Th contribution to the total beta dose rate.

the inhomogeneous distributions of U and Th in the mineral.

In this study, the simulation results have raised a critical issue about the non-negligible influence of minerals with high U and Th concentrations on beta dose rate calculations. However, the impact of zonation and varied U and Th concentrations in different grains could not be addressed in this study. In the future, these scenarios need to be systematically examined, and the quantification of their impact on beta dose rate should first be carried out on simulations under controlled conditions.

4.3. Error calculation in dose rate simulation

The mean values and standard deviations in the results section were calculated from the beta dose rate histograms based on each voxel in a certain mineral. In D_e estimations, however, minerals of specific grain sizes are used for analysis, and dose rate dispersions for such grains need to be calculated. For example, usually quartz grains of the size fraction of 150–250 μm are used for D_e estimations. When rocks are crushed, grains of such size fractions may originate from aggregates of smaller grains or bigger grains. To get a better handle on the calculation of the average beta dose rate, areas where one dimension is smaller than < 150 μm can be excluded. For single grain analyses in luminescence thermochronometry, it will be important to simulate the dose rate distributions for randomly selected 150–250 μm areas. For ESR analysis, where typically > 100 mg aliquots are used, containing several thousands of grains, it is only relevant how well the mean dose value can be estimated. The random uncertainty of the mean dose rate will be very small as the standard deviation of the mean is divided by the square root of the number of measurements (grains).

5. Conclusion

DosiVox-2D enables direct measurements of beta dose rate distributions in heterogeneous rocks. The reliability of the results depends on the accuracy of the uploaded mineral map and radioactive element concentrations. This study assessed the procedure of using DosiVox-2D for beta dose rate calculations. To apply this method in routine dose rate estimations, several issues need to be addressed in future studies: (1) quantify the influence of U and Th enriched minerals by modelling, including the effects of their abundance, radionuclide concentrations and spatial distributions; (2) develop methods for the calculation of the mean dose rate and appropriate uncertainties for the grain size used for luminescence and ESR analyses; (3) verify the use of arithmetic vs geometric mean dose rates in the age calculations for rocks, including luminescence analysis using single grains and ESR dating by multiple aliquots.

Acknowledgement

This work was funded by an ANU-CSC Scholarship to FF, and carried out as part of a PhD project supervised by Dr Marnie Forster. FF thanks Dr Forster, Prof. Gordon Lister and members of the RSES Structure and Tectonic team for providing some samples, U-Th analyses and assistance. The authors thank Mr. Shane Paxton for sample preparation and Mr. Leslie Kinsley for his help in LA-ICP-MS analysis. The authors are grateful to two anonymous reviewers for their constructive comments.

References

Aitken, M.J., 1985. Thermoluminescence Dating. Academic press.
Ayling, B., Rose, P., Petty, S., Zemach, E., Drakos, P., 2012. QEMSCAN® (quantitative evaluation of minerals by scanning electron microscopy): capability and application to fracture characterization in geothermal systems. In: Proceedings of the Thirty-Seventh Workshop on Geothermal Reservoir Engineering, Stanford University, Stanford, California.
Boone, M., Dewanckele, J., Boone, M., Cnudde, V., Silversmit, G., Van Ranst, E., Jacobs, P., Vincze, L., Van Hoorebeke, L., 2011. Three-dimensional phase separation and identification in granite. Geosphere 7, 79–86.
Chappell, B., White, A., Williams, I., 1991. In: A Transverse Section through Granites of the Lachlan Fold Belt, Australian Bureau of Mineral Resources, Record, pp. 74.
Chauhan, N., Singhvi, A., 2011. Distribution in SAR palaeodoses due to spatial heterogeniety of natural beta dose. Geochronometria 38, 190–198.
Cunningham, A.C., DeVries, D.J., Schaart, D.R., 2012. Experimental and computational simulation of beta-dose heterogeneity in sediment. Radiat. Meas. 47, 1060–1067.
Duval, M., 2012. Dose response curve of the ESR signal of the Aluminum center in quartz grains extracted from sediment. Ancient TL 30, 41–49.
Fain, J., Soumana, S., Montret, M., Miallier, D., Pilleyre, T., Sanzelle, S., 1999. Luminescence and ESR dating Beta-dose attenuation for various grain shapes calculated by a Monte-Carlo method. Quat. Geochronol. 18, 231–234.
Gieré, R., Sorensen, S.S., 2004. Allanite and other REE-rich epidote-group minerals. Rev. Mineral. Geochem. 56, 431–493.
Gregory, C.J., Rubatto, D., Allen, C.M., Williams, I.S., Hermann, J., Ireland, T., 2007. Allanite micro-geochronology: a LA-ICP-MS and SHRIMP U-Th-Pb study. Chem. Geol. 245, 162–182.
Grün, R., Tani, A., Gurbanov, A., Koshchug, D., Williams, I., Braun, J., 1999. A new method for the estimation of cooling and denudation rates using paramagnetic centers in quartz: a case study on the Eldzhurtinskiy Granite, Caucasus. J. Geophys. Res.: Solid Earth 104, 17531–17549.
Guérin, G., 2011. Modélisation et simulations numériques des effets dosimétriques dans les sédiments quaternaires: application aux méthodes de datation par luminescence, Physique des archéomatériaux. Université Michel de Montaigne Bordeaux3, Bordeaux, pp. 242.
Guérin, G., Jain, M., Thomsen, K.J., Murray, A.S., Mercier, N., 2015. Modelling dose rate to single grains of quartz in well-sorted sand samples: the dispersion arising from the presence of potassium feldspars and implications for single grain OSL dating. Quat. Geochronol. 27, 52–65.
Guérin, G., Mercier, N., Adamiec, G., 2011. Dose-rate conversion factors: update. Ancient TL 29, 5–8.
Hanchar, J., Miller, C., 1993. Zircon zonation patterns as revealed by cathodoluminescence and backscattered electron images: implications for interpretation of complex crustal histories. Chem. Geol. 110, 1–13.
Heaman, L., Parrish, R., 1991. U-Pb geochronology of accessory minerals: mineralogical Association of Canada. Short Course Handb. 9, 59–102.
Herman, F., Rhodes, E.J., Braun, J., Heiniger, L., 2010. Uniform erosion rates and relief amplitude during glacial cycles in the Southern Alps of New Zealand, as revealed from OSL-thermochronology. Earth Planet Sci. Lett. 297, 183–189.
Ketcham, R.A., 2005. Computational methods for quantitative analysis of three-dimensional features in geological specimens. Geosphere 1, 32–41.
King, G.E., Herman, F., Guralnik, B., 2016. Northward migration of the eastern Himalayan syntaxis revealed by OSL thermochronometry. Science 353, 800–804.
Knappett, C., Pirrie, D., Power, M., Nikolakopoulou, I., Hilditch, J., Rollinson, G.,, 2011. Mineralogical analysis and provenancing of ancient ceramics using automated SEM-EDS analysis (QEMSCAN®): a pilot study on LB I pottery from Akrotiri, Thera. J. Archaeol. Sci. 38, 219–232.
Martin, L., Fang, F., Mercier, N., Incerti, S., Grün, R., Lefrais, Y., October 2018. 2D modelling: A Monte Carlo approach for assessing heterogeneous beta dose rate in luminescence and ESR dating: Paper I, theory and verification. Quat. Geochronol. 48, 25–37.
Martin, L., Incerti, S., Mercier, N., 2015. DosiVox: implementing Geant 4-based software for dosimetry simulations relevant to luminescence and ESR dating techniques. Ancient TL 33, 1–10.
Mayya, Y., Morthekai, P., Murari, M.K., Singhvi, A., 2006. Towards quantifying beta microdosimetric effects in single-grain quartz dose distribution. Radiat. Meas. 41, 1032–1039.
Mejdahl, V., 1979. Thermoluminescence dating: beta-dose attenuation in quartz grains. Archaeometry 21, 61–72.
Meyer, M.C., Austin, P., Tropper, P., 2013. Quantitative evaluation of mineral grains using automated SEM-EDS analysis and its application potential in optically stimulated luminescence dating. Radiat. Meas. 58, 1–11.
Murray, A.S., Wintle, A.G., 2000. Luminescence dating of quartz using an improved single-aliquot regenerative-dose protocol. Radiat. Meas. 32, 57–73.
Nathan, R., Thomas, P., Jain, M., Murray, A., Rhodes, E., 2003. Environmental dose rate

heterogeneity of beta radiation and its implications for luminescence dating: Monte Carlo modelling and experimental validation. Radiat. Meas. 37, 305–313.
Pirrie, D., Butcher, A.R., Power, M.R., Gottlieb, P., Miller, G.L., 2004. Rapid quantitative mineral and phase analysis using automated scanning electron microscopy (QemSCAN); potential applications in forensic geoscience. Geol. Soc., Lond. Spec. Publ. 232, 123–136.
Plachy, A., Sutton, S., 1982. Determination of the dose-rate to quartz in granite. PACT 188–194.
Poller, U., Huth, J., Hoppe, P., Williams, I.S., 2001. REE, U, Th, and Hf distribution in zircon from western Carpathian Variscan granitoids: a combined cathodoluminescence and ion microprobe study. Am. J. Sci. 301, 858–867.
Prescott, J.R., Fox, P., 1993. Three-dimensional thermoluminescence spectra of feldspars. J. Phys. Appl. Phys. 26, 2245.
Rollinson, G.K., Andersen, J.C., Stickland, R.J., Boni, M., Fairhurst, R., 2011. Characterisation of non-sulphide zinc deposits using QEMSCAN®. Miner. Eng. 24, 778–787.
Schellmann, G., Radtke, U., 2001. Progress in ESR dating of Pleistocene corals-a new approach for D E determination. Quat. Sci. Rev. 20, 1015–1020.
Selo, M., Valladas, H., Mercier, N., Joron, J., Bassinot, F., Person, A., Nouet, J., 2009. Investigations of uranium distribution in flints. Radiat. Meas. 44, 615–619.
Spooner, N., 1992. Optical dating: preliminary results on the anomalous fading of luminescence from feldspars. Quat. Sci. Rev. 11, 139–145.
Tissoux, H., Voinchet, P., Lacquement, F., Prognon, F., Moreno, D., Falguères, C., Bahain, J.-J., Toyoda, S., 2012. Investigation on non-optically bleachable components of ESR aluminium signal in quartz. Radiat. Meas. 47, 894–899.
Voinchet, P., Toyoda, S., Falgueres, C., Hernandez, M., Tissoux, H., Moreno, D., Bahain, J.-J., 2015. Evaluation of ESR residual dose in quartz modern samples, an investigation on environmental dependence. Quat. Geochronol. 30, 506–512.
Williams, I., Buick, I., Cartwright, I., 1996. An extended episode of early Mesoproterozoic metamorphic fluid flow in the Reynolds Range, central Australia. J. Metamorph. Geol. 14, 29–47.
Williams, I., Compston, W., Chappell, B., Shirahase, T., 1975. Rubidium-strontium age determinations on micas from a geologically controlled, composite batholith. J. Geol. Soc. Aust. 22, 497–505.
Zhao, H., Li, S.-H., 2005. Internal dose rate to K-feldspar grains from radioactive elements other than potassium. Radiat. Meas. 40, 84–93.

5 ESR thermochronometric evidence for accelerated Mid-Pleistocene exhumation of the Namche Barwa massif, eastern Himalayan syntaxis

This chapter is in preparation for submitting to Geology: Fang, F., Grün, R. ESR thermochronometric evidence for accelerated Mid-Pleistocene exhumation of the Namche Barwa massif, eastern Himalayan syntaxis, Geology.

The authors' contributions to the publication are: Fang F. has conducted the ESR analyses, evaluated the data and wrote the article. Grün R. provided suggestions on the experiment and data analysis, and corrected the manuscript.

Abstract

The eastern Himalayan syntaxis at the collision boundary between the Indian and Asian plates is characterised by a clockwise structural deflection, active tectonism and intense surface processes. Rapid exhumation rates of ~ 10 mm/a within the past 1 Ma have been reported in the Namche Barwa massif, the northern third of the syntaxis, and in the adjacent Lhasa block to the north. The thermal history of the south side of the syntaxis is less well known. The first electron spin resonance (ESR) dating of quartz from a vertical transect near the southern boundary of the Namche Barwa massif has revealed an acceleration in cooling rate from 88 ± 9 ºC/Ma to 358 ± 30 ºC/Ma between 663 ± 25 ka to 187 ± 6 ka (Ti centre) and 113 ± 15 ºC/Ma to 353 ± 40 ºC/Ma between 389 ± 19 ka to 144 ± 6 ka (Al centre). Depending on the assumed geothermal gradient (50–100 ºC/Ma), this is equivalent to an acceleration in exhumation rate from 1–2 mm/a to 3.5–7 mm/a. Thermochronometric data indicate that the late-stage domal pop-up of the Namche Barwa massif in response to the SW-NE shortening of the crust resulted in the coeval rapid cooling and exhumation extending to the north and south to the massif.

Keywords: ESR of quartz, exhumation, Namche Barwa, ESR thermochronometry

5.1 Introduction

Due to the ongoing orogeny and contemporaneous environmental feedbacks in the region, the eastern Himalayan syntaxis (EHS) at the south-eastern margin of the Tibetan Plateau is a natural laboratory for exploring the relationship between tectonic uplift and denudation (Burg et al., 1998; Finnegan et al., 2008; Wang et al., 2014; Whipple, 2014; Zeitler et al., 2014; King et al., 2016a; Yang et al., 2018). Low-temperature thermochronometry previously applied to bedrocks and detrital minerals (Seward and Burg, 2008; Zeitler et al., 2014; Gong et al., 2015; Bracciali et al., 2016; King et al., 2016a) indicates that the rapid multi-stage exhumation of the syntaxis started in the Late Miocene. The late-stage (< 1 Ma) development of the syntaxis is not fully understood, but rapid exhumation of ~ 10 mm/a has been recorded in the Namche Barwa massif and the region to its north. To the south of the massif, thermochronometric age measurements are sparse because of the complex geological setting and the limitations of thermochronometric methods. Thus, the exhumation history over the last million years remains poorly constrained.

Opinions regarding the driving force (i.e. tectonics or erosion) of the rapid exhumation are divided. Based on the coupling between young ages and highly active surface processes within the Yarlung Tsangpo Grand Canyon (Finnegan et al., 2008), Zeitler et al. (2001, 2014) proposed the crustal aneurysm model, emphasising sustainable positive feedback between erosion and uplift. Wang et al. (2014), on the other hand, demonstrated that the high erosion rates within the Tsangpo Gorge were the result of uplift, showing that the steepening of the gorge began at 2.5–2.0 Ma, long after the rapid exhumation started. Several models have been proposed that highlight the impact of tectonics on the development of the syntaxis (Ratschbacher et al., 1994; Burg et al., 1998; Ding et al., 2001; Yin et al., 2006). Prominent amongst these is the northward expansion model (Seward and Burg, 2008), which posits that crustal shortening and folding have led to lateral expansion of the syntaxis towards the Asian plate, accompanied by vertical growth. This model is supported by thermochronometric data (Seward and Burg, 2008; King et al., 2016a), and the model comparison of Yang et al. (2018). It has also raised a question, however, as to whether the exhumation centre of the syntaxis has migrated at the late-stage in its evolution.

In order to evaluate the timing and rate of the most recent exhumation, electron spin resonance (ESR) thermochronometry has been applied to a vertical transect near the southern boundary of the Namche Barwa massif. ESR thermochronometry has the dating range from 10 ka to 2 Ma (Rink et al., 2007), which constrains the time since quartz grains commenced

trapping charge in appropriate electron traps in response to environmental ionising radiation (mainly *in situ* radioactive decay) once they have cooled through the effective closure temperature range. Specifically, the records of the Al and Ti centres in quartz start at 48-62 ºC and 64-79 ºC respectively, corresponding to cooling rates between 100 and 1000 ºC/Ma (Fang and Grün, in review). The thermochronometric data collected in this study and in other related studies of the eastern Himalayan syntaxis shed new light on the late-stage evolution of the Namche Barwa massif.

5.2 Background

5.2.1 Geological and geomorphological settings

The eastern Himalayan syntaxis is a north-plunging antiform located at the eastern end of the Himalayan orogen (Figure 5.1). It is composed predominantly of high-grade metasediments, part of the Greater Himalayan sequence of the Indian plate, and is separated from the Lhasa block and Gangdese unit of the Asian plate to the west, north and east by a loop of the Yarlung Tsangpo Suture Zone (YTSZ) which contains dismembered ophiolites and mélange. To the north of the YTSZ, a set of steep faults spans ~ 10 km between the syntaxis and the NW-SE striking dextral Jiali fault zone. To the south, the syntaxis is separated from the Tethys sequence of the Indian plate by the South Tibetan Detachment system (STD), and from the Lesser Himalayan sequence by the Main Central Thrust (MCT).

Reconnaissance maps that attempt to interpret the detailed tectonic structure of the region differ significantly (e.g., Burg et al., 1998; Ding et al., 2001; Zhang et al., 2004; Geng et al., 2006; Booth et al., 2009; Xu et al., 2012). Sampling and data interpretation for the present study have been based mainly on the map of Geng et al. (2006), and combined the observations of Ding et al. (2001), Booth et al. (2009) and remote sensing images. The bounding YTSZ is overprinted by two NE-SW oriented structures, the left-lateral Dongjiu-Milin fault zone in the west and the right-lateral Aniqiao-Motuo fault zone in the east. In order from the periphery to core, a ductile detachment zone (DF1) and ductile thrust shear zones (DF2 and DF3) further divide the lithological sequence within the syntaxis into the Zhibai complex (high-pressure granulite bearing gneiss), the Paixiang complex (marble-bearing gneiss) and the Duoxiongla migmatite. The time constraints, however, were poorly reported on the initial and later movements of these shear zones. The E-W trending and N-dipping Nam-La thrust zone is an important tectonic boundary within the syntaxis (Liu

and Zhong 1997), which defines the Namche Barwa massif in its northern zone as a pop-up dome (Ding et al., 2001; Bracciali et al., 2016). This zone extends ~10 km (Geng et al., 2006), and the thrusts change progressively from brittle to ductile towards the south (Zeitler et al., 2014). The Nam-La thrusts became active at no later than 5 Ma. Current observations show they are virtually aseismic (Sol et al., 2007), but Zeitler et al. (2014) suggests that they still remain active in accumulating strain.

The eastern Himalayan syntaxis is characterised by high relief, stream power and precipitation. The Yarlung Tsangpo drops ~ 2000 m in elevation over a river distance of < 100 km (Finnegan et al., 2008). The river flows along the YTSZ before entering the syntaxis near the town of Luxia. Thereafter it turns to the north-east, where it has carved the deepest canyon in the world between the peaks of Namche Barwa and Gyala Peri. The river then turns nearly 180° to the south-east, and again flows along the YTSZ. The glacier equilibrium line was as low as ~ 4000 m during the Quaternary glaciations (Shi et al., 2009; Yao et al., 2010; Yao et al., 2012) and the precipitation reached > 4000 mm/a near the mountain front (Finnegan et al., 2008).

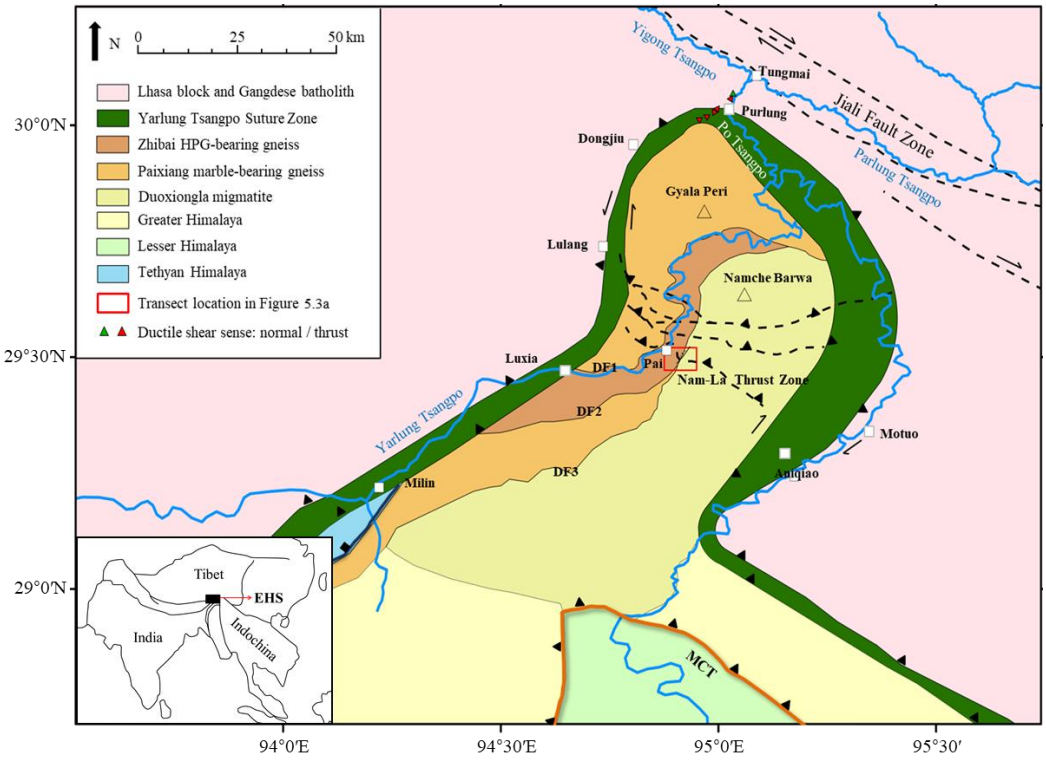

Figure 5.1: The geological map of the eastern Himalayan syntaxis (EHS) and its surrounding area, showing major lithological units, faults, towns, and the transect location (after Geng et al., 2006; Booth et al., 2009; Bracciali et al., 2016). Regional geographic location of the eastern Himalayan syntaxis shown in inset.

5.2.2 Previous thermochronometric constraints

Thermochronometry provides an estimate of the time elapsed since the mineral targeted by a particular thermochronometric technique passed through its distinctive closure temperature (T_c), which is a function of cooling rate. For a cooling rate of 100 ºC/Ma, approximate closure temperatures for the following thermochronometers are: biotite $^{40}Ar/^{39}Ar$ (BAr), 385 ºC; zircon (U-Th)/He (ZHe), 208 ºC; apatite (U-Th)/He (AHe), 82 ºC; apatite fission track (AFT), 137 ºC; feldspar optically simulated luminescence (OSL), 46 ºC (Ehlers et al., 2005; Guralnik et al., 2015a).

Much of the previous thermochronometric studies in the region of the eastern Himalayan syntaxis have been done by the BAr technique (Figure 5.2a; Malloy, 2004; Seward and Burg, 2008; Gong, 2009; Gong et al., 2015). Within the syntaxis the BAr ages are mostly < 5 Ma and show sharp discontinuities at observed fault zones and terrane boundaries. The ages rise abruptly to > 15 Ma outside the syntaxis boundary. Along a transect from Parlung to Tungmai, at increasing distance from the northern boundary of the syntaxis, the BAr ages increase progressively from 1.68 to 15.12 Ma over about 10 km. The youngest results (< 2 Ma) come from the Namche Barwa massif within the syntaxis, increasing progressively southwards to a maximum of 8 Ma. Similarly, most of the ZHe (Figure 5.2b) and AHe (Figure 5.2c) ages inside the syntaxis are < 2 Ma (Zeitler et al., 2014; Yang et al., 2018). Those outside fall into two groups: < 2 Ma to the north and northwest, and > 2 Ma to the east and southwest. The ages decrease northwards towards Parlung, but the trend does not extend beyond the Jiali shear zone.

Eight feldspar OSL ages are available from the area (Figure 5.2d). Five samples have been dated along the Parlung River across the northern end of the rapidly exhuming area, only one of which comes from within the syntaxis (King et al., 2016a). The ages increase from 30 to 150 ka to the NNE, at increasing distance from the northern boundary of the syntaxis, corresponding to a decrease in cooling rates from 1500 to 300 ºC/Ma. These ages, when combined with the other thermochronometric data, indicate that the rate of exhumation of the syntaxis increased significantly within the last 1 Ma. Depending on the initial thermal gradient assumed for the calculation (30 or 100 ºC/km), the mean exhumation rate ranges from 5–9 to 3–4 mm/year since 1 Ma, respectively. Three additional samples from farther south record only minimum ages of 200 ka and maximum cooling rates of 200 ºC/Ma due to signal field saturation.

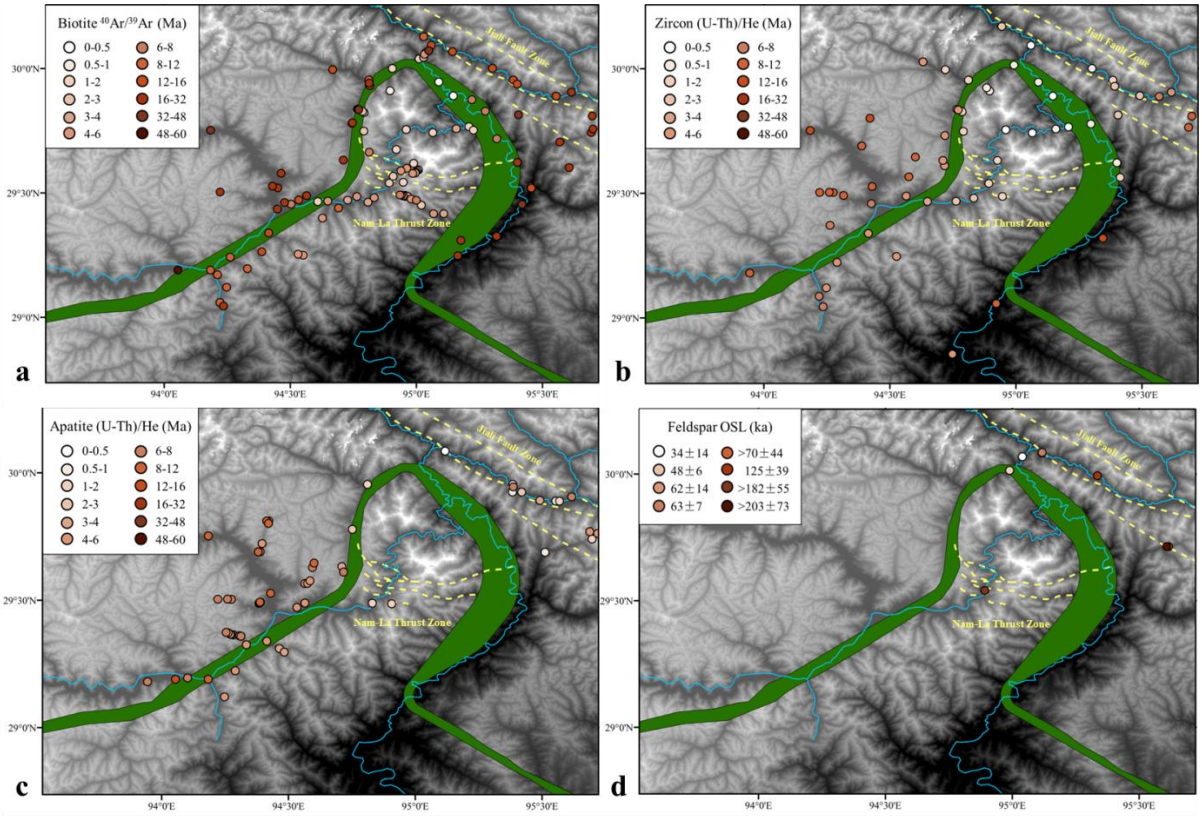

Figure 5.2: Maps of cooling ages determined using various thermochronometric techniques. (a) $^{40}Ar/^{39}Ar$ biotite ages. (b) (U-Th)/He zircon ages. (c) (U-Th)/He apatite ages. (d) OSL feldspar ages.

5.3 Methodology

5.3.1 Sample collection and preparation

For the present study eight rock specimens were collected from a region immediately to the south of the Namche Barwa massif (Figure 5.1). The sample sites were located along a vertical profile that spanned ~ 1000 m in elevation (2956-3990 m) and ~ 7 km in horizontal distance (Figure 5.3). Based on the available reconnaissance maps, two thrusts separate the sample sites into three zones. Zone A (samples PC-1, PC-5, PC-6) is located in the hanging wall of thrust NML1, which is part of the Nam-La system. Ductile thrust zone DF2 and a normal fault (Ding et al., 2001) divide the rest of the sample sites into zone B (PC-3, PC-4, PC-7), which is located in the footwall, and zone C (PC-8, PC-9) in the hanging wall, respectively.

The samples were prepared at the University of Hong Kong. The crushed rocks were screened to extract the 150–250 μm grain size. Density separation in sodium polytungstate

was used to extract quartz in the density range 2.62–2.68 g/cm^3. The quartz-rich fractions were etched in 40% HF for 40 min to remove both a surface layer from the quartz (possibly alpha damaged) and remaining feldspars, and subsequently rinsed with 10% HCl to dissolve fluorides. Samples were then dried at room temperature and re-screened at 100 μm.

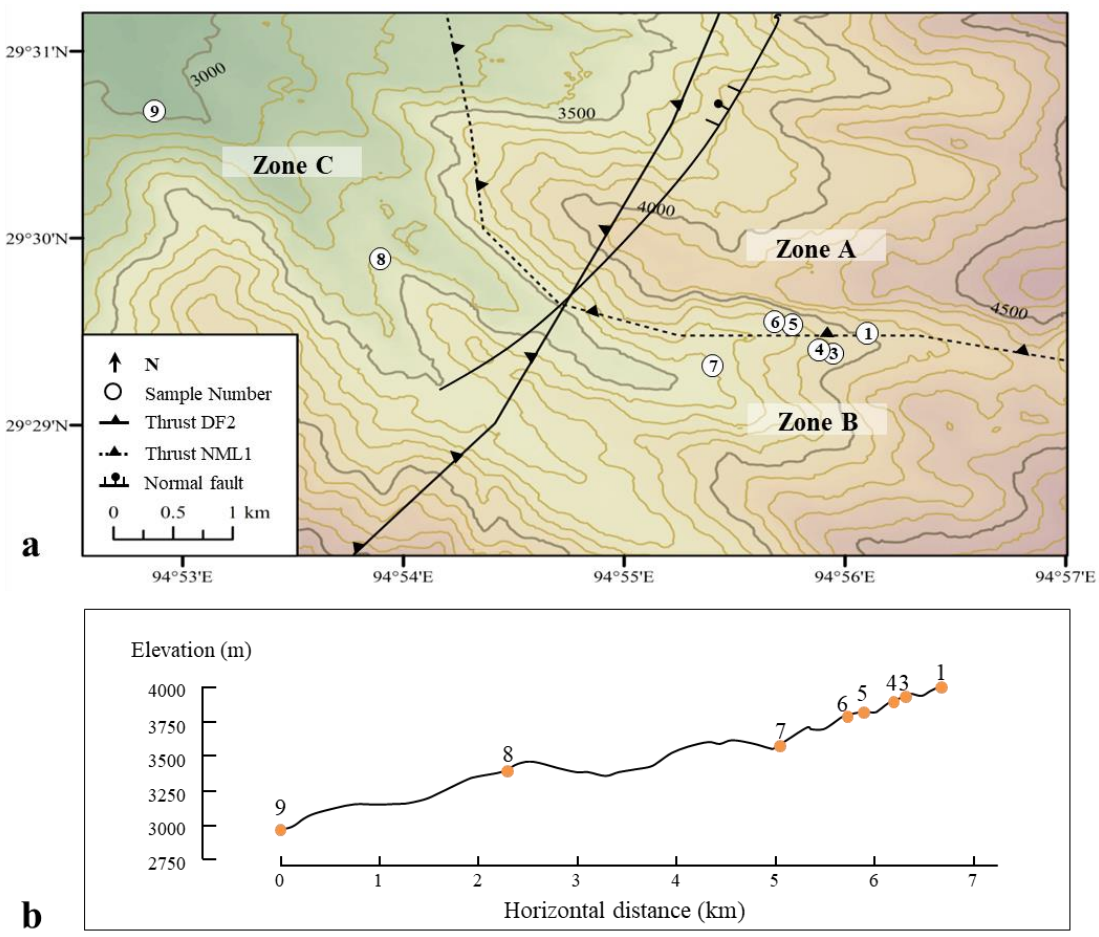

Figure 5.3: (a) Topographic map of sample locations. Thrust NML1 belongs to the south part of the Nam-La thrust zone, separating zone A on its north side. Thrust DF2 and a normal fault separate zone B (footwall) and zone C (hanging wall). (b) The elevation as a function of horizontal distance from sample PC-9 to PC-1.

5.3.2 ESR measurements

The ESR measurements were carried out on an X-band Bruker spectrometer with a 1.5T magnet and a rectangular 4102 ST cavity. The E' centre was measured at the Australian National University (ANU) both before and after the samples were heated isothermally at 250 ºC for 100 min. The parameters for measuring the E' centre were: room temperature, 0.05 mT modulation amplitude, 40.96 ms conversion factor, 40.96 ms time constant, 1024 bit spectrum resolution, and 0.05 mW microwave power, accumulation of 200-400 scans for

heated samples and accumulation of 4000–7000 scans for non-heated samples. The detailed selections of isothermal annealing time and microwave power were listed in appendix 8.2. The intensity of the E' centre was calculated as the peak to peak height at g = 2.0005 (Figure 5.4a).

Measurements of the Al and Ti centres were conducted at the University of Queensland using a Bruker X-band spectrometer equipped with a 77 °K finger dewar. The parameters for measuring the Al and Ti centres were: accumulation of 20 scans with 0.1 mT modulation amplitude, 10.24 ms conversion factor, 20.48 ms time constant, 1024 bit spectrum resolution, 5.065 mW microwave power. To avoid anisotropy, the dewar was rotated by 60° between measurements. The peak to peak height (A1 to A2) between g = 2.018 and g = 1.993 was used as the intensity of the Al centre. The ESR intensity of the Ti-Li centre (i.e. the Ti centre below) was defined as the amplitude between the top of the peak (T1) at g = 1.979 and the bottom of the peak (T2) around g = 1.913 (Figure 5.4b).

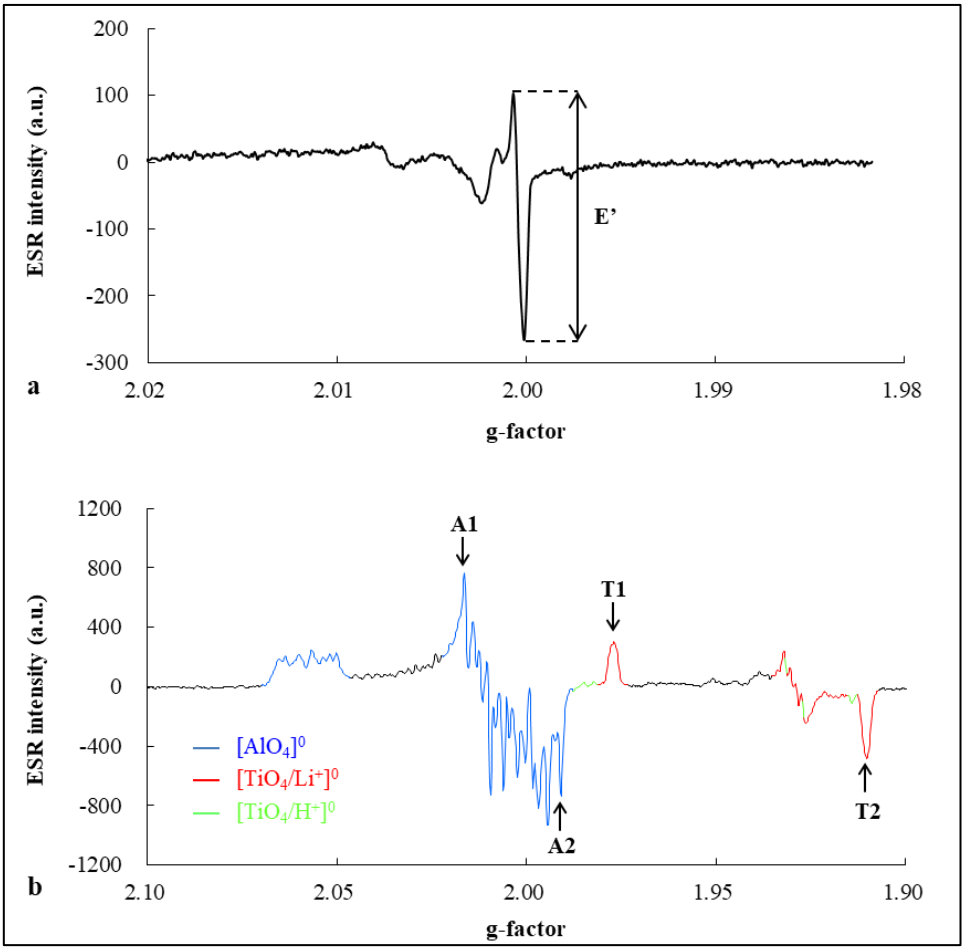

Figure 5.4: (a) ESR spectrum of the E' centre obtained at room temperature. (b) ESR spectrum of the Al and Ti centres measured at a temperature of 77 °K.

5.3.3 Estimation of equivalent dose (D_e) and dose rate ($\dot{D}$)

The equivalent dose values (D_e) were determined using the multi-aliquots regenerative method. The intensities of the Al and Ti centres were measured on natural, annealed and irradiated samples, respectively. Samples were heated at 350 ºC for 120 min and irradiated with total dose steps of 0, 153, 306, 612, 1224, 1836, 2754 and 4590 Gy delivered by an X-ray source (RS2000 irradiator) at the ANU. The single saturation exponential (SSE) function was applied for fitting the dose response curves.

The total dose rate is the combined contribution from alpha and beta particles, gamma and cosmic rays. Due to the negligible radioelement concentrations in quartz, only the external dose rate was calculated. The etching of the quartz with HF to remove the outermost surfaces eliminated the influence of the alpha dose rate. Simulation by DosiVox-2D (Martin et al., 2018) is an ideal method for estimating beta dose rate, but the effects of zonation and varied U and Th concentrations in grains of different minerals (e.g., zircon, epidote, and monazite) hindered its application, especially in deformed Himalayan rocks (Fang et al., 2018). Obtaining direct U and Th maps from a rock slice is challenging and still under investigation. For the present study therefore, the beta and gamma dose rates were estimated by bulk analysis and assuming an infinite matrix.

The bulk sample radionuclide concentrations were determined by ICP-OES (K) and ICP-MS (U, Th) at Genalysis, Perth, Australia. The crushed grain size of 150–250 μm with etching depth of 10–20 μm was utilised in the calculations. A water content of 4 ± 2% was assumed for all samples. The dose rate from cosmic rays was estimated from the sampling locations. The dose rate calculation was conducted in DRAC 1.2 (Durcan et al., 2015), using the conversion factors of Guérin et al. (2011), the beta attenuation factors of Guérin et al. (2012), and the beta etch depth attenuation factor of Bell (1979).

5.3.4 The calculation of cooling rate

The apparent ESR age of a paramagnetic centre is determined by the processes of accumulation and annihilation. In the natural geological system, the trapping and detrapping of a paramagnetic centre were assumed to follow a first order kinetic, and thus their relation is quantified by the equation (Li and Li, 2012):

$$\frac{d}{dt}\left(\frac{n}{N}\right) = \frac{\dot{D}}{D_0}\left(1 - \frac{n}{N}\right) - \nu_0 e^{-E_a/k_B T}\left(\frac{n}{N}\right) = \frac{\dot{D}}{D_0}\left(1 - \frac{n}{N}\right) - \frac{1}{\tau}\left(\frac{n}{N}\right) \quad (5.1),$$

where n is number of occupied traps at time t, N is total number of traps, $\dot{D}$ (Gy/s) is total dose rate, D_0 (Gy) is characteristic saturation dose, τ (s) is the mean life time at temperature T, E_a (eV) is the activation energy, ν_0 (s^{-1}) is the escape frequency factor, and k_B is Boltzmann's constant (8.617×10^{-5} eV/K). Due to the influence of D_0 and $\dot{D}$, the effective lifetime (τ') of the trapped charges is described by equation (5.2). The values of τ and τ' are the same at high temperatures, and τ' gradually gets smaller with decreasing temperature.

$$\tau' = \left(\frac{\dot{D}}{D_0} + \frac{1}{\tau}\right)^{-1} = \left(\frac{\dot{D}}{D_0} + \nu_0 e^{-E_a/k_B T}\right)^{-1} \quad (5.2)$$

At a fixed temperature, the apparent age (t_a) increases with the change of isothermal holding time (t), and the maximum age that can be measured is within $2D_0/\dot{D}$.

$$t_a = -\frac{D_0}{\dot{D}} \ln\left(1 - \frac{\dot{D}}{D_0}\tau'\left(1 - e^{-\frac{t}{\tau'}}\right)\right) \quad (5.3)$$

At a time-averaged cooling rate (η, ºC/s), the temperature (T, ºK) is a function of cooling time (t, s^{-1}) and initial temperature (T_0, ºK), and the apparent ESR age at time t is defined as:

$$T(t) = T_0 - \eta t \quad (5.4)$$

$$\frac{dt_a}{dt} = 1 - \frac{D_0}{\dot{D}\tau}\left(e^{\frac{t_a}{\dot{D}D_0}} - 1\right) \quad (5.5)$$

For example, for the assumed trap parameters for the Al centre of D_0 = 3000 Gy, E_a = 1.6 eV and $\nu_0 = 10^{12}$ s^{-1}, an exhumation from the upper crust (100 ºC) to the Earth's surface (10 ºC) with a constant *in situ* dose rate $\dot{D}$ = 3 Gy/ka, the relationships between apparent ESR ages and cooling rates are shown in Figure 5.5. If the trap parameters and the corresponding apparent ESR ages are known, the average cooling rate can be evaluated.

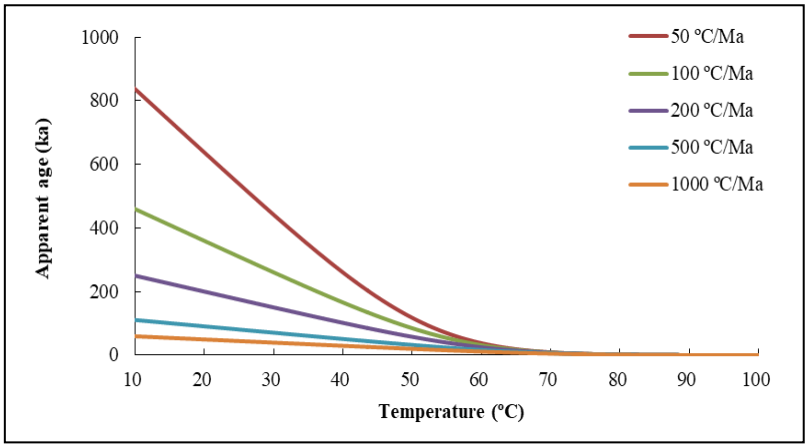

Figure 5.5: Apparent ages of the Al centre for an exhumation from 100 ºC to 10 ºC for a range of average cooling rates.

The estimation of trap parameters (i.e., kinetic order, activation energy and frequency factor) is difficult but essential for ESR thermochronometry. The conventional annealing method requires extrapolation of data from high temperatures to natural geological conditions, which can result in large uncertainties. Also, the reported parameters are disputed (Imai et al., 1985; Melnikov et al., 1989; Fukuchi, 1992; Toyoda and Ikeya, 1991, 1994). Fang and Grün (in review) were able to derive realistic trap parameters by analysing borehole samples with a well-constrained thermal history and directly-measured present-day downhole temperatures. Assuming first order kinetics, consistent results were obtained for the Al centre from two boreholes at different locations with different thermal histories (steady state and fast cooling conditions) and containing quartz of different origins. The parameters derived for the Ti centre apply only to samples that have cooled relatively rapidly.

The averaged cooling rates of the samples from the present study have been calculated using equations 5.4 and 5.5, and the trap parameters reported by Fang and Grün (in review), namely an activation energy and frequency factor of 1.5 eV and 1.0×10^{11} s^{-1}, respectively, for the Al centre, and 1.6 eV and 2.4×10^{11} s^{-1}, respectively, for the Ti centre. The D_0 values of the Al and Ti centres were calculated from the measured dose response curves. The ages of Al and Ti centres and total dose rates of ssamples were listed in Table 5.1. The surface temperature in the sampling area was assumed to be 5 ± 5 ºC.

5.4 Results

5.4.1 I_1/I_2 ratio

Analysis of the E' centre in quartz can be used for palaeothermometry because its intensity increases to its maximum value after heating at 250 ºC, and decreases rapidly at higher temperatures (McMorris, 1970). The ratio of the intensity of the unheated sample (I_1) over the maximum intensity (I_2) at 250 ºC is positively correlated with storage temperature (Chen et al., 1997; Grün et al., 1999). The ESR intensity of the natural samples is within a relatively narrow range, while those of the heated samples (250 ºC for 100 min) differ significantly (Figure 5.6a). Sample PC-5 has a significantly higher I_1/I_2 ratio (~ 0.26) than the rest samples, which are in the range of 0.16–0.20 (Figure 5.6b). This indicates that PC-5 was stored in a higher temperature environment than the other samples before being rapidly exhumed to the surface. Possible causes of the elevated I_1/I_2 ratio, which will need to be explored in a future study, are the presence of hydrothermal fluid (Grün et al., 1999) or shear heating by fault

movement.

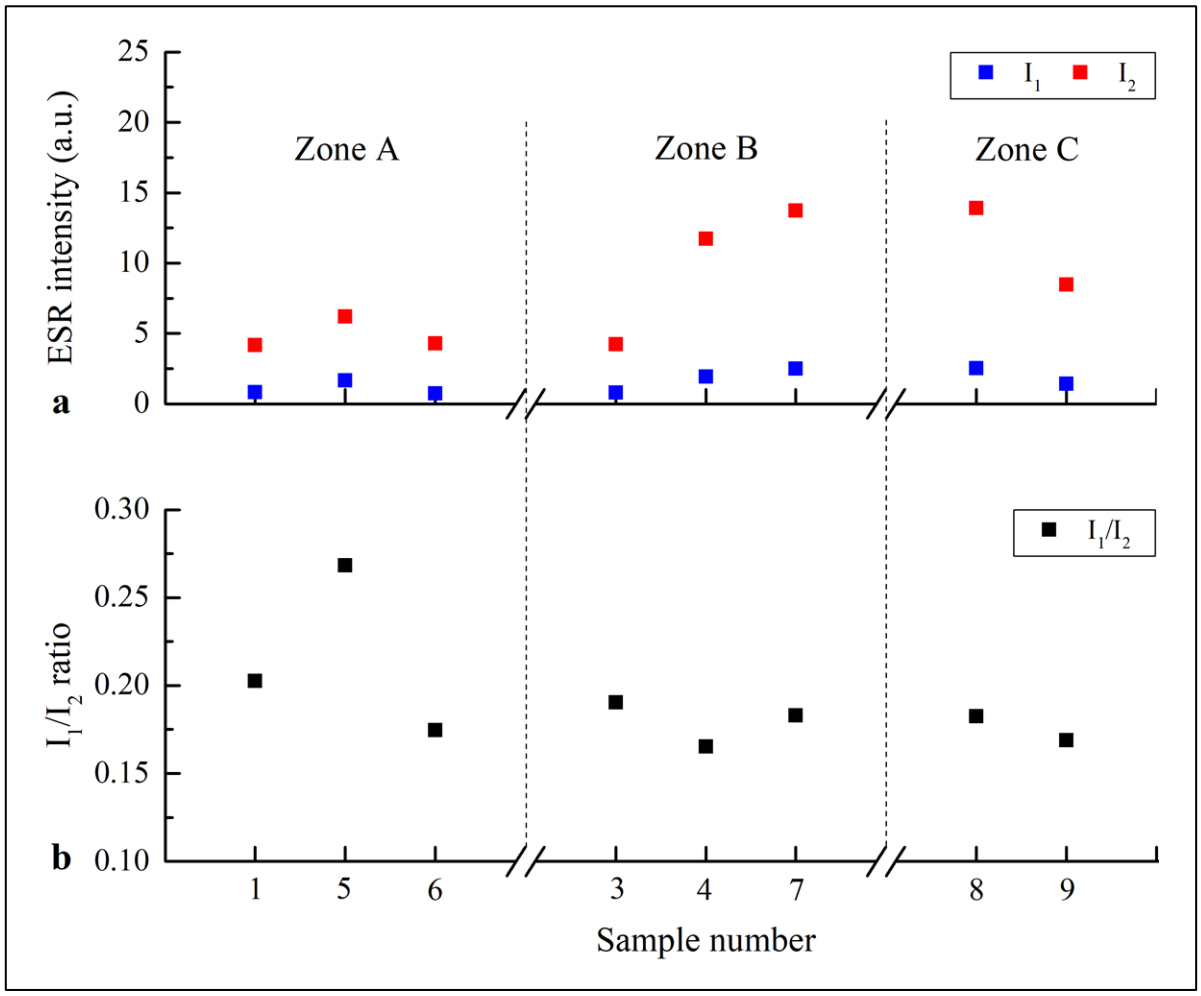

Figure 5.6: (a) ESR intensity of the natural E' centre (I_1) and heated at 250 °C for 100 min (I_2). (b) The I_1/I_2 ratio is related to palaeotemperature, and sample PC-5 shows a higher ratio than the rest of the samples.

5.4.2 ESR ages of Al and Ti centres

The apparent ages of the Ti centre are systematically higher than those of the Al centre (Table 5.1), indicating that in each case the Ti centre has higher thermal stability. Sample PC-5 falls out of the general trends having distinctively young apparent ages for Al and Ti centres. This is consistent with the elevated I_1/I_2 ratio, indicating a high temperature exposure of this sample. The apparent ages show no correlation with elevation across the structural zones over a horizontal distance of ~ 7 km (Table 5.1). At a shorter wavelength, however, within each structural zone (except for sample PC-5), apparent age and elevation are positively correlated (Figure 5.7). In zone A, the Ti age of PC-1 is slightly higher than that of PC-6, while the Al ages are equal within the uncertainties. In zone B, the ages of both the Al and Ti centres

decrease significantly with the small (~ 50 m) elevation difference between PC-3 and PC-4, which might reflect an acceleration of cooling. PC-3 (zone B) is much older than PC-1 (zone A), despite their similar elevations, but at lower elevations the ages from these two zones converge. Between zones B and C, Sample PC-8 (zone C) shows a huge age jump over PC-7 (zone B), the Ti age in particular.

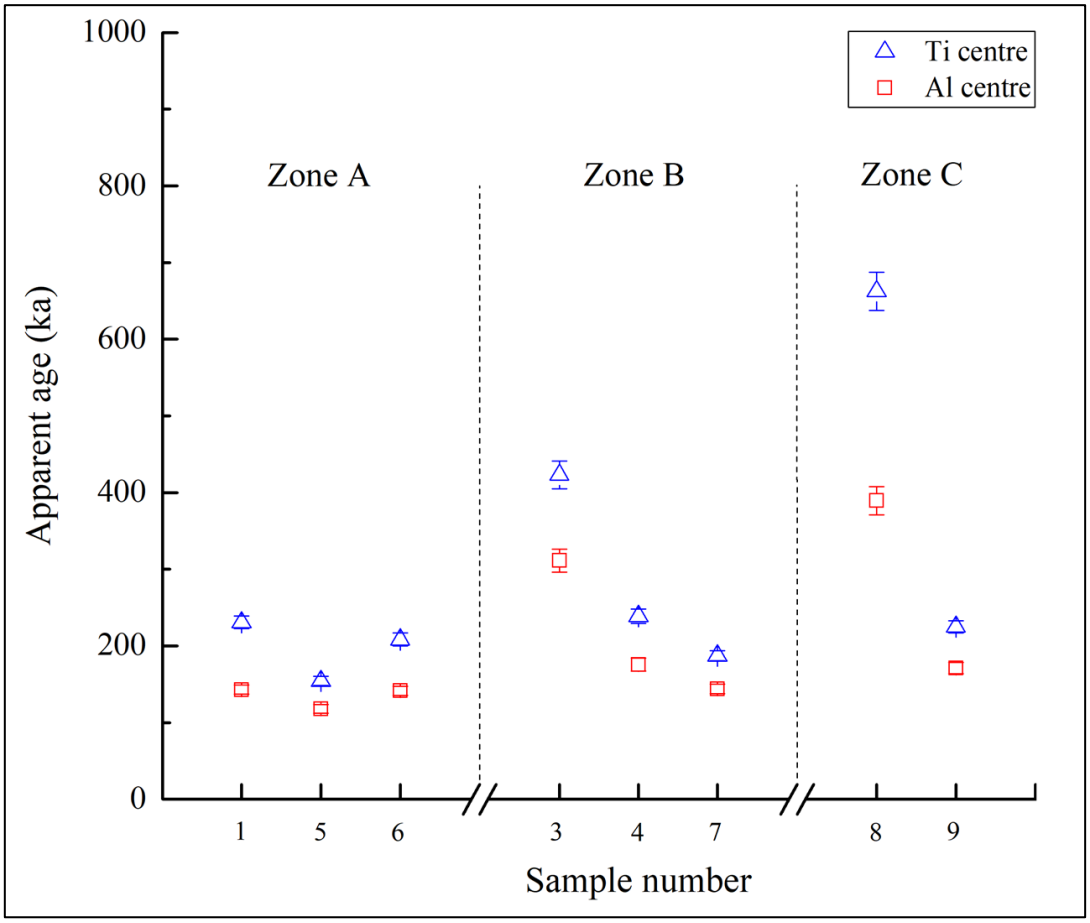

Figure 5.7: The apparent ages of Ti (triangle) and Al centres (square) are sorted for the three zones. In each zone, the elevation of samples decreases from left to right.

Table 5.1: The results of chemical analyses, total dose rate calculations, ESR ages of Al and Ti centres, and their corresponding cooling rates.

Sample	Elevation	Bulk sample				Al centre				Ti centre			
		U	Th	K	$\dot{D}$	D_0	D_e	Age	Cooling rate	D_0	D_e	Age	Cooling rate
	m	ppm	ppm	%	Gy/ka	Gy	Gy	ka	ºC/Ma	Gy	Gy	ka	ºC/Ma
PC-1	3990	9.12	46.85	3.27	8.09±0.21	6341±1063	1157±37	143±6	357±40	3751±366	1866±48	231±9	284±24
PC-3	3933	1.19	12.65	1.99	2.95±0.09	4463±477	918±35	311±15	147±19	2865±83	1248±39	423±18	145±13
PC-4	3894	2.55	33.81	4.82	7.27±0.22	4729±572	1278±48	176±9	282±33	3395±173	1737±45	239±9	273±23
PC-5	3828	7.78	56.78	3.84	8.97±0.24	6759±956	1058±41	118±6	444±48	3469±404	1385±36	154±6	442±36
PC-6	3791	4.13	33.91	3.52	6.40±0.18	4739±315	905±30	141±6	361±40	2672±134	1334±40	208±9	318±27
PC-7	3550	7.21	68.57	4.55	10.28±0.28	4019±268	1481±49	144±6	353±40	3257±201	1925±39	187±6	358±30
PC-8	3395	3.51	16.29	1.19	2.94±0.08	3214±519	1143±46	389±19	113±15	2324±239	1946±53	663±25	88±9
PC-9	2956	4.91	25.62	2.60	5.17±0.14	5744±677	885±30	171±7	291±33	3154±323	1163±27	225±8	293±25

5.4.3 The cooling and exhumation rates

The cooling rates for the Namche Barwa samples estimated from the Al and Ti centres are broadly consistent with each other (Figure 5.8). The slight differences in calculated rate between the Al and Ti centres of samples PC-1, PC-6 and PC-8 might be due to applying trap parameters are not specific to the location. The averaged cooling rate of zone A were 359 ± 40 ºC/Ma at 142 ± 6 ka (Al centre) and 301 ± 26 ºC/Ma at 220 ± 9 ka (Ti centre), excluding the results of sample PC-5. In zones B and C, the acceleration of cooling was recorded by Ti and Al centres of ESR thermochronometry, from 88 ± 9 ºC/Ma to 358 ± 30 ºC/Ma between 663 ± 25 ka at 187 ± 6 ka and 113 ± 15 ºC/Ma to 353 ± 40 ºC/Ma between 389 ± 19 ka at 144 ± 6 ka, respectively.

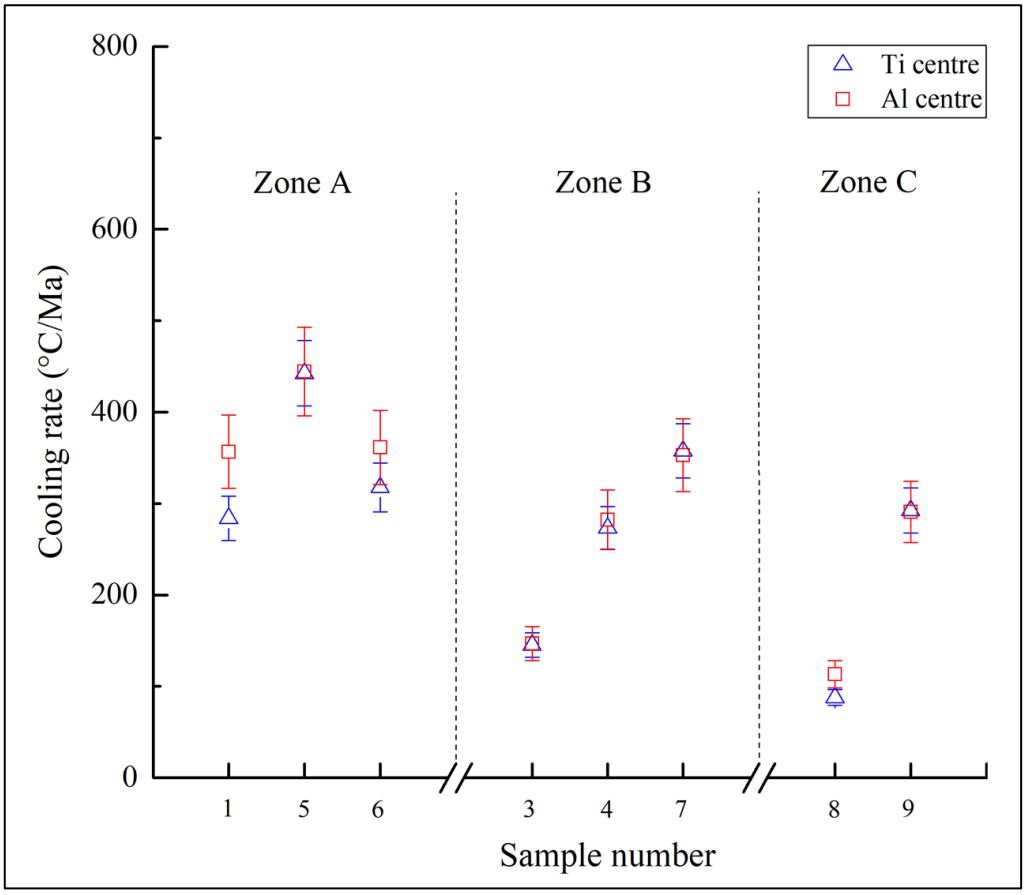

Figure 5.8: The estimated cooling rates from the Ti and Al centres. In each structural zone, the elevations of samples decrease from left to right.

To obtain estimates of the exhumation rate from these cooling rates it is necessary to have an accurate measurement of the local geothermal gradient, but this has proved difficult to obtain. Available estimates range from 50 ºC/km (Gong et al., 2015) to 100 ºC/km (Zeitler et al., 2014), both of which we have used for our calculations. Given the

relatively small distance between our sample sites and small differences in their elevation, we assume that the geothermal gradient in the upper crust (< 2 km) is the same for all three structural zones. Assuming a thermal gradient of 50 ºC/km, the exhumation rates yielded for zone A were ~ 7 mm/a (Al centre) and ~ 6 mm/a (Ti centre). For zones B and C, the exhumation rates increased from ~ 2 to ~ 7 mm/a. If the geothermal gradient was 100 ºC/km, then the exhumation rate (and late acceleration) was less, increasing from ~ 1 to ~ 3.5 mm/a.

5.5 Discussion

5.5.1 The localised geological structure and thermochronometric results

The ESR ages from the eastern Himalayan syntaxis are influenced by their localised structural setting, so in turn can be used to understand the faulting of the syntaxis since the Mid-Pleistocene. Thrust NML1 separates our sample sites into zone A (the hanging wall to the north) and zones B and C (in the footwall to the south). A decrease in the ESR age difference between zones A and B with decreasing elevation implies that the NML1 became less active after 423 ± 18 ka. The ESR ages of the Al centre in the two zones are almost the same after 144 ± 6 ka, suggesting that by then the vertical motion of the thrust had ceased. This is consistent with current geophysical observations that show the Nam-La thrusts to be aseismic (Sol et al., 2007). Thrust DF2 and a normal fault separate zone B (in the footwall) from zone C (in the hanging wall). Based on the reported reverse sense of shear (Geng et al., 2006), we expected to find the ESR ages in zone C to be younger than those in zone B, but in fact found the opposite. The age data are consistent with the geological mapping by Ding et al. (2001) and the reported normal fault could be the result of late-stage (possibly Pleistocene) movement that overprinted earlier structural events. The vertical displacement across this fault is about 700 m, but its time of initiation and rate of movement remain to be determined. More detailed structural investigations and thermochronometric studies along the length of the fault will be required to determine when and how it evolved.

At the south boundary of the Namche Barwa massif, Nam-La thrust zone is composed of several south-verging sub-thrusts, and the cross-cutting fault DF2 has made the structure even more complex. The exhumation history of the massif can be inferred from the thermochronometric records across this zone. North of the thrust zone, cooling from 330

(T_c of BAr) to 110 ºC (T_c of AFT) occurred at a constant rate of ~ 100 ºC/Ma during the last 2–5 Ma, but from 110 to 0 ºC the rate increased gradually to 250 ºC/Ma at 0.5 Ma (Tu et al., 2015). Within the thrust zone (zone A), the BAr ages range from 6.8 to 1.8 Ma and show no relationship between age and elevation (Gong et al., 2015; Tu et al., 2015). The AFT ages also exhibit no age-elevation trend within the analytical uncertainty, but the boomerang-shaped pattern of those data has been interpreted as indicating a recent rapid cooling event at 0.6–0.8 Ma (Burg et al., 1998; Lei, 2006; Kang et al., 2016a). Assuming a closure temperature of 120 ºC, the cooling rate was approximately 170 ± 30 ºC/Ma in this time interval. The cooling rate reported from feldspar OSL thermochronometry in this region is < 178 ± 49 °C/Ma at a minimum age of 182 ± 55 ka (King et al., 2016a). ESR results yield a much higher cooling rate of 359 ± 40 ºC/Ma at 142 ± 6 ka (Al centre) and 301 ± 26 ºC/Ma at 220 ± 9 ka (Ti centre). South of the thrust zone (zones B and C), AHe ages distribute according to the fault setting (Zeitler et al., 2014; Yang et al., 2018) and the estimated cooling rate is ~ 50 °C/Ma at 1.6 Ma assuming a closure temperature of 80 °C. The ESR thermochronometry records cooling rates of 88 ± 9 ºC/Ma at 663 ± 25 ka (Ti centre) and 113 ± 15 ºC/Ma at 389 ± 19 ka (Al centre). The rates accelerated to 358 ± 30 ºC/Ma at 187 ± 6 ka (Ti centre) and 355 ± 35 ºC/Ma at 166 ± 6 ka (Al centre), which were consistent with the late-stage cooling at a similar time in zone A. These records imply that rapid cooling and exhumation have extended to the south of the Namche Barwa massif no later than 663 ± 25 ka.

5.5.2 The development of the Namche Barwa massif during the Mid to Late Pleistocene

The domal pop-up structure of the Namche Barwa massif is characterised by the occurrence of very young ages with this region which was produced by a distinct initiation and/or acceleration of uplift and exhumation in the Plio-Pleistocene (Bracciali et al., 2016). The movements along the massif-bounding shear zones can be inferred from the distribution of reported thermochronometric results on three sides. Our ESR results have documented the vertical motion of the Nam-La thrust zone during the mid-Pleistocene cooling event. To understand the late-stage domal development, the north and south regions adjacent to the massif need to be compared. In both regions, a set of faults extends ~ 10 km away from the massif, and the cooling rate increases gradually towards the core of the massif. The late-stage cooling in these two regions began within the same time interval (0.6–1.0 Ma). We agree that tectonics (i.e., SW-NE crustal

shortening) is the major driving force of the mid-Pleistocene cooling, but the accelerated cooling not only extended northwards to the Asian plate (Seward and Burg, 2008; King et al., 2016a), but also the south of the massif. Although the estimated cooling rate is extremely high (1509 ± 133 °C/Ma at 34 ± 14 ka; King et al., 2016a) in the north adjacent to the massif, this might be influenced by the combined contributions of tectonics-related domal development and erosion-related river capture. In regard to the migration of the exhumation centre, the higher cooling rate cannot be directly equal to higher exhumation in regions with the varied geological and geomorphological setting. For example, the exhumation rate can be the same in two regions: one has a higher cooling rate and a higher geothermal gradient, and the other has a lower cooling rate and lower geothermal gradient. Thus, the accurate estimation of the geothermal gradient is essential, but requires detailed future studies to further investigate the evolution of exhumation in the Namche Barwa massif.

5.6 Summary and conclusions

Rapid exhumation within the last 1 Ma has been reported for the late-stage development of the eastern Himalayan syntaxis, but direct quantification of Mid-Pleistocene thermal histories is a challenge for existing low-temperature thermochronometers. The present study is the first to apply quartz ESR thermochronometry to the southern boundary of the Namche Barwa massif, where the local structural settings and late-stage cooling history are less studied and not well-known. The ESR results have shown that the vertical movement of the Nam-La thrust at the south boundary of the Namche Barwa massif and accelerated cooling extended to the south of the massif. Thermochronometric measurements to the south and north of the massif show that coeval rapid cooling occurred on both sides as a result of SW-NE crustal shortening. The migration of the exhumation centre, however, remains unresolved due to large uncertainties in the local geothermal gradient. Such a measurement is required, as is ESR thermochronometry over a broader area around the Namche Barwa massif, before the exhumation history of this key portion of the collision zone between the Indian and Asian plates in the eastern Himalayan syntaxis can be determined in more detail.

6 Conclusions and future directions

This research project aimed to (1) determine trap parameters of Al and Ti centres in quartz under natural geological settings, (2) develop a 2D model and analytical procedure for calculating beta dose rate in heterogeneous rocks, and (3) apply ESR thermochronometry to determine the exhumation history of the Namche Barwa massif, eastern Himalayan syntaxis. The main research outcomes for each of these aims are discussed below.

(1) The analyses of borehole samples with well-constrained thermal history and ambient temperatures provide access to obtain realistic trap parameters of paramagnetic centres in quartz. The first-order kinetic model was adopted in the calculation which describes the relationship between radiation-induced charge trapping and thermally controlled detrapping. The best-fit trap parameters of Al and Ti centres were evaluated for Fergusons Hill-1 core at approximate steady-state and Eldzhurtinskiy Granite borehole in a rapid cooling condition with the rate of ~ 520 ºC/Ma. For the Al centre, the activation energy and corresponding frequency factor are consistent within two boreholes and fall in the range of published data obtained from laboratory annealing experiments. For the Ti centre, the data from the Eldzhurtinskiy Granite borehole were roughly fitted by the model and showed higher thermal stability than the Al centre, while the parameters cannot be obtained from Fergusons Hill-1 core suggesting that a first-order kinetic model is not universally applicable. ESR thermochronometry has the dating range from 10 ka to 2 Ma, which can be applied to record the thermal history under a lower cooling condition (> 30 ºC/Ma) during the Quaternary. Based on the estimated trap parameters, the closure temperatures of Al and Ti centres in quartz are 48-62 ºC and 64-79 ºC respectively, corresponding to cooling rates of between 100 and 1000 ºC/Ma. This attempt opens the door for establishing a physical formulation incorporating additional dosimetric variables and the effects of kinetic orders in ESR thermochronometry.

(2) Reliable determination of mineral types and distributions is the prerequisite for beta

dose rate simulation. 3D X-ray CT scanning is the ideal solution for heterogeneous samples, but the difficulty in mineral segmentation (e.g., quartz and plagioclase) hindered the application of 3D modelling in ESR thermochronometry. A 2D analysis is better suited for the discrimination of mineral phases while preserving information about the heterogeneous structure. XRF has the advantage of easy sample preparation and accessibility, but the mineral identification is subjective, which can lead to incorrect estimations of beta dose rates. QEM-EDS is recommended for more rapid map production and more efficient mineral identification.

The software DosiVox-2D using a Monte-Carlo approach has been developed and verified for the calculation of beta dose rates in realistic heterogeneous but isotropic geometries. Compared with 3D model and conventional method, this 2D model provides exact and accurate beta dose rate values and distribution for both virtual sediment cases and a granite sample, within the limits of the underlying modelling assumptions. The simulated beta dose rate can be widely used for trapped charge dating, usually directly or assuming the usual attenuation factors for moisture and grain size. The distribution map enables estimation of the beta dose rate at a single-grain level, and the distribution histogram provides an efficient tool for understanding the over-dispersion of equivalent dose. In addition, DosiVox-2D is easily accessible which does not require programming skills and proposes a graphical interface for the construction of the modelling and image loading, and the simulation can be run on a standard office computer.

To apply this method in routine dose rate estimations, the procedure of using DosiVox-2D has been assessed on rocks with even texture and regular mineral distribution patterns. The reliability of the results depends on the accuracy of the uploaded mineral map and radioactive element concentrations. For mineral mapping, the resolution should be higher than the size of target minerals, and a lower resolution can result in the loss of minerals containing high content of radionuclide. To ensure the representativeness, a larger sample size is suggested. For the analysis of radionuclide concentrations, it is applicable to use the averaged K concentrations

of minerals in simulation. U and Th-bearing minerals have a non-negligible influence on the averaged beta dose rate especially in quartz, but it is still challenging to estimate the radioelement concentrations of U and Th-bearing minerals due to the impact of zonation and concentration variations in different grains.

(3) ESR thermochronometry of quartz has been successfully applied to the Namche Barwa massif in the eastern Himalayan syntaxis. Eight rocks from a vertical transect were collected from the less studied area adjacent to the south boundary of the massif. Due to the complex fault settings, these samples were divided into three structural zones. The I_1/I_2 ratio of E' centre indicated sample PC-5 had been stored in a higher temperature environment than the rest. Despite this sample, the apparent ages of Al and Ti centres were positively correlated with elevation in each zone, and could reflect the shear senses of the faults. The NML1 showed thrust sense agreeing with reported reconnaissance maps. A normal fault was indicated between zones B and C, consistent with the mapping of Ding et al. (2001). Using the trap kinetics reported by Fang and Grün (in review), the cooling rate of each sample was accurately estimated through the first-order kinetic model. The results indicated an accelerated cooling from 88 ± 9 ºC/Ma at 663 ± 25 ka to 358 ± 30 ºC/Ma at 187 ± 6 ka (Ti centre) and 113 ± 15 ºC/Ma at 389 ± 19 ka to 353 ± 40 ºC/Ma at 144 ± 6 ka (Al centre). Compared with the thermal history reported to the north of the massif, a coeval rapid cooling event was recognised in both sides to the Namche Barwa massif. This suggests that a late-stage development of the massif grew as a pop-up dome in response to the crustal shortening in a SW-NE direction. In the calculation of exhumation rate, large uncertainties can result from using an inaccurate local thermal gradient. Therefore, improved knowledge is necessary on geothermal gradient.

Based on the above research outcomes, immediate future works are required to solve the important questions which have been identified in this project. For trap parameter estimation, realistic kinetic orders of trapping and annealing processes are essential to be

investigated, and a systematic comparison of trap kinetics needs to be carried out for samples from different origins and locations. For applying 2D modelling in beta dose rate calculations, the influence of U and Th enriched minerals needs to be quantified, including the effects of their abundance, radionuclide concentrations and spatial distributions. Besides, a method needs to be developed for the calculation of the mean dose rate and appropriate uncertainties for the grain size used for luminescence and ESR analyses. The verification should be carried out on the use of arithmetic or geometric mean dose rates in the age calculations for rocks, including luminescence analysis using single grains and ESR dating by multiple aliquots. To better understand the development of the Namche Barwa massif within the last 1 Ma, a detailed field geological survey and thermochronometric analysis are necessary for obtaining more information on the shapes and displacements of the internal fault systems in the massif. Moreover, ESR thermochronometry needs to be broadly applied to the eastern Himalayan syntaxis, and combined with multi-thermochronometric techniques to shed light on the mechanism and processes generating and currently sustaining the syntaxial development.

7 References

Adams, J., 1980. Contemporary uplift and erosion of the Southern Alps, New Zealand. Geological Society of America Bulletin 91, 1-114.

Ahnert, F., 1970. Functional relationships between denudation, relief, and uplift in large, mid-latitude drainage basins. American Journal of Science 268, 243-263.

Aitken, M.J., 1985. Thermoluminescence dating. Academic press.

Andrews-Speed, C., Oxburgh, E.R., Cooper, B., 1984. Temperatures and depth-dependent heat flow in western North Sea. AAPG Bulletin 68, 1764-1781.

Asagoe, M., Toyoda, S., Voinchet, P., Falguères, C., Tissoux, H., Suzuki, T., Banerjee, D., 2011. ESR dating of tephra with dose recovery test for impurity centers in quartz. Quaternary international 246, 118-123.

Baldwin, S.L., Lister, G.S., 1998. Thermochronology of the South Cyclades Shear Zone, Ios, Greece: Effects of ductile shear in the argon partial retention zone. Journal of Geophysical Research: Solid Earth 103, 7315-7336.

Beerten, K., Pierreux, D., Stesmans, A., 2003. Towards single grain ESR dating of sedimentary quartz: first results. Quaternary science reviews 22, 1329-1334.

Beerten, K., Stesmans, A., 2007. ESR dating of sedimentary quartz: possibilities and limitations of the single-grain approach. Quaternary Geochronology 2, 373-380.

Bell, W., 1979. Attenuation factors for the absorbed radiation dose in quartz inclusions for thermoluminescence dating. Ancient TL 8, 12.

Bernet, M., 2009. A field-based estimate of the zircon fission-track closure temperature. Chemical Geology 259, 181-189.

Biswas, R.H., Herman, F., King, G.E., Braun, J., 2018. Thermoluminescence of feldspar as a multi-thermochronometer to constrain the temporal variation of rock exhumation in the recent past. Earth and Planetary Science Letters 495, 56-68.

Blackwell, B.A., Skinner, A.R., Blickstein, J.I., Montoya, A.C., Florentin, J.A., Baboumian, S.M., Ahmed, I.J., Deely, A.E., 2016. ESR in the 21st century: From buried valleys and deserts to the deep ocean and tectonic uplift. Earth-Science Reviews 158, 125-159.

Bonnet, S., Crave, A., 2003. Landscape response to climate change: Insights from experimental modeling and implications for tectonic versus climatic uplift of topography. Geology 31, 123-126.

Boone, M., Dewanckele, J., Boone, M., Cnudde, V., Silversmit, G., Van Ranst, E., Jacobs, P., Vincze, L., Van Hoorebeke, L., 2011. Three-dimensional phase separation and identification in granite. Geosphere 7, 79-86.

Booth, A.L., Chamberlain, C.P., Kidd, W.S.F., Zeitler, P.K., 2009. Constraints on the metamorphic evolution of the eastern Himalayan syntaxis from geochronologic and petrologic studies of Namche Barwa. Geological Society of America Bulletin 121, 385-407.

Bracciali, L., Parrish, R.R., Najman, Y., Smye, A.J., Carter, A., Wijbrans, J.R., 2016. Plio-Pleistocene exhumation of the eastern Himalayan syntaxis and its domal 'pop-up'. Earth-Science Reviews 160, 350-385.

Braun, J., Van Der Beek, P., Valla, P., Robert, X., Herman, F., Glotzbach, C., Pedersen, V., Perry, C., Simon-Labric, T., Prigent, C., 2012. Quantifying rates of landscape evolution and tectonic processes by thermochronology and numerical modeling of crustal heat transport using PECUBE. Tectonophysics 524, 1-28.

Brown, N.D., 2017. Using luminescence signals from bedrock feldspars for low-temperature thermochronology. University of California, Los Angeles.

Brown, N., Rhodes, E., Harrison, T.M., 2017. Using thermoluminescence signals from feldspars for low-temperature thermochronology. Quaternary Geochronology 42, 31-41.

Burg, J.-P., Nievergelt, P., Oberli, F., Seward, D., Davy, P., Maurin, J.-C., Diao, Z., Meier, M., 1998. The Namche Barwa syntaxis: evidence for exhumation related to compressional crustal folding. Journal of Asian Earth Sciences 16, 239-252.

Chauhan, N., Singhvi, A., 2011. Distribution in SAR palaeodoses due to spatial heterogeniety of natural beta dose. Geochronometria 38, 190-198.

Chen, Y., Feng, J., Gao, J., Grün, R., 1997. Investigation of the potential use of ESR signals in quartz for palaeothermometry. Quaternary Science Reviews 16, 495-499.

Clark, D., McPherson, A., Collins, C., 2011. Australia's seismogenic neotectonic record. Geoscience Australia Record 11, 1-95.

Cooper, G., Hill, K., 1997. Cross-section balancing and thermochronological analysis of the Mesozoic development of the eastern Otway Basin. The APPEA Journal 37, 390-414.

Cunningham, A.C., DeVries, D.J., Schaart, D.R., 2012. Experimental and computational simulation of beta-dose heterogeneity in sediment. Radiation Measurements 47, 1060-1067.

Dickinson, J.A., Wallace, M.W., Holdgate, G.R., Gallagher, S.J., Thomas, L., 2002. Origin and timing of the Miocene-Pliocene unconformity in southeast Australia. Journal of Sedimentary Research 72, 288-303.

Ding, L., Zhong, D., Yin, A., Kapp, P., Harrison, T.M., 2001. Cenozoic structural and metamorphic evolution of the eastern Himalayan syntaxis (Namche Barwa). Earth and Planetary Science Letters 192, 423-438.

Dodson, M.H., 1973. Closure temperature in cooling geochronological and petrological systems. Contributions to Mineralogy and Petrology 40, 259-274.

Duddy, I., 1994. The Otway Basin: thermal, structural, tectonic and hydrocarbon generation histories, Extended abstracts, NGMA/PESA Otway Basin Symposium, Melbourne, pp. 35-42.

Duddy, I.R., 1983. The geology, petrology and geochemistry of the Otway Formation volcanogenic sediments.

Durcan, J.A., King, G.E., Duller, G.A., 2015. DRAC: Dose Rate and Age Calculator for trapped charge dating. Quaternary Geochronology 28, 54-61.

Duval, M., 2012. Dose response curve of the ESR signal of the Aluminum center in quartz grains extracted from sediment. Ancient TL 30, 41-49.

Duval, M., Guilarte, V., 2015. ESR dosimetry of optically bleached quartz grains extracted from Plio-Quaternary sediment: evaluating some key aspects of the ESR signals associated to the Ti-centers. Radiation Measurements 78, 28-41.

Ehlers, T.A., Chaudhri, T., Kumar, S., Fuller, C.W., Willett, S.D., Ketcham, R.A., Brandon, M.T., Belton, D.X., Kohn, B.P., Gleadow, A.J., 2005. Computational tools for low-temperature thermochronometer interpretation. Reviews in Mineralogy and Geochemistry 58, 589-622.

Fain, J., Soumana, S., Montret, M., Miallier, D., Pilleyre, T., Sanzelle, S., 1999. Luminescence and ESR dating Beta-dose attenuation for various grain shapes calculated by a Monte-Carlo method. Quaternary Geochronology 18, 231-234.

Falguères, C., Miallier, D., Sanzelle, S., Fain, J., Laurent, M., Montret, M., Pilleyre, T., Bahain, J., 1994. Potential use of the E' center as an indicator of initial resetting in TL/ESR dating of volcanic materials. Quaternary Science Reviews 13, 619-623.

Fang, F., Martin, L., Williams, I., Brink, F., Mercier, N., Grün, R., 2018. 2D modelling: A Monte Carlo approach for assessing heterogeneous beta dose rate in luminescence and ESR dating: Paper II, Application to igneous rocks. Quaternary Geochronology, 48, 195-206.

Fang, F., Grün, R. ESR thermochronometry of Al and Ti centres in quartz: A case study of the Fergusons Hill-1 borehole from the Otway Basin, Australia. Radiation measurements (in review).

Fattibene, P., Callens, F., 2010. EPR dosimetry with tooth enamel: a review. Applied Radiation and Isotopes 68, 2033-2116.

Feigl, F.J., Fowler, W.B., Yip, K.L., 1974. Oxygen vacancy model for the E_1' center in SiO_2. Solid State Communications 14, 225-229.

Finnegan, N.J., Hallet, B., Montgomery, D.R., Zeitler, P.K., Stone, J.O., Anders, A.M., Yuping, L., 2008. Coupling of rock uplift and river incision in the Namche Barwa-Gyala Peri massif, Tibet. Geological Society of America Bulletin 120, 142-155.

French, D., 1984. An interpretation of the geothermal history of the Otway Basin based on vitrinite reflectance and fission track analyses. University of Wollongong.

Fukuchi, T., 1992. ESR studies for absolute dating of fault movements. Journal of the Geological Society 149, 265-272.

Garlick, G., Gibson, A., 1948. The electron trap mechanism of luminescence in sulphide and silicate phosphors. Proceedings of the physical society 60, 574.

Geng, Q., Guitang, P., Zheng, L., Chen, Z., Fisher, R.D., Sun, Z., Ou, C., Dong, H., Wang, X., Li, S., 2006. The Eastern Himalayan syntaxis: major tectonic domains, ophiolitic mélanges and geologic evolution. Journal of Asian Earth Sciences 27, 265-285.

Gong, J., 2009. Thermal evolution history and $^{40}Ar/^{39}Ar$ geochronological constrains on Central-East Himalaya. Peking University, Beijing.

Gong, J., Ji, J., Zhou, J., Tu, J., Sun, D., Zhong, D., Han, B., 2015. Late Miocene thermal evolution of the eastern Himalayan syntaxis as constrained by biotite $^{40}Ar/^{39}Ar$ thermochronology. The Journal of Geology 123, 369-384.

Green, P., Crowhurst, P., Duddy, I., 2004. Integration of AFTA and (U-Th)/He thermochronology to enhance the resolution and precision of thermal history reconstruction in the Anglesea-1 well, Otway Basin, SE Australia.

Griffiths, J., Owen, J., Ward, I., 1954. Paramagnetic resonance in neutron-irradiated diamond and smoky quartz. Nature 173, 439.

Grün, R., 1989. Electron spin resonance (ESR) dating. Quaternary International 1, 65-109.

Grün, R., 1994. The kinetics of TL peaks and its effect on the dose versus temperature plot. Radiation measurements 23, 175-194.

Grün, R., Tani, A., Gurbanov, A., Koshchug, D., Williams, I., Braun, J., 1999. A new method for the estimation of cooling and denudation rates using paramagnetic centers in quartz: A case study on the Eldzhurtinskiy Granite, Caucasus. Journal of Geophysical Research: Solid Earth 104, 17531-17549.

Guérin, G., Mercier, N., Adamiec, G., 2011. Dose-rate conversion factors: update. Ancient TL 29, 5-8.

Guérin, G., Mercier, N., Nathan, R., Adamiec, G., Lefrais, Y., 2012. On the use of the infinite matrix assumption and associated concepts: a critical review. Radiation Measurements 47, 778-785.

Guérin, G., Jain, M., Thomsen, K.J., Murray, A.S., Mercier, N., 2015. Modelling dose rate to single grains of quartz in well-sorted sand samples: The dispersion arising from the presence of potassium feldspars and implications for single grain OSL dating. Quaternary Geochronology 27, 52-65.

Guralnik, B., Jain, M., Herman, F., Ankjærgaard, C., Murray, A.S., Valla, P.G., Preusser, F., King, G.E., Chen, R., Lowick, S.E., 2015a. OSL-thermochronometry of feldspar from the KTB borehole, Germany. Earth and planetary science letters 423, 232-243.

Guralnik, B., Li, B., Jain, M., Chen, R., Paris, R.B., Murray, A.S., Li, S.-H., Pagonis, V., Valla, P.G., Herman, F., 2015b. Radiation-induced growth and isothermal decay of infrared-stimulated luminescence from feldspar. Radiation Measurements 81, 224-231.

Harrison, T.M., 1981. Diffusion of ^{40}Ar in hornblende. Contributions to Mineralogy and Petrology 78, 324-331.

Harrison, T.M., Duncan, I., Mcdougall, I., 1985. Diffusion of ^{40}Ar in biotite: temperature, pressure and compositional effects. Geochimica et Cosmochimica Acta 49, 2461-2468.

Harrison, T.M., Célérier, J., Aikman, A.B., Hermann, J., Heizler, M.T., 2009. Diffusion of ^{40}Ar in muscovite. Geochimica et Cosmochimica Acta 73, 1039-1051.

Herman, F., Rhodes, E.J., Braun, J., Heiniger, L., 2010. Uniform erosion rates and relief amplitude during glacial cycles in the Southern Alps of New Zealand, as revealed from OSL-thermochronology. Earth and Planetary Science Letters 297, 183-189.

Holford, S.P., Hillis, R.R., Duddy, I.R., Green, P.F., Tassone, D.R., Stoker, M.S., 2011. Paleothermal and seismic constraints on late Miocene-Pliocene uplift and deformation in the Torquay sub-basin,southern Australian margin. Australian Journal of Earth Sciences 58, 543-562.

House, M.A., Farley, K.A., Kohn, B.P., 1999. An empirical test of helium diffusion in apatite: borehole data from the Otway basin, Australia. Earth and Planetary Science Letters 170, 463-474.

House, M., Kohn, B., Farley, K., Raza, A., 2002. Evaluating thermal history models for the Otway Basin, southeastern Australia, using (U-Th)/He and fission-track data from borehole apatites. Tectonophysics 349, 277-295.

Ikeya, M., 1975. Dating a stalactite by electron paramagnetic resonance. Nature 255, 48.

Ikeya, M., Toyoda, S., 1991. Thermal effect in metamorphic rock around an intrusion zone with ESR studies. Applied Magnetic Resonance 2, 69.

Imai, N., Shimokawa, K., Hirota, M., 1985. ESR dating of volcanic ash. Nature 314, 81.

Isoya, J., Bowman, M., Norris, J., Weil, J., 1983. An electron spin echo envelope modulation study of lithium nuclear hyperfine and quadrupole coupling in the A

(Ti-Li) center of α-quartz. The Journal of Chemical Physics 78, 1735-1746.

Jani, M., Bossoli, R., Halliburton, L., 1983. Further characterization of the E1' center in crystalline SiO2. Physical Review B 27, 2285.

Kalchgruber, R., Fuchs, M., Murray, A., Wagner, G., 2003. Evaluating dose-rate distributions in natural sediments using α-Al_2O_3: C grains. Radiation Measurements 37, 293-297.

Kang, W., Xu, X., Yu, G., Tan, X., Li, K., 2016. Thermochronological evidence for division of quarterary uplifting stages of Mt. Namjagbarwa Chinese J. Geophys. (in Chinese) 59, 1753-1761.

King, G.E., Herman, F., Guralnik, B., 2016a. Northward migration of the eastern Himalayan syntaxis revealed by OSL thermochronometry. Science 353, 800-804.

King, G., Herman, F., Lambert, R., Valla, P., Guralnik, B., 2016b. Multi-OSL-thermochronometry of feldspar. Quaternary Geochronology 33, 76-87.Lei, Y., 2006. Geochronologic studies on tectono-geomorphic evolution of the eastern Himalayan syntaxis since Late Miocene time, Institute of Geology and Geophysics. Chinese Academy of Science, Beijing, p. 90.

King, G.E., Tsukamoto, S., Herman, F., Biswas, R.H., Sueoka, S., Tagami, T.,. ESR-thermochronometry of the Hida range of the Japanese Alps: Validation and future potential. Geochronology Discuss, https://doi.org/10.5194/gchron-2019-6, in review.

Lambert, R., 2018. Investigating thermal decay in K-feldspar for the application of IRSL thermochronometry on the Mont Blanc Massif, Faculty of Geosciences and the Environment. University of Lausanne.

Lei, Y., 2006. Geochronologic studies on tectono-geomorphic evolution of the eastern Himalayan syntaxis since Late Miocene time, Institute of Geology and Geophysics. Chinese Academy of Science, Beijing, p. 90.

Li, B., Li, S.-H., 2011. Luminescence dating of K-feldspar from sediments: a protocol without anomalous fading correction. Quaternary Geochronology 6, 468-479.

Li, B., Li, S.-H., 2012. Determining the cooling age using luminescence-thermochronology. Tectonophysics 580, 242-248.

Liu, Y., Zhong, D., 1997. Petrology of high-pressure granulites from the eastern Himalayan syntaxis. Journal of Metamorphic Geology 15, 451-466.

Malloy, M., 2004. Rapid erosion at the Tsangpo knickpoint and exhumation of southeastern Tibet. Lehigh University.

Marfunin, A.S., 2012. Spectroscopy, luminescence and radiation centers in minerals. Springer Science & Business Media.

Martin, L., Incerti, S., Mercier, N., 2015. DosiVox: Implementing Geant 4-based software for dosimetry simulations relevant to luminescence and ESR dating techniques. Ancient TL 33, 1-10.

Martin, L., Fang, F., Mercier, N., Incerti, S., Grün, R., Lefrais, Y., 2018. 2D modelling: A Monte Carlo approach for assessing heterogeneous beta dose rate in luminescence and ESR dating: Paper I, theory and verification. Quaternary Geochronology 48, 25-37.

Mayya, Y., Morthekai, P., Murari, M.K., Singhvi, A., 2006. Towards quantifying beta microdosimetric effects in single-grain quartz dose distribution. Radiation Measurements 41, 1032-1039.

McMorris, D.W., 1970. ESR detection of fossil alpha damage in quartz. Nature 226, 146.

Mejdahl, V., 1979. Thermoluminescence dating: Beta-dose attenuation in quartz grains. Archaeometry 21, 61-72.

Mejdahl, V., Bøtter-Jensen, L., 1994. Luminescence dating of archaeological materials using a new technique based on single aliquot measurements. Quaternary Science Reviews 13, 551-554.

Melnikov, P.V., Moiseev, B.M., Shekhvatov, D.B., 1989. Natural radiation parameters of Al-center in quartz. Geokhimiya 7, 1015-1020.

Molnar, P., England, P., 1990. Late Cenozoic uplift of mountain ranges and global climate change: chicken or egg? Nature 346, 29-34.

Nathan, R., Thomas, P., Jain, M., Murray, A., Rhodes, E., 2003. Environmental dose rate heterogeneity of beta radiation and its implications for luminescence dating: Monte Carlo modelling and experimental validation. Radiation Measurements 37, 305-313.

Nuttall, R., Weil, J., 1981. The magnetic properties of the oxygen-hole aluminum centers

in crystalline SiO_2. I.$[AlO_4]^0$. Canadian Journal of Physics 59, 1696-1708.

Peyton, S.L., Carrapa, B., 2013. An Introduction to Low-temperature Thermochronologic Techniques, Methodology, and Applications.

Plachy, A., Sutton, S., 1982. Determination of the dose-rate to quartz in granite, PACT, pp. 188-194.

Prescott, J.R., Hutton, J.T., 1988. Cosmic ray and gamma ray dosimetry for TL and ESR. International Journal of Radiation Applications and Instrumentation. Part D. Nuclear Tracks and Radiation Measurements 14, 223-227.

Prescott, J.R., Huntley, D.J., Hutton, J.T., 1993. Estimation of equivalent dose in thermoluminescence dating—the Australian slide method. Ancient TL 11, 1-5.

Prêt, D., Sammartino, S., Beaufort, D., Meunier, A., Fialin, M., Michot, L.J., 2010. A new method for quantitative petrography based on image processing of chemical element maps: Part I. Mineral mapping applied to compacted bentonites. American Mineralogist 95, 1379-1388.

Randall, J., Wilkins, M.H.F., 1945. Phosphorescence and electron traps-I. The study of trap distributions. Proc. R. Soc. Lond. A 184, 365-389.

Ratschbacher, L., Frisch, W., Liu, G., Chen, C., 1994. Distributed deformation in southern and western Tibet during and after the India-Asia collision. Journal of Geophysical Research 99, 19917-19945.

Reiners, P.W., Ehlers, T.A., Zeitler, P.K., 2005. Past, present, and future of thermochronology. Reviews in Mineralogy and Geochemistry 58, 1-18.

Reiners, P.W., Farley, K.A., 1999. Helium diffusion and (U–Th)/He thermochronometry of titanite. Geochimica et Cosmochimica Acta 63, 3845-3859.

Rink, W.J., 1997. Electron spin resonance (ESR) dating and ESR applications in Quaternary science and archaeometry. Radiation Measurements 27, 975-1025.

Rink, W.J., Bartoll, J., Schwarcz, H.P., Shane, P., Baryosef, O., 2007. Testing the reliability of ESR dating of optically exposed buried quartz sediments. Radiation Measurements 42, 1618-1626.

Rinneberg, H., Weil, J., 1972. EPR studies of Ti^{3+}-H^+ centers in X-irradiated α-quartz. The Journal of Chemical Physics 56, 2019-2028.

Romanyukha, A.A., Cunningham, A.C., George, S.P., Guatelli, S., Petasecca, M., Rosenfeld, A.B., Roberts, R.G., 2017. Deriving spatially resolved beta dose rates in sediment using the Timepix pixelated detector. Radiation Measurements 106, 483-490.

Rudra, J.K., Fowler, W.B., 1987. Oxygen vacancy and the E_1' center in crystalline SiO_2. Physical Review B 35, 8223.

Rufer, D., Preusser, F., 2009. Potential of autoradiography to detect spatially resolved radiation patterns in the context of trapped charge dating. Geochronometria 34, 1-13.

Sandiford, M., 2003. Geomorphic constraints on the Late Neogene tectonics of the Otway Range, Victoria. Australian Journal of Earth Sciences 50, 69-80.

Scherer, T., Agel, A., Hafner, S., 1993. Determination of uplift rates using EPR investigations of quartz. KTB Report, 121-124.

Scherer, T., Plötze, M., Hafner, S., 1994. Paramagnetic defects of quartz in KTB and a drilling profile from Eldzhurtinskiy Granite, Russia. KTB Rep. 94, B25.

Schnadt, R., Räuber, A., 1971. Motional effects in the trapped-hole center in smoky quartz. Solid State Communications 9, 159-161.

Seward, D., Burg, J., 2008. Growth of the Namche Barwa Syntaxis and associated evolution of the Tsangpo Gorge: Constraints from structural and thermochronological data. Tectonophysics 451, 282-289.

Shi, Y., Liu, C., Kang, E., 2009. The Glacier Inventory of China. Annals of Glaciology 50, 1-4.

Shimokawa, K., Imai, N., 1987. Simultaneous determination of alteration and eruption ages of volcanic rocks by electron spin resonance. Geochimica et Cosmochimica Acta 51, 115-119.

Shimokawa, K., Imai, N., Moriyama, A., 1988. ESR dating of volcanic and baked rocks. Quaternary Science Reviews 7, 529-532.

Siddiqui, S., Khamees, A.A., 2004. Dual-energy CT-scanning applications in rock characterization, SPE annual technical conference and exhibition. Society of Petroleum Engineers.

Sol, S., Meltzer, A.S., Burgmann, R., Der Hilst, R.D.V., King, R.W., Chen, Z., Koons,

P.O., Lev, E., Liu, Y.P., Zeitler, P.K., 2007. Geodynamics of the southeastern Tibetan Plateau from seismic anisotropy and geodesy. Geology 35, 563-566.

Struckmeyer, H.I., 1988. Source rock and maturation characteristics of the sedimentary sequence of the Otway Basin, Australia. University of Wollongong.

Tagami, T., Carter, A., Hurford, A.J., 1996. Natural long-term annealing of the zircon fission-track system in Vienna Basin deep borehole samples: constraints upon the partial annealing zone and closure temperature. Chemical Geology 130, 147-157.

Tang, S., 2015. Low temperature thermochronological luminescence dating study and its application to the Fugong valley of Nujiang River and the Longyangxia gorge of Yellow River in the eastern Tibetan Plateau. University of Hong Kong.

Toyoda, S., Ikeya, M., 1991a. Thermal stabilities of paramagnetic defect and impurity centers in quartz: Basis for ESR dating of thermal history. Geochemical Journal 25, 437-445.

Toyoda, S., Ikeya, M., 1991b. ESR dating of quartz and plagioclase from volcanic ashes using E'1, A1 and Ti centers. International Journal of Radiation Applications and Instrumentation. Part D. Nuclear Tracks and Radiation Measurements 18, 179-184.

Toyoda, S., Ikeya, M., 1994. ESR dating of quartz with stable component of impurity centers. Quaternary Science Reviews 13, 625-628.

Toyoda, S., Schwarcz, H.P., 1997. The hazard of the counterfeit E_1' signal in quartz to the ESR dating of fault movements. Quaternary Science Reviews 16, 483-486.

Toyoda, S., Falguères, C., 2003. The method to represent the ESR signal intensity of the aluminium hole center in quartz for the purpose of dating. Advances in ESR applications 20, 7-10.

Toyoda, S., Tsukamoto, S., Hameau, S., Usui, H., Suzuki, T., 2006. Dating of Japanese Quaternary tephras by ESR and luminescence methods. Quaternary Geochronology 1, 320-326.

Toyoda, S., Miura, H., Tissoux, H., 2009. Signal regeneration in ESR dating of tephra with quartz. Radiation Measurements 44, 483-487.

Toyoda, S., 2015. Paramagnetic lattice defects in quartz for applications to ESR dating. Quaternary Geochronology 30, 498-505.

Tsukamoto, S., Toyoda, S., Tani, A., Oppermann, F., 2015. Single aliquot regenerative dose method for ESR dating using X-ray irradiation and preheat. Radiation Measurements 81, 9-15.

Tsukamoto, S., Long, H., Richter, M., Li, Y., King, G.E., He, Z., Yang, L., Zhang, J., Lambert, R., 2018. Quartz natural and laboratory ESR dose response curves: A first attempt from Chinese loess. Radiation Measurements 120, 137-142.

Tu, J., Ji, J., Sun, D., Gong, J., Zhong, D., Han, B., 2015. Thermal structure, rock exhumation, and glacial erosion of the Namche Barwa Peak, constraints from thermochronological data. Journal of Asian Earth Sciences 105, 223-233.

Wagner, G., Gleadow, A., Fitzgerald, P., 1989. The significance of the partial annealing zone in apatite fission-track analysis: Projected track length measurements and uplift chronology of the Transantarctic Mountains. Chemical Geology: Isotope Geoscience Section 79, 295-305.

Wagner, G.A., Glasmacher, U.A., Greilich, S., 2005. Spatially resolved dose-rate determination in rocks and ceramics by neutron-induced fission tracks: fundamentals. Radiation measurements 40, 26-31.

Wang, P., Scherler, D., Liuzeng, J., Mey, J., Avouac, J., Zhang, Y., Shi, D., 2014. Tectonic control of Yarlung Tsangpo Gorge revealed by a buried canyon in Southern Tibet. Science 346, 978-981.

Weeks, R., 1956. Paramagnetic resonance of lattice defects in irradiated quartz. Journal of Applied Physics 27, 1376-1381.

Weeks, R.A., 1994. The many varieties of E' centers: a review. Journal of non-crystalline solids 179, 1-9.

Weil, J.A., 1984. A review of electron spin spectroscopy and its application to the study of paramagnetic defects in crystalline quartz. Physics and Chemistry of Minerals 10, 149-165.

Whipple, K.X., 2014. Can erosion drive tectonics. Science 346, 918-919.

Whitehead, L., Whitehead, R., Valeur, B., Berberan-Santos, M., 2009. A simple function for the description of near-exponential decays: The stretched or compressed hyperbola. American Journal of Physics 77, 173-179.

Woda, C., Wagner, G., 2007. Non-monotonic dose dependence of the Ge-and Ti-centres in quartz. Radiation Measurements 42, 1441-1452.

Wolf, R., Farley, K., Kass, D., 1998. Modeling of the temperature sensitivity of the apatite (U–Th)/He thermochronometer. Chemical Geology 148, 105-114.

Xu, Z., Ji, S., Cai, Z., Zeng, L., Geng, Q., Cao, H., 2012. Kinematics and dynamics of the Namche Barwa Syntaxis, eastern Himalaya: Constraints from deformation, fabrics and geochronology. Gondwana Research 21, 19-36.

Yang, R., Herman, F., Fellin, M.G., Maden, C., 2018. Exhumation and topographic evolution of the Namche Barwa Syntaxis, eastern Himalaya. Tectonophysics 722, 43-52.

Yao, T., Li, Z., Yang, W., Guo, X., Zhu, L., Kang, S., Wu, Y., Yu, W., 2010. Glacial distribution and mass balance in the Yarlung Zangbo River and its influence on lakes. Chinese Science Bulletin 55, 2072-2078.

Yao, T., Thompson, L.G., Yang, W., Yu, W., Gao, Y., Guo, X., Yang, X., Duan, K., Zhao, H., Xu, B., 2012. Different glacier status with atmospheric circulations in Tibetan Plateau and surroundings. Nature Climate Change 2, 663-667.

Yin, A., Dubey, C.S., Kelty, T.K., Gehrels, G.E., Chou, C.Y., Grove, M., Lovera, O.M., 2006. Structural evolution of the Arunachal Himalaya and implications for asymmetric development of the Himalayan orogen. Current Science 90, 195-206.

Ypma, P.J., Hochman, M.B., 1991. Thermoluminescence geothermometry—a case study of the Otway Basin. The APPEA Journal 31, 312-324.

Zeitler, P.K., Meltzer, A.S., Koons, P.O., Craw, D., Hallet, B., Chamberlain, C.P., Kidd, W.S.F., Park, S.K., Seeber, L., Bishop, M.P., 2001. Erosion, Himalayan geodynamics, and the geomorphology of metamorphism. Gsa Today 11, 4-9.

Zeitler, P.K., Meltzer, A.S., Brown, L., Kidd, W.S., Lim, C., Enkelmann, E., 2014. Tectonics and topographic evolution of Namche Barwa and the easternmost Lhasa block, Tibet. Toward an Improved Understanding of Uplift Mechanisms and the Elevation History of the Tibetan Plateau: Geological Society of America Special Paper 507, 23.

Zeller, E., Levy, P., Mattern, P., 1967. Geologic dating by electron spin resonance, Proceedings of the Symposium on radioactive dating and low level counting (IAEA,

Wien), pp. 531-540.

Zeller, E.J., 1968. Use of electron spin resonance for measurement of natural radiation damage, Thermoluminescence of geological materials. Academic Press London, pp. 271-279.

Zhang, P., Molnar, P., Downs, W.R., 2001. Increased sedimentation rates and grain sizes 2-4 Myr ago due to the influence of climate change on erosion rates. Nature 410, 891.

Zhang, J., Ji, J., Zhong, D., Ding, L., He, S., 2004. Structural pattern of eastern Himalayan syntaxis in Namjagbarwa and its formation process. Science China-earth Sciences 47,

Zhou, J., Tits, A., Lawrence, C., 1997. User's Guide for FFSQP Version 3.7: A Fortran code for solving optimization programs, possibly minimax, with general inequality constraints and linear equality constraints, generating feasible iterates. Institute for Systems Research, University of Maryland, Technical Report SRC-TR-92-107r5, College Park, MD 20742, 1997.

8 Appendix

This chapter contains the supplementary materials from the journal publications included in the main content of the thesis, and the first pages of publications which have resulted from the measurements of a range of tooth samples.

Section 8.1: Supplementary material: ESR thermochronometry of Al and Ti centres in quartz: A case study of the Fergusons Hill-1 borehole from the Otway Basin, Australia

Section 8.2: Supplementary material: ESR thermochronometric evidence for accelerated Mid-Pleistocene exhumation of the Namche Barwa massif, eastern Himalayan syntaxis

Section 8.3: Willmes, M., Grün, R., Douka, K., Michel, V., Armstrong, R., Benson, A., Crégut-Bonnoure, E., Desclaux, E., Fang, F., Kinsley, L., Saos, T., Defleur, A.R., 2016. A comprehensive chronology of the Neanderthal site Moula-Guercy, Ardèche, France. Journal of Archaeological Science: Reports, 9, 309-319.

Section 8.4: Villa, P., Soriano, S., Grün, R., Marra, F., Nomade, S., Pereira, A., Boschian, G., Pollarolo, L., Fang, F., Bahain, J-J., 2016. The Acheulian and Early Middle Paleolithic in Latium (Italy): Stability and Innovation. PLoS ONE 11(8): e0160516.

Section 8.5: Duval, M., Fang, F., Grün, R., Suraprasit, K., Jaeger, J-J., Benammi, M., Chaimanee, Y., 2019. U-series and combined US-ESR dating of fossil teeth from the late Middle Pleistocene vertebrate locality Khok Sung, Nakhon Ratchasima Province, Northeastern Thailand. Palaeontologia Electronica 22.3.69, 1-25.

8.1 Supplementary material: ESR thermochronometry of Al and Ti centres in quartz: A case study of the Fergusons Hill-1 borehole from the Otway Basin, Australia

In ESR dating, the irradiation of quartz grains is generally delivered by a Gamma source. Due to occupational health and safety regulations, such an irradiation source is not available in Canberra. Instead, an X-ray irradiator has been used in the study. The key question is to determine the X-ray dose rate on quartz. In the first step, the in-air X-ray dose rate is estimated. In the second step, the ESR intensities of Al and Ti centres in quartz were compared after irradiation by a calibrated Gamma source and the X-ray irradiator.

8.1.1 The calibration of in-air X-ray dose rate

The RS2000 X-ray irradiator (160 kV, 25 mA) is installed at the John Curtin School of Medical Research, the Australian National University. A real-time monitor (Rad Cal Real-Time ion-chamber dosimeter, see Figure 8.1a) was applied to estimate the in-air dose rate. Firstly, a probe was placed in the centre of the chamber at the same place and height which the sample holder (Figure 8.1b) would be sited during irradiation. The in-air dose rate was calculated as the average rate for 5 minutes. This process was repeated in three days and the results were consistent as 6.445 Gy/min, indicating the X-ray irradiator is stable for sample irradiation. Secondly, the probe was placed in several locations within the range of positions where the sample holder would be sited. The detected in-air dose rates were constant indicating that the samples could be evenly dosed.

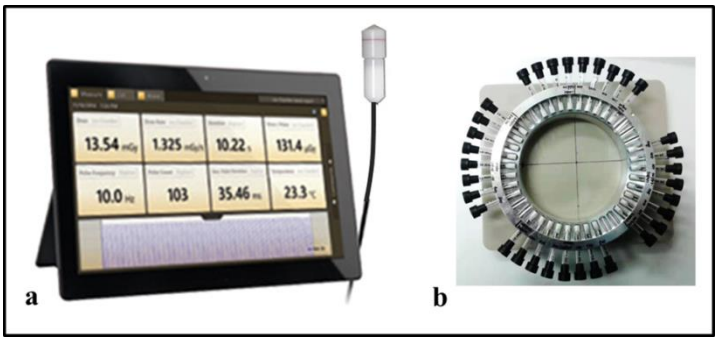

Figure 8.1: (a) Rad Cal Real-Time dosimeter and probe for in-air dose rate calibration. (b) In the sample holder, weighted aliquots are enclosed in quartz tubes for irradiation.

8.1.2 The calibration of X-ray dose rate on quartz

8.1.2.1 Quartz extraction

Sample preparation was carried out on a granitic rock collected from the eastern Himalayan syntaxis at the University of Hong Kong. The crushed sample was sieved to extract the 150–250 μm grain size. Density separation in sodium polytungstate was used to obtain quartz in the density range 2.62–2.68 g/cm^3. The quartz-rich fractions were etched in 40% HF for 40 min to remove both possibly alpha damaged surfaces and remaining feldspars, and subsequently rinsed with 10% HCl to dissolve fluorides. This sample was dried at room temperature and re-sieved at 100 μm.

8.1.2.2 Gamma and X-ray irradiation

The sample was divided into 12 aliquots, and each aliquot contained 60 mg quartz grains. The Gamma irradiation was carried out at Centro de Nacional de Investigación Sobre la Evolución Humana (CENIEH) by a Best Theratronics Cs-137 Gammacell-1000 irradiator. Its dose rate on quartz is calibrated as 6.9 Gy/min. Six aliquots were irradiated with dose steps of 0, 38, 100, 197, 390, 807 Gy, respectively. For X-ray irradiation, the other six aliquots were irradiated with dose steps (in-air dose) of 0, 40, 100, 200, 400 and 800 Gy, respectively.

8.1.2.3 ESR measurements

ESR measurements were carried out on an X-band Bruker spectrometer with a 1.5T magnet and a rectangular 4102 ST cavity. The measurements of Al and Ti centres were conducted at 77 °K by inserting a quartz-glass tube into a finger dewar filled with liquid nitrogen. The parameters for Al and Ti centres were accumulation of 20 scans with 100 kHz modulation frequency, 0.1 mT modulation amplitude, 10.24 ms conversion factor, 20.48 ms time constant, 1024 bit spectrum resolution, 5.065 mW microwave power, centre field of 3410 G and sweep width of 360 G. Considering the angular dependence of the ESR signal, each aliquot was measured six times after a 60° rotation of the dewar in the cavity. The peak to peak height between g = 2.018 and g = 1.993 was used as the intensity of the Al centre. The ESR intensity of Ti-Li centre was defined as the amplitude

between the top of peak at g = 1.979 and the bottom of peak around g = 1.913.

8.1.2.4 Results

To calibrate the dose rate of X-ray irradiation on quartz, the ESR intensities of Al and Ti centres generated by Gamma and X-ray irradiation were calculated by subtracting the natural intensities from those after irradiation with additive doses. The increased intensities show a linear correlation between Gamma and X-ray irradiations (Figure 8.2). For Al and Ti centres, the Gamma dose rates on quartz are 0.66 and 0.70 of X-ray in-air dose rates, respectively. The dose rate of Gamma source is 6.9 Gy/min, and therefore the average X-ray dose rate is 10.15 Gy/min.

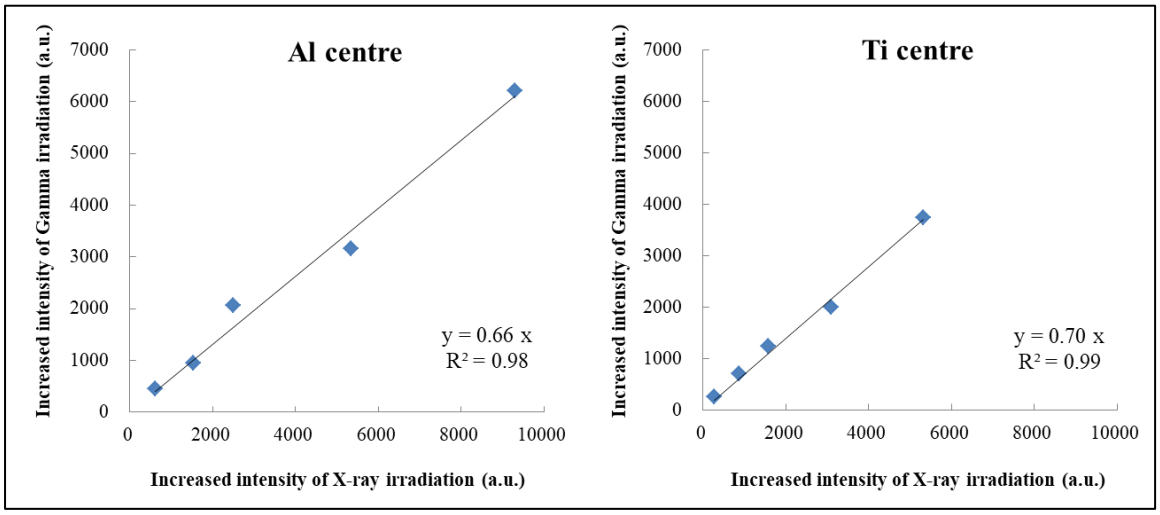

Figure 8.2: Increased ESR intensities of X-ray irradiation versus that of Gamma irradiation. The data points start with the dose step of 40 Gy and end with the dose step of 800 Gy.

8.2 Supplementary material: ESR thermochronometric evidence for accelerated Mid-Pleistocene exhumation of the Namche Barwa massif, eastern Himalayan syntaxis

The I_1/I_2 ratio of E' centre is the intensity of the unheated sample (I_1) over the maximum intensity (I_2) after heating at 250 °C. Thus, the selection of microwave power and annealing time is essential. In the previous studies of Chen et al. (1997) and Grün et al. (1999), samples were annealed at 250 °C for 60 min and measured in the microwave power of 0.2 mW and 0.05 mW, respectively. The following experiments aim to determine suitable measurement parameters for samples collected from the eastern Himalayan syntaxis.

8.2.1 Sample collection and preparation

Six granitic rocks (NB13-02, NB13-12, NB13-13, NB13-20, NB13-23, NB13-33) were collected from the eastern Himalayan syntaxis and its surrounding area in 2013 (Figure 8.3). The quartz extraction followed the same procedure as described in section 5.3.1.

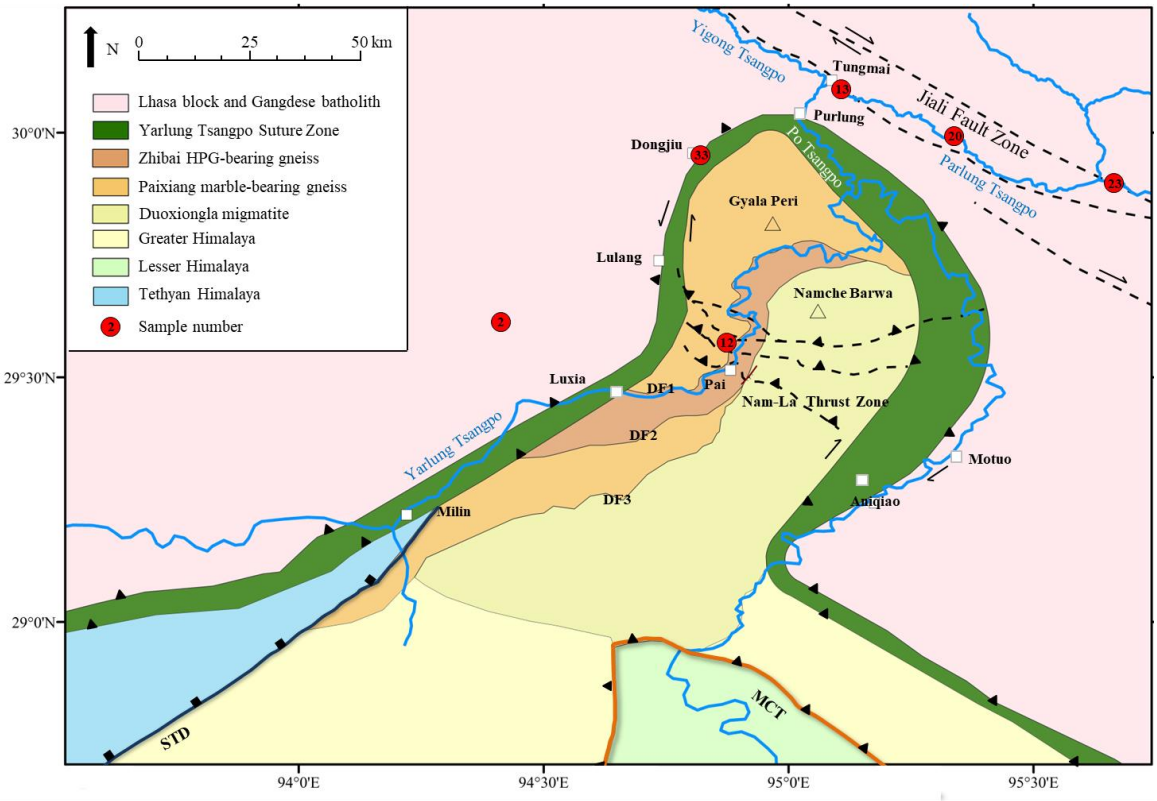

Figure 8.3: The geological map of eastern Himalayan syntaxis.

8.2.2 Microwave power

The optimal microwave power setting can minimize the contribution from unwanted peaks and maximize that of the desired peaks. As its strength has a relationship with the attenuation factor shown in Figure 8.4, the value of the attenuation factor was used instead in the following part to simplify the description.

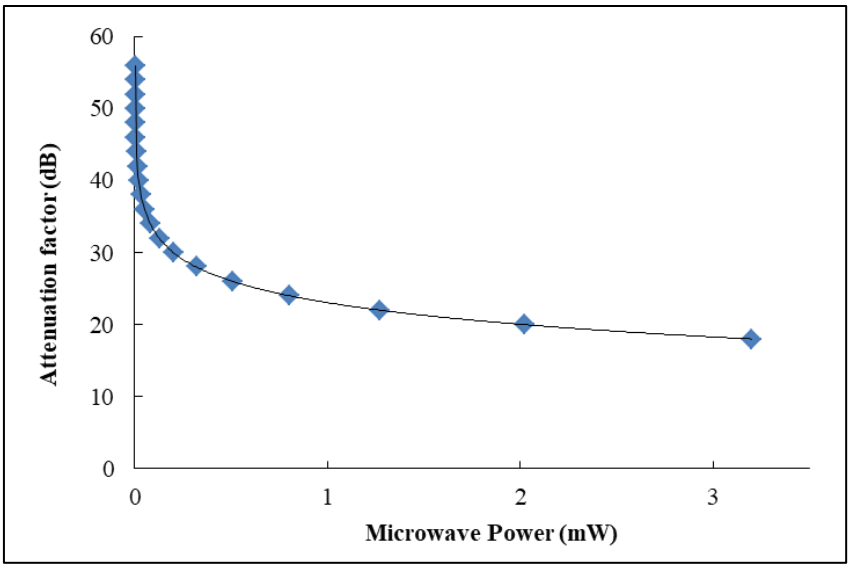

Figure 8.4: The relationship between microwave power and attenuation factor.

One aliquot containing 60 mg quartz grains was analysed for each sample. The measurements were carried out at: room temperature, accumulation of 10 scans with 0.05 mT modulation amplitude, 40.96 ms conversion factor, 40.96 ms time constant, 1024 bit spectrum resolution, and the attenuation factor increasing from 18 to 56 dB with a step width of 2 dB. The intensity of E' centre was calculated as the peak to peak height at g = 2.0005.

During the measurements, the ESR spectra showed that the peaks of E' centre could be masked by interference peaks when the attenuation factor was lower than 28 dB, and the tuning process became difficult when the attenuation factor was higher than 50 dB. The E' intensities of all samples had normal distribution patterns with increasing attenuation factor (Figure 8.5) and reached to the maximum between the factor of 34 and 40 dB. Compared to the parameters used in Chen et al. (1997) and Grün et al. (1999), the microwave power of 0.05 mW (corresponding to attenuation of 36 dB) was selected for

further analysis.

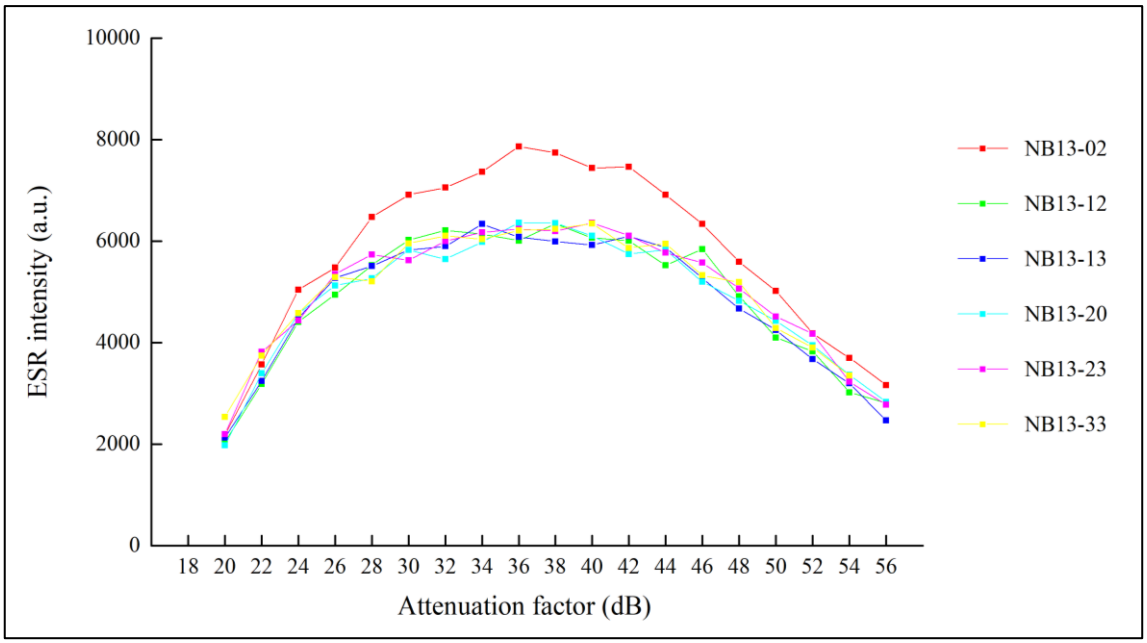

Figure 8.5: ESR intensity of E' centre as a function of increasing attenuation factor.

8.2.3 Isothermal annealing time

In the isothermal annealing experiment at 250 °C, one aliquot of each sample (NB13-02, NB13-12, NB13-23) containing 60 mg of quartz grains was used. Samples were filled into quartz tubes, and then the tubes were inserted into a furnace (Figure 8.6a) for heating with total time steps of 0, 10, 20, 30, 40, 50, 60, 80, 100, 120, 140, 160, 180, 210 and 240 min. The effective temperature inside the furnace was checked by a thermocouple thermometer. After each heating step, E' intensity of each sample was measured when the aliquot cooled to room temperature. Microwave power of 0.05 mW was used in the measurements and other parameters remained the same as listed in section 8.2.2.

The results show that ESR intensities of E' centre increase exponentially with annealing time (Figure 8.6b). After a rapid increase in the first 10 min, intensity plateau was formed after about 30 min for sample NB13-12 and NB13-23, while about 100 min for NB13-02. To ensure the signal of E' centre can be enhanced to its maximum at 250 °C, heating of 100 min has been selected for determining I_2 intensity.

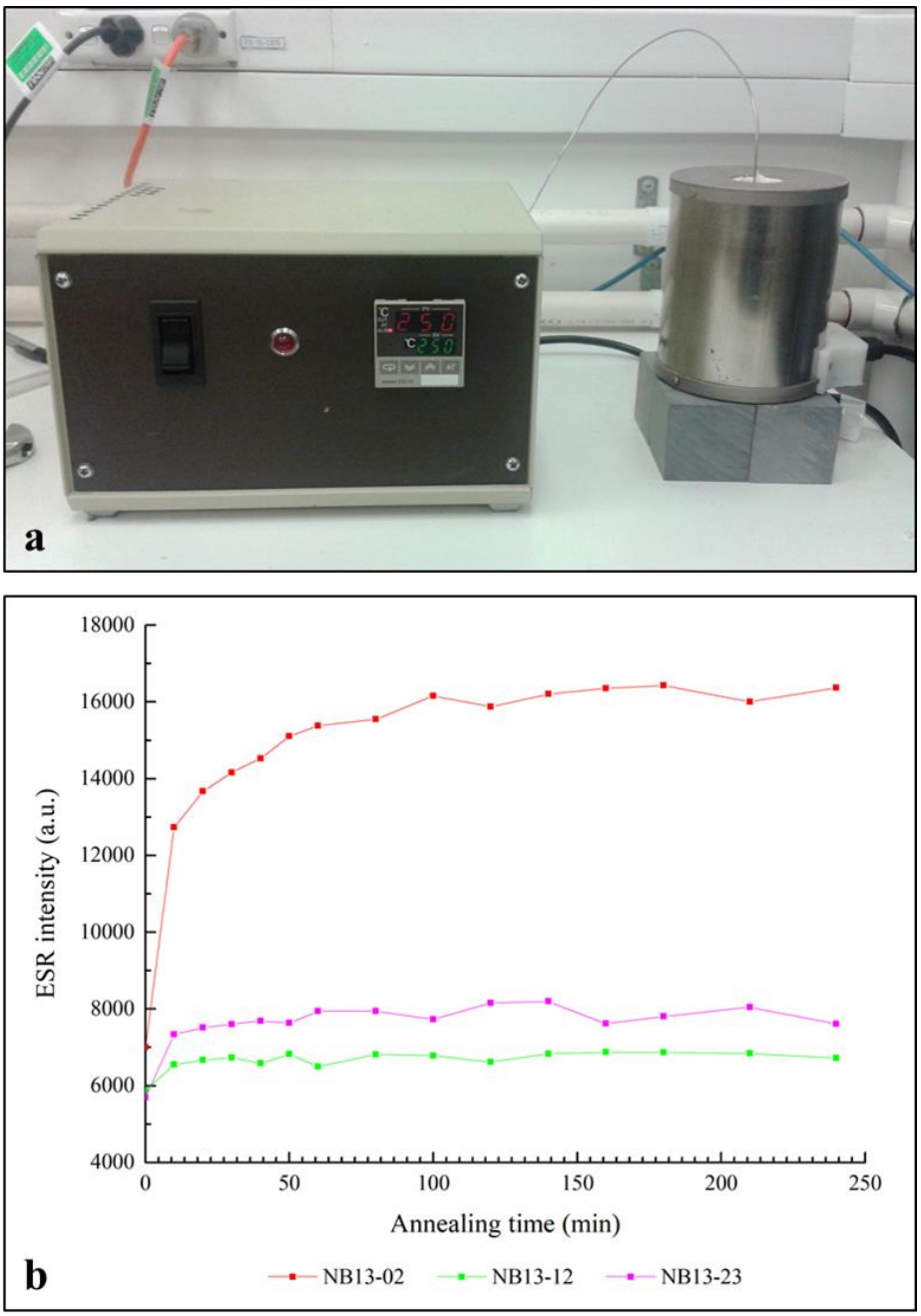

Figure 8.6: (a) The furnace used for isothermal annealing experiment at 250 °C. (b) ESR intensity of E'centre as a function of increasing annealing time at 250 °C.

Journal of Archaeological Science: Reports 9 (2016) 309–319

Contents lists available at ScienceDirect

Journal of Archaeological Science: Reports

journal homepage: www.elsevier.com/locate/jasrep

A comprehensive chronology of the Neanderthal site Moula-Guercy, Ardèche, France

Malte Willmes [a,*], Rainer Grün [a,1], Katerina Douka [b], Véronique Michel [c,d], Richard A. Armstrong [a], Alexa Benson [a,2], Evelyne Crégut-Bonnoure [e,f], Emmanuel Desclaux [g], Fang Fang [a], Leslie Kinsley [a], Thibaud Saos [h], Alban R. Defleur [i]

[a] Research School of Earth Sciences, The Australian National University, 142 Mills Road, 2601 Acton, ACT, Australia
[b] Research Laboratory for Archaeology and the History of Art, University of Oxford, Dyson Perrins Building, South Parks Road, OX1 3QY Oxford, UK
[c] Université Nice Côte d'Azur, CNRS, CEPAM, SJA3, 24 Avenue des Diables bleux, 06357 Nice, Cedex 4, France
[d] Université Nice Côte d'Azur, CNRS, OCA, IRD, Géoazur, France
[e] Museum Réquien, 67 Rue Joseph Vernet, Avignon, France
[f] UMR 5608 TRACES (UTM), 5 allées Antonio Machado, 31058 Toulouse Cedex 1, Toulouse, France
[g] Laboratoire départemental de Préhistoire du Lazaret – UMR7194 CNRS, 33 Bis Boulevard Franck Pilatte, 06300 Nice, France
[h] Université de Perpignan Via Domitia, UMR-CNRS 7194, EPCC Centre Européen de Recherches Préhistoriques, Avenue Léon-Jean Grégory, 66720 Tautavel, France
[i] CNRS UMR 5276 - Laboratoire de Géologie de Lyon, Ecole Normale Supérieure de Lyon, 46, Allée d'Italie, 69364 Lyon Cedex 07, France

ARTICLE INFO

Article history:
Received 7 March 2016
Received in revised form 8 August 2016
Accepted 8 August 2016
Available online 15 August 2016

Keywords:
Fossil teeth
Radiocarbon dating
U-series dating
ESR dating
Biostratigraphy
Neanderthal

ABSTRACT

The Baume (cave) Moula-Guercy, in southeast France, contains an important sedimentary sequence, which includes the remains of a cannibalised group of Neanderthals. The chronology of the upper layers of the cave is currently constrained by a thermoluminescence date of 72 ± 12 ka, obtained from a tephra deposit (layer VI). The middle and lower layers of the cave have been constrained by biostratigraphy, pointing towards the end of MIS 5 for the Neanderthal bearing layer XV. In order to refine the chronology of the site, we applied radiocarbon, $^{40}Ar/^{39}Ar$, U-series and ESR dating analyses. Radiocarbon dates on bone samples from layer IV showed ages older than 50 ka. $^{40}Ar/^{39}Ar$ dating on sanidines from tephra of layer VI revealed, that these volcanic minerals derived probably from the Hercynian basement, and thus provided no tangible chronological constrain. Combined CSUS/ESR results on faunal teeth place layer IV at the end of MIS 3 to MIS 4, in agreement with the radiocarbon dates and in stratigraphic order with the thermoluminescence age for layer VI. Layer VIII, with only one sample, is tentatively placed to the end of MIS 4. The age estimates for layer XIV are not conclusive, preventing an age estimation for this layer. The younger age result for layer XIV does not agree with the stratigraphy and biostratigraphy of the site and more direct dating of material from this layer is needed to resolve this discrepancy. Located just below, the crucial Neanderthal bearing layer XV is placed to the end of MIS 5 and younger than MIS 6, in agreement with the climatological and chronological deductions from the stratigraphy and biostratigraphy of the site. Direct U-series analyses on two Neanderthal teeth agree with an age for layer XV corresponding to at least MIS 5 *sensu lato*. The U-series results on the Neanderthal tooth 3525 show that U-mobilisation even into small teeth is highly complex, but nevertheless give an indication that this sample corresponds to MIS 5e. This is in agreement with the CSUS/ESR results from faunal teeth as well as the stratigraphy and biostratigraphy of the cave. The refined chronology corroborates the existing stratigraphic and biostratigraphic framework. Moula-Guercy layer XV, with its many human remains showing cannibalism, now stands as a reference site for this particular aspect of human behaviour.

1. Introduction

1.1. The site of Moula-Guercy

The Baume (cave) Moula-Guercy is located 80 m above the west bank of the Rhône River near the city of Valence, southeastern France, in the parish of Soyons, Ardèche (Fig. 1). The site was discovered in 1970 and excavated between 1975 and 1982 by P. Payen

* Corresponding author at: Department of Wildlife, Fish, & Conservation Biology, University of California Davis, CA, USA.
E-mail address: malte.willmes@googlemail.com (M. Willmes).
[1] Now at: Research Centre of Human Evolution, Environmental Futures Research Institute, Griffith University, Nathan, QLD 4111, Australia.
[2] Now at: Department of Human Evolution, Max Planck Institute of Evolutionary Anthropology, 04103 Leipzig, Germany.

http://dx.doi.org/10.1016/j.jasrep.2016.08.003
2352-409X/

PLOS ONE

RESEARCH ARTICLE

The Acheulian and Early Middle Paleolithic in Latium (Italy): Stability and Innovation

Paola Villa[1,2,3]*, Sylvain Soriano[4], Rainer Grün[5,6], Fabrizio Marra[7], Sebastien Nomade[8], Alison Pereira[8,9,10,11], Giovanni Boschian[12], Luca Pollarolo[3,13], Fang Fang[5,6], Jean-Jacques Bahain[9]

1 University of Colorado Museum, Boulder, Colorado, 80309–0265, United States of America, **2** Istituto Italiano di Paleontologia Umana, Rome, Italy, **3** School of Geography, Archaeology and Environmental Studies, University of the Witwatersrand, Johannesburg, South Africa, **4** ArScAn, AnTET, CNRS, Université Paris Ouest, 92023, Nanterre, France, **5** Research School of Earth Sciences, The Australian National University, Canberra, ACT, 2601, Australia, **6** Research Centre of Human Evolution, Griffith University, Nathan, QLD, 4111, Australia, **7** Istituto Nazionale di Geofisica e Vulcanologia, 00147, Roma, Italy, **8** Laboratoire des Sciences du climat et de l'environnement, CEA Saclay, UMR 8212, UVSQ et Université de Paris-Saclay, 91198, Gif-sur-Yvette, France, **9** Département de Préhistoire, Museum National d'Histoire Naturelle, UMR 7194, 75013, Paris, France, **10** Sezione di Scienze Preistoriche e Antropologiche, Dipartimento di Studi Umanistici, Università di Ferrara, Ferrara, Italy, **11** Ecole française, Roma, Italy, **12** Dipartimento di Biologia, Università di Pisa, 56126, Pisa, Italy, **13** Laboratoire Archéologie et Peuplement de l'Afrique, Department of Genetics and Evolution, University of Geneva, 1211, Geneva, Switzerland

* villap@colorado.edu

OPEN ACCESS

Citation: Villa P, Soriano S, Grün R, Marra F, Nomade S, Pereira A, et al. (2016) The Acheulian and Early Middle Paleolithic in Latium (Italy): Stability and Innovation. PLoS ONE 11(8): e0160516. doi:10.1371/journal.pone.0160516

Editor: Nuno Bicho, Universidade do Algarve, PORTUGAL

Received: April 21, 2016

Accepted: July 20, 2016

Published: August 15, 2016

Data Availability Statement: All relevant data are within the paper and its Supporting Information files.

Funding: This work is funded by the National Science Foundation, BCS 1118143, grant to PV, SS. CNRS, UMR 7041, ArScAn/AnTET, Nanterre, grant to SS.

Competing Interests: The authors have declared that no competing interests exist.

Abstract

We present here the results of a technological and typological analysis of the Acheulian and early Middle Paleolithic assemblages from Torre in Pietra (Latium, Italy) together with comparisons with the Acheulian small tools of Castel di Guido. The assemblages were never chronometrically dated before. We have now $^{40}Ar/^{39}Ar$ dates and ESR-U-series dates, within a geomorphological framework, which support correlations to marine isotope stages. The Acheulian (previously correlated to MIS 9) is now dated to MIS 10 while the Middle Paleolithic is dated to MIS 7. Lithic analyses are preceded by taphonomic evaluations. The Levallois method of the Middle Paleolithic assemblage is an innovation characterized by the production of thin flake blanks without cortex. In contrast, the small tool blanks of the Acheulian were either pebbles or thick flakes with some cortex. They provided a relatively easy manual prehension. The choice of Levallois thin flake blanks in the Middle Paleolithic assemblage suggest that the new technology is most likely related to the emergence of hafting. Accordingly, the oldest direct evidence of hafting technology is from the site of Campitello Quarry in Tuscany (Central Italy) where birch-bark tar, found on the proximal part of two flint flakes, is dated to the end of MIS 7. Nevertheless, a peculiar feature of the Middle Paleolithic at Torre in Pietra is the continuous presence of small tool blanks on pebbles and cores and on thick flake albeit at a much lower frequency than in the older Acheulian industries. The adoption of the new technology is thus characterized by innovation combined with a degree of stability. The persistence of these habits in spite of the introduction of an innovative technique underlies the importance of cultural transmission and conformity in the behavior of Neandertals.

Palaeontologia Electronica
palaeo-electronica.org

Direct ESR dating of the Pleistocene vertebrate assemblage from Khok Sung locality, Nakhon Ratchasima Province, Northeast Thailand

Mathieu Duval, Fang Fang, Kantapon Suraprasit, Jean-Jacques Jaeger, Mouloud Benammi, Yaowalak Chaimanee, Javier Iglesias Cibanal, and Rainer Grün

ABSTRACT

We report here the first direct dating study of the faunal assemblage from Khok Sung locality, Thailand. This palaeontological site is of great biochronological, palaeoenvironmental and biogeographical significance. Firstly, it has yielded a rich and diversified Pleistocene vertebrate fauna with up to 15 mammalian species from 13 genera, 10 reptile species, as well as fish and bird remains. Interestingly, while most of the mainland Southeast Asian Pleistocene mammal fossils originate from cave deposits, the Khok Sung fossil layer is located within an 8 m thick fluvial terrace. Secondly, it is geographically located in an area of major importance for reconstructing the migration pathway of large mammals between South China and Java.

Combined US-ESR dating of five teeth provides two possible ages of 130 ± 29 ka and 217 ± 36 ka for the fossils. The reason for the occurrence of these two age groups lies in the fact that it was not possible to obtain sediments that were directly associated with the measured samples, nor was it possible to carry out in situ gamma dose rate measurements due to the high water level. Sediment samples recovered from museum specimens show significantly variable concentrations of radioelements. Both options are equally plausible, as independent methods did not provide firm evidence favouring one or the other age range. The results illustrate the intrinsic limitations of the ESR dating method when fossil teeth are not collected in situ during the excavation.

Regardless whether the age of the Khok Sung fauna corresponds to MIS 7 or early MIS5, it is nevertheless one of the oldest assemblages directly dated in the region. Further efforts are required for more accurate fossil identification and attribution and for additional numerical dating in this region to improve the biochronological framework of the Pleistocene mammalian faunas in Southeast Asia, which presently remains quite imprecise.

Duval, Mathieu, Fang, Fang, Suraprasit, Kantapon, Jaeger, Jean-Jacques, Benammi, Mouloud, Chaimanee, Yaowalak, Iglesias Cibanal, Javier, and Grün, Rainer. 2019. Direct ESR dating of the Pleistocene vertebrate assemblage from Khok Sung locality, Nakhon Ratchasima Province, Northeast Thailand. *Palaeontologia Electronica* 22.3.69 1-25. https://doi.org/10.26879/941
palaeo-electronica.org/content/2019/2794-esr-dating-of-khok-sung-site